Catalytic conversion of CO_2 to methanol via CO_2 hydrogenation

An investigation of metal oxide promoted catalysts

by

Kristian Stangeland

Thesis submitted in fulfilment of
the requirements for the degree of
PHILOSOPHIAE DOCTOR
(PhD)

Faculty of Science and Technology
Department of Energy and Petroleum Engineering
2020

University of Stavanger
NO-4036 Stavanger
NORWAY
www.uis.no

ISBN:978-82-7644-988-4
ISSN:1890-1387
PhD: Thesis UiS No. 574

Acknowledgements

Firstly, I would like to express my sincere gratitude to my supervisor Professor Zhixin Yu. He's guidance and contributions has been extremely valuable over the course of this Ph.D. project. I would also like to thank Professor Hailong Li for his co-supervision.

I am very grateful for the help and support of my colleagues at the University of Stavanger. Thanks to Jostein Djuve, Inger Johanne M. Olsen, Per Eirik K. Widvey, Kim Andre N. Vorland, Ola Ketil Siqveland, Jon Arne Evjenth, and Svein Myhren for their support with the laboratory work, Wakshum M. Tucho for his help with the TEM, and Emanuela I. Kallesten and Caroline Ruud for XRD.

Thanks to my fellow Ph.D. candidates for their support over the course of the Ph.D. Special mention to Dori Yosef Kalai, Kun Guo, and Huong Lan Huynh for the interesting discussion and collaboration within the catalysis group. I would also like to thank the bachelor and master students that have been a part of the catalysis group over the years. Special thanks to Fawzi Chamssine and Hans Herrera Navarro for your assistance in the lab.

I would also like to thank Professor Xuezhi Duan for the productive and highly enjoyable research stay at East China University of Science and Technology. Thanks to Zikun Huang for the help with XRD, ICP, and HAADF STEM and Wenzhao Fu for XPS.

The financial support of the Research Council of Norway and the Department of Energy and Petroleum Engineering is also greatly acknowledged.

Abstract

CO_2 hydrogenation to methanol is a promising process for converting renewable energy into valuable fuels and chemicals, which can combat the emissions of greenhouse gases associated with the use of fossil resources. Developing novel reactors to overcome the severe thermodynamic restrictions and designing high-performance catalysts are of vital importance for the industrial implementation of the CO_2-to-methanol process. In this work, a thorough investigation of the thermodynamics and the role of metal oxide on the activity of Co- and Cu-based catalysts for CO_2-to-methanol is carried out.

First, the most promising catalyst systems for the industrial implementation of the CO_2-to-methanol process are reviewed. For the conventional Cu-based catalysts, the interaction between the active metal and the metal oxide promoters is a determining factor for the methanol synthesis activity of the catalyst. Alloying and metal-oxide interaction also play a determining role in the performance of the catalysts. The interaction between the main active component and the promoter(s) is also a determining factor for the performance of other methanol synthesis catalysts based on In_2O_3 or other transition metals.

Thereafter, a comprehensive thermodynamic analysis of CO_2 hydrogenation to methanol/CO and methanol/dimethyl ether/CO is performed. It is demonstrated that product condensation occurs at relevant reaction conditions for the CO_2-to-methanol process, which could be utilized to bypass the thermodynamic restrictions on the methanol yield. The condensation of products allows almost complete conversion of CO_2 into methanol and increases the methanol selectivity. Another option to increase the CO_2 conversion is to produce methanol and dimethyl ether in a single-step process. Product condensation also improves the yield of methanol and dimethyl ether.

The new catalyst system comprising of Co-Mn oxides is investigated. Mesoporous Co, Mn, and Co-Mn spinel oxide catalysts is prepared by a modified sol-gel inverse micelle method. The activity tests reveal that the Co-Mn oxide catalysts contain highly active sites for methanol synthesis that are not present on the monometallic Co and Mn oxide catalysts. Furthermore, the Co-Mn oxide catalyst exhibits very high methanol formation rates at low pressure compared to conventional Cu-based catalysts. Thus, the Co-Mn oxide system is a promising candidate for the low-pressure methanol synthesis process. However, further effort is needed to limit the formation of hydrocarbons to reduce the high methane selectivity.

For Cu based catalysts, the role of the Cu-ZnO interaction is studied by comparing the performance of $Cu/ZnO/Al_2O_3$ obtained from a hydrotalcite-like (HT) precursor to that of a malachite-derived Cu/ZnO catalysts. The HT-derived catalysts contain Cu particles partially embedded within a Zn-Al oxide matrix. The results show that the stronger Cu-ZnO interaction of the HT-derived catalyst increases the intrinsic activity and methanol selectivity. Sintering of the Zn-Al oxide phase during long-term tests is observed to decrease the methanol formation rate and selectivity. The influence of In promotion is also investigated. The addition of In can stabilize the Zn-Al oxide phase but the presence of In on the Cu surface seems to inhibit the active sites. The results demonstrate that optimizing and stabilizing the Cu-ZnO interaction is crucial to enhance the performance of Cu/ZnO-based catalysts.

The Cu-oxide interaction is further investigated to elucidate the role of Zn, Zr, and In oxide as promoters for CO_2 hydrogenation to methanol. The activity of Cu/ZnO and Cu/ZrO_2 is strongly linked to the Cu-oxide interaction. A facile approach to increase the activity of Cu/ZnO is presented in which impregnating a small amount of ZrO_2 onto the catalyst can increase the activity and methanol selectivity, which is attributed to the formation of $Cu\text{-}ZrO_2$ interfacial sites. It is found that In

inhibits the active sites but increases the methanol selectivity of Cu/ZnO. However, new active sites for methanol synthesis are present for the In-doped Cu/ZrO_2 catalyst. This is attributed to the formation of In-Zr oxide sites that enhance the methanol formation rate, methanol selectivity, and stability of the catalyst above 250 °C. This study highlights that tuning both the Cu-oxide and oxide-oxide interaction is key to develop more active and stable Cu-based catalysts.

List of Publications

I. CO_2 hydrogenation to methanol: the structure–activity relationships of different catalyst systems.
K. Stangeland, H. Li, Z. Yu.
Energy, Ecology and Environment, 2020, 5, 272–285.
DOI: 10.1007/s40974-020-00156-4

II. Thermodynamic Analysis of Chemical and Phase Equilibria in CO_2 Hydrogenation to Methanol, Dimethyl Ether, and Higher Alcohols.
K. Stangeland, H. Li, Z. Yu.
Industrial & Engineering Chemistry Research, 2018, 57(11), 4081–4094.
DOI: 10.1021/acs.iecr.7b04866

III. Mesoporous manganese-cobalt oxide spinel catalysts for CO_2 hydrogenation to methanol.
K. Stangeland, D.Y. Kalai, Y. Ding, Z. Yu.
Journal of CO_2 Utilization, 2019, 32, 146–154
DOI: 10.1016/j.jcou.2019.04.018

IV. CO_2 hydrogenation to methanol over partially embedded Cu within Zn-Al oxide and the effect of indium promotion
K. Stangeland, F. Chamssine, W. Fu, Z. Huang, X. Duan, Z. Yu.
Submitted

V. Tuning the interfacial sites between copper and metal oxides (Zn, Zr, In) for CO_2 hydrogenation to methanol.
K. Stangeland, H. Herrera Navarro, H. L. Huynh, W. M. Tucho, Z. Yu.
Submitted.

This thesis is based on the above five papers.

Additional Publications

I. D. Y. Kalai, **K. Stangeland**, W. M. Tucho, Y. Jin, Z. Yu. Biogas reforming on hydrotalcite-derived Ni-Mg-Al catalysts: the effect of Ni loading and Ce promotion. *Journal of CO_2 Utilization*, 2019, 33, 189–200.

II. D. Y. Kalai, **K. Stangeland**, Y. Jin, Z. Yu. Active and stable hydrotalcite derived Ni catalysts for CO_2 reforming of methane: Comparison with catalysts by incipient wetness. *Journal of CO_2 Utilization*, 2018, 25, 346–355.

III. D. Y. Kalai, **K. Stangeland**, Y. Jin, W. M. Tucho, Z. Yu. Biogas dry reforming for syngas production on La promoted hydrotalcite-derived Ni catalysts. *International Journal of Hydrogen Energy*, 2018, 43(42), 19438–19450.

IV. **K. Stangeland**, D. Y. Kalai, H. Li, Z. Yu. Active and stable Ni based catalysts and processes for biogas upgrading: The effect of temperature and initial methane concentration on CO_2 methanation. *Applied Energy*, 2018, 227, 206–212.

V. D. Y. Kalai, **K. Stangeland**, H. Li, Z. Yu. The effect of La on the hydrotalcite derived Ni catalysts for dry reforming of methane. *Energy Procedia*, 2017, 143, 3721–3726.

VI. **K. Stangeland**, D. Y. Kalai, H. Li, Z. Yu. CO_2 methanation: the effect of catalysts and reaction conditions. *Energy Procedia*, 2017, 105, 2022–2027.

VII. **K. Stangeland**, D. Y. Kalai, H. Li, Z. Yu. The Effect of Temperature and Initial Methane Concentration on Carbon Dioxide Methanation on Ni Based Catalysts. *Energy Procedia*, 2017, 105, 2016–2021.

Conference Presentations and Proceedings

I. **K. Stangeland**, X. Duan, Z. Yu. Indium promotion of Cu-Zn-Al catalysts derived from hydrotalcite for CO_2 hydrogenation to methanol. *Oral* presentation at the Norwegian Catalysis Symposium. Bergen, Norway, 4–5 Desember, 2019.

II. H. L. Huynh, H. Berg, D. Y. Kalai, K. Stangeland, **Z. Yu**. Dry reforming of methane on hydrotalcite-derived NiFe catalysts: the effect of Fe and supersaturation. *Oral* presentation at the Norwegian Catalysis Symposium. Lillestrøm, Norway, 16–17 October, 2018.

III. **K. Stangeland**, D. Y. Kalai, Z. Yu. Mesoporous manganese-cobalt oxide catalysts for CO_2 hydrogenation to methanol. *Oral* presentation at the Norwegian Catalysis Symposium. Lillestrøm, Norway, 16–17 October, 2018.

IV. H. L. Huynh, H. Berg, D. Y. Kalai, K. Stangeland, **Z. Yu**. Bimetallic Ni-Fe hydrotalcite-derived catalysts for dry reforming of methane. *Poster* presentation at the 18th Nordic Catalysis Symposium. Copenhagen, Denmark, 26–28 August, 2018.

V. **K. Stangeland**, D. Y. Kalai, Z. Yu. Mesoporous manganese-cobalt oxide spinel catalysts for CO_2 hydrogenation to methanol. *Poster* presentation at the 18th Nordic Catalysis Symposium. Copenhagen, Denmark, 26–28 August, 2018.

VI. K. Stangeland, H. Li, **Z. Yu**. Thermodynamic analysis of chemical and phase equilibria in CO_2 hydrogenation to alcohols and dimethyl ether. *Poster* presentation at the Norwegian Catalysis Symposium. Hurdal, Norway, 6–7 November, 2017.

VII. **D. Y. Kalai**, K. Stangeland, H. Li, Z. Yu. Hydrotalcite-derived Ni-Mg-Al catalysts for CO_2 reforming of methane. *Oral* presentation at The 15th International Conference on Carbon

Dioxide Utilization (ICCDU XV). Shanghai, China, 17–21 October, 2017.

VIII. K. Stangeland, D. Y. Kalai, H. Li, **Z. Yu**. The effect of temperature and initial methane concentration on carbon dioxide methanation on Ni based catalysts. *Poster* presentation at the International Conference on Applied Energy. Beijing, China, 8–11 October, 2016.

Table of Contents

Table of Figures

List of Tables

Abbreviations and symbols

Abbreviations

BET	Brunauer–Emmet–Teller
BJH	Barret–Joyner–Halenda
DCS	differential scanning calorimetry
DME	dimethyl ether
GC	gas chromatography
JCPDS	Joint Committee on Powder Diffraction Standards
HAADF-STEM	high-angle annular dark-field scanning transmission electron microscopy
HT	hydrotalcite
ICP-AES	inductively coupled plasma atomic emission Spectroscopy
MB	moderate-strength basic
NP	nanoparticle
PV	pore volume
RWGS	reverse water-gas shift
SA_{Cu}	Cu surface area
SB	strong basic
SSA	specific surface area
STY	space-time yield
TEM	transmission electron microscopy
TGA	thermal gravimetric analysis
TOF	turnover frequency
TPD	temperature-programmed desorption
TPR	temperature-programmed reduction
WB	weak basic
XPS	X-ray photoelectron spectroscopy
XRD	X-ray diffraction

Symbols

C_M	copper surface atom density
$\hat{f}_i$	fugacity of species i
G_T	total Gibbs free energy
$G_{f_i}^0$	standard Gibbs energy of formation of species i
λ	wavelength
λ_i	Lagrange multiplier for species i
n_i	moles of species i
P	pressure
P^0	standard-state pressure
R	universal gas constant
T	absolute temperature
φ_i	fugacity coefficient of component i
μ_i	chemical potential of component i
N_A	Avogadro's number

1 Introduction

Capturing and recycling CO_2 has emerged as a promising strategy for mitigating the impact of CO_2 on the environment. Currently, fossil resources dominate the world economy and are used for producing various fuels and chemicals. Thus, CO_2 hydrogenation to synthetic fuels and chemicals is an effective approach for sustainable production of these compounds. Among the CO_2-derived candidates, methanol is at the forefront due to its versatility. Methanol is a viable alternative fuel as well as an important feedstock for producing synthetic fuels and chemicals such as dimethyl ether (DME), formaldehyde, acetic acid, methyl tert-butyl ether (MTBE), olefins, and propylene [1].

1.1 *Methanol synthesis*

1.1.1 History

Up until the 20th century, the volumes of methanol that could be produced by the distillation of wood was very modest. There was a growing need for methanol in the chemical industry at the end of the 19th century, which increased the interest in developing processes for methanol production. As a result, several leading scientists at the time worked on the methanol synthesis technology.

In 1905, Paul Sabatier proposed that a synthetic pathway for producing methanol could be achieved by reacting CO and H_2 [2]. Copper (Cu) was quickly identified as a promising candidate for methanol synthesis. The problem with the Cu-based catalysts was that they were easily poisoned by sulphur impurities in the syngas. Consequently, Paul Alwin Mittasch developed a poisoning resistant zinc-chromite (Zn/Cr_2O_3) catalyst for methanol synthesis. A Zn/Cr_2O_3-based catalyst was used in the first high-pressure methanol synthesis process (300 bar, 300–400 °C) developed by BASF. The BASF process produced methanol from syngas supplied

from coal gasification and was the first industrial-scale process implemented in 1923 in Leuna, Germany.

The breakthrough that would allow Cu-based catalysts to be utilized in methanol synthesis was the emergence of steam reforming of natural gas. Due to sulphur poisoning of the reforming catalyst, extensive research led to the development of a desulfurization catalyst that made it possible to produce high-purity syngas [3]. In 1966, ICI developed a low-pressure process (50–100 bar, 200–300 °C) utilizing the significantly more active Cu-zinc-alumina ($Cu/ZnO/Al_2O_3$) catalyst [4]. The low-pressure process offered reduced compression costs, longer catalyst life, larger capacity, and enhanced productivity compared to the high-pressure process. Currently, methanol is primarily produced from a syngas mixture ($CO/CO_2/H_2$) obtained by reforming natural gas. Most plants use the more active Cu-based catalyst and are based on the low-pressure process.

1.1.2 Methanol market

The methanol market is expected to grow significantly over the next decades due to an increase in methanol-based fuel consumption and production of methanol-derived fuels and chemicals. The increase in the methanol demand is largely driven by oil displacement, particularly from the methanol to olefins (MTO) and methanol to propylene (MTP) processes [5].

Methanol is used as a component of fuel in the transportation sector either directly in fuel blends or in the form of ether (MTBE) in gasoline and fatty acid ester (FAME) in diesel. Recently, projects on mid- and high-level methanol fuel blends have been implemented in many countries, such as China, Denmark, Israel, and Australia [6]. The consumption of mid- to high-level methanol fuel blends is also expected to continue to grow, predominantly in the Asia-Pacific region.

The use of methanol-based fuels has several advantages over conventional fuels to meet market and regulatory demands of cleaner fuels. It can help alleviate air pollution due to lower emissions of particulate matter, NO_x, SO_x, and hydrocarbons [7]. As a marine fuel, methanol could be compliant with the most stringent legislation currently being considered to limit marine pollution at a reasonable cost [8]. The energy density of methanol is about two times lower than conventional fuels but competitive with alternatives such as ethanol and liquefied natural gas (LNG) (Figure 1.1). Furthermore, methanol can be produced from renewable feedstock, which makes it an ideal transition fuel for a renewable-powered transportation sector.

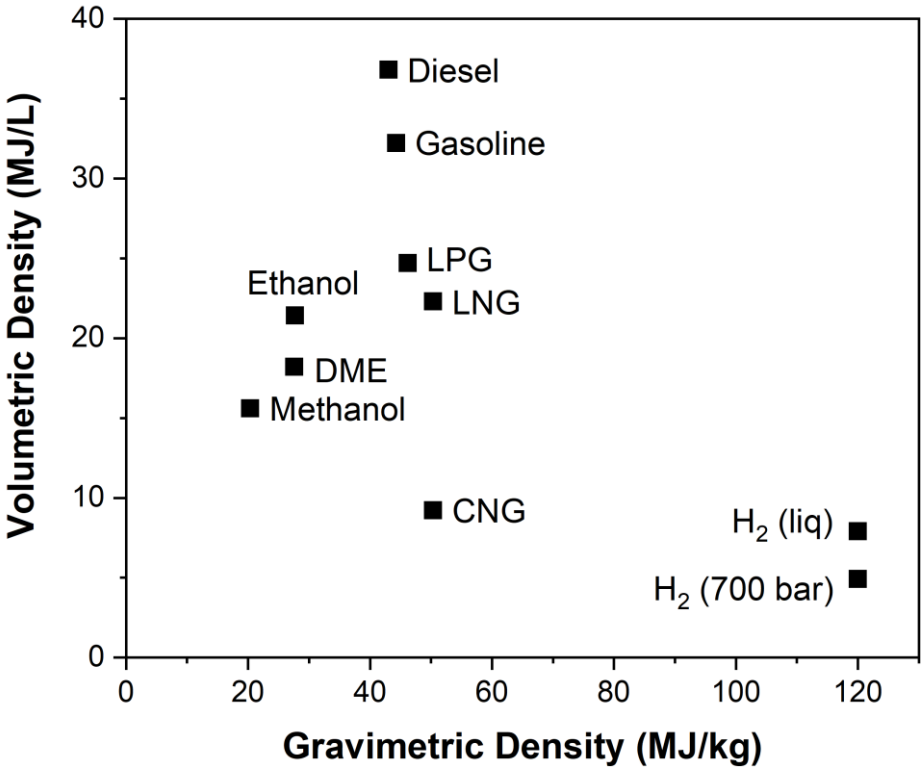

Figure 1.1 Specific energy and energy density of different fuels.

Methanol is also a viable candidate for use within transportation sector since it is readily available worldwide. The infrastructure costs are modest as methanol is a liquid at ambient conditions. There is also a long history of handling and using methanol in various applications with well-developed safety procedures. Furthermore, the environmental impact of methanol spill is much lower compared to oil because it is biodegradable.

The main driver for renewable methanol is government regulations on emissions due to environmental concerns. The need for renewable energy storage might also increase the implementation of the CO_2-to-methanol process. Renewable methanol fuel can drastically reduce the emissions of CO_2 by up to 95% and NO_x by up to 80%, and eliminate SO_x and particulate matter emissions [9]. There are numerous feedstock sources around the world that can be used to produce renewable methanol, such as converting sustainable biomass or reacting CO_2 with H_2 produced from renewable electricity. Provided a sustainable source of hydrogen becomes available at reasonable costs, recycling CO_2 could become economically viable with sufficient political incentives.

1.1.3 Current status of commercial production of renewable methanol

There are numerous projects currently underway for CO_2-to-methanol, bio-methanol, and low-carbon methanol production [9]. The MefCO_2 project in Germany utilizes surplus renewable electricity to perform CO_2-to-methanol for renewable energy storage [10]. In 2012, the first large-scale plant for CO_2 hydrogenation to methanol was opened in Svartsengi, Iceland. The plant is operated by Carbon Recycling International (CRI) with an annual production of 4,000 metric tons. CRI has partnered with Gelly Holdings and Zixin Industrial Co., Ltd. to promote and establish renewable methanol production facilities in China [9]. An agreement has also been signed between Henan Shuncheng Group and CRI to design a CO_2-to-methanol plant in Anyang city, China

[11]. The plant is expected to be in operation in 2021, with a production capacity of 110,000 tons of methanol per year.

Renewable methanol is also produced at a large-scale from solid waste and biomass [9]. Enerkem has developed a process for producing renewable methanol by extracting and reusing the carbon in non-recyclable waste. In 2017, Enerkem produced nearly 60,000 tons of renewable methanol. Netherlands-based company BioMCN produces renewable methanol from biogas at a facility in Delfzijl with a capacity of 900,000 tons [12]. Södra has developed a process for producing bio-methanol from wood, which was implemented in March 2020 at the Södra Cell Mönsterås pulp mill in southeastern Sweden [13].

1.2 CO_2 hydrogenation to methanol

1.2.1 Reaction chemistry and equilibrium thermodynamics

The main reactions in CO_2 hydrogenation to methanol are methanol synthesis from CO_2 (Eq. 1.1), CO hydrogenation to methanol (Eq. 1.2), and the reverse water-gas shift reaction (Eq. 1.3.).

$$CO_2 + 3H_2 \rightleftharpoons CH_3OH + H_2O, \quad \Delta H^0_{273k} = -49.5 \text{ kJ/mol} \tag{1.1}$$

$$CO + 2H_2 \rightleftharpoons CH_3OH \quad \Delta H^0_{273k} = -90.5 \text{ kJ/mol} \tag{1.2}$$

$$CO_2 + H_2 \rightleftharpoons CO + H_2O \quad \Delta H^0_{273k} = 41.2 \text{ kJ/mol} \tag{1.3}$$

The preferred thermodynamic conditions for methanol synthesis are low temperatures and higher pressures. This allows high methanol selectivity as the RWGS reaction is endothermic and therefore, suppressed at low temperatures (Figure 1.2). The methanol yield is significantly limited by the thermodynamics for CO_2 hydrogenation compared to methanol

synthesis from syngas. The thermodynamic restrictions on the methanol yield can be circumvented by condensation of methanol and water at high pressure and low temperatures [14]. Product condensation occurs at lower pressure for CO_2/H_2 feeds compared to syngas and can increase the methanol yield up to 100%.

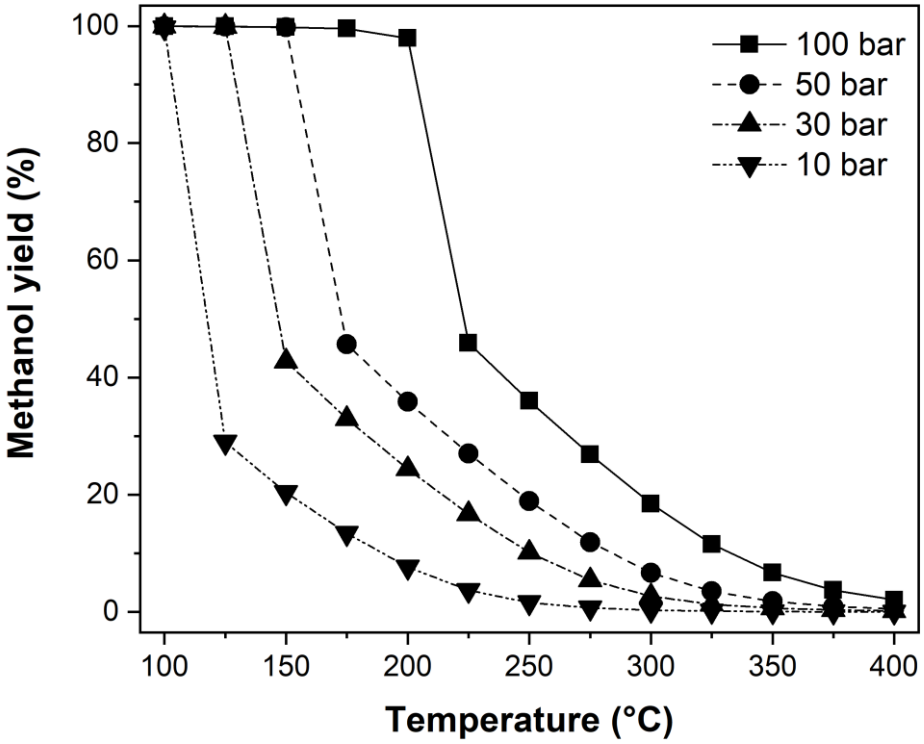

Figure 1.2 Thermodynamic limit on methanol yield at different pressures as a function of temperature (H_2/CO_2 = 3/1) [14].

1.2.2 Catalysts

The most studied CO_2 hydrogenation to methanol catalysts are based on Cu supported on different metal oxides. The main issue with the traditional $Cu/ZnO/Al_2O_3$ catalyst is the moderate methanol selectivity and rapid water-induced sintering. Cu/ZrO_2 and $Cu/ZnO/ZrO_2$ catalysts have been reported to have higher activities, selectivities, and stabilities

relative to Cu/ZnO for CO_2-to-methanol. It has also been demonstrated that other metal oxides (i.e., Ce_2O_3 [15, 16], La_2O_3 [17], Ga_2O_3 [18], Y_2O_3 [19]) can promote methanol synthesis over Cu-based catalysts. Furthermore, halogens have been used to enhance the methanol selectivity of Cu-based catalysts, such as by the addition of F [20] and generating surface $CuBr_2$ halide [21].

Pd-based catalysts have also been extensively studied, but their large-scale industrial application might be limited due to the relatively higher cost of Pd. The Pd-oxide interface and alloying (e.g., PdZn, PdGa) are important factors of high-performance methanol synthesis catalysts based on Pd [22]. Methanol synthesis has also been studied over Ni- and Co-based catalysts, which can produce methanol only when combined with suitable promoters.

Recently, In_2O_3-based catalysts have gained significant research interest due to their high methanol selectivity even at higher temperatures (200-320 °C). The oxygen vacancies of In_2O_3 play a crucial role in the activation and conversion of CO_2 to methanol. It has been demonstrated that the activity of In_2O_3 can be improved by the addition of metal oxides (ZrO_2, Y_2O_3), Pd, Ni, and Cu by promoting the formation of oxygen vacancies and enhancing H_2 activation [23].

1.3 *Scope of this work*

1.3.1 Scientific objectives

The thermodynamics of CO_2 hydrogenation to methanol is of practical importance for the industrial implementation of the process. The more severe thermodynamic restrictions of CO_2-to-methanol compared to the conventional syngas route pose an additional challenge on the process design of CO_2 hydrogenation to methanol. Paper II presents an in-depth analysis of the thermodynamics of CO_2 hydrogenation to methanol.

The second part of the thesis focuses on the catalytic aspect of CO_2 hydrogenation to methanol. Among the most important open questions is the nature of the metal-oxide and oxide-oxide synergy within the different catalytic systems for CO_2 hydrogenation to methanol. Although the effect of various metal oxides on methanol synthesis has been thoroughly studied, their influence on the catalytic properties is still debated. The purpose of the experimental works is to gain further insight into the role of the metal-oxide and oxide-oxide interaction in methanol synthesis, which can be used to develop high-performance CO_2-to-methanol catalysts. I started by investigating the promising new Co/Mn oxide-based system, and then worked on improving the conventional Cu/ZnO-based catalysts.

Paper III investigates the role of Mn oxide promotion of Co for the low-pressure methanol synthesis process. High Co-Mn oxide interaction is achieved via a mixed Co-Mn spinel oxide structure. The Co:Mn ratio and the effect of reaction conditions on the methanol synthesis activity is studied.

In Paper IV, the influence of the Cu-ZnO interaction on the activity and selectivity is elucidated. Different Cu-ZnO interaction is achieved by utilizing hydrotalcite and malachite precursors. The promotional effect of In on the catalytic performance is also explored. Furthermore, the spent catalysts are characterized to identify the deactivation mechanism.

The effect of the Cu-oxide and oxide-oxide (Zn, Zr, In oxides) interaction in binary Cu/oxide and ternary Cu/oxides is studied in Paper V. Based on the evaluation of the different catalysts, a simplified model is presented that describes the key features of the interaction between the different components.

1.3.2 Outline

The outline of this thesis is as follows: Chapter 2 presents the literature review of the relevant studies for this work, which is based on Paper I.

Chapter 3 gives all the necessary information to reproduce the computational and experimental work.

The main results are discussed in Chapter 4. Chapter 4.1 presents the thermodynamic analysis (Paper II). CO_2 hydrogenation to methanol over Co/Mn oxide system is covered in Chapter 4.2 (Paper III). The work on Cu-based catalysts is presented in Chapter 4.3 (Paper IV) and Chapter 4.4 (Paper V).

Chapter 5 concludes the thesis and addresses key research questions and gives suggestions for further study.

All the papers are attached at the end of the thesis.

2 Literature review

CO_2 hydrogenation catalysts can be divided into four groups based on the active metal component: conventional Cu catalysts, Pd catalysts, In_2O_3 catalysts, and other transition metal catalysts. Metal oxides and the formation of alloys play a crucial role in the performance of CO_2-to-methanol catalysts. The synergy between the catalyst's components is currently not fully understood. This is largely due to the dynamic nature and complexity of these systems, which pose a significant challenge in identifying the role of the different phases. This section covers the relevant studies for the experimental part of this work, which includes Cu-, In_2O_3-, and transition metal-based catalysts.

2.1 *CO_2 hydrogenation to methanol over Cu-based catalysts*

Single-crystal studies over different Cu facets indicate that the turnover frequencies (TOF) for methanol synthesis from CO_2 depends on the exposed Cu facet, and is in the order of Cu(110) > Cu(100) > Cu(111). For instance, Rasmussen et al. [24, 25] found that the methanol synthesis rate over Cu(100) was ~30 times faster than that on Cu(110). However, the TOF for the RWGS reaction is reported to be higher than methanol synthesis from H_2/CO_2 mixtures over Cu. Yoshira and Campbell [26] found that the TOF for methanol synthesis was $\sim 8 \times 10^{-3}$ s^{-1} on Cu(110), whereas the TOF for CO production was ~ 5 s^{-1} (H_2/CO_2 = 11/1, 5.1 bar, 530 K).

A large Cu surface area is typically indicative of high catalytic activity. However, the different behavior of metal oxide-promoted Cu catalysts, in terms of activity and stability under different feeds ($CO_2/CO/H_2$), highlights that the metal oxide promoter plays a determining role in the performance of methanol synthesis catalysts. [27-31]. Consequently, a highly active catalyst for syngas conversion to methanol can show poor

performance and even be quite inactive when switching to a CO_2/H_2 feed. This was demonstrated in a recent study, which showed that a relatively inactive Cu/MgO catalyst (highly active for CO hydrogenation to methanol) can be converted into an efficient CO_2-to-methanol catalyst by impregnating ZnO onto Cu/MgO [28]. Therefore, the Cu-oxide interaction is a determining factor for the catalytic performance of methanol synthesis catalysts.

2.1.1 Active sites of Cu/ZnO

The nature of the active phase in Cu/ZnO catalysts has been debated for decades and is still under vigorous research. The proposed promotional effect of ZnO on Cu include (1) increasing the exposure of highly active Cu metal surfaces, (2) decoration of the Cu surface by Zn or ZnO_x species, (3) Cu-ZnO interfacial sites, and (4) reverse spillover of hydrogen from ZnO in which ZnO serves as a reservoir for hydrogen [32]. Regarding proposal (1), the presence of Cu lattice strain and defects has been identified as indicative of high activity, which can be influenced by the ZnO phase [33-35]. Furthermore, it has been reported that the activity of Cu(100) is comparable to the activity of unoptimized Cu/ZnO [24, 25].

There is compelling evidence that Zn or ZnO_x decorated Cu surfaces is considerably more active than pure Cu surfaces for methanol synthesis from CO_2 (proposal 2). Nakamura and co-workers demonstrated that the TOF increases by several orders of magnitude when Zn is deposited on Cu(111) [36] and polycrystalline Cu [37]. Kuld et al. [38] observed that the TOF for methanol increases with increasing Zn coverage of Cu over an industrial-type $Cu/ZnO/Al_2O_3$ catalyst. Senanayake et al. [16] showed that the ZnO decorated Cu surface was about 2 times more active than the inverse Cu NPs deposited on the ZnO surface. Kettel et al. [39] found that the Zn species were easily oxidized to ZnO_x during reaction, which enhanced the activity. Recently, a combination of ZnO and Zn formate was identified by *in situ* characterization under industrially relevant

reaction conditions during CO_2 hydrogenation to methanol [40]. The promoting effect of these Zn or ZnO_x species has been attributed to stabilizing the formate intermediate and facilitating the hydrogenation of formate to methanol [35, 40, 41]. Thus, the coverage of Cu by ZnO_x or Zn formate species seems to be key to generate a high number of active sites for Cu/ZnO-based catalysts, and the intimate contact between the Cu and Zn promotes the formation of these species on the Cu surface [40].

The presence of oxygen vacancies at the Cu-ZnO interface has also been proposed to facilitate the activation and hydrogenation of CO_2 to methanol (proposal 3) [42, 43]. Liao et al. [43] showed that the morphology of ZnO influence the methanol production from CO_2 hydrogenation, where the methanol formation rate is higher for Cu in intimate contact with plate-like ZnO compared to rod-shaped ZnO. A higher intrinsic activity has also been reported for Cu partially embedded within a Zn-Al oxide matrix [44, 45]. These studies indicate that optimizing the Cu-ZnO interface and the interfacial area are important parameters for maximizing the methanol synthesis activity of Cu/ZnO-based catalysts.

2.1.2 Active sites of Cu/ZrO_2

The Cu-oxide interaction has also been extensively studied for the Cu/ZrO_2 system. The interfacial sites appear to be the dominant factor for the activity of Cu/ZrO_2 catalysts. The Cu/ZrO_2 catalysts are typically reported to operate as a bifunctional catalyst in which H_2 is dissociatively adsorbed on Cu, whereas CO_2 activation and hydrogenation of the intermediates occurs at the interfacial sites. In a recent study, Polierer et al. [46] found that the intermediates are too strongly adsorbed on the Cu/ZrO_2 interface and ZrO_2 phase for further conversion to methanol. Instead, the promotional effect of ZrO_2 was attributed to electronic promotion of Cu surface sites near the ZrO_2 phase.

The activity of Cu/ZrO_2 is critically linked to the properties of the ZrO_2 phase, which is illustrated by the activity of Cu promoted by different polymeric phases of ZrO_2 (e.g., monoclinic (*m*-), tetragonal (*t*-), and amorphous (*a*-) ZrO_2). Bell and co-workers reported that the activity of $Cu/m\text{-}ZrO_2$ is superior compared to $Cu/t\text{-}ZrO_2$ [47, 48]. In contrast, the results of Baiker et al. [49], Koppel et al. [50], Ma et al. [51], and Samson et al. [52] suggest that $t\text{-}ZrO_2$ is more suitable to promote methanol synthesis over Cu/ZrO_2 catalysts. Samson et al. [52] found that the activity of Cu/ZrO_2 is correlated to the number of Brønsted and Lewis acidic sites rather than the Cu surface area. Thus, the higher activity of $t\text{-}ZrO_2$ compared to $m\text{-}ZrO_2$ was attributed to a higher number of active interfacial sites for $Cu/t\text{-}ZrO_2$.

Tada et al. [53] observed that the methanol production rate and selectivity are higher for $Cu/a\text{-}ZrO_2$ compared to $Cu/t\text{-}ZrO_2$. The higher selectivity of $Cu/a\text{-}ZrO_2$ was attributed to weaker adsorption of methanol, which reduces the CO production by limiting methanol decomposition into CO. On the other hand, Witoon et al. [54] found that the intrinsic activity and methanol selectivity of $Cu/t\text{-}ZrO_2$ was higher than that of $Cu/a\text{-}ZrO_2$. From the above discussion, it seems that the nature of the $Cu\text{-}ZrO_2$ interfacial sites is not fully understood. However, these studies indicate that the number of interfacial sites and the properties of the ZrO_2 phase (e.g., surface acidity, basicity, and oxygen vacancies) are crucial factors for optimizing the activity of Cu/ZrO_2 catalysts.

2.1.3 Influence of metal oxide promoters on Cu-based catalysts

The $Cu/ZnO/Al_2O_3$ catalyst is typically prepared using an aqueous solution of Cu, Zn, and Al by co-precipitation near neutral pH [55]. The essence is to achieve high Cu-Zn intermixing, which is typically obtained from a Cu, Zn, hydroxy-carbonate (zincian malachite) precursor [56]. The Zn content of the zincian malachite phase is typically limited to

about 30%. At higher Cu:Zn, the formation of Zn rich by-phases occurs, such as aurichalcite and hydrozincite. The formation of these Zn-rich phases is not desirable because the activity of the final catalyst is reduced due to lower Cu dispersion and Cu-ZnO interaction [57]. Recently, georgeite, the trancient amorpous phase in the preparation of malachite, has shown superior performance compared to zincian malachite, which to some extent can be attributed to improved Cu-ZnO interaction [58, 59]. Layered double hydroxides (LDHs), also referred to as hydrotalcite (HT), can form in ternary Cu, Zn, Al systems when the pH is above neutral. Typically, the HT-derived catalysts exhibit higher intrinsic activity due to the strong interaction with the metal oxide phase, but lower Cu surface area [44].

The most active catalysts reported in literature for CO_2 hydrogenation to methanol typically consist of multiple metal oxide promoters. ZrO_2 is widely employed in ternary Cu/ZnO/ZrO_2 (CZZ) catalysts to enhance the activity and stability of the catalyst. The hydrophilic character of ZrO_2 enhances the desorption of produced water, which benefits both the methanol production rate and selectivity [60]. The influence of ZrO_2 in the CZZ system has also been related to (1) metal properties such as Cu dispersion and particle size, (2) state of the Zr and Zn oxides (e.g., crystallinity and particles size), (3) surface properties (concentration of acidic, basic, and oxygen vacant sites), and (4) metal-oxide interaction generating new sites for binding and converting active intermediates.

The CZZ catalysts prepared by co-precipitation usually exhibit methanol selectivities between 40–70% (at CO_2 conversion of ~10–25%, 30–50 bar, 220–250 °C) [61-63]. Recently, Wang et al. [61] developed a CZZ catalyst with a large number of Cu-ZnO and Cu-ZrO_2 interfacial sites. The catalyst consisted of a three-dimensional ordered macroporous framework of Cu with ZnO and ZrO_2 well-dispersed on the wall of the macropores. This unique structure resulted in a high number of interfacial sites and very high activity (18.2% CO_2 conversion and 80.2% methanol selectivity at 220 °C and 30 bar).

The atomic-level interaction between Cu, ZnO, and ZrO_2 is relatively complex and has not been extensively studied *in situ*. It has been proposed that the ZnO-ZrO_2 interface can transform the carbonate intermediate into more reactive species (e.g. formate) [60, 61]. Abbas et al. [32] ascribed the superior performance of Cu/ZnO/ZrO_2 compared to the bimetallic catalysts (Cu/ZnO and Cu/ZrO_2) to reverse spillover of hydrogen from ZnO that enhanced the methanol synthesis rate at Cu/ZrO_2 interfacial sites.

Other metal oxides have also been utilized to enhance the activity of Cu-based catalysts. Li et al. [64] found that the addition of Ga enhanced the Cu dispersion and promoted the formation of CuZn surface species. The CO_2 conversion and methanol selectivity of Cu/ZnO calcined at different temperature and the Ga-promoted Cu/ZnO catalysts was correlated to the number of CuZn alloy species. Natesakhawat et al. [65] observed that the dispersion and intrinsic activity increases with the incorporation of multiple metal oxides in the order of CuZnZrGaY > CuZnZrY > CuZnZr > CuZn > CuZr. The higher dispersion significantly improved the methanol formation rate. However, the higher intrinsic activity indicates that Cu-oxide interaction also contributed to the enhanced activity. Zhang et al. [66] reported that the catalytic performance of Cu/ZrO_2 could be enhanced by incorporating In into the ZrO_2 phase. The superior performance of the In-promoted catalysts was attributed to an increase in the surface basicity, which was proposed to enhance the number of Cu-ZrO_2 interfacial sites for CO_2 conversion to methanol.

2.1.4 Reaction mechanism over Cu-based catalysts

Despite the considerable research on the reaction mechanism of methanol synthesis on Cu-based catalysts, there are still unanswered questions regarding the mechanism of methanol formation and the chemical nature of the active sites. The proposed reaction mechanisms of CO_2 hydrogenation to methanol can be divided into two primary groups: the formate mechanism and the RWGS reaction to produce CO,

followed by CO hydrogenation to methanol (RWGS + CO hydrogenation pathway). Besides the mechanism for CO_2 hydrogenation to methanol, further mechanistic insight into the undesired RWGS reaction could also help develop more selective Cu-based catalysts. These issues can be addressed in the context of the following questions: (1) what are the key intermediates and elementary steps in CO_2 hydrogenation to methanol; (2) what is the rate-determining step, (3) what mechanistic roles do metal and metal oxides play; (4) can CO formed from the RWGS reaction be further hydrogenated to methanol; and (5) which sites are responsible for CO formation.

The mechanistic investigation of methanol synthesis from CO_2 over Cu/ZnO and Cu/ZrO_2 catalysts mostly favor methanol formation directly from CO_2 via the formate intermediate. This is supported by experimental data from isotopic labeling experiments [67-71] and *in situ* transient kinetic experiments [55, 71, 72]. The comprehensive investigations by Larmier et al. [71] offer compelling evidence that methanol synthesis from CO_2/H_2 over Cu/ZrO_2 occurs via the formate intermediate at relevant reaction conditions. However, studies conducted at lower pressures have concluded that methanol is produced from the RWGS + CO hydro route over Cu/ZrO_2 [73-76]. The RWGS + CO hydrogenation pathway has also been proposed over CeO_x/Cu(111) [15] and Cu/TiO_2 [73]. The reaction conditions might influence the preferred reaction channel [77], which highlights the need to study the catalytic systems under realistic working conditions.

Bartholomew et al. [78] concluded that methanol synthesis from syngas most likely occurs through $CO_2^* \rightarrow HCOO^* \rightarrow H_2COO^* \rightarrow H_3CO^* \rightarrow H_3COH^*$ where the hydrogenation of H_2COO was the rate-determining step ($H_2COO^* + H^* \rightleftharpoons H_3CO^* + O^*$). This was largely based on the model of Askgard et al. [79] for Cu surfaces and later amended to incorporate support effects by Ovesen et al. [80]. The model predicts TOF for methanol formation over a wide range of reaction conditions, in good agreement with measured TOF values for Cu/ZnO-based catalysts.

Most experimental and computational studies on the reaction mechanism over Cu/ZnO and Cu/ZrO_2 also support that methanol is produced through a similar reaction pathway. However, CO_2 is typically reported to form HCOO through an Eley-Rideal (ER) mechanism and H_2CO has been identified as an intermediate by density functional theory (DFT) in the formate route. Thus, in response to *Question 1*, research points to the following reaction pathway on Cu/ZnO and Cu/ZrO_2: $CO_2(g) + H^* \rightarrow HCOO^* \rightarrow H_2COO^* \rightarrow H_2COOH^* \rightarrow H_2CO^* \rightarrow H_3CO^* \rightarrow H_3COH^*$. Most studies also find that the rate-determining step is either the hydrogenation of HCOO or H_2COO (*Question 2*).

The proposals for the role of different metal oxides (*Question 3*) include (i) enhancing CO_2 activation [81-86], (ii) stabilizing reaction intermediates [35, 36, 41, 87-91], (iii) lowering the energy barrier of reaction steps [39, 81, 92-94], (iv) electron transfer from the metal oxide to the Cu surface [46, 95, 96], (v) creating new, more favorable reaction pathway [83], Cu-oxide interfacial sites [71, 86] and offering sites for part of or the entire reaction mechanism [61]. Several studies have pointed to a combination of pathways being responsible for converting CO_2 to methanol [82, 92-94, 97]. Therefore, several of the phenomena (i-v) are probably responsible for the Cu-oxide synergism and could be chemically related.

A comprehensive analysis of the RWGS reaction is often lacking. Many of the factors that enhance methanol synthesis has also been reported to improve the water-gas shift (WGS) or RWGS reaction activity, such as step sites in Cu [98] and the Cu-oxide interaction [99, 100]. Therefore, it might be challenging to eliminate CO formation for the conventional catalytic systems composed of Cu and metal oxides. Recently, Chen et al. [21] reported very high methanol selectivity of 99.6–79.1% at a CO_2 conversion of ~7–15%, 210–330 °C, and 5 MPa over CuZnZr by generating surface $CuBr_2$ halide through impregnation. Based on the activity measurements and *in situ* DRIFTS results, they proposed that $CuBr_2$ composite passivates the RWGS activity on the Cu surface and

that methanol is formed through the formate pathway. Therefore, further investigation into CuBr halides or other composites that inhibit the RWGS reaction could result in the development of highly selective Cu-based methanol synthesis catalysts.

2.2 CO_2 hydrogenation to methanol over In_2O_3-based catalysts

Recently, In_2O_3 has emerged as a highly selective catalytic system for methanol synthesis over a wide temperature range (200–320 °C). However, higher temperatures are required to achieve similar or greater methanol synthesis rates compared to Cu-based catalysts. The experimental and computational studies indicate that the oxygen vacancies in In_2O_3 are crucially involved in the active sites for methanol synthesis [101]. It is also important to avoid reducing In_2O_3 to metallic In, which is inactive for CO_2 hydrogenation to methanol [102]. Thus, promoters that can generate and stabilize oxygen vacancies have been demonstrated to enhance the activity of In_2O_3-based catalysts. Martin et al. [102] observed that ZrO_2 could promote the formation and stabilization of oxygen vacancies in In_2O_3, which significantly increased the activity compared to bulk In_2O_3. On the other hand, In_2O_3 supported on other metal oxides (TiO_2, ZnO, SiO_2, Al_2O_3, SnO_2, and MgO) resulted in the formation of inactive metallic In, which reduced the activity. Chou et al. [103] found that Y_2O_3 and La_2O_3 could also enhance the performance of In_2O_3 by increasing the number of oxygen defects.

The performance In_2O_3 can be improved by the addition of noble or transition metals. So far, the use of Pd to promote In_2O_3 has been more widely studied compared to the others. In this case, it is critical to maintain the In_2O_3 phase after reduction as Pd-In alloy mostly produces CO [104]. Furthermore, the formation of Pd clusters on the surface of In_2O_3 also promotes the RWGS reaction, which leads to lower methanol selectivity [23]. Frei et al. [23] observed that Pd atoms highly dispersed in the bulk of In_2O_3 increased the number of oxygen vacancies, which

enhanced the methanol synthesis activity. The agglomeration of Pd species on the surface was avoided when the catalyst was prepared by co-precipitation with a Pd loading of less than 1 wt%. Snider et al. [105] suggested that a synergetic effect between the Pd-In alloy particles and the In_2O_3 phase results in highly active catalysts. The active site configuration was proposed to consist of Pd-In alloy particles covered by In_2O_3 species. The formation of the In_2O_3/Pd-In configuration was more favourable at a Pd:In ratio of 1:2, which showed significantly higher activity and methanol selectivity compared to pure In_2O_3 and Pd. Furthermore, increasing the Pd content reduced the methanol formation rate and methanol selectivity.

2.3 *Transition metal-based catalysts for CO_2 hydrogenation to methanol*

CO_2 hydrogenation to methanol over various transition metals has been explored to a lesser extent. This is because the other transition metals besides Cu are not particularly selective towards methanol without alloying or careful promotion. For instance, obtaining a high-purity Ni_5Ga_3 alloy phase is critical for achieving high methanol selectivity for Ni-Ga catalysts because Ni-rich regions are very active for CO_2 methanation [106, 107]. Hegne et al. [108] observed that the methane selectivity was 99% for Ni/ZrO_2, whereas methanol could be produced over Ni-Sn alloy supported on ZrO_2. The methanol selectivity was further improved from 54% to 99% by In addition for Ni-Sn alloy supported on In-Zr oxide.

Similar to Ni, CO_2 methanation is the main reaction over Co [109]. Methanol synthesis over Co-based catalysts is challenging as it seems to require careful tuning of the oxidation state of Co. Furthermore, promoters are essential to generate active sites for methanol synthesis. Li et al. [110] investigated CO_2 hydrogenation over Mn oxide NPs dispersed on mesoporous Co_3O_4. They found that the methanol selectivity was significantly higher for MnO_x deposited on Co_3O_4

compared to MnO_x, Co_3O_4, and Co_3O_4 supported on Mn_3O_4. The active site configuration was proposed to consist of a CuO surface covered by MnO_x particles in which the interfacial sites facilitated the conversion of CO_2 to methanol. However, the hydrocarbon selectivity was higher than 50%. Thus, tuning the Co-Mn oxide interaction or addition of other promoters that limit hydrocarbon formation is highly desirable for the Co-Mn system.

2.4 *Perspectives*

There are many open questions for the catalytic systems under investigation for CO_2 hydrogenation to methanol. Some of these aspects are relevant to all the catalytic systems addressed in this chapter, which can be summarized as follows:

- What is the role of alloying and metal oxides in methanol synthesis?
- How can the active sites responsible for by-product formation be inhibited?
- How can the active site configuration(s) be stabilized?

Regarding Cu-based catalysts, the following questions are under rigorous debate and require further study:

- What is the main factor responsible for the promotional effect of ZnO on Cu?
- What is the role of the Cu-oxide synergy and oxide-oxide interaction on methanol synthesis?
- How can the interfacial sites be tuned and stabilized to enhance the catalytic performance?

3 Experimental

3.1 *Thermodynamic analysis*

In paper II, the thermodynamics of CO_2 hydrogenation to methanol, methanol and dimethyl ether (DME), and methanol and higher alcohols were studied using the Gibbs free energy minimization method. CO was also included in all the simulations as it is the primary by-product in CO_2 hydrogenation over typical catalysts used for the synthesis of oxygenates. Methane and higher hydrocarbons are not included in the thermodynamic analysis since the production of hydrocarbons is limited over typically employed catalysts for the synthesis of oxygenates.

At thermodynamic equilibrium, the total Gibbs free energy (G_T) of the mixture is at the minimum and its differential is zero. The $d(G_T)$ of a two-phase system composed of different compounds at a constant temperature and pressure can be expressed as (Eq. 3.1) [111]:

$$dG_T = \sum_i^N \mu_i^v dn_i^v + \sum_i^N \mu_i^l dn_i^l = 0 \qquad (3.1)$$

where N is the number of species in the reaction system, n_i is the moles of species i, μ_i is the chemical potential of component i, v and l denotes the vapor and liquid phase, respectively. Introducing Lagrange multipliers for species i subject to mass balance constraints yields Eq. 3.2.

$$\mu_i + \sum_j \lambda_i a_{ji} = 0 \qquad (3.2)$$

where λ_i is the Lagrange multiplier for species i, a_{ji} is the number of atoms of element j in species i. The chemical potential is given by Eq. 3.3.

$$\mu_i = \Delta G_{f_i}^0 + RTln\frac{\hat{f}_i}{P^0} \qquad (3.3)$$

where $\Delta G_{f_i}^0$ is the standard Gibbs energy of formation of species i, R is the universal gas constant, T is the absolute temperature, $\hat{f}_i$ is the fugacity of species i, and P^0 is the standard-state pressure. Combining Eq. 3.2 and 3.3 gives (Eq. 3.4):

$$\Delta G_{f_i}^0 + RTln\frac{\hat{f}_i}{P^0} + \sum_j \lambda_i a_{ji} = 0 \qquad i = 1, 2, \ldots, N \qquad (3.4)$$

The basic relationship for every component i in the vapor and liquid phases of a system at equilibrium can be defined as (Eq. 3.5):

$$\hat{f}_i^v = \hat{\varphi}_i^v y_i P = \hat{\varphi}_i^l x_i P = \hat{f}_i^v \qquad (3.5)$$

where φ_i is the fugacity coefficient of component i obtained from equation of state, P is the pressure, and y_i and x_i are the mole fraction of component i in the vapor and liquid phase, respectively. The equilibrium state is determined by minimizing the Gibbs free energy for a given set of species without any specification of the possible reactions within the system. This yields a set of N equilibrium equations (Eq. 3.4) along with mass balance constraints and phase equilibrium equations that are solved following an iterative procedure.

The Gibbs free energy minimization method was employed for the thermodynamic analysis using the RGibbs module in Aspen plus. The thermodynamic properties of the components were obtained using the Soave-Redlich-Kwong equation of state. The binary interaction parameters of CO_2, CO, H_2, H_2O, and methanol were taken from van Bennekom et al. [112], whereas these parameters for DME and ethanol were estimated by the UNIFAC method in Aspen plus.

3.2 *Materials and chemicals*

Table 3.1 summarizes the chemicals and materials used in this thesis. All the materials and chemicals were used as received without further purification.

Table 3.1 Summary of materials and chemicals used in this thesis.

Chemical	Chemical formula	Purity	Supplier
Cobalt (II) nitrate hexahydrate	$Co(NO_3)_2{\cdot}6H_2O$	>99%	Sigma-Aldrich
Manganese (II) nitrate hydrate	$Mn(NO_3)_2{\cdot}H_2O$	>99.8%	Sigma-Aldrich
1-butanol	C_4H_9OH	>99.8%	Sigma-Aldrich
PEO_{20}–PPO_{70}–PEO_{20}	Pluronic P123	–	Sigma-Aldrich
Nitric acid (66%)	HNO_3	–	Sigma-Aldrich
Ethanol	C_2H_5OH	99%	Sigma-Aldrich
Copper (II) nitrate trihydrate	$Cu(NO_3)_2{\cdot}3H_2O$	>99.5%	Acros Organics
Zinc (II) nitrate hexahydrate	$Zn(NO_3)_2{\cdot}6H_2O$	>99.9%	Alfa Aesar
Aluminum (III) nitrate nonahydrate	$Al(NO_3)_3{\cdot}9H_2O$	>98.5%	Emsure
Zirconium (IV) oxynirate hydrate	$ZrO(NO_3)_2{\cdot}H_2O$	>99.9%	Alfa Aesar
Indium (III) nitrate hydrate	$In(NO_3)_3{\cdot}H_2O$	>99.99%	Alfa Aesar
Sodium hydroxide	NaOH	>99.2%	Emsure
Sodium carbonate	Na_2CO_3	>99.9%	Emsure
Silicon carbide (40 mesh, powder)	SiC	–	Alfa Aesar
Alpha alumina	α-Al_2O_3	–	Sigma-Aldrich

3.3 *Catalyst preparation*

3.3.1 Synthesis of mesoporous Co-Mn oxides

The mesoporous Co, Co-Mn, and Mn catalysts in paper III were prepared by a modified sol-gel inverse micelle method. The metal nitrates were dissolved in a beaker containing a 200 mL solution of 1-butanol, HNO_3, and P123 under magnetic stirring. The obtained clear gel was placed in an oven at 100 °C for 6 h to evaporate the solvent. The resulting powder was crushed and washed several times with ethanol to remove the surfactants. The powder was separated from the ethanol-surfactant solution using a centrifuge and then dried in an oven at 100 °C overnight. The dried powders were calcined under flowing air at 150 °C for 12 h, 250 °C for 4 h, and 350 °C for 2 h with a heating rate of 2 °C/min.

3.3.2 Synthesis of CuZnAl and In-doped CuZnAl HT-derived catalysts

The CuZnAl and In-doped CuZnAl HT-derived catalysts in Paper IV were prepared by co-precipitation at low supersaturation and room temperature. Appropriate amounts of metal nitrates were dissolved in 400 mL of deionized water to form a cation solution with a total ion concentration of 0.5M. The anion solution of 400 mL was obtained by dissolving 16 g of NaOH and 5.3 g of $NaCO_3$. The cation solution was added dropwise into the anion solution over 2 h. The pH of the precursor solution was adjusted to 9.0 ± 0.2 if needed. The precipitate solution was aged in the mother liquor for 15 h under vigorous stirring at 60 °C using a three-neck round bottom flask under N_2 atmosphere. After that, the precipitate was filtered and washed with deionized water until the pH of the filtering liquid was 7. The obtained filter cake was dried overnight at 90 °C and then calcined at 500 °C for 4 h with a heating rate of 2 °C/min.

3.3.3 Synthesis of CuM (M = Zn,Zr, In) and CuZrIn catalysts

The CuM (Zn, Zr, In) catalyst in Paper IV and V was prepared by co-precipitation. An aqueous nitrate solution containing an appropriate molar ratio of metal nitrates was co-precipitated at a constant pH of 6.5 ± 0.2 using Na_2CO_3 as precipitating agent. The precipitate solution was aged in a three-neck round-bottom flask for 14 h at 65 °C under vigorous stirring and N_2 atmosphere. The precipitate was filtered and washed several times with deionized water. The precursors were dried at 90 °C and then calcined at 350 or 500 °C for 3 h. The CuZrIn catalyst was prepared using the same procedure.

3.3.4 Synthesis of impregnated M-CuZn (M = Zr, In) and M-CuZr (M = Zn, In) catalysts

The CuZn sample calcined at 350 °C was impregnated with In nitrate or Zr nitrate solution to yield a In/Zr content of 1 mol%. The metal nitrate was dissolved in deionized water before the catalyst sample was added to the solution. The mixture was then ultrasonicated for 0.5 h and stirred overnight. Finally, the impregnated samples were dried in an oven at 90 °C and then calcined again at 350 °C for 3 h. Similarly, the CuZr sample calcined at 350 °C was impregnated with In or Zn nitrate to obtain the Zn/CuZr and In/CuZr catalysts.

3.4 Catalyst characterization

The crystallographic information of the precursors and catalysts was obtained using Powder X-ray diffraction (XRD). The diffraction patterns were recorded on a Bruker-AXS Microdiffractometer (D8 ADVANCE) instrument using a Cu Kα radiation source (λ = 1.5406, 40 kV, and 40 mA). The XRD patterns of the reduced-passivated catalysts in Paper IV were obtained from a Rigaku D/Max 2550 VB/PC instrument. The patterns were recorded at 2θ between 10–90° with a step interval of 2 °/min. The peaks were indexed according to the Joint Committee on Powder Diffraction Standards (JCPDS) database. The crystallite sizes were calculated using the Scherrer equation.

The microstructure and morphology of the catalysts were characterized by transmission electron microscopy (TEM, JOEL JEM-2100F, 200 kV) in Paper III and V, whereas high-angle annular dark-field scanning transmission microscopy (HAADF-STEM, Tecnai G2F20 S-Twin, 200 kV) was used in Paper IV. The samples were prepared by dispersing the catalysts in ethanol by ultrasonication and then depositing one droplet of the solution onto a holey carbon-coated support grid.

N_2 adsorption-desorption measurements were conducted at 77 K using a Micromeritics TriStar II instrument. The samples were degassed under vacuum using a sample degas system (Micromeritics VacPrep 061) prior to analysis. The specific surface area (SSA) and pore size distribution of the catalysts were calculated using the Brunauer–Emmet–Teller (BET) and Barret–Joyner–Halenda (BJH) method, respectively. The total pore volume (PV) was calculated from the quantity of gas adsorbed at P/P_0 of 0.99.

The elemental composition of the catalysts was analyzed by inductively coupled plasma atomic emission spectroscopy (ICP-AES) using a Perkin Elmer OPTIMA 4300 DV or Agilent 725-ES apparatus. The sample was dissolved in boiling HNO_3:HCl mixture with a ratio of 1:3. The sample was further diluted and filtered before elemental analysis.

Simultaneous thermal gravimetric analysis (TGA) and differential scanning calorimetry (DSC) was performed on a Netzsch STA449 Jupiter F3 instrument. About 10 mg of sample was heated from room temperature to 700 ^oC at a heating rate of 10 °C/min in synthetic air at a flow rate of 20 mL/min.

The X-ray photoelectron spectroscopy and Auger (XAES) spectra were recorded on an ESCALAB250Xi (ThermoFisher) instrument utilizing a monochromatic Al Kα source (1486.6 eV). The High-resolution spectra were obtained at a pass energy of 30.0 eV, step size of 0.05 eV, and dwell time of 500 ms per step. All spectra were referenced to the C 1s peak (284.8 eV). In paper III, a step size of 0.1 eV was used.

The reducibility of the catalysts was studied by temperature-programmed reduction (H_2-TPR). The H_2-TPR measurements were performed on a Micromeritics Autochem II ASAP 2920 instrument. The samples were pretreated at 200 °C in He flow for 0.5 h prior to the measurements. The TPR profiles were recorded while passing a 7 vol% H_2/Ar mixture at 50 mL/min over the sample and increasing the temperature from ambient to 700 °C at 10 °C/min.

The temperature-programmed desorption (CO_2-TPD) experiments were carried out using a Micromeritics Autochem II ASAP 2920 instrument. The samples were first pretreated with He at 200 °C for 0.5 h, reduced in 7 vol% H_2/Ar (Paper III: 250 °C, 0.5 h; Paper V: 350 °C, 2 h), and then purged under He flow for 1 h. Then, CO_2 adsorption was performed with a 6 vol% CO_2/Ar mixture at 50 °C for 1 h, followed by purging in He. The CO_2-TPD profiles were obtained under constant He flow (40 mL/min) from ambient to 800 °C at a ramp rate of 10 °C/min.

The exposed Cu surface area was determined by dissociative N_2O adsorption using a Micromeritics Autochem II ASAP 2920 instrument. Prior to N_2O adsorption, the sample was heated to 200 °C under He flow for 0.5 h, reduced in 7 vol%H_2/Ar at 350 °C for 2 h, and then purged with He until the temperature reached 50 °C. The N_2O adsorptive decomposition was carried out in a 1% N_2O/He mixture at 50 °C for 1 h following a procedure described by Van Der Grift et al. [113-115]. After that, the sample tube was purged with He for 1 h to remove the physisorbed N_2O. The N_2O consumption was determined by a H_2-TPR experiment from 50 to 400 °C at a rate of 10 °C/min in a 7 vol% H_2/Ar mixture. The Cu surface area (SA_{Cu}) was estimated from the H_2 consumption using Eq. 3.6.

$$SA_{Cu}\ (m^2 \cdot g_{cat}^{-1}) = \frac{Y \times SF \times N_A}{C_M \times W_{cat}} \qquad (3.6)$$

where Y is the moles of H_2 consumed in the TPR following N_2O chemisorption, SF is the stoichiometric factor (2), N_A is Avogadro's number (6.022×10^{23} mol^{-1}), C_M is the number of surface Cu atoms per unit surface area (1.47×10^{19} $atoms \cdot m^{-2}$), and W_{cat} is the amount of catalyst (g).

3.5 *Catalyst evaluation*

The schematic diagram of the CO_2 hydrogenation setup is presented in Figure 3.1. A fixed-bed continuous flow reactor was used to evaluate the

catalyst, which was made from a stainless steel tube with an internal diameter of 0.5 cm and a length of 50 cm. The gas flows (H_2, CO_2, N_2) were controlled by digital mass flow controllers (F-201CV, Bronkhorst), which were calibrated using a manual bubble flow meter. The pressure is measured prior to the reactor, and a back-pressure regulator (Tescom) is installed at the outlet of the reactor. All post-reactor lines and valves were heated to 140 °C to avoid condensation of liquid products. The temperature was measured by a thermocouple located close to the center of the reactor.

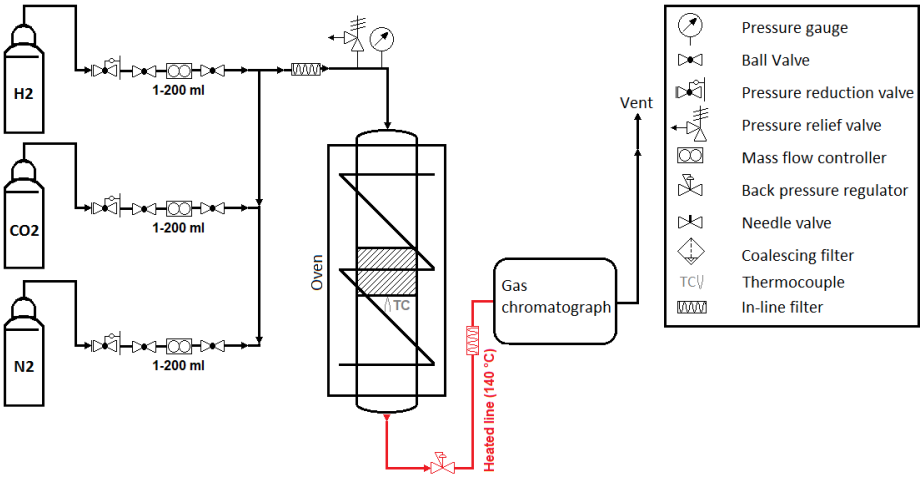

Figure 3.1 Schematic diagram of the CO_2 hydrogenation setup.

The catalysts used for activity tests were crushed and sieved to obtained granules between 40–60 mesh and mixed with SiC (α-Al_2O_3 was used in Paper III). The weight ratio of the catalysts and the inert was approximately 1:5 for all the activity tests. A quartz wool plug was used to keep the catalyst bed in place. Prior to the activity tests, the catalysts were typically reduced in 10 vol% H_2/N_2 (50 ml/min) at 350 °C for 2h with a heating rate of 2 °C/min. After reduction, the reactor was cooled to ambient temperature under N_2 flow. After cooling the reactor, the system was pressurized with the reaction mixture, and then the temperature was increased to the desired temperature. The reaction

mixture typically consisted of 50–100 ml/min of H_2:CO_2:N_2 at a ratio of 3:1:1.

The products were analyzed via on-line gas chromatography (GC) using an Agilent 7890 B system containing two channels equipped with TCD detectors. A HayeS Q (length 0.25 m, diameter 1 mm, thickness 80/100 μm) and a Mols 5A (length 1.5 m, diameter 1 mm, thickness 80/100 μm) column is used for the separation of H_2, N_2, and CO. The CO_2, C_1-C_3 hydrocarbons, and C_1-C_3 oxygenates in the product is separated by a GS-carbonplot column (length 60 m, diameter 0.32, thickness 1.5 μm). The calibration of gaseous components (H_2, CO_2, CO, N_2, C_1-C_3 hydrocarbons) was performed using a gas mixture with a predetermined composition purchased from Praxair. The calibration of methanol and dimethyl ether was done by injecting known concentrations of N_2-vapour mixtures into the heated sampling loop with different methanol/DME concentrations.

The CO_2 conversion (X_{CO2}) was calculated utilizing N_2 as internal standard based on Eq. 3.7.

$$X_{CO_2}(\%) = \left[1 - \frac{\text{moles } CO_{2,out}}{\text{moles } CO_{2,in}} \times \frac{\text{moles } N_{2,in}}{\text{moles } N_{2,out}}\right] \times 100 \qquad (3.7)$$

The selectivity of product *i* (S_i) and space-time yield of methanol ($STY_{methanol}$) were calculated using Eq. 3.8 and Eq. 3.9, respectively.

$$S_i(\%) = \frac{moles\ product_{i,out}}{\sum moles\ product_{i,out}} \times 100 \qquad (3.8)$$

$$STY_{methanol}\left(\frac{mmol}{g_{cat} \cdot h}\right) = \frac{F_{CO_2,in} \times X_{CO_2}/100 \times S_{methanol}/100}{W_{cat}} \qquad (3.9)$$

where $F_{CO2,in}$ (mmol/h) is the molar flow rate of CO_2 at the inlet of the reactor and Wcat (g) is the amount of catalyst.

The TOF of methanol for the Cu-based catalysts was calculated according to the number of Cu surface atoms determined by N_2O chemisorption using Eq. 3.10.

$$TOF_{methanol}\left(\frac{molecules_{methanol}}{second \cdot Cu_{site}}\right) = \frac{R_{methanol} \times N_A}{SA_{Cu} \times C_M} \qquad (3.10)$$

where $R_{methanol}$ is the methanol production rate ($mol \cdot g^{-1} \cdot s^{-1}$),

4 Results and discussion

4.1 *Paper II: Thermodynamic analysis of CO_2 hydrogenation to methanol and oxygenates*

The products considered in the thermodynamic analysis of CO_2 hydrogenation is methanol, CO, H_2O, DME, and C_2–C_4 alcohols. Both single-phase and two-phase models were applied to investigate the influence of product condensation on the thermodynamic equilibrium. Although methane formation is thermodynamically favourable at the investigated reaction conditions, the methane production over typically employed catalysts is low. Therefore, methane is not considered in the thermodynamic analysis.

4.1.1 Equilibrium in CO_2 hydrogenation to methanol

4.1.1.1 Effect of temperature and pressure

Figure 4.1 shows the CO_2 conversion (a) and methanol selectivity (b) at different reaction temperatures and pressures for the stoichiometric H_2/CO_2 ratio of 3/1. It can be seen that high CO_2 conversion and methanol selectivity is achieved at low temperatures and high pressures. This is because the methanol synthesis reaction is exothermic and a volume reducing reaction. The CO_2 conversion curves merge as the temperature increases due to the endothermic RWGS reaction, which is not affected by the reaction pressure. Product condensation occurs at low temperatures, which drives the methanol synthesis reaction nearly to completion. The positive effect of condensation on the methanol yield has been confirmed experimentally, and the formation of a liquid phase has been visually observed using a view-cell reactor [116]. Thus, reactor designs that utilize product condensation could increase the methanol yield per pass.

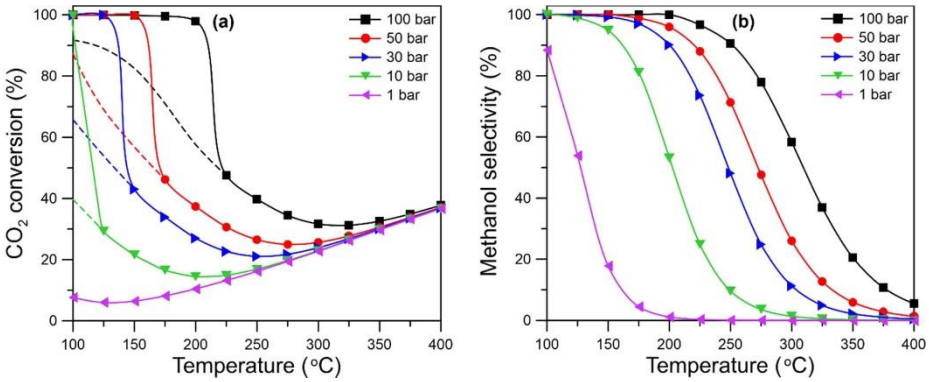

Figure 4.1 Effect of temperature and pressure on (a) CO_2 conversion and (b) methanol selectivity at vapor-liquid and chemical equilibrium. The dashed lines in (a) represent the single-phase equilibrium.

Figure 4.2a–c shows the influence of the phase transition from vapor to liquid on the CO_2 conversion and methanol selectivity at 100 bar. It can be seen that the phase transition occurs over a narrow temperature range between 197–207 °C (Figure 4.2c). The condensation of methanol and H_2O is accompanied by a significant increase in CO_2 conversion. The effect of condensation on the methanol selectivity is relatively small because the RWGS reaction is limited at low temperatures.

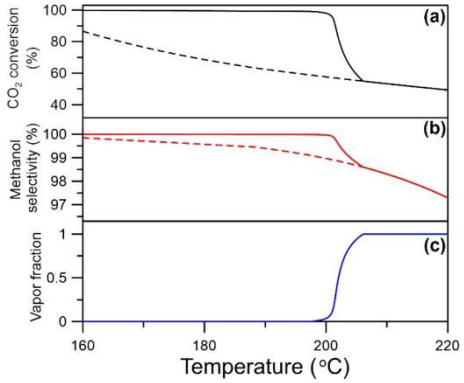

Figure 4.2 (a) CO_2 conversion, (b) methanol selectivity, and (c) vapor fraction over the two-phase region at 100 bar and H_2/CO_2 = 3/1. The dashed lines in (a) and (b) represent the single-phase equilibrium.

4.1.1.2 Effect of H_2/CO_2 ratio

Excess hydrogen is typically employed to limit the molar fraction of H_2O in the reactor, which enhances the reaction rate and also limits the adverse effects of H_2O on the catalyst (e.g., blocking active sites and accelerates deactivation) [117, 118]. The effect of the H_2/CO_2 ratio on the CO_2 conversion and methanol selectivity at 100 bar is shown in Figure 4.3a and b, respectively. The CO_2 conversion increases with increasing H_2/CO_2 ratio throughout the investigated temperature range. The methanol selectivity also increases with increasing H_2/CO_2 ratio because the methanol synthesis reaction is more sensitive to the partial pressure of H_2. A significant deviation from the stoichiometric H_2/CO_2 ratio limits product condensation due to lower yield of condensable methanol and water. Thus, operating close to the stoichiometric ratio is ideal to utilize the positive effect of product condensation on the methanol yield.

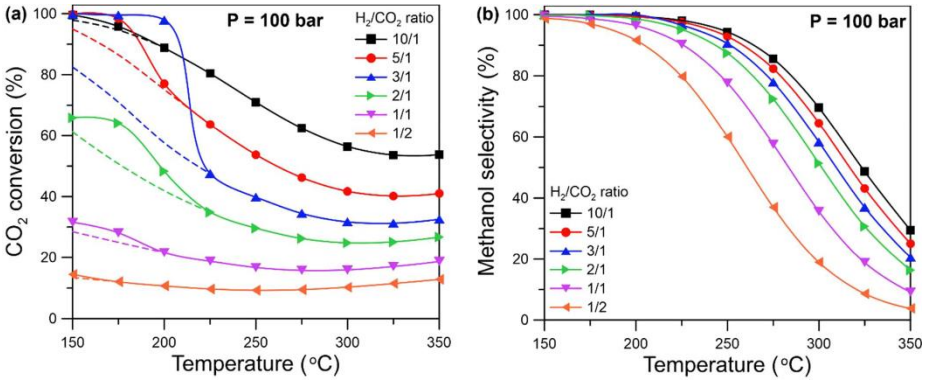

Figure 4.3 Effect of H_2/CO_2 ratio on the (a) CO_2 conversion, (b) methanol selectivity at different temperatures and 100 bar. The dashed lines in (a) represent the single-phase equilibrium.

4.1.1.3 Effect of co-feeding H_2O

The influence of co-feeding H_2O on the thermodynamics is illustrated in Figure 4.4. As expected, the CO_2 conversion decreases above the bubble point because H_2O is a product in both the methanol synthesis and RWGS reaction. However, the addition of H_2O to the feed allows

condensation of products to occur at higher temperatures. Interestingly, the CO_2 conversion and methanol selectivity are higher between 202–213 °C when 20 mol% water is present in the feed compared to the H_2O-free feed mixture. Consequently, condensation can be enhanced by the presence of H_2O within the reactor. This could be utilized in the reactor design to facilitate the removal of H_2O and methanol from the reacting gas-phase mixture.

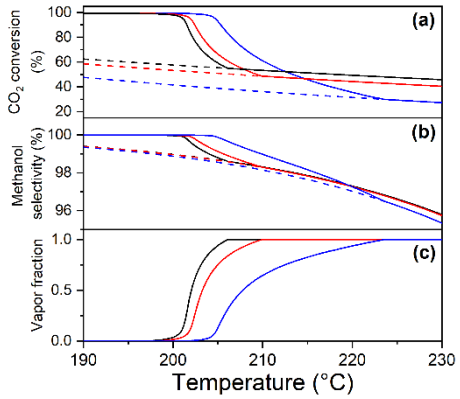

Figure 4.4 Effect of co-feeding H_2O on the (a) CO_2 conversion, (b) methanol selectivity, and (c) vapor fraction over the two-phase region at 100 bar. The dashed lines in (a) and (b) represent the single-phase equilibrium.

4.1.1.4 Recycle ratio in CO_2-to-methanol process

Figure 4.5 shows the contour plots of the recycle ratio needed for reaching a CO_2 conversion of >99% at a H_2/CO_2 ratio of 3/1 (a) and 5/1 (b). The data points were obtained using gas-phase thermodynamics. It can be seen that the recycle volume is larger than the volumetric feed rate even at relevant reaction conditions (200–300 °C, 50–100 bar). This poses a significant challenge to the industrial implementation of the CO_2-to-methanol process due to the high cost of the recycling units. Thus, higher pressure is needed to avoid large recycle volumes. Another option is to remove the products from the reacting gas-phase, such as via condensation or using permselective membranes.

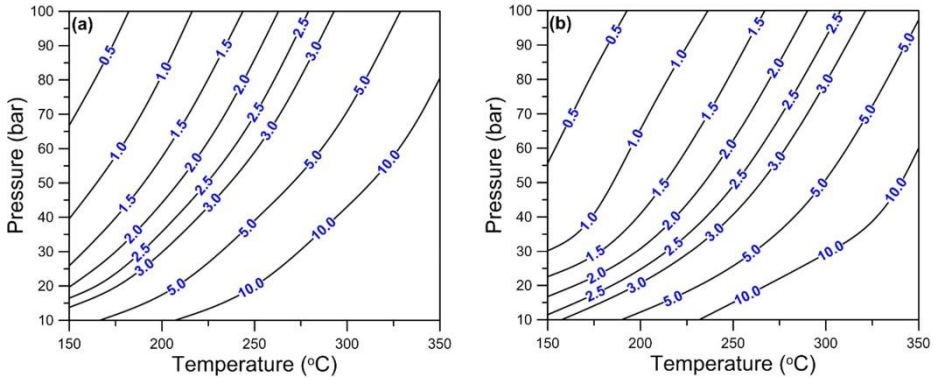

Figure 4.5 Contour plot of required recycle ratio (blue numbers) based on gas-phase thermodynamics to achieve a CO_2 conversion of >99% at a H_2/CO_2 ratio (a) 3/1 and (b) 5/1.

4.1.2 Equilibrium in CO_2 hydrogenation to methanol and DME

Solid acid catalysts are currently used to produce DME from methanol, and Zeolites has been most extensively studied. However, one-pot synthesis of DME has also been explored, which is typically performed by combining a methanol synthesis catalyst with zeolite [119]. The conversion of methanol to DME occurs via the exothermic methanol dehydration reaction (Eq 4.1). Kinetic studies indicate that the methanol dehydration step is very fast and that the reaction rate is controlled by the methanol synthesis reaction over hybrid catalysts [120, 121], which is encouraging for the industrial implementation of the one-pot synthesis of methanol and DME.

$$2CH_3OH \rightleftharpoons CH_3OCH_3 + H_2O, \quad \Delta H^0_{273k} = -23.4 \text{ kJ/mol} \qquad (4.1)$$

The thermodynamics of CO_2 hydrogenation to methanol and DME was studied by single- and two-phase models at different temperatures and pressures. The CO_2 conversion is shown in Figure 4.6a, while Figure 4.6b presents the selectivity of methanol and DME. The simultaneous production of methanol and DME is also favored at low temperature and high pressure. The thermodynamic limitation on the CO_2 conversion is

significantly lower for the one-pot synthesis of methanol and DME compared to methanol synthesis. Product condensation occurs at low temperatures, which increases the CO_2 conversion to almost 100%. Furthermore, the RWGS reaction is less favorable when DME is included in the analysis. The selectivity towards DME is significantly higher than that of methanol at lower temperatures, and the DME selectivity decreases with increasing temperature. On the other hand, the methanol selectivity shows a volcano-type trend in which the maximum shifts towards higher temperature with increasing pressure.

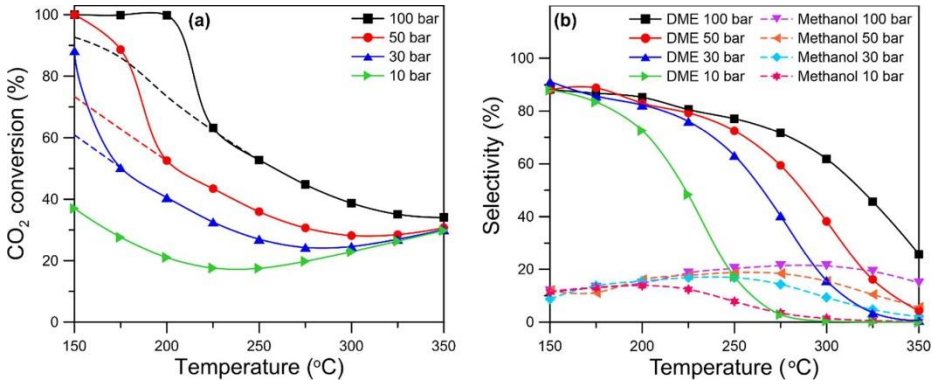

Figure 4.6 (a) CO_2 conversion and (b) methanol and DME selectivity at equilibrium in CO_2 hydrogenation to a mixture of methanol, DME, and CO. The dashed lines in (a) represent the single-phase equilibrium.

The influence of product condensation was examined over the two-phase region, and the CO_2 conversion, methanol selectivity, and vapor fraction at 100 bar are shown in Figure 4.7a–c. The onset of product condensation occurs at a higher temperature for the product mixture of DME, methanol, and H_2O compared to methanol synthesis. Near complete conversion of CO_2 can be achieved at about 206 °C. The methanol and DME selectivity are mildly affected by product condensation, which slightly increases the DME selectivity.

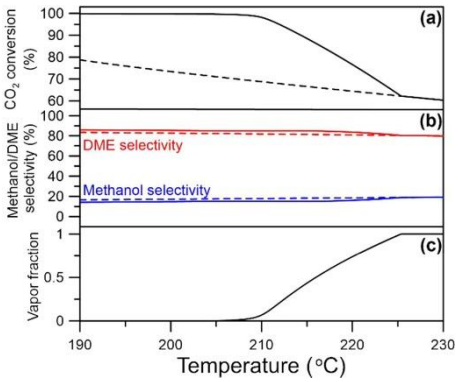

Figure 4.7 CO_2 conversion and (b) methanol and DME selectivity, and (c) vapor fraction over the two-phase region at 100 bar and H_2/CO_2 ratio of 3/1. The dashed lines in (a) and (b) represent the single-phase equilibrium.

4.2 *Paper III: Mesoporous Co-Mn oxide catalysts for CO_2 hydrogenation*

4.2.1 Catalyst characterization

4.2.1.1 N_2 adsorption-desorption

The SSA, PV, and pore diameter of the Co_3O_4, *X*MnO_x-Co_3O_4, and MnO_x catalysts are summarized in Table 4.1. The N_2 adsorption-desorption isotherms of all catalysts were of type IV, indicating mesoporous structure. The SSA of Co_3O_4 (56 m_2/g) and MnO_x (60 m_2/g) is similar, whereas the PV is higher for Co_3O_4 (0.27 cm^3/g) compared to MnO_x (0.20 cm^3/g). The SSA increases significantly for the catalysts with a Mn content of 20 and 50 mol% to 106 and 197 m^2/g, respectively. The PV of the *X*MnO_x-Co_3O_4 catalysts is in the range of 0.21 to 0.31 cm^3/g.

Table 4.1 Summary of N_2 adsorption-desorption results, metal oxide spinel crystallite size, and Mn content determined by ICP-AES.

Catalyst	SSA (m^2/g)	PV (cm^3/g)	Pore diameter (nm)	$d_{M_3O_4}$ (M = Mn, Co) (nm)[a]	Mn content (mol %)
Co_3O_4	56	0.27	13.7	14	–
10MnO_x-Co_3O_4	54	0.21	9.5	13	13.6
20MnO_x-Co_3O_4	106	0.31	7.9	10	21.0
50MnO_x-Co_3O_4	197	0.24	4.4	8	55.4
MnO_x	60	0.20	10.3	14	–

[a] Calculated from the (311) diffraction peak located at 2θ of ~37°.

4.2.1.2 XRD

XRD was conducted to obtain information on crystal phase and crystallinity of the calcined Co_3O_4, *X*MnO_x-Co_3O_4, and MnO_x catalysts and the XRD patterns are shown in Figure 4.10. The pattern of the MnO_x sample matches fairly well with that of crystalline Mn_3O_4 (PDF #80-0382), while the peaks of Co_3O_4 correspond to cubic Co_3O_4 (PDF #74-

1657). A shift in the peaks is observed for the $10MnO_x$-Co_3O_4 and $20MnO_x$-Co_3O_4 catalysts, which is attributed to the incorporation of Mn into a mixed Co-Mn oxide spinel-like structure. The XRD pattern of $50MnO_x$-Co_3O_4 is ascribed to structured (Co, Mn)$(Mn,Co)_2O_4$ spinel (#PDF 18-0410), which typically exhibit a broad reflection around 2θ of 36.5° [122, 123].

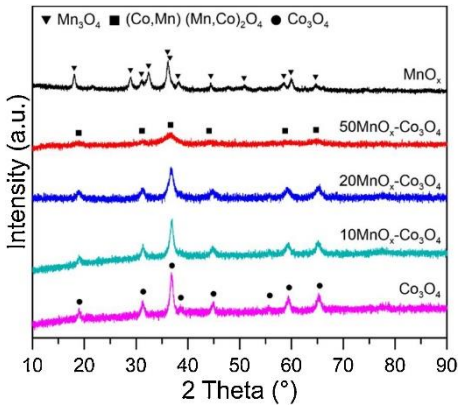

Figure 4.8 XRD patterns of the calcined Co_3O_4, *X*MnO_x-Co_3O_4, and MnO_x catalysts.

The crystallite size of the Co_3O_4, *X*MnO_x-Co_3O_4, and MnO_x catalysts are listed in Table 4.1. The crystallite size of Co_3O_4, $10MnO_x$-Co_3O_4, and MnO_x is similar in the range of 13–14 nm. At higher Mn content, the crystallite size decreases to 10 nm and 8 nm for the $20MnO_x$-Co_3O_4 and $50MnO_x$-Co_3O_4 catalysts, respectively.

4.2.1.3 TEM

The morphology and particle size of the catalysts was studied by TEM, and the TEM images are shown in Figure 4.11. The catalysts consist of well-defined NPs with a narrow particle size distribution. The average particle size calculated statistically from the TEM images is close to the crystallite size obtained from XRD.

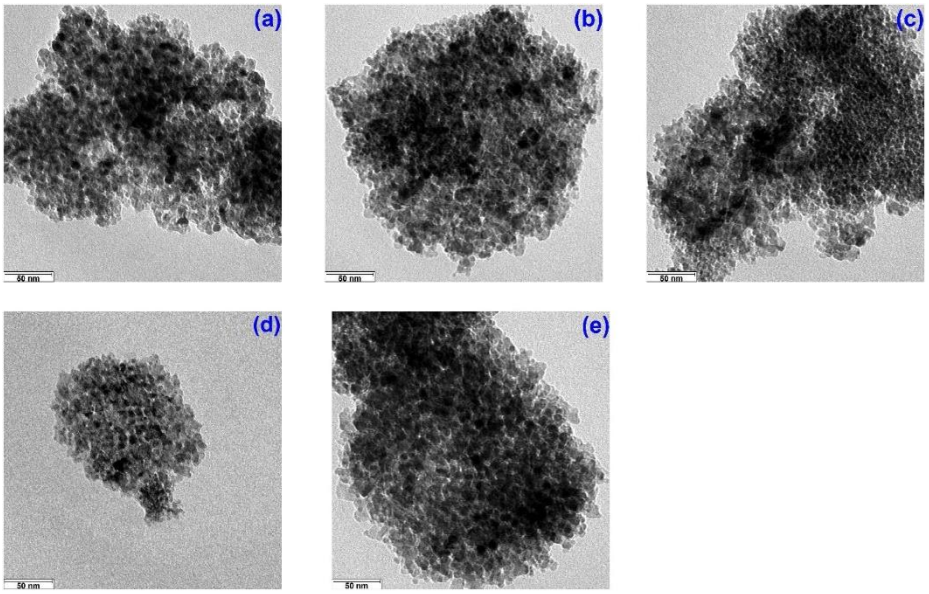

Figure 4.9 TEM images of calcined (a) Co_3O_4, (b) $10MnO_x$-Co_3O_4, (c), $20MnO_x$-Co_3O_4 (d) $50MnO_x$-Co_3O_4, and (e) MnO_x.

4.2.1.4 XPS

High-resolution XPS of the *X*MnO_x-Co_3O_4 catalysts was conducted to investigate the composition and elemental states of the surface species. The Co 2p and Mn 2p regions are presented in Figure 4.12 (a) and (b), respectively. For the Co 2p spectra, two spin-orbit doublets corresponding to Co $2p_{3/2}$ and Co $2p_{1/2}$ and two satellite peaks are present. The Co 2p spectra were deconvoluted according to the fitting parameters reported by Biesinger et al. [124]. To qualitatively assess the Co^{2+}/Co^{3+} fraction of the catalysts, the ratio of the Cu^{2+} (~786 eV) peak area relative to the Cu^{3+} (~789 eV) peak area of the $2p_{3/2}$ satellite feature was calculated [125-128]. The Co^{2+}/Co^{3+} ratio of the catalysts is summarized in Table 4.2. The Co^{2+}/Co^{3+} ratio of $10MnO_x$-Co_3O_4 (1.16) and $20MnO_x$-Co_3O_4 (0.93) is close to the reference value of Co_3O_4 [124]. On the other hand, the higher Co^{2+}/Co^{3+} ratio of the $50MnO_x$-Co_3O_4 catalyst (2.25) indicates a larger fraction of Co^{2+} species compared to the other catalysts.

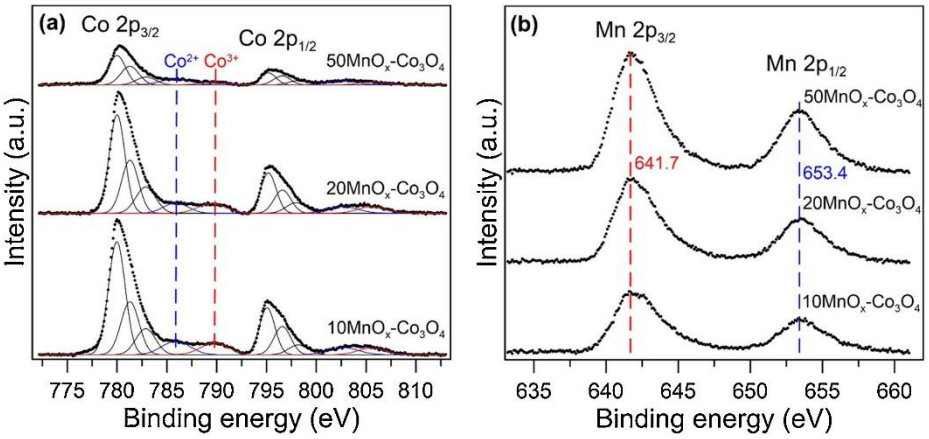

Figure 4.10 High-resolution XPS spectra of the (a) Co 2p and (b) Mn 2p regions of the *X*MnO_x-Co_3O_4 catalysts.

Table 4.2 Surface atomic composition, binding energy of Co 2p and Mn 2p peaks, and Co^{2+}/Co^{3+} ratio of the *X*MnO_x-Co_3O_4 catalysts.

Catalyst	Surf. comp. (mol %)		Binding energy (eV)				Co^{2+}/Co^{3+}
	Co	Mn	Co $2p_{3/2}$	Co $2p_{1/2}$	Mn $2p_{3/2}$	Mn $2p_{1/2}$	
10MnO_x-Co_3O_4	84.7	15.3	780.0	795.1	641.6	653.3	1.16
20MnO_x-Co_3O_4	78.2	21.8	780.1	795.3	641.7	653.5	0.93
50MnO_x-Co_3O_4	44.5	55.5	780.3	795.6	641.7	653.4	2.25

The Mn 2p spectrum contains two spin-orbit doublets at 641.7 eV and 653.4 eV corresponding to Mn $2p_{1/2}$ and Mn $2p_{3/2}$, respectively. For the *X*MnO_x-Co_3O_4 catalysts, the position and shape of the Mn $2p_{1/2}$ and Mn $2p_{3/2}$ peaks are close to the values reported for $MnCo_2O_4$ [123, 129] and $CoMn_2O_4$ [130]. Furthermore, the Co 2p3/2 and Co 2p1/2 peak position shift slightly towards higher binding energy with increasing Mn content, which is consistent with previous studies on Co-Mn mixed oxide spinel materials [123, 129, 130]. Thus, the XPS analysis indicates that Co and Mn are incorporated into a Co-Mn oxide spinel phase, which is consistent with the XRD analysis.

4.2.1.5 H_2-TPR

The reducibility of the catalysts was studied by H_2-TPR, and the profiles are shown in Figure 4.13. The reduction peaks at 264 and 347 °C of the Co_3O_4 catalyst can be ascribed to the sequential reduction of Co_3O_4 to metallic Co via the CuO intermediate [131]. The TPR profile of MnO_x exhibits a low-temperature peak around 279 °C and a wide signal centered at 426 °C. The low-temperature peak is attributed to the reduction of Mn^{3+} ions located in tetrahedral sites, whereas the complete reduction of Mn_3O_4 into MnO occurs at higher temperature [132]. The high-temperature reduction peak shifts towards higher temperatures for $10MnO_x$-Co_3O_4 (412 °C) and $20MnO_x$-Co_3O_4 (377 °C) compared to Co_3O_4. The TPR profile of the $50MnO_x$-Co_3O_4 catalyst is similar to that of the MnO_x sample but the maximum of the second reduction peak is located at a higher temperature (474 °C). The results indicate that the mixed metal oxide phase is more stable when both Co and Mn is present, which requires a higher temperature to be reduced.

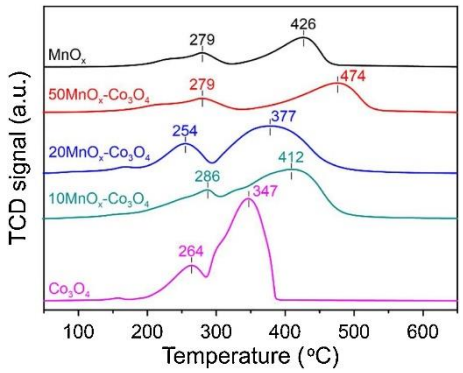

Figure 4.11 H_2-TPR profiles of the Co_3O_4, *X*MnO_x-Co_3O_4, and MnO_x catalysts.

The H_2-consumption of the catalysts was estimated from the peak areas and is summarized in Table 4.3. The H_2-consumption is higher for the Co_3O_4 (182 mmol/g_{cat}) catalyst compared to MnO_x (56 mmol/g_{cat}) because MnO is the final reduction product. Consequently, the H_2-consumption also decreases with increasing Mn content for the *X*MnO_x-Co_3O_4 catalysts.

Table 4.3 H_2-consumption estimated by H_2-TPR and surface basicity determined from CO_2-TPD.

Catalyst	H_2-consump. (mmol/g_{cat})	Number of basic sites (μmol/g_{cat})	Basic site composition (μmol/g_{cat}) and peak temperature (°C)		
			WB, (T)	MB, (T)	SB, (T)
Co_3O_4	182	1.2	0.5 (179)	0.2 (297)	0.4 (383)
$10MnO_x$-Co_3O_4	168	3.8	0.8 (152)	0.1 (219)	2.9 (354)
$20MnO_x$-Co_3O_4	159	7.0	1.1 (154)	1.8 (223)	4.1 (386)
$50MnO_x$-Co_3O_4	104	7.5	2.5 (163)	0.8 (206)	4.2 (327)
MnO_x	56	2.9	0.2 (122)	0.2 (184)	2.5 (389)

4.2.1.6 CO_2-TPD

The surface basicity of the catalysts was studied by CO_2-TPD after reduction at 250 °C, and the profiles are shown in Figure 4.14. The profiles were deconvoluted into three Gaussian peaks (dotted curves), corresponding to weak (WB), medium-strength (MB), and strong basic (SB) sites. It can be seen that the surface basicity of the Co_3O_4 catalyst is much lower than the other catalysts and consists of a mixture of WB, MB, and SB sites (Table 4.3). For the *X*MnO_x-Co_3O_4 catalysts, the number of WB, MB, and SB sites increases significantly with increasing Mn content. On the other hand, the MnO_x sample mainly exhibits a large number of SB sites.

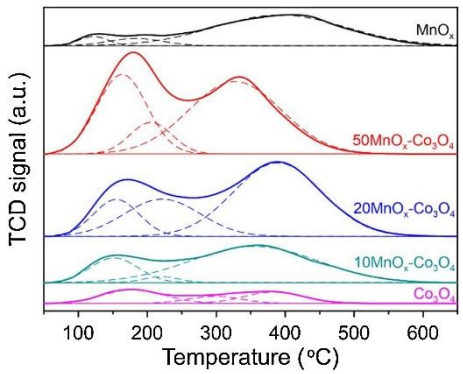

Figure 4.12 CO_2-TPD profiles of the Co_3O_4, *X*MnO_x-Co_3O_4, and MnO_x catalysts.

4.2.2 Methanol synthesis activity test

4.2.2.1 Catalyst activity and selectivity

The CO_2 hydrogenation activity of the catalysts was compared at 250 °C and 10 bar. Figure 4.15 shows the steady-state CO_2 conversion and selectivity of the Co_3O_4, *X*MnO_x-Co_3O_4, and MnO_x catalysts. The Co_3O_4 catalyst exhibits the highest CO_2 conversion of 56.5%, whereas a CO_2 conversion of 2.9% is obtained over MnO_x. When Mn is incorporated into Co_3O_4, the activity of the catalyst decreases. The higher CO_2 conversion of 20MnO_x-Co_3O_4 (45.1%) compared to 10MnO_x-Co_3O_4 (36.9%) is attributed to the significantly larger SSA of the 20MnO_x-Co_3O_4 catalyst. The methane selectivity is higher than 65% for the Co_3O_4 and *X*MnO_x-Co_3O_4 catalysts, whereas the CO selectivity of MnO_x is 70.2%. The methanol selectivity shows a volcano-type trend with respect to Mn content, and the highest methanol selectivity of 22.1% is achieved at 20 mol% Mn. The CO selectivity increases with Mn content from 1.0% (Co_3O_4) to 9.1% (50MnO_x-Co_3O_4). A small fraction of C_2H_4 is also produced over the catalysts. The C_2H_4 selectivity increases from 1.8% (Co_3O_4) to 3.4% and 3.2% for 10MnO_x-Co_3O_4 and 20MnO_x-Co_3O_4, respectively. Only traces of C_{3+} and DME could be detected for the Co_3O_4, 10MnO_x-Co_3O_4, and 20MnO_x-Co_3O_4 catalysts.

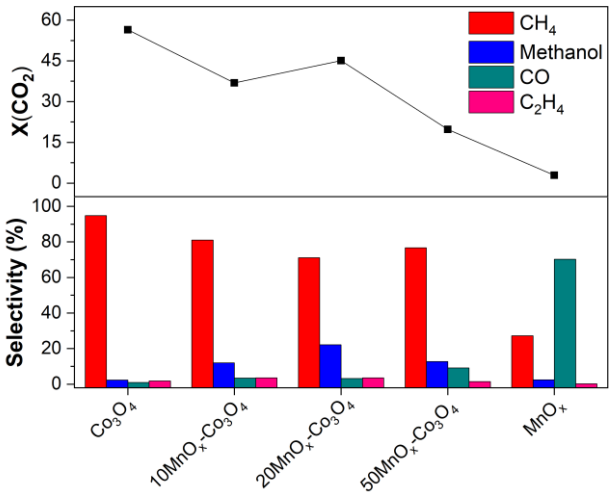

Figure 4.13 CO_2 conversion and product selectivity over different catalysts after reduction at 250 °C. Reaction conditions: 250 °C, 10 bar, $H_2/CO_2/N_2$ ratio of 3/1/1, and 88 800 h^{-1}.

The space-time yield (STY, $mmol \cdot h^{-1} \cdot m^{-2}_{SSA}$) of methane, methanol, CO, and C_2H_4 are summarized in Table 4.4. It can be seen that the STY of methane decreases drastically with increasing Mn content, whereas the STY of methanol is significantly higher for the catalysts with 10 and 20 mol% Mn. For instance, the STY of methane is three times higher over Co_3O_4 compared to $20MnO_x$-Co_3O_4, whereas the STY of methanol is four times higher over the $20MnO_x$-Co_3O_4 catalyst. The activity of the $50MnO_x$-Co_3O_4 and MnO_x catalysts is much lower than the other catalysts. Thus, the Co:Mn composition significantly affects the activity and selectivity of the catalyst.

Table 4.4 Production rate per SSA of methane, methanol, CO, and C_2H_4 over the Co_3O_4, *X*MnO_x-Co_3O_4, and MnO_x catalysts. Reaction conditions: 250 °C, 10 bar, $H_2/CO_2/N_2$ ratio of 3/1/1, and 88 800 h^{-1}.

Catalyst	STY of CH_4 ($mmol/m^2$)	STY of methanol ($mmol/m^2$)	STY of CO ($mmol/m^2$)	STY of C_2H_4 ($mmol/m^2$)
Co_3O_4	6.95	0.17	0.07	0.13
$10MnO_x$-Co_3O_4	4.03	0.60	0.17	0.17
$20MnO_x$-Co_3O_4	2.20	0.68	0.10	0.11
$50MnO_x$-Co_3O_4	0.56	0.09	0.07	0.01
MnO_x	0.10	<0.01	0.25	<0.01

4.2.2.2 *Influence of reaction parameters on $10MnO_x$-Co_3O_4 and $20MnO_x$-Co_3O_4*

The effect of reaction temperature on the CO_2 conversion and selectivity over the $10MnO_x$-Co_3O_4 and $20MnO_x$-Co_3O_4 catalysts is shown in Figure 4.16 (a) and (b), respectively. The catalysts exhibit similar trends in terms of CO_2 conversion and selectivity as the temperature is increased. The CO_2 conversion increases significantly up to 250 °C for both catalysts. Reaction intermediates or products might be inhibiting the active sites and thereby, influence the CO_2 conversion at higher temperatures since CO_2 methanation is not particularly limited by thermodynamics at these reaction conditions [133]. The methane selectivity first decreases until 250 °C and then increases with temperature. On the other hand, the methanol selectivity shows a volcano-type trend in which the highest methanol selectivity is achieved at 250 °C. This is probably due to the severe thermodynamic limitations on methanol above 250 °C. A slight increase in C_2H_4 and CO selectivity occurs as the temperature is increased.

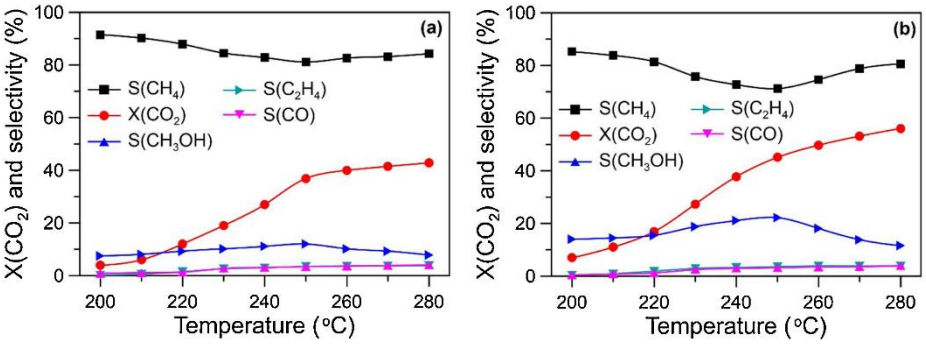

Figure 4.14 Effect of reaction temperature on CO_2 conversion and selectivity over (a) $10MnO_x$-Co_3O_4 and (b) $20MnO_x$-Co_3O_4. Reaction conditions: 10 bar, $H_2/CO_2/N_2$ ratio of 3/1/1, and 88 800 h^{-1}.

Figure 4.17a and b show the influence of reaction pressure on the CO_2 conversion and selectivity over $10MnO_x$-Co_3O_4 and $20MnO_x$-Co_3O_4, respectively. It can be seen that the CO_2 conversion and methanol

selectivity increases with pressure, whereas the selectivity of methane, CO, and C_2H_4 decreases. At a pressure of 20 bar, the methanol selectivity is 28.2% over $20MnO_x$-Co_3O_4, while a methanol selectivity of 19.1% is achieved over the $10MnO_x$-Co_3O_4 catalyst. The trends in selectivity indicate that methanol synthesis is more sensitive to the reaction pressure compared with CO_2 methanation. This agrees well with the literature on methanol synthesis and CO_2 methanation. The activity and selectivity increase significantly with pressure over typical methanol synthesis catalysts [134], whereas CO_2 methanation is not particularly dependent on elevated pressures [135].

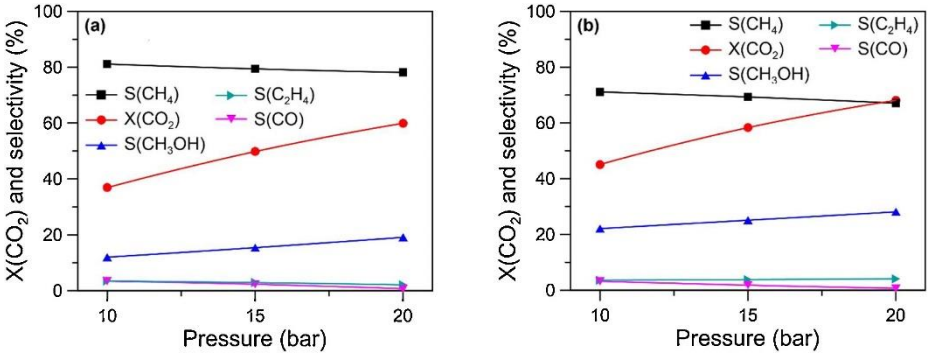

Figure 4.15 Effect of reaction pressure on CO_2 conversion and selectivity over (a) $10MnO_x$-Co_3O_4 and (b) $20MnO_x$-Co_3O_4. Reaction conditions: 250 °C, $H_2/CO_2/N_2$ ratio of 3/1/1, and 88 800 h^{-1}.

The influence of GHSV on the CO_2 conversion and selectivity over the $10MnO_x$-Co_3O_4 and $20MnO_x$-Co_3O_4 catalysts is presented in Figure 4.18a and b, respectively. Evaluating the catalytic performance is challenging at these reaction conditions because it is difficult to assess the influence of the adsorbed surface species on the formation rate of the different products. Similar trends in CO_2 conversion and selectivity can be observed. The higher methanol selectivity at lower GHSV is probably due to the slower kinetics of methanol synthesis compared to CO_2 methanation. The CO selectivity increases while the selectivity to C_2H_4 decreases with increasing GHSV. The ability of Co to generate higher hydrocarbons is significantly higher from syngas compared to CO_2/H_2

mixtures [109, 136]. Therefore, the trends in the selectivity of CO and C_2H_4 indicate that CO is involved in the formation of C_2H_4. Furthermore, the higher methanol selectivity at lower GHSV suggests that CO might also play a role in methanol synthesis.

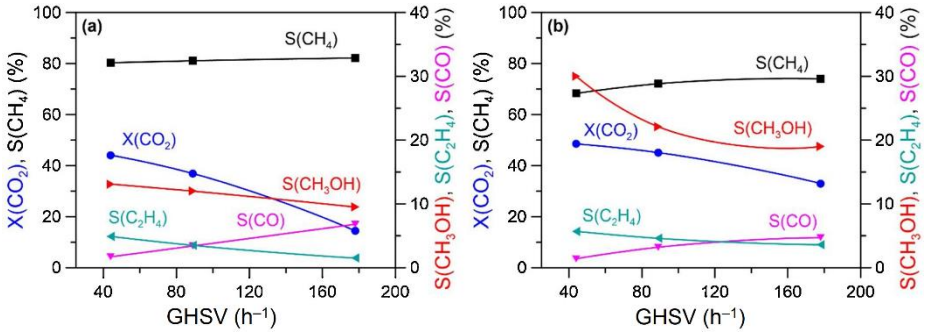

Figure 4.16 Effect of GHSV on the CO_2 conversion and selectivity over (a) $10MnO_x$-Co_3O_4 and (b) $20MnO_x$-Co_3O_4. Reaction conditions: 250 °C, 10 bar, and $H_2/CO_2/N_2$ ratio of 3/1/1.

4.2.2.3 The effect of catalyst reduction temperature

The catalytic performance after reduction at 200, 250, and 300 °C is summarized in Table 4.5. The CO_2 conversion is very low (<5%) after reduction at 200 °C, which indicates that the activity of largely unreduced Co_3O_4 is relatively low. It can also be seen that the CO selectivity is significantly higher when the catalysts are reduced at 200 °C. Furthermore, only traces of methanol can be detected for all the catalysts. The CO_2 conversion is substantially higher after reduction at 250 °C and increases slightly when the catalysts are reduced at 300 °C. The highest methanol selectivity is obtained after reduction at 250 °C for all the catalysts. This indicates that the oxidation state of the cobalt phase significantly influences the selectivity of the Co-Mn oxide catalysts, which is in agreement with literature on CO_2 hydrogenation over Co-based catalysts [109, 110, 137].

Table 4.5 CO_2 conversion and selectivity after reduction at different temperatures (T_R). Reaction conditions: 250 °C, 10 bar, $H_2/CO_2/N_2$ ratio of 3/1/1, and 88 800 h^{-1}.

Catalyst	T_R (°C)	X(CO_2) (%)	S(CH_4) (%)	S(methanol) (%)	S(CO) (%)
10MnO_x-Co_3O_4	200	3.9	72.7	Traces	24.9
	250	36.9	81.1	12.0	3.4
	300	40.8	87.1	7.5	2.1
20MnO_x-Co_3O_4	200	5.0	72.3	Traces	24.8
	250	45.1	71.1	22.1	3.2
	300	47.4	82.1	14.8	2.3
50MnO_x-Co_3O_4	200	3.4	36.7	Traces	63.1
	250	19.8	76.7	12.7	9.1
	300	30.3	87.3	4.7	7.3

4.2.2.4 Intrinsic activity

The turnover frequency (TOF) was calculated to compare the intrinsic activity of the catalysts. The TOF was estimated from the SSAs and known surface packing densities of cubic (space group Fm-3 m) CuO [110] since the TPR analysis indicate that Co_3O_4 is not fully reduced at 250 °C. It can be seen from Figure 4.19 that the TOF for CO_2 conversion decreases with increasing Mn surface content. This is mostly because of the inhibiting effect of Mn on methane formation (Table 4.4). Thus, the active sites for methanol synthesis are not able to compensate for the loss in the active sites for methane formation.

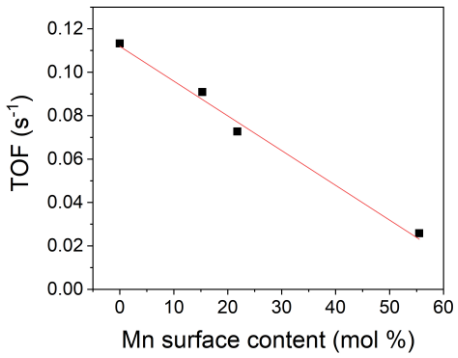

Figure 4.17 TOF of CO_2 conversion as a function of Mn surface content. Reaction conditions: 250 °C, 10 bar, $H_2/CO_2/N_2$ ratio of 3/1/1, and 88 800 h^{-1}.

An important parameter to compare the *X*MnO_x-Co_3O_4 catalysts to the conventional Cu-based catalyst is the TOF for methanol formation ($TOF_{methanol}$). The $TOF_{methanol}$ related to the CuO surface area as a function of Mn surface content is shown in Figure 4.20. It can be observed that the $TOF_{methanol}$ increases significantly when 10 and 20 mol% Mn is incorporated into the catalyst. The $TOF_{methanol}$ of the 20MnO_x-Co_3O_4 catalyst (0.016 s^{-1}) is in the medium to high range of typical values reported in literature for Cu-based catalysts despite the lower pressure: ~0.003–0.026 at 220–250 °C and 30–80 bar [44, 65, 138]. Thus, the Co-Mn oxide system is promising alternative to the conventional catalysts, particularly for low-pressure applications.

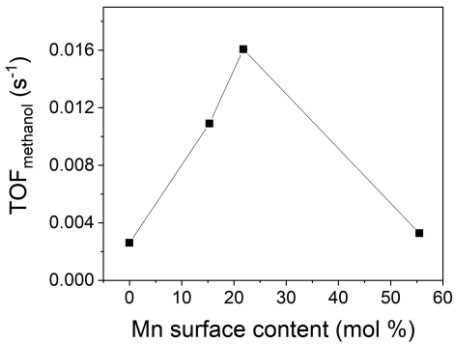

Figure 4.18 TOF for methanol formation as a function of Mn surface content. Reaction conditions: 250 °C, 10 bar, $H_2/CO_2/N_2$ ratio of 3/1/1, and 88 800 h^{-1}.

4.3 *Paper IV: Influence of Cu-metal oxide interaction and effect of indium promotion on Cu-ZnO-Al_2O_3 catalysts*

4.3.1 Catalyst characterization

4.3.1.1 Textural and structural properties

The nominal and actual metal content of the catalysts is given in Table 4.6. For the HT-derived catalysts (2CZA-In*Y*), the Cu:Zn ratio is fixed at 2, while the Al content is replaced by In depending on the desired In loading. It can be seen that the actual metal content is in good agreement with the nominal composition for the prepared catalysts.

Table 4.6 Nominal and actual composition determined by ICP-AES of the 2CZA-In*Y*, Cu-ZnO, and In/Cu-ZnO catalysts.

Catalysts	Nominal composition (mol%)				Composition determined by ICP-AES (mol%)			
	Cu	Zn	Al	In	Cu	Zn	Al	In
2CZA-In0	50	25	25	0	51.3	24.3	24.4	–
2CZA-In2	50	25	23	2	50.9	24.1	22.9	2.1
2CZA-In3	50	25	22	3	51.5	24.6	20.8	3.1
2CZA-In5	50	25	20	5	51.7	23.9	19.3	5.1
Cu-ZnO	83	17	–	–	83.2	16.8	–	–
In/Cu-ZnO	82	17	–	1	82.2	16.5	–	1.3

The N_2-physisorption results of the calcined 2CZA-In*Y*, Cu-ZnO, and In/Cu-ZnO catalysts are summarized in Table 4.7. The incorporation of In into the HT-derived catalysts slightly increases the specific surface area, which is in the range of 36–41 m^2/g. The specific surface area of the Cu-ZnO catalyst is 72 m^2/g, which decreases to 46 m^2/g after impregnation with In.

Table 4.7 Summary of N_2-physisorption results, crystallite size and particle size of the 2CZA-In*Y*, Cu-ZnO, and In/Cu-ZnO catalysts.

Catalyst	SSA (m^2/g)	d_{Cu} (nm)[a]	d_{Cu} (nm)[b]	H_2/CuO (%)[c]	SA_{Cu} (m^2/g_{cat})[b]
2CZA-In0	36	13.1	9.5	99	13
2CZA-In2	39	11.8	9.4	101	16
2CZA-In3	41	12.1	9.4	101	15
2CZA-In5	37	12.3	8.7	103	11
Cu-ZnO	72	23.7	–	98	18
In/Cu-ZnO	46	20.1	–	101	14

[a] Calculated from the (111) peak by the Scherrer equation

[b] Determined by counting particles in HAADF-STEM images

[c] Calculated from H_2-consumption during H_2-TPR

[d] Estimated by N_2O chemisorption

The XRD patterns of the 2CZA-In*Y* catalyst precursors are shown in Figure 4.21a. The precursors crystallize in a HT-like structure and match the pattern reported for $Cu_2Zn_4Al_2(OH)_{16}CO_3{\cdot}H_2O$ (PDF #38-0484) [44]. The peaks at 2θ of 35.5° and 38.7° indicate the formation of crystalline CuO. These CuO species can form during ageing or drying of the precursors [139]. For the 2CZA-In5 catalyst, additional reflections are present at 22.3° and 31.7°, corresponding to $In(OH)_3$ (PDF #76-1463). The full width at half maximum (FWHM) of the 003 reflection (2θ of 11.8°) shows a volcano-type trend with a maximum at 3 mol% In (Figure 4.21b). The increase in the FWHM indicates either an increase in lattice strain or a decrease of the crystal domain size in the stacking direction, which is attributed to the presence of In within the HT-like structure [140-142]. The XRD pattern of the Cu-ZnO precursor is typical of Cu, Zn malachite (Figure 4.21c). The shift in the $(20\bar{1})$ and $(21\bar{1})$ peaks in the 2θ-range of 31–33° is indicative of Zn incorporation into the malachite structure [143].

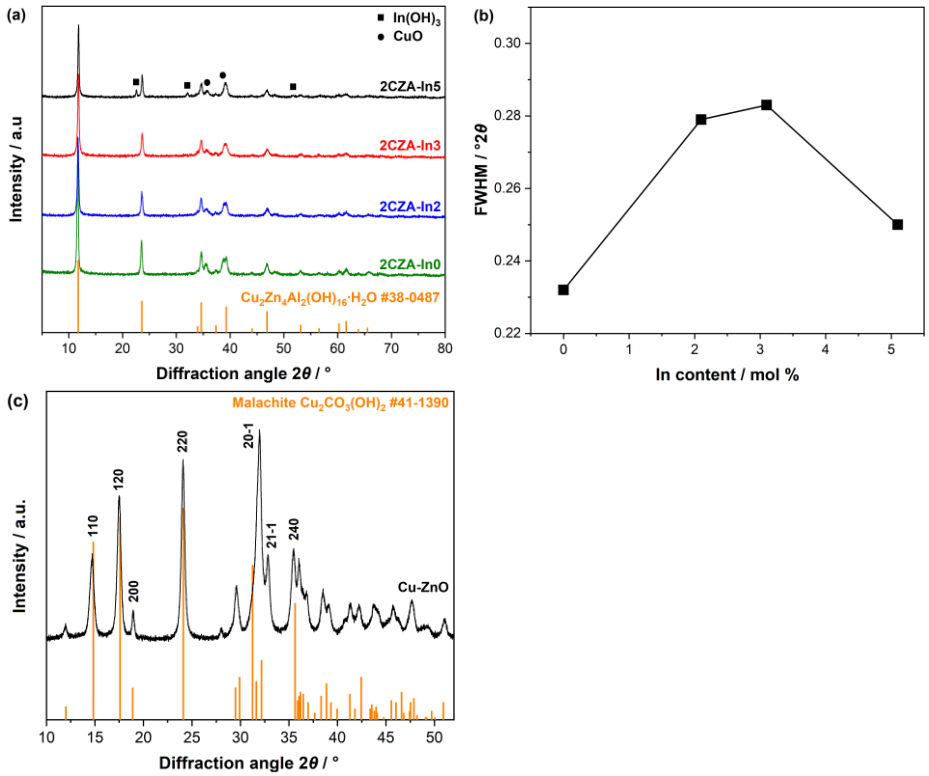

Figure 4.19 (a) XRD patterns of the 2CZA-In*Y* precursors, (b) FWHM of the 003 peak as a function of In content, and (c) XRD pattern of the Cu-ZnO precursor.

The XRD patterns of the reduced 2CZA-InY catalysts are shown in Figure 22a. The reflections at 2θ of 43.3°, 50.4°, and 74.1° correspond to metallic Cu (PDF #04-0836). The crystallite size was estimated from the Cu(111) peak and is relatively similar for the 2CZA-In*Y* catalysts between 11.8–13.1 nm (Table 4.7). The weak reflections between 31–36° are attributed to ZnO (PDF #36-1415), which indicates that the Zn and Al oxide species are largely amorphous after reduction. For the In-containing HT-derived catalysts, the Cu peaks shift towards lower diffraction angles with increasing In content. Furthermore, weak reflections are present between 42–43° for the 2CZA-In5 catalyst. This is indicative of Cu_xIn_y alloys as the most intense peaks of different Cu_xIn_y alloys are located in this region.

The XRD patterns of the reduced Cu-ZnO and In/Cu-ZnO indicate that both crystalline Cu and ZnO NPs are present (Figure 4.22b). The crystallite size of Cu is higher for Cu-ZnO (23.7nm) and In/Cu-ZnO (20.1 nm) compared to the 2CZA-In*Y* catalysts. The shift in the Cu peaks for the In/Cu-ZnO catalyst might be due to the presence of In within the bulk of the Cu NPs.

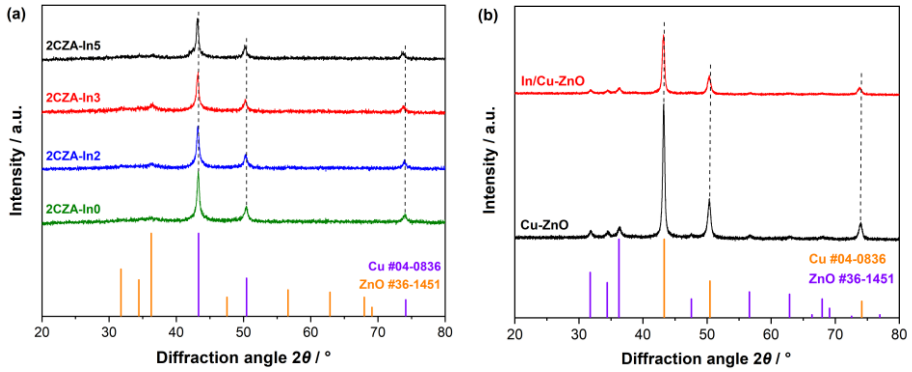

Figure 4.20 XRD patterns of the reduced (a) 2CZA-In*Y* and (b) Cu-ZnO and In/Cu-ZnO catalysts.

The microstructure of the catalysts was investigated by HAADF-STEM for the 2CZA-In*Y* catalysts and TEM for the Cu-ZnO and In/ZnO catalysts. For the 2CZA-In0 catalyst (Figure 4.23a), an amorphous mixed oxide phase is present after calcination, which is typical of HT-derived catalysts [144]. After reduction, the 2CZA-In*Y* catalysts consist of larger Cu particles embedded within a Zn-Al oxide matrix (Figure 23b–d). The average Cu particle size is similar for the 2CZA-In*Y* catalysts at around 9 nm (Table 4.7). Thus, HT-derived catalysts resemble more closely to a traditional supported system, and the Zn-Al oxide phase is reported to have a spinel-like $ZnAl_2O_4$ structure [44, 139]. In contrast, the Cu-ZnO catalyst exhibits a typical porous aggregated structure of Cu and ZnO NPs (Figure 4.24a) [34]. As shown in Figure 4.24b, the structure of the impregnated In/Cu-ZnO catalysts is similar to that of the Cu-ZnO catalyst.

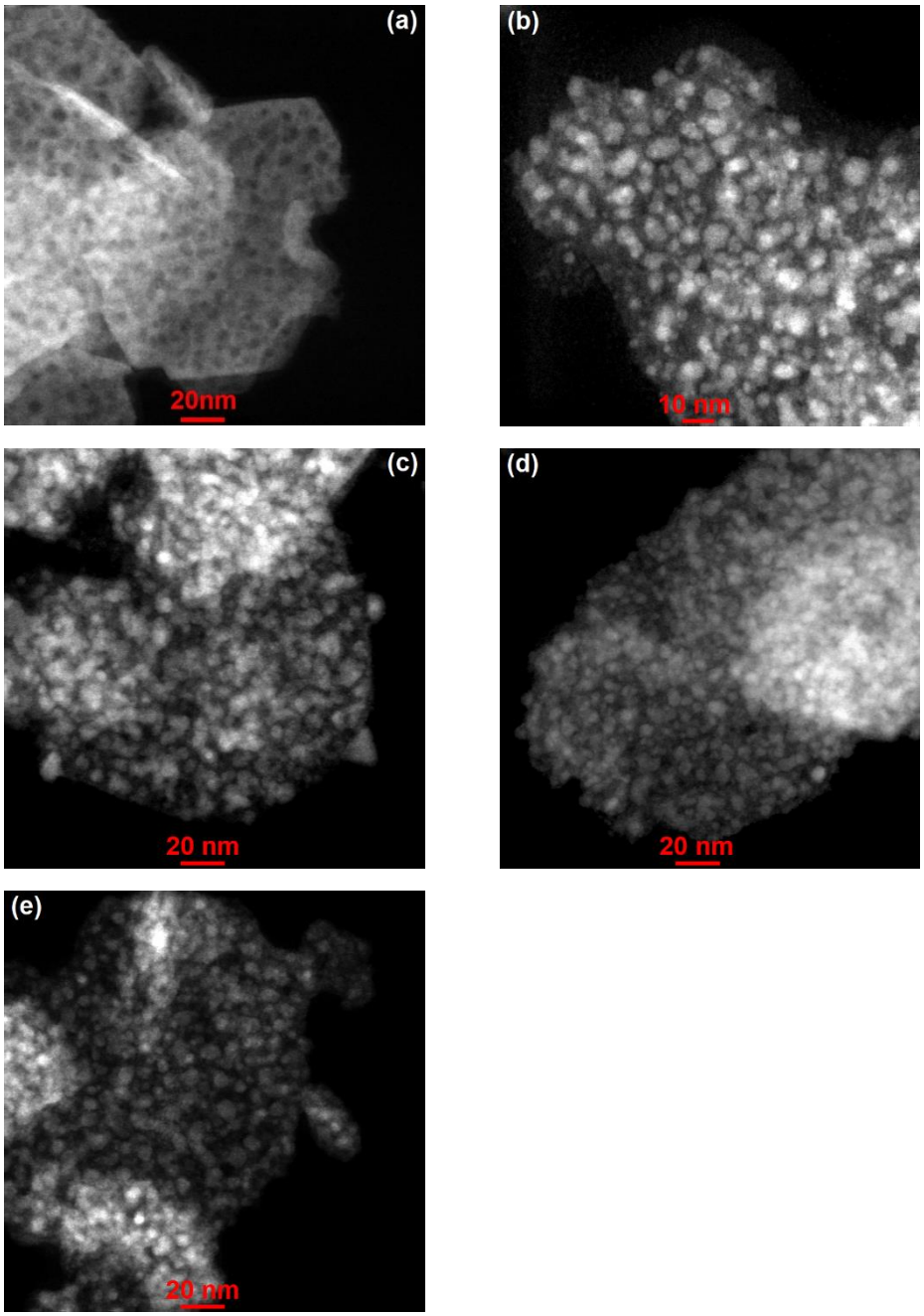

Figure 4.21 HADF STEM images of (a) 2CZA-In0 after calcination and reduced (b) 2CZA-In0, (c) 2CZA-In2, (d) 2CZA-In3, and (e) 2CZA-In4.

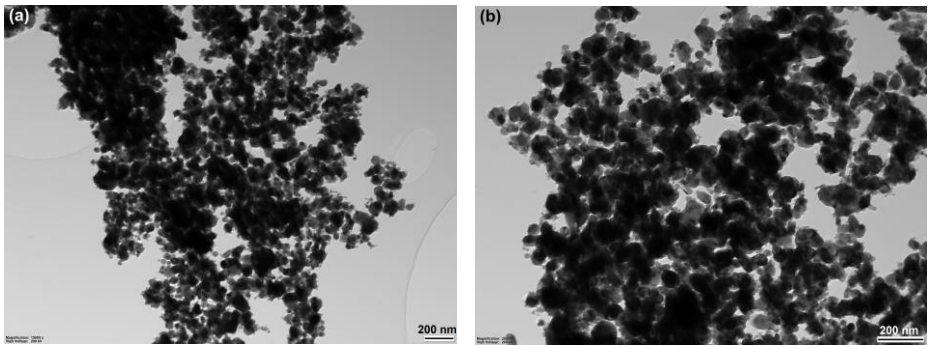

Figure 4.22 TEM images of the reduced (a) Cu-ZnO and (b) In/Cu-ZnO catalysts.

4.3.1.2 H_2-TPR

The reducibility of the catalysts was investigated by H_2-TPR. The TPR profiles of the 2CZA-In*Y* catalysts are shown in Figure 4.25a. The profiles were deconvoluted into four peaks (α, β, γ_1, and γ_2). The α and β peaks are ascribed to the reduction of surface and bulk CuO particles, respectively [19, 145]. The γ_1, and γ_2 peaks are ascribed to the reduction of Cu^{2+} species present in the mixed metal oxide matrix. The strong interaction with the Zn-Al oxide phase has been reported to stabilize the Cu_2O intermediate, leading to a stepwise reduction of these Cu^{2+} species ($CuO \rightarrow Cu_2O$ and $Cu_2O \rightarrow Cu$) [33, 44]. It can be seen that the reduction of Cu-ZnO and In/Cu-ZnO occurs at lower temperatures compared to the HT-derived catalysts (Figure 4.25b). This indicates a stronger Cu-oxide interaction for the HT-derived catalysts. The H_2 consumption relative to the Cu content of the catalysts is summarized in Table 4.7. The H_2/CuO ratio is close to 100%, indicating that the CuO species are completely reduced. The slightly higher H_2/CuO ratio of the In-containing catalysts suggests that In oxide species are also reduced to some extent.

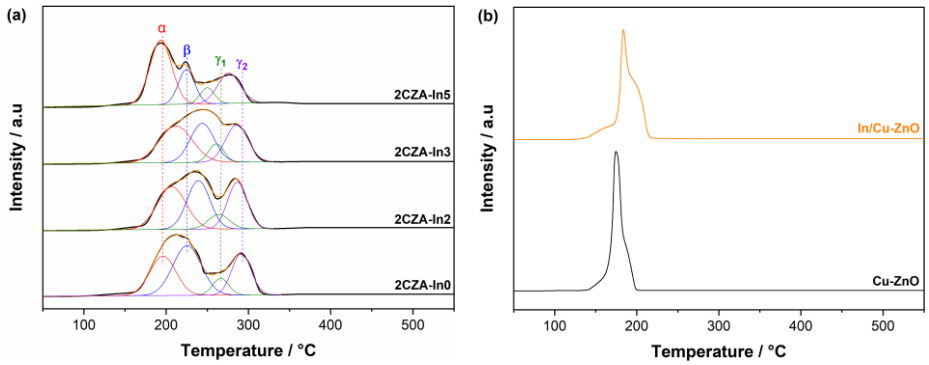

Figure 4.23 (a) Deconvoluted H_2-TPR profiles of the 2CZA-In*Y* catalysts and (b) H_2-TPR profiles of the Cu-ZnO and In/Cu-ZnO catalysts.

4.3.1.3 N_2O chemisorption

The Cu surface area of the catalysts was estimated by N_2O dissociative adsorption. The addition of 2 mol% In to the HT-derived catalyst increases the Cu surface area from 13 to 16 m^2/g, whereas the Cu surface area decreases at higher In content (Table 4.7). Although the Cu particles are much smaller for the HT-derived catalysts, the Cu surface area is lower than that of the Cu-ZnO catalyst (18 m^2/g). This is probably due to the higher interfacial contact between the Cu particles and the oxide phase for the HT-derived catalysts. The Cu surface area decreases to 14 m^2/g when In is impregnated onto the Cu-ZnO catalysts.

4.3.1.4 XPS study of the 2CZA-InY catalysts

The surface composition of the calcined and reduced 2CZA-In*Y* catalysts is summarized in Table 4.8. It can be seen that the surface concentration of metal oxides is higher than the nominal composition. The Cu:Zn ratio obtained from XPS is close to 1.2 after calcination and between 0.6–0.9 for the reduced samples, whereas the nominal Cu:Zn ratio is around 2. The lower Cu surface content after reduction is probably due to the agglomeration of Cu species into larger Cu particles during reduction. Furthermore, the Cu surface concentration of the reduced samples decreases with increasing In content.

Table 4.8 Surface composition of calcined and reduced 2CZA-In*Y* catalysts determined by XPS.

Catalyst	Surface composition after calcination (atom%)				Surface composition after reduction (atom%)				$Cu^0/(Cu^+ + Cu^0)$
	Cu	Zn	Al	In	Cu	Zn	Al	In	
2CZA-In0	37	31	32	0	33	36	30	0	0.15
2CZA-In2	38	31	28	3	32	37	28	3	0.17
2CZA-In3	38	32	25	5	30	40	25	5	0.22
2CZA-In5	39	33	22	6	27	42	24	7	0.21

The Cu $2p_{3/2}$ spectra of the calcined and reduced 2CZA-In*Y* catalysts are shown in Figure 4.26a. The calcined catalysts exhibit a peak at 934 eV and a satellite feature between 940–944 eV, which is characteristic of CuO [146]. For the reduced samples, the main peak shifts towards lower binding energy and the satellite feature disappears, indicating that CuO species are not present after reduction. The Cu L_3VV Auger line was recorded to elucidate the chemical state of Cu after reduction (Figure 4.26b). The Auger peak was deconvoluted into Cu^0 (~918.5 eV) eV) and Cu^+ (~916.4 eV), which is widely used to estimate the relative amount of Cu^0 and Cu^+ species [145, 147-150]. The catalysts contain a relatively higher number of Cu^+ species than Cu^0 (Table 4.8), which might be due to the strong interaction with the Zn-Al oxide phase [145, 147]. It is found that the Cu^0 fraction increases with increasing In content.

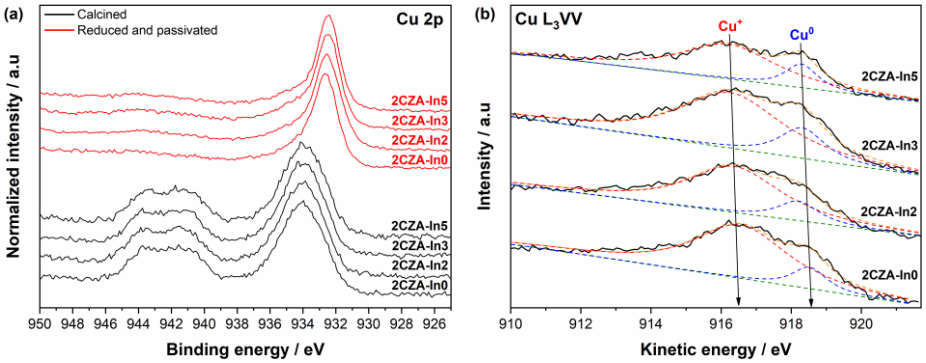

Figure 4.24 (a) Cu $2p_{3/2}$ XPS spectra of the calcined and reduced 2CZA-In*Y* catalysts and (b) Cu L_3VV Auger spectra of the reduced 2CZA-In*Y* catalysts.

The Zn $L_3M_{4,5}M_{4,5}$ Auger spectra of the calcined and reduced 2CZA-In*Y* catalysts are relatively similar (Figure 4.27a), which indicates that the chemical state of ZnO is largely unchanged after reduction. On the other hand, a shift in the In $3d_{5/2}$ and In $3d_{3/2}$ spin-orbit doublets towards lower binding energy can be observed after reduction (Figure 4.27b). This is attributed to the reduction of In oxide species, which are probably present as Cu_xIn_y alloy species [151-153].

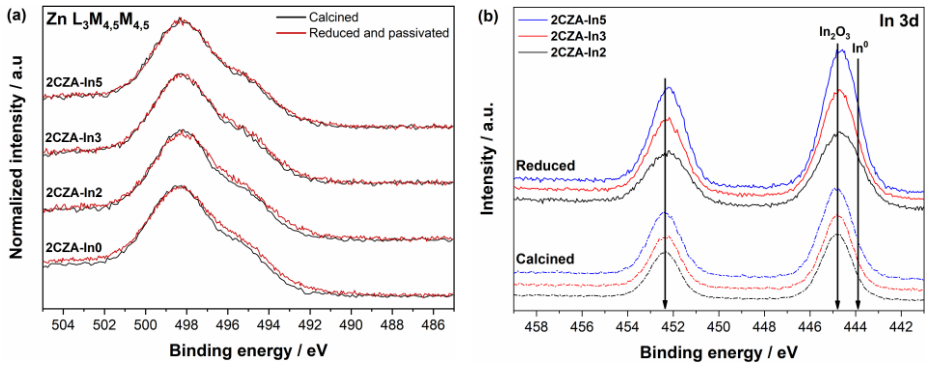

Figure 4.25 (a) Zn $L_3M_{4,5}M_{4,5}$ Auger spectra of the calcined and reduced 2CZA-In*Y* catalysts and (b) In 3d XPS spectra of calcined and reduced 2CZA-In*Y* catalysts.

4.3.1.5 Characterization of HT-derived CZA-InY catalysts with Cu:Zn ratio of 1 and 4

We also prepared series of 1CZA-In*Y* (Cu:Zn=1)and 4CZA-In*Y* (Cu-Zn=4) catalysts for comparison, according to the same procedure as the 2CZA-In*Y* catalysts. The Al content of the 1CZA-In*Y* and 4CZA-In*Y* is similar to that of 2CZA-In*Y*. A summary of the characterization results of the 1CZA-In*Y* and 4CZA-In*Y* catalysts are presented in Table 4.9. XRD confirmed that the metal oxide phase is also largely amorphous after reduction for the 1CZA-In*Y* and 4CZA-In*Y* catalysts. Thus, we expect that the HT-derived catalysts contain a similar microstructure. The Cu crystallite size is smaller for the 1CZA-In*Y* compared to the 2CZA-In*Y* catalysts, whereas larger Cu particles are obtained when the Cu:Zn ratio is 4. Furthermore, the Cu surface area of the In-free catalysts

increases with increasing Cu content and the highest Cu surface area is obtained for the 4CZA-In0 catalysts. It can be seen that the Cu surface area also decreases at high In content for the 1CZA-In*Y* and 4CZA-In*Y* catalysts.

Table 4.9 The SSA, Cu crystallite size, and Cu surface area of the 1CZA-In*Y* and 4CZA-In*Y* catalysts.

Catalyst	SSA (m^2/g)	d_{Cu} (nm)[a]	Cu surface area (m^2/g)[b]
1CZA-In0	38	10.4	10
1CZA-In2	112	11.0	11
1CZA-In4	116	11.4	9
1CZA-In6	96	10.4	6
4CZA-In0	29	18.1	14
4CZA-In2	52	15.3	17
4CZA-In5	51	16.0	13
4CZA-In7	43	17.4	11

[a] Calculated from the (111) peak by the Scherrer equation;

[b] Cu SA determined by N_2O chemisorption

4.3.2 Catalytic activity tests

4.3.2.1 Influence of Cu-oxide interface and In promotion on activity

To assess the influence of the Cu surface area on the catalytic activity, the CZA-In*Y*, Cu-ZnO, and In/Cu-ZnO were assessed at 250 °C, 30 bar, and WHSV of 30 000 $cm^3\ g_{cat}^{-1}\ h^{-1}$. The space-time yield (STY) of methanol as a function of the Cu surface area is presented in Figure 4.28. It can be seen that the STY of methanol is correlated to the Cu surface area for the In-free catalysts obtained from the HT-like precursor. The highest STY of methanol (12.4 mmol $g_{cat}^{-1}\ h^{-1}$) is achieved over the 4CZA-In0 catalyst despite the lower Cu surface area compared to the Cu-ZnO catalyst. This indicates that not only the Cu surface area but also the Cu-oxide interaction influences the activity of the catalyst. The addition of In significantly reduces the activity of the catalyst regardless

of the preparation method. However, the STY of methanol is also related to the Cu surface area for the In-containing CZA-In*Y* catalysts.

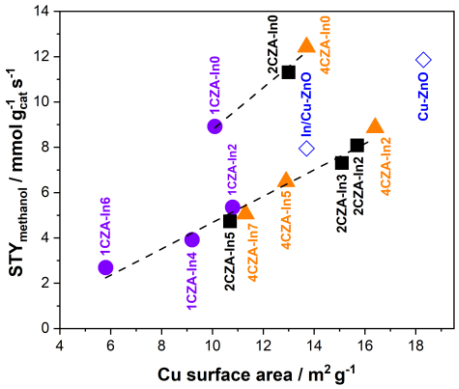

Figure 4.26 (a) STY of methanol as a function of Cu surface area. Reaction conditions: 250 °C, 30 bar, $H_2/CO_2/N_2$ = 3/1/1, WHSV = 30 000 $cm^3\ g_{cat}^{-1}\ h^{-1}$.

Figure 4.29 shows the TOF for methanol formation. The TOF of the CZA-In0 catalysts is similar around 0.018 s^{-1}, while the TOF of the Cu-ZnO catalyst is 0.014 s^{-1}. This is attributed to the stronger Cu-oxide interaction of the HT-derived catalysts. The higher activity of the CZA-In0 catalysts might be due to the promotion of the Cu surface sites through inducing defects, facilitating the decoration of Cu and formation of CuZn/$CuZnO_x$ alloy sites, or a higher number of active interfacial sites [33-35, 43]. Interestingly, the TOF of the CZA-In0 catalysts seems to be unaffected by the Cu particle size. Since smaller Cu particles typically contain a higher number of defects, it is likely that the higher activity is related to the formation of CuZn/$CuZnO_x$ species or interfacial sites. The significantly lower intrinsic activity of the In-containing catalysts indicates that the Cu_xIn_y surface or bulk alloy species inhibit the active sites.

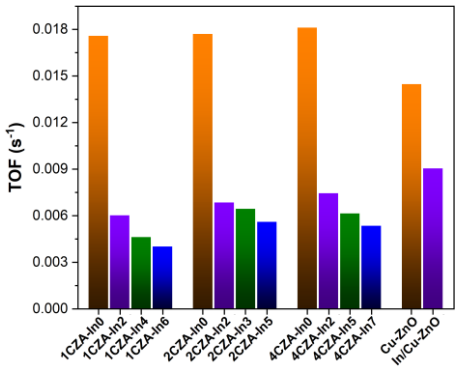

Figure 4.27 TOF of methanol formation of the CZA-In*Y*, Cu-ZnO, and In/Cu-ZnO catalysts. Reaction conditions: 250 °C, 30 bar, $H_2/CO_2/N_2$ = 3/1/1, CO_2 conversion ≈ 5%.

4.3.2.2 Influence of Cu-oxide interaction and In promotion on methanol selectivity

It is important to compare the methanol selectivity at similar CO_2 conversion because the methanol selectivity decreases with increasing CO_2 conversion for Cu-based catalysts. Figure 4.30 shows the methanol selectivity as a function of CO_2 conversion for the 2CZA-In*Y*, Cu-ZnO, and In/Cu-ZnO catalysts. The methanol selectivity is higher for the 2CZA-In0 catalyst compared to Cu-ZnO, indicating that the stronger Cu-oxide interaction also increases the selectivity. Furthermore, the methanol selectivity is improved when In is incorporated into the catalyst regardless of the preparation method. The highest methanol selectivity is obtained over the 2CZA-In3 catalyst. The inhibition of CO formation has also been observed in methanol steam reforming, which was attributed to the presence of In on the Cu surface [154].

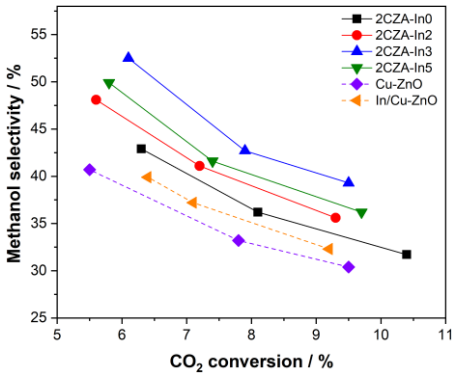

Figure 4.28 Methanol selectivity as a function of CO_2 conversion. The CO_2 conversion was varied by changing the contact time between 10 000 to 100 000 $cm^3/(g_{cat}\ h)$. Reaction conditions: 250 °C, 30 bar, $H_2/CO_2 = 3$.

4.3.3 Stability of HT-derived catalysts

To assess the stability of the HT-derived catalysts, long-term activity tests were performed over the 2CZA-In0 and 2CZA-In3 catalysts. Figure 4.31 shows the CO_2 conversion and methanol over 72 h time on stream (TOS). For the 2CZA-In3 catalyst, the CO_2 conversion and methanol selectivity remains relatively stable. On the other hand, the CO_2 conversion increases slightly for 2CZA-In0 catalysts, whereas the methanol selectivity decreases from 35 to 28%. This results in a decrease in the STY of methanol of 8% for the 2CZA-In0 catalyst. Thus, the incorporation of In stabilizes the activity of the catalysts.

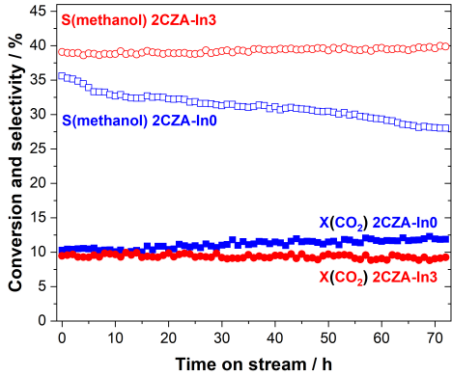

Figure 4.29 CO_2 conversion and methanol selectivity over the 2CZA-In0 and 2CZA-In3 catalysts over 72 h TOS. Reaction conditions: 250 °C, 30 bar, H_2/CO_2 = 3.

The spent catalysts were characterized by N_2-physisorption, XRD, and N_2O chemisorption. The Cu crystallite size, SSA, and Cu surface area of the spent 2CZA-In0 and 2CZA-In3 catalysts are summarized in Table 4.10. The Cu surface area is relatively similar after reaction for the 2CZA-In3 catalyst. However, the Cu surface area increases from 13 to 21 m^2/g for the 2CZA-In0 catalyst. It can be seen in Figure 4.32 that significant sintering of the Cu particles and the Zn-Al oxide phase occurs for the 2CZA-In0 catalyst. These structural changes seems to increase the SSA and the number of Cu atoms exposed on the surface. Thus, the increase in CO_2 conversion is attributed to the larger Cu surface. On the other hand, the continuous decrease in methanol selectivity is probably due to the gradual loss of Cu-oxide interfacial contact. The intrinsic activity of the 2CZA-In0 is substantially reduced after 72 h TOS, which decreases by 43%. This highlights the important role of the Cu-oxide interaction on the intrinsic activity. Consequently, the higher stability of 2CZA-In3 is attributed to the stabilization of the Cu-oxide interaction.

Table 4.10 Cu crystallite size, SSA, and Cu surface area of the spent 2CZA-In0 and 2CZA-In3 catalysts.

Catalyst	d_{Cu} (nm)[a]	SA_{BET} (m^2/g)	SA_{Cu} (m^2/g)
2CZA-In0	20.3	74 (56)[b]	21
2CZA-In3	14.5	58 (54)[b]	16

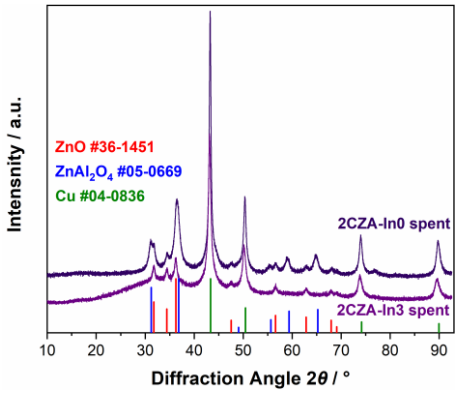

Figure 4.30 XRD patterns of the spent 2CZA-In0 and 2CZA-In3 catalysts.

4.4 *Paper V: The role of interfacial sites between copper and metal oxides (Zn, Zr, In) for CO_2 hydrogenation to methanol*

4.4.1 Catalyst characterization

4.4.1.1 ICP-AES

The nominal and actual composition determined by ICP-AES of the prepared catalysts are summarized in Table 4.11. The catalysts prepared by co-precipitation are denoted as CuZn-*X*, CuZr-*X*, and CuZrIn-*X*, where *X* refers to the calcination temperature. The impregnated catalysts are denoted as M/CuZn (M = In or Zr) and M/CuZr (In or Zn). The Zr content of the CuZr-350 and CuZrIn-350 catalysts prepared by co-precipitation is lower than the nominal content. The actual metal content is close to the nominal content for the other co-precipitation and impregnated catalysts.

Table 4.11 Nominal and actual metal content determined by ICP-AES of the prepared catalysts.

Catalyst	Nominal metal content (mol%)				Metal content determined by ICP-AES (mol%)			
	Cu	Zn	Zr	In	Cu	Zn	Zr	In
CuZn-350	83.3	16.7	–	–	83.2	16.8	–	–
In/CuZn-350	82.5	16.5	–	1.0	82.2	16.5	–	1.3
Zr/CuZn-350	82.5	16.5	1.0	–	82.2	16.7	1.1	–
CuZr-350	83.3	–	16.7	–	89.1	–	10.9	–
CuZrIn-350	82.9	–	16.6	0.5	88.7	–	11.0	0.3
In/CuZr-350	82.5	–	16.5	1.0	88.0	–	10.9	1.1
Zn/CuZr-350	82.5	1.0	16.5	–	87.8	1.0	11.2	–

4.4.1.2 XRD

Figure 4.33 shows the XRD patterns of the CuZn, CuZr, and CuZrIn precursors. It can be seen that the diffraction patterns of the CuZr and CuZrIn catalysts are in excellent agreement with the reference pattern of crystalline malachite (PDF #41-1390). This indicates that the In and Zr

species are not incorporated into the malachite phase, which is probably due to their larger size compared to Zn. The samples exhibit comparable SSA and pore volume after calcination at 350 °C, which decreases to some extent after impregnation (Table 4.12).

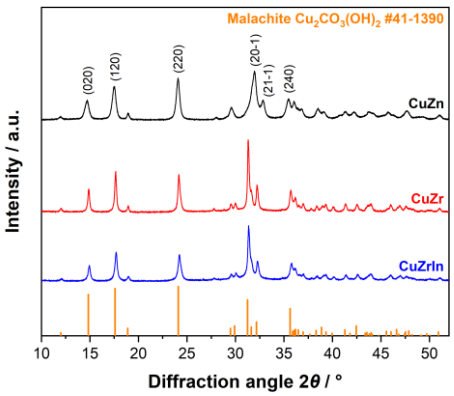

Figure 4.31 XRD patterns of the CuZn, CuZr, and CuZrIn precursors.

Table 4.12 Summary of N_2-physisorption results and crystallite size of CuO and Cu of CuZn-based and CuZr-based catalysts.

Catalyst	SA_{BET} (m^2/g)	PV (cm^3/g)	Pore diameter (nm)	$d_{CuO(111)}$ (nm)[a]	$d_{Cu(111)}$ (nm)[b]
CuZn-350	72	0.17	7.7	5.9	23.7
CuZn-500	42	0.10	6.7	11.9	26.4
In/CuZn-350	46	0.11	7.6	7.6	20.1
Zr/CuZn-350	48	0.11	7.4	7.4	21.8
CuZr-350	73	0.18	7.9	7.9	21.3
CuZr-500	55	0.14	7.2	9.1	23.1
CuInZr-350	77	0.18	8.8	8.8	21.7
In/CuZr-350	63	0.15	9.2	9.2	22.2
Zn/CuZr-350	61	0.15	7.8	7.8	21.9

[a] CuO crystallite size after calcination

[b] Cu crystallite size of the reduced catalysts

The XRD patterns of the reduced CuZn-based and CuZr-based catalysts are shown in Figure 4.34a and b, respectively. The peaks at 2θ of 43.3°, 50.4°, 74.1°, and 89.9° correspond to metallic Cu (PDF #04-0836). The

Cu crystallite size is similar for the CuZn-based and CuZr-based catalysts between 20–24 nm (Table 4.12). Crystalline ZrO_2 is not detected for the CuZr-based catalysts, indicating that the ZrO_2 species are amorphous or highly dispersed. No additional peaks are present for the impregnated samples.

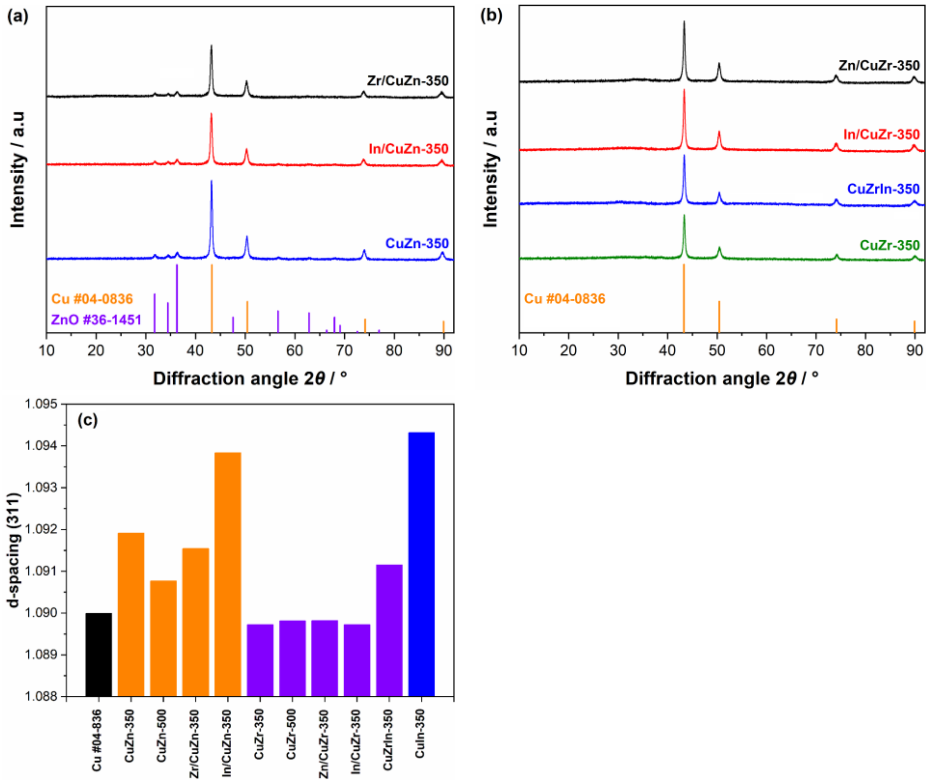

Figure 4.32 XRD patterns of (a) the reduced CuZn-350, In/CuZn-350, and Zr/CuZn-350 catalysts; (b) XRD patterns of the reduced CuZr-350, CuZrIn-350, In/CuZr-350, and Zn/CuZr-350 catalysts; and (c) d-spacing of the Cu(311) peak of the reduced catalysts.

The d-spacing of the Cu(311) peak is shown in Figure 4.34c. The higher d-spacing of the CuZn-based catalysts might be related to a distortion of the Cu lattice by Zn [33]. It seems that both a higher calcination temperature and a second calcination treatment results in a greater segregation of the Cu and Zn species, as evidenced by the lower d-spacing of the CuZn-500 and Zr/CuZn-350 catalysts. The increase in d-

spacing for the In/CuZn-350 and CuZrIn-350 catalysts is attributed to the presence of In within the bulk of Cu.

4.4.1.3 TEM

The TEM images of the reduced CuZn-350 and In/CuZn-350 catalysts are shown in Figure 4.36a and b, respectively. The microstructure of the catalysts is typical for CuZn-based catalysts, which can be characterized by larger Cu particles spaced by smaller ZnO particles [155]. In contrast, the Cu phase seems to agglomerate to a larger extent for the CuZr-based catalysts (Figure 4.37a–c). This is probably because of the significantly smaller size of ZrO_2, which has a particle size of 5 nm (Figure 4.37d). The ZrO_2 coverage of Cu seems to range from fully covered Cu species to practically uncovered ones. Although optimal mixing of the Cu and ZrO_2 species is not obtained for the CuZr-based catalysts, a significant number of Cu-ZrO_2 interfacial sites can be observed in the TEM images.

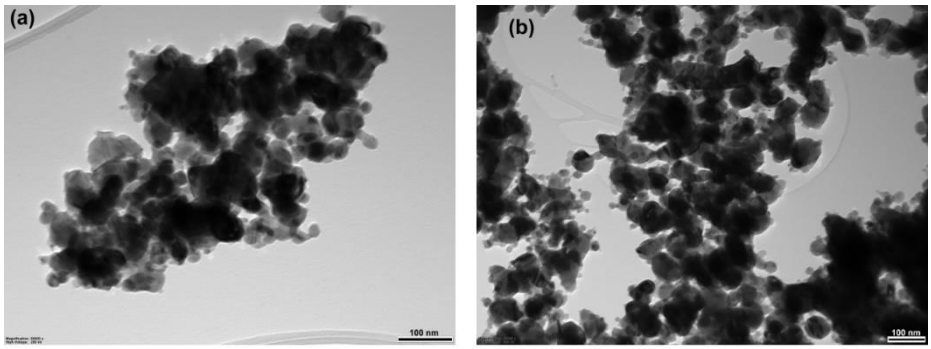

Figure 4.33 TEM images of the reduced (a) CuZn-350 and (b) In/CuZn-350 catalysts.

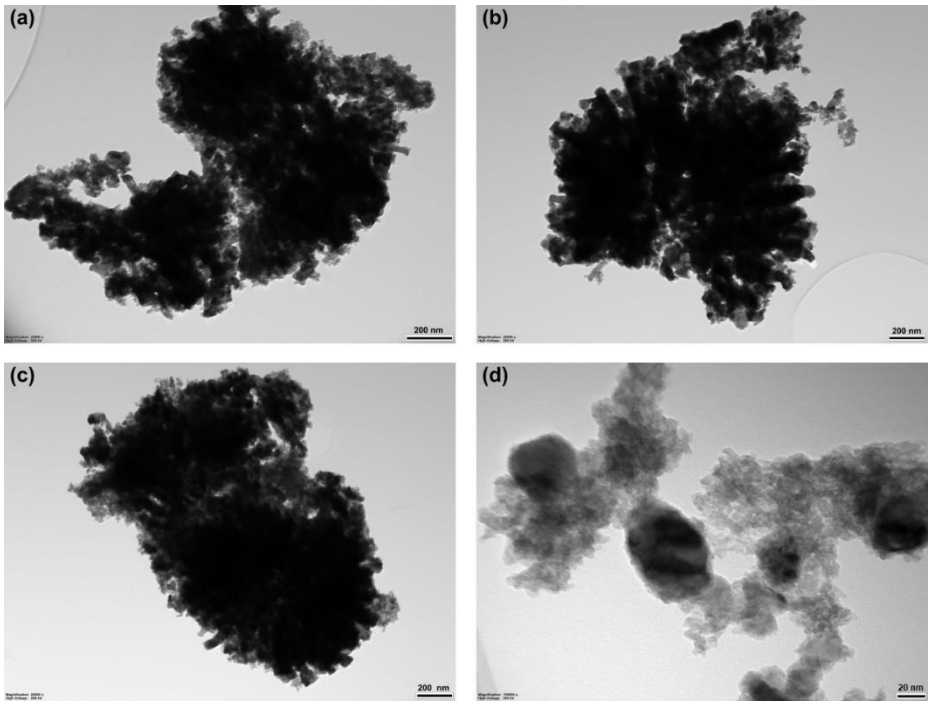

Figure 4.34 TEM images of the reduced (a) CuZr-350, (b) CuZrIn-350, (c) In/CuZr-350, and (d) CuZr-350 (higher magnification) catalysts.

4.4.1.4 H_2-TPR

The TPR profiles of the CuZn-based and CuZr-based catalysts are shown in Figure 4.38a and b, respectively. The profiles were deconvoluted into three peaks (α, β, and γ). The CuZn-350 catalyst exhibits β and γ peaks, corresponding to the reduction of surface and bulk CuO particles [19, 145]. For the CuZr-based catalysts, an additional α peak is observed at lower temperature, which is attributed to the enhanced reducibility of CuO in contact with ZrO_2. It can also be seen that a small α peak is also present when In or Zr is impregnated onto the CuZn catalysts.

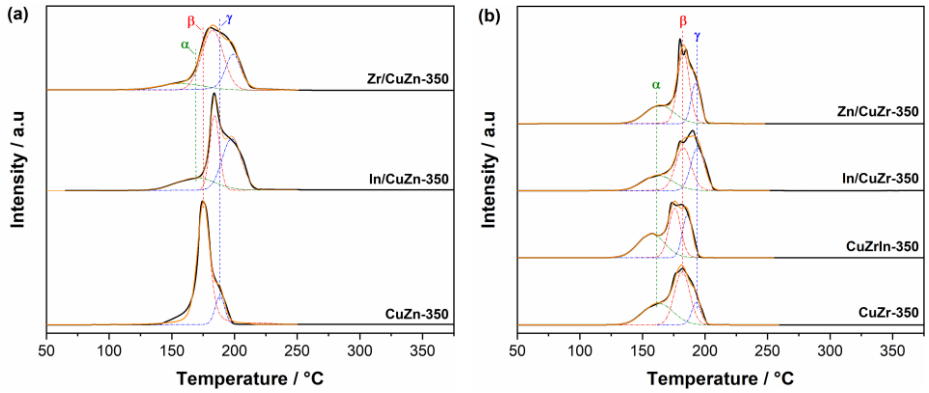

Figure 4.35 Deconvoluted H_2-TPR profiles of the (a) CuZn-based and (b) CuZr-based catalysts.

4.4.1.5 N_2O chemisorption

The Cu surface area estimated by N_2O chemisorption is summarized in Table 4.13. Impregnating In onto the CuZn-350 catalyst reduces the Cu surface area from 18 m^2/g to 14 m^2/g. On the other hand, the Cu surface area is relatively unchanged for the Zr/CuZn-350 catalyst (17 m^2/g). The Cu surface area of the CuZr-based catalysts is significantly larger than that of the CuZn-based catalysts in the range of 26–36 m^2/g. A decrease in Cu surface area occurs when In is impregnated onto the CuZr catalyst, whereas the Cu surface area is not greatly affected by Zn impregnation. The lower Cu surface area of the catalyst impregnated with In might be related to the presence of In species on the Cu surface.

Table 4.13 Cu surface area, relative number of MB sites, and ratio of high-temperature MB sites to total number of MB sites of the catalysts.

Catalyst	SA_{Cu} (m^2/g)[a]	Relative number of MB sites[b]	$A_{HT\text{-}MB}/A_{MB}$[c]
CuZn-350	18	0.22	0
CuZn-500	19	0.14	0
In/CuZn-350	14	0.18	0
Zr/CuZn-350	17	0.35	0
CuZr-350	34	1.00	0.24
CuZr-500	31	0.71	0.25
CuZrIn-350	36	0.86	0.42
In/CuZr-350	26	0.55	0.35
Zn/CuZr-350	32	0.88	0.26

[a] Estimated by N_2O chemisorption

[b] Relative number of MB sites compared to CuZr-350

[c] Ratio of high-temperature MB sites to the total number of basic sites

4.4.1.6 CO_2-TPD

The surface basicity of the catalysts was studied by CO_2-TPD. The CO_2 TPD profiles of the CuZn-based and CuZr-based catalysts are shown in Figure 4.39a and b, respectively. The weak basic (WB) sites located between 50–200 °C are related to the Cu surface or OH^- groups [156], while the medium-strength basic (MB) sites between 200–500 °C are ascribed to metal-oxygen pairs (e.g. Zr–O, In–O, oxygen defects in ZnO, or CuZn/$CuZnO_x$ species) [66, 157]. The strong basic (SB) sites might be related to higher energy defects [158]. Based on previous studies [20, 159-161], we expect that the number of MB sites is indicative of the methanol synthesis activity.

The surface basicity of the Cu-ZnO catalyst decreases when the catalyst is calcined at higher temperature (Table 4.13), which indicates weaker Cu-ZnO interaction. Impregnating In onto CuZn-350 decreases the basicity of the catalyst. On the other hand, new types of MB sites are formed when Zr is impregnated onto the CuZn-350 catalysts, which results in a higher number of MB sites. The surface basicity is significantly higher for the CuZr-based catalysts compared to the CuZn-based catalysts. The CuZr-350 catalyst exhibits the highest number of MB sites. In-promotion of the CuZr-based catalysts reduces the quantity of MB sites but leads to a relatively higher number of high-temperature MB sites regardless of the preparation method ($A_{HT\text{-}MB}/A_{MB}$, Table 4.13).

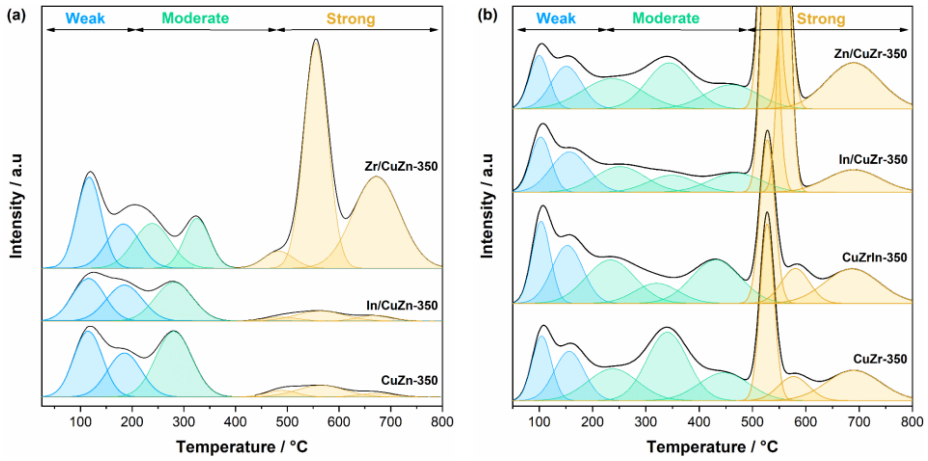

Figure 4.36 CO_2 TPD profiles of the (a) CuZn-based and (b) CuZr-based catalysts. The y-scale is 2x higher in b compared to a.

4.4.2 Catalytic activity tests

4.4.2.1 Influence of Zn and Zr oxide on activity

Figure 4.40a shows the steady-state production rate of methanol and Cu for the CuZn-350, CuZn-500, and Zr/CuZn-350 catalysts. The methanol formation rate of the CuZn-350 catalyst is 14.7 $mmol \cdot g_{cat}^{-1} \cdot h^{-1}$, which decreases to 12.4 $mmol \cdot g_{cat}^{-1} \cdot h^{-1}$ after calcination at 500 °C. Li et al. [64] observed that the metallic Zn content significantly decreases with increasing calcination temperature for a bimetallic Cu-ZnO catalyst. Our CO_2-TPD and XRD results also indicate weaker Cu-ZnO interaction for the CuZn-500 catalysts, whereas the Cu crystallite size and Cu surface area are similar. Therefore, the lower activity after calcination at 500 °C is attributed to the reduced Cu-ZnO interaction. The methanol formation rate increases to 15.6 $mmol \cdot g_{cat}^{-1} \cdot h^{-1}$ for the Zr/CuZn-350 catalyst. This is ascribed to the formation of Cu-ZrO_2 interfacial sites for CO_2 conversion to methanol. The initial activity is almost two times higher for the Zr/CuZn-350 catalysts but decreases significantly within the first 10 h, which is probably due to the loss of Cu-ZrO_2 interfacial sites

(Figure 4.40b). The steady-state methanol selectivity is also higher for the Zr/CuZn-350 catalysts (Figure 4.40c).

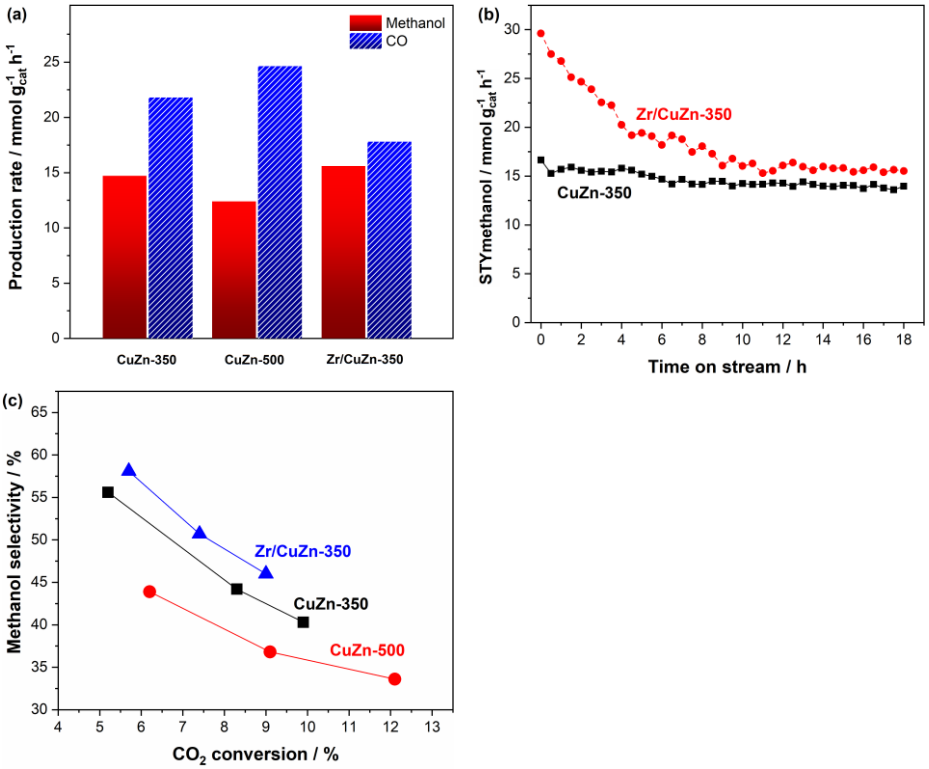

Figure 4.37 (a) Methanol and CO production rate over the CuZn-based and CuZr-based catalysts (WHSV = 38 000 $cm^3 \cdot g_{cat}^{-1} \cdot h^{-1}$); (b) STY of methanol over 18 h TOS of the CuZn-350 and Zr/CuZn-350 catalysts (WHSV = 38 000 $cm^3 \cdot g_{cat}^{-1} \cdot h^{-1}$); and (c) methanol selectivity as a function of CO_2 conversion. Reaction conditions: 230 °C, 30 bar, H_2/CO_2 = 3.

The steady-state formation rate of methanol and CO for the CuZr-350, CuZr-500, and Zn/CuZr-350 are presented in Figure 4.41a. The methanol formation rate of the CuZr-350 catalysts is 13.1 $mmol \cdot g_{cat}^{-1} \cdot h^{-1}$. The relatively low activity despite the high Cu surface area indicates that methanol formation mainly occurs on Cu-ZrO_2 interfacial sites, in agreement with literature [52, 61, 162-164]. It can also be seen that the methanol formation rate is significantly lower after calcination at 500 °C, which might be related to structural changes in the ZrO_2 phase.

Interestingly, impregnating ZnO onto the CuZr-350 catalyst reduces the activity of the catalyst, which suggests that the ZnO-ZrO_2 interaction is not the reason for the increase in activity of the Zr/CuZn-350 catalyst. It can be seen in Figure 4.41b that the methanol selectivity is also reduced after calcination at 500 °C and when Zn is impregnated onto the CuZr-350 catalyst.

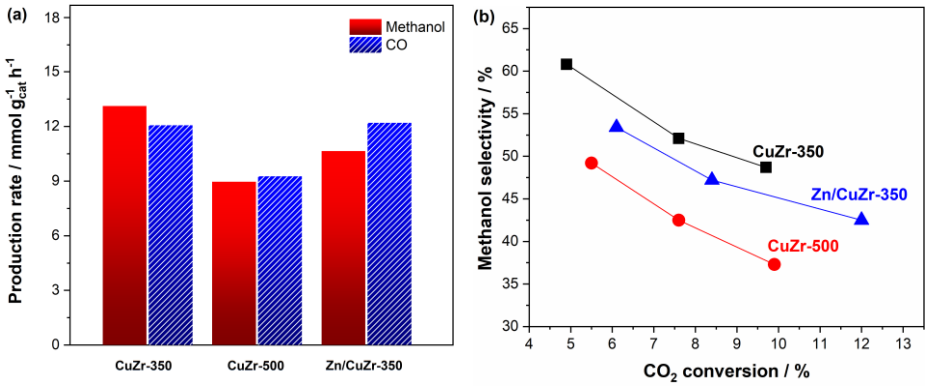

Figure 4.38 (a) Methanol and CO production rate over the CuZn-based and CuZr-based catalysts (WHSV = 38 000 $cm^3 \cdot g_{cat}^{-1} \cdot h^{-1}$) and (b) methanol selectivity as a function of CO_2 conversion. Reaction conditions: 230 °C, 30 bar, H_2/CO_2 = 3.

4.4.2.2 Influence of In on CuZn-based and CuZr-based catalysts

The influence of In on the steady-state methanol formation rates at 230 °C and 270 °C is shown Figure 4.42a. The methanol formation rate is higher for CuZr-350 compared to CuZn-350 at 270 °C, which is in agreement with literature [54]. This is probably due to the superior activity of Cu/ZnO catalysts for the RWGS and methanol decomposition reaction compared to Cu/ZrO_2. Impregnating In onto the CuZn-350 and CuZr-350 catalyst significantly reduces the methanol formation rate. In contrast, the highest methanol formation rate at 270 °C is obtained over the CuZrIn-350 catalyst. We expect that this is related to In-Zr oxide sites that become more active at higher temperatures, similarly to In_2O_3-based catalysts [102]. The methanol selectivity is higher for the In-containing

catalysts (* refers to a second calcination cycle at 350 °C), indicating that In also inhibits the formation of CO (Figure 4.42b and c). For the CuZrIn-350 catalyst, the methanol selectivity is only higher than that of the CuZr-350* catalyst at 270 °C. Furthermore, the STY of methanol remains stable over CuZrIn-350 at 270 °C, which might be due to a stabilizing effect of In on the Cu-oxide interfacial sites (Figure 4.42d).

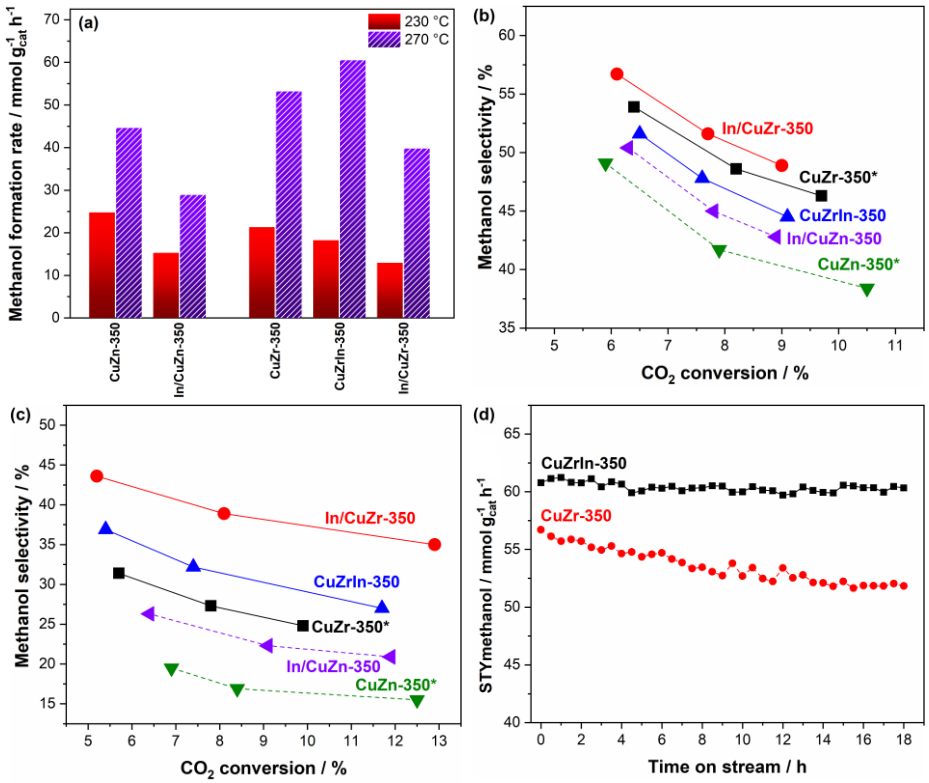

Figure 4.39 (a) Steady-state methanol formation rate of the CuZn-350, In/CuZn-350, CuZr-350, CuZrIn-350, and In/CuZr-350 catalysts at 230 °C and 270 °C (WHSV = 80 000 cm^3/(g$_{cat}$ h)); methanol selectivity as a function of CO_2 conversion at (b) 230 °C and (c) 270 °C; and (d) STY of methanol over 18 h TOS of the CuZr-350 and CuZrIn-350 catalysts at 270 °C and 80 000 cm^3/(g$_{cat}$ h). Reaction conditions: 30 bar, H_2/CO_2 = 3.

4.4.2.3 Influence of surface properties on catalytic performance

Figure 4.43a shows the STY of methanol as a function of the Cu surface area. No correlation between the methanol formation rate and the Cu surface area can be deduced for the CuZn-based or CuZr-based catalysts. On the other hand, the STY of CO is strongly related to the Cu surface for both the CuZn-based and CuZr-based catalysts. The trendline for the CuZn-based catalysts is very steep, which suggests that the interaction of Cu with metal oxides or In also influences the CO formation rate. The number of MB sites seems to be indicative of the methanol formation rate of the catalysts with the exception of the In/CuZn-350 catalyst (Figure 4.43c). This indicates that the Cu-oxide interaction is a determining factor for the methanol synthesis activity of the catalysts.

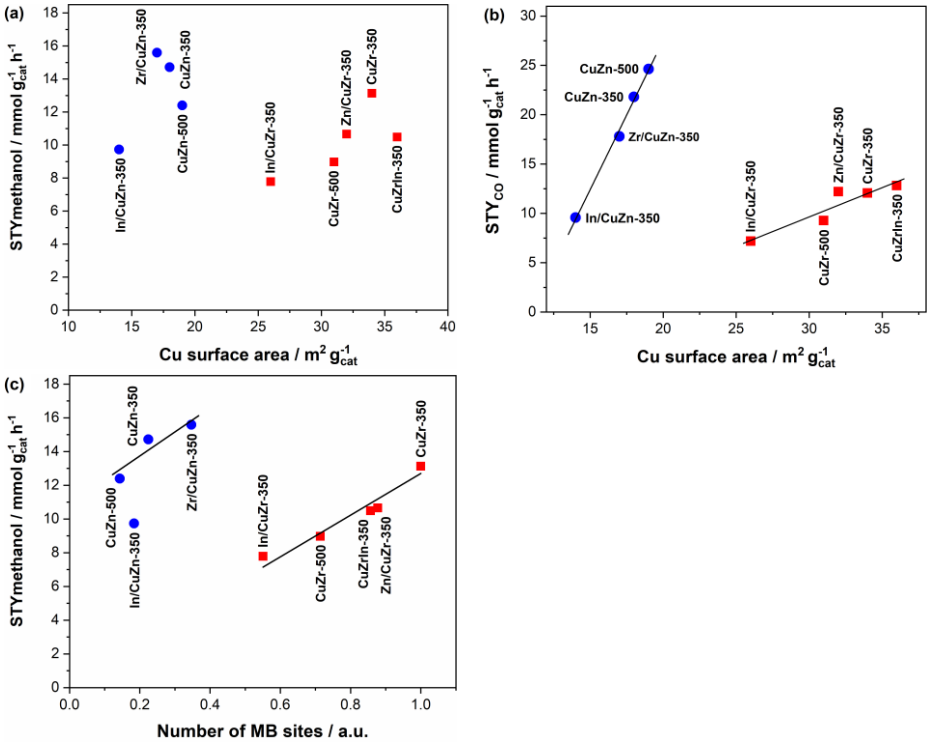

Figure 4.40 (a) STY of methanol as a function of the Cu surface area; (b) STY of CO as a function of Cu surface area; and (c) STY of methanol as a function of the relative number of MB sites. Reaction conditions: 230 °C, 30 bar, H_2/CO_2 = 3, WHSV = 38 000 $cm^3 \cdot g_{cat}^{-1} \cdot h^{-1}$.

4.4.3 Discussion

The $CuZn(O_x)$ alloy or Cu-ZnO interfacial sites are considered as the active sites for methanol synthesis from CO_2 for the Cu-ZnO system [40], while the Cu-ZrO_2 interfacial sites facilitate the activation and hydrogenation of CO_2 to methanol for Cu-ZrO_2 catalysts [60]. It has been reported that the apparent activation energy is lower for the Cu-ZrO_2 system compared to Cu-ZnO and Cu-ZnO-ZrO_2 catalysts [63]. Thus, the superior activity of CuZn-350 compared to CuZr-350 at 230 °C indicates a higher number of active sites for the CuZn-350 catalyst.

In literature, the key difference between ZnO and ZrO_2 seems to be the formation of small Zn clusters on the Cu surface [60]. For our catalysts, this can to some extent be expected due to the differences in the precursor materials of the CuZn and CuZr catalysts, where only Zn can be incorporated into the Cu malachite phase. Thus, the catalyst surface of the CuZn catalyst can be characterized by relatively large crystalline Cu and ZnO particles with small clusters of Zn species on the Cu surface, which is illustrated in Figure 4.44a. On the other hand, the CuZr catalyst seems to primarily contain interfacial sites between Cu and ZrO_2 particles (Figure 4.44e). This model explains the higher activity of the CuZn-350 catalysts despite having a Cu surface area that is about 50% lower than the CuZr-350 catalyst. Furthermore, increasing the calcination temperature to 500 °C probably decreases the Zn coverage of the Cu surface due to the greater segregation of CuO and ZnO prior to reduction.

It follows that the higher activity of the Zr/CuZn-350 catalyst is due to the generation of additional Cu-ZrO_2 interfacial sites (Figure 4.44b). The lower activity of the Zn/CuZr-350 catalyst indicates that the Zn species are stabilized on the ZrO_2 phase rather than present as Zn clusters on the Cu surface (Figure 4.44d). Consequently, these results highlight that the interplay between Cu and the metal oxides is crucial in promoting the conversion of CO_2 to methanol.

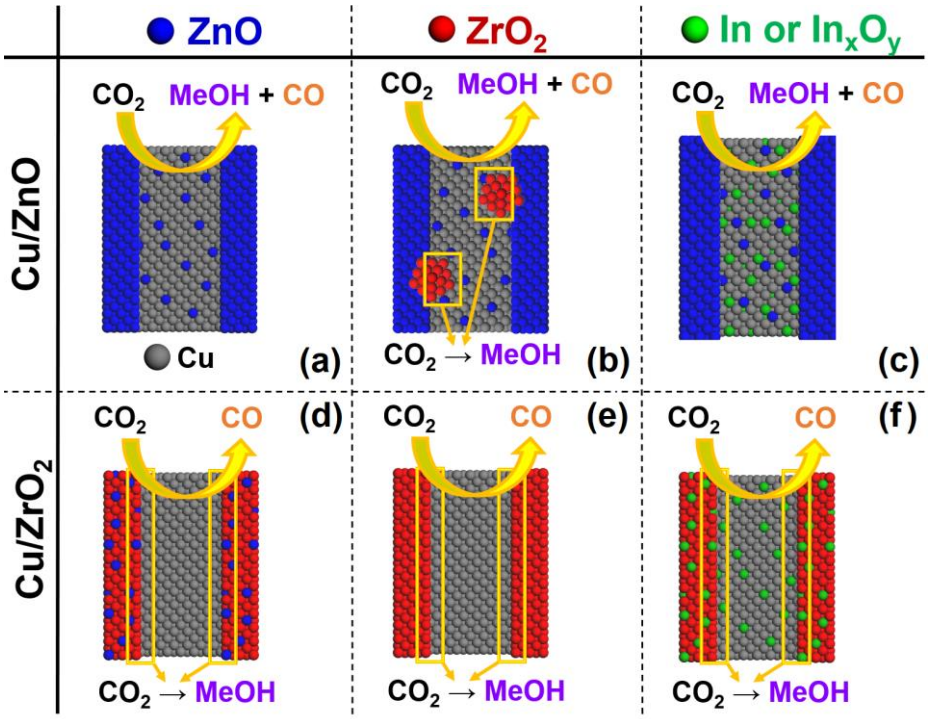

Figure 4.41 Simplified sketch of the catalyst surface of (a) CuZn, (b) Zr/CuZn, (c) In/CuZn, (d) Zn/CuZr, (f) CuZr, and (g) In/CuZr.

The impregnation of In onto the CuZn-350 and CuZr-350 results in In coverage of the Cu surface, as indicated by the significant drop in Cu surface area. The stronger inhibiting effect of In on the activity of the CuZn-350 catalyst is probably due to the blockage of the active sites on the Cu surface. In contrast, it seems that In reduces the methanol formation rate of CuZr-350 by modifying the interfacial sites. The superior performance of the CuZrIn catalyst prepared by co-precipitation demonstrates that properties of the Zr-In oxide can be tuned by optimizing the composition and preparation method. This could be used to enhance the reactivity of the interfacial sites.

The correlation between the Cu surface area and CO formation rate suggests that CO production is related to the metallic Cu sites. This is also consistent with the lower CO formation rate when In is present on

the Cu surface for both CuZn-350 and CuZr-350. The higher CO formation rate of CuZn-based catalysts indicates that the RWGS reaction or methanol decomposition into CO is also promoted when ZnO is present.

The results show that enhancing the interaction between Cu and metal oxides increases both the activity and methanol selectivity. This study indicates that optimizing the Cu-ZnO interaction while generating a high number of Cu-ZrO_2 interfacial sites is key to maximize the performance of Cu-ZnO-ZrO_2 catalysts. This could result in a high number of active Cu-ZnO and Cu-ZrO_2 sites for methanol synthesis. The interaction between ZnO-ZrO_2 is found to have a negative effect on the activity of the catalyst. However, the ZnO-ZrO_2 interaction might be structure sensitive and could therefore, play a role in methanol synthesis over Cu-ZnO-ZrO_2 catalysts.

5 Concluding remarks

5.1 *Conclusions*

The thermodynamic aspects of CO_2 hydrogenation to methanol pose a significant challenge for the industrialization of the CO_2-to-methanol process. The thermodynamics significantly limits the equilibrium conversion of CO_2 to methanol at typical methanol synthesis conditions. Thus, high recycle ratios are required for the complete conversion of CO_2 into methanol. Paper II shows that the methanol yield can be significantly increased by utilizing product condensation. The condensation of water and methanol can occur at relevant reaction conditions (200 °C, 100 bar) and could, therefore, be utilized to increase the methanol yield per pass in the CO_2-to-methanol process. Eliminating the CO formation of methanol synthesis catalysts or employing hybrid catalysts for the simultaneous production of methanol and other oxygenates (e.g., dimethyl ether or higher alcohols) could also circumvent the thermodynamic restrictions on the CO_2 conversion to the target product(s).

The main scientific objective of experimental work was to investigate the role of metal oxides in CO_2 hydrogenation to methanol. The complexity of these systems makes it challenging to identify and tailor the configuration of the active sites. For the Co and Cu-based catalysts investigated in this work, the interaction with the oxide promoter has a pronounced effect on the activity of the catalysts. Thus, optimizing the metal-oxide interaction has the potential to further enhance the catalytic performance of the catalysts in CO_2 hydrogenation to methanol.

In Paper III, it was demonstrated that intimate contact of Co and Mn oxides generates highly active sites for methanol synthesis, which are not present on the surface of pure Co oxide. The Co-Mn oxide system is an interesting alternative to the conventional Cu-based catalysts for low-pressure applications. This is because the CO production rate is very low

over the Co-Mn oxide catalyst, which seems to be a highly inhibiting factor on the methanol yield from a thermodynamic perspective. However, further effort is needed to minimize the formation of hydrocarbons on the Co sites.

Paper IV showed that the catalytic performance of Cu/ZnO-based catalysts can be enhanced by modifying the Cu-oxide interfacial contact. The partial embedment of Cu particles in a Zn-Al oxide matrix significantly increases the intrinsic activity and methanol selectivity. This indicates that a compromise between high Cu surface area and Cu-oxide interfacial area is needed to maximize the activity of Cu/ZnO-based catalysts. The loss of the Cu-oxide interface is identified as the main reason for catalyst deactivation. The addition of In could stabilize the microstructure but the presence of In on the Cu surface seems to inhibit the active sites for methanol synthesis.

The influence of Cu-oxide and oxide-oxide (Zn, Zr, and In oxides) interaction on the catalytic performance was investigated in Paper V. The Cu-ZrO_2 and Cu-ZnO systems are similar in that the activity is linked to the Cu-oxide interaction. The incorporation of Zn into the Cu precursor phase leads to significantly higher intrinsic activity compared to Cu-ZrO_2, which is attributed to superior Cu-oxide interfacial contact. The results also indicate that the formation of new Cu-ZrO_2 interfacial sites is responsible for the higher activity and selectivity of the ZrO_2 impregnated Cu-ZnO catalyst. On the other hand, the ZrO_2-ZnO interaction seems to decrease the catalytic performance when ZnO is impregnated onto Cu-ZrO_2. The presence of In on the Cu surface limits the CO_2 hydrogenation ability of the active sites on the Cu surface. However, In oxide is more stable on the ZrO_2 phase and can generate active Zr-In oxide interfacial sites. This study demonstrates that optimizing the different active configurations in Cu-based catalysts can significantly affect the catalytic performance.

5.2 *Future work*

The development of novel reactors that can facilitate the removal of methanol and water could have practical significance for the large-scale implementation of the CO_2-to-methanol process. This includes reactor designs that utilize product condensation or permselective membranes to remove the products from the reacting gas-phase mixture.

The low-pressure methanol synthesis process could be viable in certain applications. The Co-Mn oxide system exhibits superior methanol synthesis activity compared to the Cu-based catalysts at low-pressure. Future work should focus on improving the selectivity of the Cu-Mn oxide catalysts by identifying suitable promoters to limit the formation of hydrocarbons and appropriate supports to lower the cost of the catalyst.

For Cu-based catalysts, there is still great potential for improving the activity and selectivity by optimizing the Cu-oxide and oxide-oxide interaction. Efforts to elucidate the nature of the active sites and interaction between the active components, promoters, and support is needed to tune the different active phases. In addition, stabilizing the different components is also a significant challenge to limit the deactivation of the catalyst. Developing novel synthesis methods that can target the Cu-oxide and oxide-oxide interaction separately warrants further study.

Bibliography

1. Aresta, M., A. Dibenedetto, and E. Quaranta, State of the art and perspectives in catalytic processes for CO_2 conversion into chemicals and fuels: The distinctive contribution of chemical catalysis and biotechnology. *Journal of Catalysis*, 2016. **343**: p. 2-45.
2. Smith, J.K., History of catalysis. *Encyclopedia of catalysis*, 2002.
3. Murkin, C. and J. Brightling, Eighty years of steam reforming. *Johnson Matthey Technology Review*, 2016. **60**(4): p. 263-269.
4. Sheldon, D., Methanol Production‐A Technical History. *Johnson Matthey Technology Review*, 2017. **61**(3): p. 172-182.
5. Research and Markets (2020) *Methanol - Global Market Trajectory & Analytics*. [Accessed September 2020]; Available from: www.researchandmarkets.com.
6. Methanol Institute (2016) *Methanol road transportation fuels*. [Accessed September 2020]; Available from: http://www.methanol.org/wp-content/uploads/2016/07/6-Combined-Side-Deck-GFBC-1.pdf.
7. Verhelst, S., et al., Methanol as a fuel for internal combustion engines. *Progress in Energy & Combustion Science*, 2019. **70**: p. 43-88.
8. Andersson, K. and C.M. Salazar, Methanol as a marine fuel report. *FCBI Energy, prepared for Methanol Institute*, 2015.
9. Hobson, C. and C. Márquez, *Renewable Methanol Report*. 2018, Technical report.
10. MofCO2 [Accessed September 2020]; Available from: http://www.mefco2.eu/.
11. Carbon Recycling International, *Agreement Signed For CRI's First CO_2-To-Methanol Plant in China*. [Accessed September 2020] Available from: https://www.carbonrecycling.is/news-media/co2-to-methanol-plant-china
12. OCI N.V. (2019) *Q4 and FY 2018 Results Presentation*. [Accessed September 2020]; Available from: https://www.oci.nl/media/1678/oci-nv-q4-and-fy-2018-results-presentation.pdf.

13. Södra (2020) *Nytt bränsle åt framtidstankarna*. [Accessed September 2020]; Available from: https://www.sodra.com/sv/se/bioprodukter/biometanol/.
14. Stangeland, K., et al., Thermodynamic analysis of chemical and phase equilibria in CO_2 hydrogenation to methanol, dimethyl ether, and higher alcohols. *Industrial & Engineering Chemistry Research*, 2018. **57**(11): p. 4081-4094.
15. Graciani, J., et al., Highly active copper-ceria and copper-ceria-titania catalysts for methanol synthesis from CO_2. *Science*, 2014. **345**(6196): p. 546-550.
16. Senanayake, S.D., et al., Hydrogenation of CO_2 to Methanol on CeO_x/Cu(111) and ZnO/Cu(111) Catalysts: Role of the Metal–Oxide Interface and Importance of Ce^{3+} Sites. *The Journal of Physical Chemistry C*, 2016. **120**(3): p. 1778-1784.
17. Chen, K., et al., CO_2 hydrogenation to methanol over Cu catalysts supported on La-modified SBA-15: The crucial role of Cu–LaO_x interfaces. *Applied Catalysis B: Environmental*, 2019. **251**: p. 119-129.
18. Kühl, S., et al., Ternary and quaternary Cr or Ga-containing ex-LDH catalysts—Influence of the additional oxides onto the microstructure and activity of Cu/$ZnAl_2O_4$ catalysts. *Catalysis Today*, 2015. **246**: p. 92-100.
19. Gao, P., et al., Influence of modifier (Mn, La, Ce, Zr and Y) on the performance of Cu/Zn/Al catalysts via hydrotalcite-like precursors for CO_2 hydrogenation to methanol. *Applied Catalysis A: General*, 2013. **468**: p. 442-452.
20. Gao, P., et al., Fluorinated Cu/Zn/Al/Zr hydrotalcites derived nanocatalysts for CO_2 hydrogenation to methanol. *Journal of CO_2 Utilization*, 2016. **16**: p. 32-41.
21. Chen, S., et al., Induced high selectivity methanol formation during CO_2 hydrogenation over a $CuBr_2$-modified CuZnZr catalyst. *Journal of Catalysis*, 2020. **389**: p. 47-59.
22. Ojelade, O.A. and S.F. Zaman, A Review on Pd Based Catalysts for CO_2 Hydrogenation to Methanol: In-Depth Activity and DRIFTS Mechanistic Study. *Catalysis Surveys from Asia*, 2020. **24**(1): p. 11-37.

23. Frei, M.S., et al., Atomic-scale engineering of indium oxide promotion by palladium for methanol production via CO_2 hydrogenation. *Nature Communications*, 2019. **10**(1): p. 1-11.
24. Rasmussen, P., et al., Methanol synthesis on Cu(100) from a binary gas mixture of CO_2 and H_2. *Catalysis Letters*, 1994. **26**(3-4): p. 373-381.
25. Rasmussen, P., M. Kazuta, and I. Chorkendorff, Synthesis of methanol from a mixture of H_2 and CO_2 on Cu(100). *Surface Science*, 1994. **318**(3): p. 267-280.
26. Yoshihara, J. and C.T. Campbell, Methanol synthesis and reverse water–gas shift kinetics over Cu(110) model catalysts: structural sensitivity. *Journal of Catalysis*, 1996. **161**(2): p. 776-782.
27. Denise, B. and R. Sneeden, Oxide-supported copper catalysts prepared from copper formate: Differences in behavior in methanol synthesis from CO/H_2 and CO_2/H_2 mixtures. *Applied catalysis*, 1986. **28**: p. 235-239.
28. Studt, F., et al., The mechanism of CO and CO_2 hydrogenation to methanol over Cu-based catalysts. *ChemCatChem*, 2015. **7**(7): p. 1105-1111.
29. Topsøe, H., et al., *Importance of dynamics in real catalyst systems*, in *Studies in Surface Science and Catalysis*. 1997, Elsevier. p. 121-139.
30. Topsøe, N.-Y. and H. Topsøe, FTIR studies of dynamic surface structural changes in Cu-based methanol synthesis catalysts. *Journal of Molecular Catalysis A: Chemical*, 1999. **141**(1-3): p. 95-105.
31. Jansen, W., et al., Dynamic behavior of the surface structure of $Cu/ZnO/SiO_2$ catalysts. *Journal of Catalysis*, 2002. **210**(1): p. 229-236.
32. Abbas, I., et al., Differences in bifunctionality of ZnO and ZrO_2 in $Cu/ZnO/ZrO_2/Al_2O_3$ catalysts in hydrogenation of carbon oxides for methanol synthesis. *Applied Catalysis B: Environmental*, 2019. **258**: p. 117971.
33. Günter, M.M., et al., Implication of the microstructure of binary Cu/ZnO catalysts for their catalytic activity in methanol synthesis. *Catalysis letters*, 2001. **71**(1-2): p. 37-44.
34. Kasatkin, I., et al., Role of lattice strain and defects in copper particles on the activity of $Cu/ZnO/Al_2O_3$ catalysts for methanol

synthesis. *Angewandte Chemie International Edition*, 2007. **46**(38): p. 7324-7327.
35. Behrens, M., et al., The active site of methanol synthesis over $Cu/ZnO/Al_2O_3$ industrial catalysts. *Science*, 2012. **336**(6083): p. 893-897.
36. Fujitani, T., et al., The kinetics and mechanism of methanol synthesis by hydrogenation of CO_2 over a Zn-deposited Cu (111) surface. *Surface science*, 1997. **383**(2-3): p. 285-298.
37. Nakamura, J., et al., A surface science investigation of methanol synthesis over a Zn-deposited polycrystalline Cu surface. *Journal of Catalysis*, 1996. **160**(1): p. 65-75.
38. Kuld, S., et al., Quantifying the promotion of Cu catalysts by ZnO for methanol synthesis. *Science*, 2016. **352**(6288): p. 969-974.
39. Kattel, S., et al., Active sites for CO_2 hydrogenation to methanol on Cu/ZnO catalysts. *Science*, 2017. **355**(6331): p. 1296-1299.
40. Zabilskiy, M., et al., The unique interplay between copper and zinc during catalytic carbon dioxide hydrogenation to methanol. *Nature communications*, 2020. **11**(1): p. 1-8.
41. Fujitani, T., et al., Methanol synthesis by hydrogenation of CO_2 over a Zn-deposited Cu(111): formate intermediate. *Applied surface science*, 1997. **121**: p. 583-586.
42. French, S., et al., Identification and characterization of active sites and their catalytic processes—the Cu/ZnO methanol catalyst. *Topics in catalysis*, 2003. **24**(1-4): p. 161-172.
43. Liao, F., et al., Morphology‐Dependent Interactions of ZnO with Cu Nanoparticles at the Materials' Interface in Selective Hydrogenation of CO_2 to CH_3OH. *Angewandte Chemie*, 2011. **123**(9): p. 2210-2213.
44. Kühl, S., et al., Cu-Based Catalyst Resulting from a Cu, Zn, Al Hydrotalcite-Like Compound: A Microstructural, Thermoanalytical, and In Situ XAS Study. *Chemistry‐A European Journal*, 2014. **20**(13): p. 3782-3792.
45. Behrens, M., et al., The potential of microstructural optimization in metal/oxide catalysts: higher intrinsic activity of copper by partial embedding of copper nanoparticles. *ChemCatChem*, 2010. **2**(7): p. 816-818.
46. Polierer, S., et al., On the reactivity of the Cu/ZrO_2 system for the hydrogenation of CO_2 to methanol: A density functional theory

study. *The Journal of Physical Chemistry C*, 2019. **123**(44): p. 26904-26911.
47. Jung, K.T. and A.T. Bell, Effects of zirconia phase on the synthesis of methanol over zirconia-supported copper. *Catalysis letters*, 2002. **80**(1-2): p. 63-68.
48. Rhodes, M.D. and A.T. Bell, The effects of zirconia morphology on methanol synthesis from CO and H_2 over Cu/ZrO_2 catalysts: Part I. Steady-state studies. *Journal of catalysis*, 2005. **233**(1): p. 198-209.
49. Baiker, A., et al., *Hydrogenation of CO_2 over copper, silver and gold/zirconia catalysts: Comparative study of catalyst properties and reaction pathways*, in *Studies in Surface Science and Catalysis*. 1993, Elsevier. p. 1257-1272.
50. Köppel, R.A., C. Stöcker, and A. Baiker, Copper-and silver–zirconia aerogels: preparation, structural properties and catalytic behavior in methanol synthesis from carbon dioxide. *Journal of Catalysis*, 1998. **179**(2): p. 515-527.
51. Ma, Z.-Y., et al., Catalytic performance of copper supported on zirconia polymorphs for CO hydrogenation. *Journal of Molecular Catalysis A: Chemical*, 2005. **231**(1-2): p. 75-81.
52. Samson, K., et al., Influence of ZrO_2 structure and copper electronic state on activity of Cu/ZrO_2 catalysts in methanol synthesis from CO_2. *ACS Catalysis*, 2014. **4**(10): p. 3730-3741.
53. Tada, S., et al., Cu species incorporated into amorphous ZrO_2 with high activity and selectivity in CO_2-to-methanol hydrogenation. *The Journal of Physical Chemistry C*, 2018. **122**(10): p. 5430-5442.
54. Witoon, T., et al., CO_2 hydrogenation to methanol over Cu/ZrO_2 catalysts: Effects of zirconia phases. *Chemical Engineering Journal*, 2016. **293**: p. 327-336.
55. Ertl, G., H. Knözinger, and J. Weitkamp, *Handbook of heterogeneous catalysis*. 1997.
56. Behrens, M. and R. Schlögl, How to prepare a good Cu/ZnO catalyst or the role of solid state chemistry for the synthesis of nanostructured catalysts. *Zeitschrift für anorganische und allgemeine Chemie*, 2013. **639**(15): p. 2683-2695.

57. Behrens, M., Meso-and nano-structuring of industrial Cu/ZnO/(Al_2O_3) catalysts. *Journal of Catalysis*, 2009. **267**(1): p. 24-29.
58. Kondrat, S.A., et al., Stable amorphous georgeite as a precursor to a high-activity catalyst. *Nature*, 2016. **531**(7592): p. 83-87.
59. Smith, P.J., et al., A new class of Cu/ZnO catalysts derived from zincian georgeite precursors prepared by co-precipitation. *Chemical science*, 2017. **8**(3): p. 2436-2447.
60. Li, K. and J.G. Chen, CO_2 hydrogenation to methanol over ZrO2-containing catalysts: Insights into ZrO_2 induced synergy. *ACS Catalysis*, 2019. **9**(9): p. 7840-7861.
61. Wang, Y., et al., Exploring the ternary interactions in Cu–ZnO–ZrO_2 catalysts for efficient CO_2 hydrogenation to methanol. *Nature communications*, 2019. **10**(1): p. 1-10.
62. Guo, X., et al., Glycine–nitrate combustion synthesis of CuO–ZnO–ZrO_2 catalysts for methanol synthesis from CO_2 hydrogenation. *Journal of Catalysis*, 2010. **271**(2): p. 178-185.
63. Arena, F., et al., Solid-state interactions, adsorption sites and functionality of Cu-ZnO/ZrO_2 catalysts in the CO_2 hydrogenation to CH_3OH. *Applied Catalysis A: General*, 2008. **350**(1): p. 16-23.
64. Li, M.M.-J., et al., Enhanced CO_2 hydrogenation to methanol over CuZn nanoalloy in Ga modified Cu/ZnO catalysts. *Journal of Catalysis*, 2016. **343**: p. 157-167.
65. Natesakhawat, S., et al., Active sites and structure–activity relationships of copper-based catalysts for carbon dioxide hydrogenation to methanol. *ACS Catalysis*, 2012. **2**(8): p. 1667-1676.
66. Zhang, G., et al., Tuning surface-interface structures of ZrO_2 supported copper catalysts by in situ introduction of indium to promote CO_2 hydrogenation to methanol. *Applied Catalysis A: General*, 2020: p. 117805.
67. Liu, G., et al., The rate of methanol production on a copper-zinc oxide catalyst: the dependence on the feed composition. *Journal of Catalysis*, 1984. **90**(1): p. 139-146.
68. Liu, G., et al., The role of CO_2 in methanol synthesis on Cu–Zn oxide: An isotope labeling study. *Journal of Catalysis*, 1985. **96**(1): p. 251-260.

69. Chinchen, G., et al., Mechanism of methanol synthesis from $CO_2/CO/H_2$ mixtures over copper/zinc oxide/alumina catalysts: use of 14C-labelled reactants. *Applied Catalysis*, 1987. **30**(2): p. 333-338.
70. Kunkes, E.L., et al., Hydrogenation of CO_2 to methanol and CO on $Cu/ZnO/Al_2O_3$: Is there a common intermediate or not? *Journal of Catalysis*, 2015. **328**: p. 43-48.
71. Larmier, K., et al., CO_2-to-methanol hydrogenation on zirconia‐supported copper nanoparticles: reaction intermediates and the role of the metal–support interface. *Angewandte Chemie International Edition*, 2017. **56**(9): p. 2318-2323.
72. Muhler, M., et al., On the role of adsorbed atomic oxygen and CO_2 in copper based methanol synthesis catalysts. *Catalysis letters*, 1994. **25**(1-2): p. 1-10.
73. Kattel, S., et al., Optimizing binding energies of key intermediates for CO_2 hydrogenation to methanol over oxide-supported copper. *Journal of the American Chemical Society*, 2016. **138**(38): p. 12440-12450.
74. Schild, C., A. Wokaun, and A. Baiker, On the hydrogenation of CO and CO_2 over copper/zirconia and palladium/zirconia catalysts. *Fresenius' journal of analytical chemistry*, 1991. **341**(5-6): p. 395-401.
75. Wokaun, A., et al., Metal/zirconia catalysts for the synthesis of methanol: characterization by vibrational spectroscopy. *Fresenius' journal of analytical chemistry*, 1994. **349**(1-3): p. 71-75.
76. Weigel, J., et al., Surface species in CO and CO_2 hydrogenation over copper/zirconia: on the methanol synthesis mechanism. *Langmuir*, 1996. **12**(22): p. 5319-5329.
77. Yang, Y., et al., Mechanistic studies of methanol synthesis over Cu from $CO/CO_2/H_2/H_2O$ mixtures: The source of C in methanol and the role of water. *Journal of catalysis*, 2013. **298**: p. 10-17.
78. Bartholomew, C.H. and R.J. Farrauto, *Fundamentals of industrial catalytic processes*. 2011: John Wiley & Sons.
79. Askgaard, T., et al., A kinetic model of methanol synthesis. *Journal of Catalysis*, 1995. **156**(2): p. 229-242.

80. Ovesen, C., et al., Kinetic implications of dynamical changes in catalyst morphology during methanol synthesis over Cu/ZnO catalysts. *Journal of Catalysis*, 1997. **168**(2): p. 133-142.
81. Reichenbach, T., et al., Ab initio study of CO_2 hydrogenation mechanisms on inverse ZnO/Cu catalysts. *Journal of catalysis*, 2018. **360**: p. 168-174.
82. Tang, Q.-L., Q.-J. Hong, and Z.-P. Liu, CO_2 fixation into methanol at Cu/ZrO_2 interface from first principles kinetic Monte Carlo. *Journal of Catalysis*, 2009. **263**(1): p. 114-122.
83. Zheng, H., et al., Methanol synthesis from CO_2: a DFT investigation on Zn-promoted Cu catalyst. *Research on Chemical Intermediates*, 2020. **46**(3): p. 1749-1769.
84. Tang, Q.-L. and Z.-P. Liu, Identification of the Active Cu Phase in the Water− Gas Shift Reaction over Cu/ZrO_2 from First Principles. *The Journal of Physical Chemistry C*, 2010. **114**(18): p. 8423-8430.
85. Hong, Q.-J. and Z.-P. Liu, Mechanism of CO_2 hydrogenation over $Cu/ZrO_2(212)$ interface from first-principles kinetics Monte Carlo simulations. *Surface science*, 2010. **604**(21-22): p. 1869-1876.
86. Tao, H., et al., What Is the Best Size of Subnanometer Copper Clusters for CO_2 Conversion to Methanol at Cu/TiO_2 Interfaces? A Density Functional Theory Study. *The Journal of Physical Chemistry C*, 2019. **123**(39): p. 24118-24132.
87. Nakamura, J., et al., *Model studies of methanol synthesis on copper catalysts*, in *Studies in surface science and catalysis*. 1996, Elsevier. p. 1389-1399.
88. Nakamura, I., et al., Evidence for a special formate species adsorbed on the Cu–Zn active site for methanol synthesis. *Surface science*, 1998. **402**: p. 92-95.
89. Morikawa, Y., et al., Ab initio study of surface structural changes during methanol synthesis over Zn/Cu(111). *Chemical physics letters*, 1999. **304**(1-2): p. 91-97.
90. Morikawa, Y., K. Iwata, and K. Terakura, First-principles study of chemical reactions at metal surfaces. *RIKEN REVIEW*, 2000: p. 9-11.

91. Morikawa, Y., K. Iwata, and K. Terakura, Theoretical study of hydrogenation process of formate on clean and Zn deposited Cu(111) surfaces. *Applied surface science*, 2001. **169**: p. 11-15.
92. Martinez-Suarez, L., et al., Reaction network of methanol synthesis over Cu/ZnO nanocatalysts. *ACS Catalysis*, 2015. **5**(7): p. 4201-4218.
93. Martínez-Suárez, L., et al., Tuning the reactivity of a Cu/ZnO nanocatalyst via gas phase pressure. *Physical review letters*, 2013. **110**(8): p. 086108.
94. Martinez-Suarez, L., J. Frenzel, and D. Marx, Cu/ZnO nanocatalysts in response to environmental conditions: surface morphology, electronic structure, redox state and CO_2 activation. *Physical Chemistry Chemical Physics*, 2014. **16**(47): p. 26119-26136.
95. Catlow, C., et al., Computational approaches to the determination of active site structures and reaction mechanisms in heterogeneous catalysts. *Philosophical Transactions of the Royal Society A: Mathematical, Physical and Engineering Sciences*, 2005. **363**(1829): p. 913-936.
96. Yang, B., et al., Copper cluster size effect in methanol synthesis from CO_2. *The Journal of Physical Chemistry C*, 2017. **121**(19): p. 10406-10412.
97. Grabow, L. and M. Mavrikakis, Mechanism of methanol synthesis on Cu through CO_2 and CO hydrogenation. *Acs Catalysis*, 2011. **1**(4): p. 365-384.
98. Fajín, J.L., et al., Influence of step sites in the molecular mechanism of the water gas shift reaction catalyzed by copper. *Journal of Catalysis*, 2009. **268**(1): p. 131-141.
99. Rodriguez, J.A., et al., Water Gas Shift Reaction on Cu and Au Nanoparticles Supported on $CeO_2(111)$ and $ZnO(000\bar{1})$: Intrinsic Activity and Importance of Support Interactions. *Angewandte Chemie International Edition*, 2007. **46**(8): p. 1329-1332.
100. Rodriguez, J.A., et al., Water-Gas Shift Reaction on a Highly Active Inverse CeO_x/Cu(111) Catalyst: Unique Role of Ceria Nanoparticles. *Angewandte chemie international edition*, 2009. **48**(43): p. 8047-8050.

101. Ye, J., et al., Active oxygen vacancy site for methanol synthesis from CO_2 hydrogenation on In_2O_3(110): a DFT study. *ACS Catalysis*, 2013. **3**(6): p. 1296-1306.
102. Martin, O., et al., Indium oxide as a superior catalyst for methanol synthesis by CO_2 hydrogenation. *Angewandte Chemie International Edition*, 2016. **55**(21): p. 6261-6265.
103. Chou, C.-Y. and R.F. Lobo, Direct conversion of CO_2 into methanol over promoted indium oxide-based catalysts. *Applied Catalysis A: General*, 2019. **583**: p. 117144.
104. Ye, J., Q. Ge, and C.-j. Liu, Effect of PdIn bimetallic particle formation on CO_2 reduction over the Pd–In/SiO_2 catalyst. *Chemical Engineering Science*, 2015. **135**: p. 193-201.
105. Snider, J.L., et al., Revealing the synergy between oxide and alloy phases on the performance of bimetallic In–Pd catalysts for CO_2 hydrogenation to methanol. *ACS Catalysis*, 2019. **9**(4): p. 3399-3412.
106. Studt, F., et al., Discovery of a Ni-Ga catalyst for carbon dioxide reduction to methanol. *Nature chemistry*, 2014. **6**(4): p. 320-324.
107. Sharafutdinov, I., et al., Intermetallic compounds of Ni and Ga as catalysts for the synthesis of methanol. *Journal of catalysis*, 2014. **320**: p. 77-88.
108. Hengne, A.M., et al., Ni–Sn-supported ZrO_2 catalysts modified by indium for selective CO_2 hydrogenation to methanol. *ACS Omega*, 2018. **3**(4): p. 3688-3701.
109. Melaet, G., et al., Evidence of highly active cobalt oxide catalyst for the Fischer–Tropsch synthesis and CO_2 hydrogenation. *Journal of the American Chemical Society*, 2014. **136**(6): p. 2260-2263.
110. Li, C.-S., et al., High-performance hybrid oxide catalyst of manganese and cobalt for low-pressure methanol synthesis. *Nature communications*, 2015. **6**(1): p. 1-5.
111. Perry, J.H., *Chemical engineers' handbook 8th edition*. 1950, ACS Publications. p. 4.1-4.38.
112. Van Bennekom, J., et al., Methanol synthesis beyond chemical equilibrium. *Chemical engineering science*, 2013. **87**: p. 204-208.

113. Van Der Grift, C., et al., Effect of the reduction treatment on the structure and reactivity of silica-supported copper particles. *Journal of Catalysis*, 1991. **131**(1): p. 178-189.
114. Gervasini, A. and S. Bennici, Dispersion and surface states of copper catalysts by temperature-programmed-reduction of oxidized surfaces (s-TPR). *Applied Catalysis A: General*, 2005. **281**(1-2): p. 199-205.
115. Liang, B., et al., Investigation on deactivation of $Cu/Zno/Al_2O_3$ catalyst for CO_2 hydrogenation to methanol. *Industrial Engineering Chemistry Research*, 2019. **58**(21): p. 9030-9037.
116. Van Bennekom, J., et al., Methanol synthesis beyond chemical equilibrium. 2013. **87**: p. 204-208.
117. Matsushita, T., T. Haganuma, and D. Fujita, *Process for producing methanol*. 2013, Google Patents.
118. Shulenberger, A.M., et al., *Process for producing liquid fuel from carbon dioxide and water*. 2012, Google Patents.
119. Catizzone, E., et al., CO_2 recycling to dimethyl ether: State-of-the-art and perspectives. *Molecules*, 2018. **23**(1): p. 31.
120. Aguayo, A.T., et al., Kinetic modeling of dimethyl ether synthesis in a single step on a $CuO{-}ZnO{-}Al_2O_3/\gamma\text{-}Al_2O_3$ catalyst. *Industrial & Engineering Chemistry Research*, 2007. **46**(17): p. 5522-5530.
121. Qin, Z.z., et al., Experimental and theoretical study of the intrinsic kinetics for dimethyl ether synthesis from CO_2 over Cu‐Fe‐Zr/HZSM‐5. *AIChE Journal*, 2015. **61**(5): p. 1613-1627.
122. Tang, W., et al., Porous Mn–Co mixed oxide nanorod as a novel catalyst with enhanced catalytic activity for removal of VOCs. *Catalysis Communications*, 2014. **56**: p. 134-138.
123. Wang, S., et al., Development of a stable $MnCo_2O_4$ cocatalyst for photocatalytic CO_2 reduction with visible light. *ACS Applied Materials & Interfaces*, 2015. **7**(7): p. 4327-4335.
124. Biesinger, M.C., et al., Resolving surface chemical states in XPS analysis of first row transition metals, oxides and hydroxides: Cr, Mn, Fe, Co and Ni. *Applied Surface Science*, 2011. **257**(7): p. 2717-2730.
125. Oku, M., X-ray photoelectron spectrum of low-spin Co(III) in $LiCoO_2$. *Journal of Solid State Chemistry*, 1978. **23**(1-2): p. 177-185.

126. Moses, A.W., et al., Surface properties of $LiCoO_2$, $LiNiO_2$ and $LiNi_{1-x}Co_xO_2$. *Applied surface science*, 2007. **253**(10): p. 4782-4791.
127. Galenda, A., et al., LaSrCoFeO and Fe_2O_3/LaSrCoFeO powders: synthesis and characterization. *Chemistry of materials*, 2007. **19**(11): p. 2796-2808.
128. Chen, Y., et al., Modified Oxygen Defect Chemistry at Transition Metal Oxide Heterostructures Probed by Hard X-ray Photoelectron Spectroscopy and X-ray Diffraction. *Chemistry of Materials*, 2018. **30**(10): p. 3359-3371.
129. Li, J., et al., Catalytic performance of manganese cobalt oxides on methane combustion at low temperature. *Applied Catalysis B: Environmental*, 2009. **90**(1-2): p. 307-312.
130. Oku, M. and K. Hirokawa, X-ray photoelectron spectroscopy of Co_3O_4, Fe_3O_4, Mn_3O_4, and related compounds. *Journal of Electron Spectroscopy Related Phenomena*, 1976. **8**(5): p. 475-481.
131. Liu, C., et al., Mesoporous Mn promoted Co_3O_4 oxides as an efficient and stable catalyst for low temperature oxidation of CO. *Solid State Sciences*, 2017. **71**: p. 69-74.
132. Piumetti, M., D. Fino, and N. Russo, Mesoporous manganese oxides prepared by solution combustion synthesis as catalysts for the total oxidation of VOCs. *Applied Catalysis B: Environmental*, 2015. **163**: p. 277-287.
133. Gao, J., et al., A thermodynamic analysis of methanation reactions of carbon oxides for the production of synthetic natural gas. *RSC advances*, 2012. **2**(6): p. 2358-2368.
134. Álvarez, A., et al., Challenges in the greener production of formates/formic acid, methanol, and DME by heterogeneously catalyzed CO_2 hydrogenation processes. *Chemical reviews*, 2017. **117**(14): p. 9804-9838.
135. Lee, W.J., et al., Recent trend in thermal catalytic low temperature CO_2 methanation: A critical review. *Catalysis Today*, 2020.
136. Li, W., et al., A short review of recent advances in CO_2 hydrogenation to hydrocarbons over heterogeneous catalysts. *RSC Advances*, 2018. **8**(14): p. 7651-7669.

137. Wang, L., et al., Selective hydrogenation of CO_2 to ethanol over cobalt catalysts. *Angewandte Chemie International Edition*, 2018. **57**(21): p. 6104-6108.
138. Słoczyński, J., et al., Catalytic activity of the M/($3ZnO \cdot ZrO_2$) system (M= Cu, Ag, Au) in the hydrogenation of CO_2 to methanol. *Applied Catalysis A: General*, 2004. **278**(1): p. 11-23.
139. Behrens, M., et al., Phase-pure Cu, Zn, Al hydrotalcite-like materials as precursors for copper rich $Cu/ZnO/Al_2O_3$ catalysts. *Chemistry of Materials*, 2010. **22**(2): p. 386-397.
140. Wang, R. and Z. Yang, Synthesis and high cycle performance of Zn–Al–In-hydrotalcite as anode materials for Ni–Zn secondary batteries. *Rsc Advances*, 2013. **3**(43): p. 19924-19928.
141. Krasnobaeva, O., et al., Indium-containing catalysts for oxidative dehydrogenation of organic compounds. *Russian Journal of Inorganic Chemistry*, 2014. **59**(7): p. 693-698.
142. Wang, R., et al., Superior cycle stability and high rate capability of Zn–Al–In-hydrotalcite as negative electrode materials for Ni–Zn secondary batteries. *Journal of Power Sources*, 2014. **251**: p. 344-350.
143. Behrens, M., et al., Minerals as model compounds for Cu/ZnO catalyst precursors: structural and thermal properties and IR spectra of mineral and synthetic (zincian) malachite, rosasite and aurichalcite and a catalyst precursor mixture. *European Journal of Inorganic Chemistry*, 2009. **2009**(10): p. 1347-1357.
144. Kuld, S., et al., Quantification of zinc atoms in a surface alloy on copper in an industrial-type methanol synthesis catalyst. *Angewandte Chemie*, 2014. **126**(23): p. 6051-6055.
145. Gao, P., et al., Preparation and activity of Cu/Zn/Al/Zr catalysts via hydrotalcite-containing precursors for methanol synthesis from CO_2 hydrogenation. *Catalysis Science Technology*, 2012. **2**(7): p. 1447-1454.
146. Biesinger, M.C., et al., Resolving surface chemical states in XPS analysis of first row transition metals, oxides and hydroxides: Sc, Ti, V, Cu and Zn. *Applied Surface Science*, 2010. **257**(3): p. 887-898.
147. Li, F., et al., *Copper-based Perovskite Design and Its Performance in CO_2 Hydrogenation to Methanol*, in *Perovskite*

Materials-Synthesis, Characterisation, Properties, and Applications. 2016, IntechOpen.

148. Yin, A., et al., The nature of active copper species in Cu-HMS catalyst for hydrogenation of dimethyl oxalate to ethylene glycol: New insights on the synergetic effect between Cu^0 and Cu^+. *The Journal of Physical Chemistry C*, 2009. **113**(25): p. 11003-11013.
149. Wu, J., et al., Cu Nanoparticles inlaid mesoporous carbon aerogels as a high performance desulfurizer. *Environmental Science Technology*, 2016. **50**(10): p. 5370-5378.
150. Zheng, X., et al., Lanthanum oxide-modified Cu/SiO_2 as a high-performance catalyst for chemoselective hydrogenation of dimethyl oxalate to ethylene glycol. *ACS Catalysis*, 2013. **3**(12): p. 2738-2749.
151. Pujilaksono, B., et al., X-ray photoelectron spectroscopy studies of indium tin oxide nanocrystalline powder. *Materials Characterization*, 2005. **54**(1): p. 1-7.
152. Jedidi, A., et al., Generation of Cu–In alloy surfaces from $CuInO_2$ as selective catalytic sites for CO_2 electroreduction. *Journal of Materials Chemistry A*, 2015. **3**(37): p. 19085-19092.
153. Shi, Z., et al., CO_2 hydrogenation to methanol over Cu-In intermetallic catalysts: Effect of reduction temperature. *Journal of Catalysis*, 2019. **379**: p. 78-89.
154. Matsumura, Y. and H. Ishibe, Durable copper–zinc catalysts modified with indium oxide in high temperature steam reforming of methanol for hydrogen production. *Journal of Power Sources*, 2012. **209**: p. 72-80.
155. Van Den Berg, R., et al., Structure sensitivity of Cu and CuZn catalysts relevant to industrial methanol synthesis. *Nature communications*, 2016. **7**(1): p. 1-7.
156. Bönicke, I.A., W. Kirstein, and F. Thieme, A study on CO_2 dissociation on a stepped (332) copper surface. *Surface science*, 1994. **307**: p. 177-181.
157. Zhao, Y., et al., An effective $CuZn–SiO_2$ bimetallic catalyst prepared by hydrolysis precipitation method for the hydrogenation of methyl acetate to ethanol. *Industrial Engineering Chemistry Research*, 2018. **57**(13): p. 4526-4534.

158. Schweke, D., et al., The interaction of CO_2 with CeO_2 powder explored by correlating adsorption and thermal desorption analyses. *The Journal of Physical Chemistry C*, 2018. **122**(18): p. 9947-9957.
159. Guo, X., et al., The influence of La doping on the catalytic behavior of Cu/ZrO_2 for methanol synthesis from CO_2 hydrogenation. *Journal of Molecular Catalysis A: Chemical*, 2011. **345**(1-2): p. 60-68.
160. Gao, P., et al., Influence of modifier (Mn, La, Ce, Zr and Y) on the performance of Cu/Zn/Al catalysts via hydrotalcite-like precursors for CO_2 hydrogenation to methanol. 2013. **468**: p. 442-452.
161. Wang, G., et al., Methanol synthesis from CO_2 hydrogenation over $CuO-ZnO-ZrO_2-M_xO_y$ catalysts (M= Cr, Mo and W). *International Journal of Hydrogen Energy*, 2019. **44**(8): p. 4197-4207.
162. Rungtaweevoranit, B., et al., Copper nanocrystals encapsulated in Zr-based metal–organic frameworks for highly selective CO_2 hydrogenation to methanol. *Nano letters*, 2016. **16**(12): p. 7645-7649.
163. Ro, I., et al., Role of the $Cu-ZrO_2$ interfacial sites for conversion of ethanol to ethyl acetate and synthesis of methanol from CO_2 and H2. *ACS Catalysis*, 2016. **6**(10): p. 7040-7050.
164. Tada, S., et al., Design of interfacial sites between Cu and amorphous ZrO_2 dedicated to CO_2-to-methanol hydrogenation. *ACS Catalysis*, 2018. **8**(9): p. 7809-7819.

Appendices

Appendix A Paper I

Paper I

CO_2 hydrogenation to methanol: the structure–activity relationships of different catalyst systems

Kristian Stangeland, Hailong Li, and Zhixin Yu

Energ. Ecol. Environ., 2020, 5, 275-285.

DOI: 10.1007/s40974-020-00156-4

Energ. Ecol. Environ. (2020) 5(4):272–285
https://doi.org/10.1007/s40974-020-00156-4

ORIGINAL ARTICLE

CO_2 hydrogenation to methanol: the structure–activity relationships of different catalyst systems

Kristian Stangeland[1] · Hailong Li[2] · Zhixin Yu[1]

[1] Department of Energy and Petroleum Engineering, University of Stavanger, 4036 Stavanger, Norway
[2] Department of Energy, Building and Environment, Mälardalen University, 73123 Västerås, Sweden

Received: 31 January 2020 / Revised: 6 March 2020 / Accepted: 11 March 2020 / Published online: 20 March 2020

Abstract CO_2 hydrogenation to methanol is a promising environmental-friendly route for combatting CO_2 emissions. Methanol can be used to produce a variety of chemicals and is also an alternative fuel. The CO_2-to-methanol process is mostly studied over multi-component catalysts in which both metal and oxide phases are present. The difficulty in elucidating the influence of the different phases on the catalytic performance has led to intense debate about the nature of the active site. Consequently, the main stumbling blocks in developing rational design strategies are the complexity of the multi-component catalytic systems and challenges in elucidating the active sites. In this paper, we reviewed the most promising catalyst systems for the industrial CO_2-to-methanol processes. Firstly, the copper-based catalysts are discussed. The focus is on the debate regarding the promotional effect of zinc, as well as other metal oxides typically employed to enhance the performance of copper-based catalysts. Other catalytic systems are then covered, which are mainly based on palladium and indium. Alloying and metal–metal oxide interaction also play a significant role in the hydrogenation of CO_2 to methanol over these catalysts. The purpose of this work is to give insight into these complex catalytic systems that can be utilized for advanced catalyst synthesis for the industrial CO_2-to-methanol process.

Keywords CO_2 hydrogenation · Methanol · Catalyst · Structure–activity

✉ Zhixin Yu
Zhixin.yu@uis.no

1 Introduction

Environmental concerns on greenhouse gas emissions have led to a large interest in CO_2 conversion and utilization from both academia and industry in the past decade. CO_2 utilization offers an alternative carbon-neutral pathway for the synthesis of valuable fuels and chemicals. CO_2 hydrogenation to methanol is an attractive process because methanol is one of the largest industrial chemicals and an essential building block for various chemical compounds (formaldehyde, olefins, acetic acid, etc.) (Behrens et al. 2012). Furthermore, methanol is widely used in fuel blends and can also be directly applied in methanol fuel cells. Besides reducing CO_2 emissions, using methanol as an alternative fuel can significantly lower the emissions of air pollutants in the transportation sector, such as hydrocarbons and NO_x (Verhelst et al. 2019). The global methanol market is also expected to grow significantly over the next decade (Triton Market Research 2019). Furthermore, CO_2 hydrogenation to methanol has been suggested as a promising method for intermittent renewable energy storage (Kiss et al. 2016).

Today, methanol is almost exclusively synthesized from fossil sources over $Cu/ZnO/Al_2O_3$ catalysts by an industrial process that converts synthesis gas ($H_2/CO/CO_2$) into methanol at elevated pressures (50–100 bar) and temperatures (200–300 °C) (Behrens et al. 2012). The interest in converting captured CO_2 to methanol by hydrogenation (Eq. 1) has increased significantly in recent years. However, the industrial implementation of CO_2 hydrogenation to methanol has so far been limited. This is mainly due to the higher costs associated with capturing CO_2 and producing H_2 from renewable energy compared to synthesis gas. There are also more significant thermodynamic

restrictions on the conversion due to the competing reverse water–gas shift (RWGS) reaction (Eq. 2) (Álvarez et al. 2017; Stangeland et al. 2018). Furthermore, the different gaseous environment containing a larger amount of water during CO_2 hydrogenation to methanol can have negative effects on the activity and stability of the catalyst (Liang et al. 2019).

$$CO_2 + 3H_2 \rightleftharpoons CH_3O + H_2O \quad \Delta H_{298\,K} = -49.5 \text{ kJ/mol} \tag{1}$$

$$CO_2 + H_2 \rightleftharpoons CO + H_2O \quad \Delta H_{298\,K} = 41.2 \text{ kJ/mol} \tag{2}$$

The most efficient catalysts for CO_2 hydrogenation to methanol are multi-component catalytic systems. For example, the industrial $Cu/ZnO/Al_2O_3$ catalyst is often used as a reference for catalytic performance. It typically consists of intermixed Cu and ZnO nanoparticles after activation, where Al_2O_3 is primarily considered as a structural promoter (Behrens et al. 2012). A large Cu surface area is important to obtain high activity, but there are differences in intrinsic activity between Cu/ZnO-based catalysts with different preparation history. This difference in the active site "quality" implies that the reaction is structure-sensitive over Cu/ZnO-based systems. Similar observations have also been reported for the interplay of Cu with other metal oxides (Chen et al. 2019). Thus, the interaction between the catalyst's components plays an important role in maximizing the catalytic performance of Cu-based systems. The exact nature of the interaction between Cu and metal oxides has been strongly debated and is currently not fully understood.

The key role of the metal–support interaction for CO_2 hydrogenation to methanol has also been demonstrated for other transition metal-based catalysts (i.e., Pd, Ni, Co). Without adequate promotion, these metals typically produce mainly CH_4 or CO during CO_2 hydrogenation. Therefore, alloying or strong metal–metal oxide interaction is needed to increase the methanol selectivity (Ojelade and Zaman 2019). More recently, In-based catalysts have gained much research interest due to its high methanol selectivity over a wide range of temperatures. Promoters can further enhance the methanol synthesis rate of In-based catalysts, which is significantly affected by the atomic-scale architecture (Frei et al. 2019).

The aim of this paper is to give insight into the interplay between species in the different multi-component catalytic systems that have been widely studied for CO_2 hydrogenation to methanol. Elucidating the nature of the active site is important for the development of more effective catalysts, which can aid in commercializing the process and enhance its economic viability.

2 Catalyst systems for CO_2 hydrogenation to methanol

2.1 Cu-based catalysts

2.1.1 Cu/ZnO-based catalysts

The industrial $Cu/ZnO/Al_2O_3$ catalyst is often referred to as the benchmark catalyst for CO_2 hydrogenation to methanol. The reported studies of Cu-based catalysts covered in this work are summarized in Table 1, where the different effects of oxides have been underlined. Initial studies led to the conclusion that Cu was the active component in methanol synthesis, while ZnO and Al_2O_3 functioned as spacers for the Cu particles and structural promoters. Single-crystal studies over different Cu facets indicate that the turnover frequencies (TOF) for methanol synthesis are lower than for the RWGS reaction for H_2/CO_2 mixtures. For instance, a TOF of $\sim 8 \times 10^{-3}$ s^{-1} was reported for methanol synthesis on Cu(110), while the TOF for CO production was ~ 5 s^{-1} (H_2/CO_2 = 11/1, 5.1 bar, 530 K) (Yoshihara and Campbell 1996). Rasmussen et al. (1994a, b) found that the methanol synthesis rate over Cu(100) was $\sim$ 30 times faster than that on Cu(110). On this basis, the role of ZnO has been proposed to increase the exposure of more active Cu sites. Furthermore, several researchers have observed a linear correlation between activity and Cu surface area with catalysts supported on different metal oxides (Natesakhawat et al. 2012). Consequently, many studies report that ZnO does not have a direct influence on methanol synthesis. However, the Cu surface area is typically determined solely from N_2O chemisorption. Recent reports suggest that reducible metal oxides may distort the measurements and that N_2O probes both Cu and the partially reducible oxide (Chatterjee et al. 2019; Fichtl et al. 2014; Kuld et al. 2014).

Evidence for an increase in the intrinsic activity of Cu by metal oxide promoters can be observed from the reported TOF of different model structures and real catalysts in the literature. For instance, a TOF several magnitudes higher than single-crystal Cu has been reported for $Cu/ZnO(000\bar{1})$ (Yang et al. 2010) and $CeO_x/Cu(111)$ (Graciani et al. 2014) model surfaces. Kuld et al. (2016) found that the TOF for methanol increased with increasing Zn coverage of Cu over an industrial-type $Cu/ZnO/Al_2O_3$. This has also been observed in model structures by deposition of Zn on polycrystalline Cu (Nakamura et al. 1996), ZnO on Cu(111) (Senanayake et al. 2016), and ZnO nanoparticles on $Cu(111)/ZnO(000\bar{1})$ (Kattel et al. 2017). Senanayake et al. (2016) observed that the intrinsic activity of Cu(111) showed a volcano-type behavior relative to the ZnO and CeO_x coverage, as shown in Fig. 1a. Furthermore,

Table 1 Summary of the reported studies of Cu-based catalysts for CO_2 hydrogenation to methanol

Catalyst	P, T, H_2/CO_2 (bar, °C)	GHSV (Ml g_{cat}^{-1} h^{-1})	SA_{Cu} (m^2 g^{-1})	X_{CO2} (%)	SMeOH (%)	STYMeOH (mg g_{cat}^{-1} h^{-1})	Ea, MeOH (kJ/mol)	TOF_{MeOH} (s^{-1} × 10^{-3})	Effect of promoter[b]	References
Cu(100)	2, 270, 2	–	–	–	–	–	69	0.27	–	Rasmussen et al. (1994a, b)
Cu(110)	5.1, 257, 10	–	–	–	–	–	67	8	–	Yoshihara et al. (1996)
$Cu/ZnO/Al_2O_3$	60, 250, 3	–	–	–	–	–	–	21	Zn: A, F, Al: S	Behrens et al. (2012)
Cu(111)	4.9, 302, 9	–	–	–	–	–	105	6.3	–	Yang et al. (2010)
$Cu/ZnO(000\bar{1})$	4.9, 302, 9	–	–	–	–	–	67	93	ZnO: S	Yang et al. (2010)
$CeO_x/Cu(111)$	4.9, 302, 9	–	–	–	–	–	50	1300	CeO_x: F	Graciani et al. (2014)
$Cu/ZnO/ZrO_2$	30, 220, 3	10[a]	10	10	91	582	–	21	$ZnO\text{-}ZrO_2$: F	Wang et al. (2019)
Cu/ZrO_2 (MOF)	10, 200, 3	–	–	5	–	–	–	23	–	Rungtaweevoranit et al. (2016)
CuZnAlZrGaY	20, 240, 3	30,000	94	5	–	–	–	21	Ga_2O_3, ZrO_2, Y_2O_3: D, R	Natesakhawat et al. (2012)
$Cu\text{-}LaO_x/SBA\text{-}15$	30, 240, 3	12,000	76	7	81	190	–	19	LaO_x: D, F	Chen et al. (2019)
Cu/SBA-15	30, 240, 3	12,000	38	3	26	20	–	1.3	–	Chen et al. (2019)
$Cu/ZnO/Al_2O_3$	30, 230, 3	–	–	–	–	1250	–	–	ZnO_x/Zn: I	Lunkenbein et al. (2015)
$Cu@ZnO_x$	30, 250, 3	1800	–	2	100	149	–	–	ZnO_x: I	Le Valant et al. (2015)
Cu–ZnO	30, 250, 3	1800	–	11	7	52	–	–	–	Le Valant et al. (2015)
$Cu/ZnO/Zr_2O_3/Y_2O_3$	50, 230, 3	10,000	35	20	69	390	–	–	Y_2O_3: D, I, S	Gao et al. (2015)
$Cu/ZnO/Ga_2O_3$	45, 240, 2.8	18,000	85	27	50	837	–	–	Ga_2O_3: A[c], S	Li et al. (2016)
$Cu/ZnO/Al_2O_3$	30, 200, 3	9000[a]	54	–	–	181	–	–	ZnO: I, R	Liang et al. (2019)
$Cu/ZnO\text{-}ZrO_2$ (MOF)	40, 250, 3	18,000[a]	–	3	100	2590	–	–	ZnO_x, ZrO_x: I	An et al. (2017)
Cu/AlCeO	40, 240, 3	6000	26	15	70	224	–	–	CeO_x: B, I	Li et al. (2019)
Cu/ZrO_2	80, 260, 3	3600[a]	3	15	86	98	–	–	ZrO_2: F, I	Samson et al. (2014)
Cu/ZrO_2	10, 230, 3	8400	8	4	59	58	–	–	ZrO_2: D, F, I	Tada et al. (2019)
Cu/ZrO_2	10, 230, 3	8400	82	4	45	35	–	–	–	Tada et al. (2019)
$Cu/ZnO/Al_2O_3/Zr$	50, 250, 3	12,000	25	25	48	490	–	–	ZrO_2: B, D	Gao et al. (2013)
Cu/ZrO_2	10, 200, 3	8800	9	2	83	–	57	–	–	Arena et al. (2008)
$Cu–ZnO/ZrO_2$	10, 200, 3	8800	61	3	65	–	69	–	ZnO: D, F, I, R ZrO_2: F, I	Arena et al. (2008)

Table 1 continued

Catalyst	P, T, H_2/CO_2 (bar, °C)	GHSV (Ml g_{cat}^{-1} h^{-1})	SA_{Cu} (m^2 g^{-1})	X_{CO2} (%)	SMeOH (%)	STYMeOH (mg g_{cat}^{-1} h^{-1})	Ea, MeOH (kJ/mol)	TOF_{MeOH} ($s^{-1} \times 10^{-3}$)	Effect of promoter[b]	References
ZnO-ZrO_2	50, 320, 3	24,000	–	10	86	730	–	–	–	Wang et al. (2017)
Au–Cu/ZnO/Al2O3	50, 230, 4	600,000[a]	11	1	92	5700	–	–	Au: A, E	Martín et al. (2015)
Pd–Cu/CeO_2	30, 250, 3	3000	–	16	27	–	–	–	Pd: D, E, R,	Choi et al. (2017)
Pd–Cu/SiO_2	41, 250, 3	3600	–	7	34	36	–	–	Pd: A	Jiang et al. (2015)
Ni–Cu/Al_2O_3	20, 250, 3	3600	–	6	59	48	–		Ni: A	Zhao et al. (2017)
Cu–Ni/CeO_2	30, 260, 3	6000[a]	–	18	79	580	–		Ni: A, D, R	Tan et al. (2018)

[a]GHSV given in the unit h^{-1}

[b]A, Alloy; I, enhanced metal–support interaction; B; enhanced surface basicity; D, dispersion; E, electronic promotion; F, facilitates CO_2 activation; R, reducibility; S, structural promoter

[c]Ga enhances CuZn alloy formation

they found that the TOF of the inverse oxide/Cu configuration [CeO_x/Cu(111) and ZnO_x/Cu(111)] was about 2 times higher than the corresponding Cu/oxide structure (Cu/ZnO and Cu/CeO_2). These structure effects are schematically illustrated in Fig. 1b. The reactivity of Cu particles deposited on ZnO single-crystal surfaces has also been reported to depend on the surface plane of ZnO [i.e., (0001), (000$\bar{1}$), and (10$\bar{1}$0)] (Didziulis et al. 1989; Ludviksson et al. 1993). Moreover, the morphology of ZnO could also influence the Cu–ZnO interaction. Liao et al. (2011) detected a strong electronic interaction between Cu and platelike ZnO, which was proposed to facilitate CO_2 activation and hydrogenation at the interface.

The increased activity due to the presence of ZnO in Cu/ZnO-based catalysts is often referred to as the Cu–ZnO synergy or strong metal–support interaction (SMSI). There has been intense debate regarding the nature of the active site and the role of Zn in promoting methanol synthesis (Behrens et al. 2012; Kattel et al. 2017; Kuld et al. 2016; Lunkenbein et al. 2015). Kasatkin et al. (2007) found that lattice strain and defect in Cu particles enhanced the catalytic activity of Cu/ZnO/Al_2O_3. Theoretical studies have also indicated that defects can improve the energetics of the reaction pathway for methanol synthesis (Kopač et al. 2019; Wu and Yang 2017).

Recently, based on a combination of experimental measurements and theoretical calculations, the synergy between Cu and ZnO arising from SMSI was attributed to the formation of surface CuZn alloy (Kuld et al. 2016). Furthermore, the Zn^0 atoms at the step edges of Cu nanoparticles (NPs) were proposed to be the active sites, and the Zn coverage was quantitatively correlated with the methanol synthesis activity. Studt et al. (2015) proposed that metallic Zn on the surface of Cu increased the binding energy of O-bound intermediates (i.e., formate), which facilitates the hydrogenation pathway from CO_2. The lower activity in the absence of ZnO was suggested to result from formate poisoning of the Cu surface. These findings were supported by activity tests in methanol synthesis from various mixtures of $H_2/CO_2/CO$ and DFT calculations. Martinez-Suáres et al. (2015) found that the formation of metallic Zn was thermodynamically favorable at low O_2 partial pressures based on molecular dynamics modeling of a Cu eight-atom cluster on a ZnO substrate.

Several authors have concluded that metallic Zn generated during reduction is not stable under reaction conditions. TEM studies revealed encapsulation of Cu particles by a ZnO overlayer (Lunkenbein et al. 2015). It has also been observed that Zn^0 in the ZnCu(111) catalyst underwent oxidation to ZnO during CO_2 hydrogenation to methanol (Kattel et al. 2017). Le Valant et al. (2015) found that the Cu and CuZn particles were inactive, while

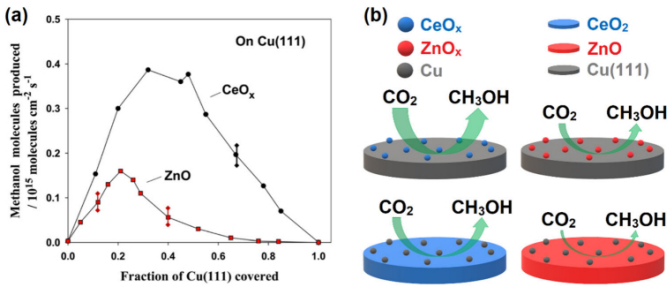

Fig. 1 **a** Rates for CO_2 conversion to methanol on Cu(111) as a function of the fraction of metal surface covered by zinc oxide or ceria oxide. [Reproduced from Ref. Senanayake et al. (2016) with permission from the American Chemical Society, copyright 2016] and **b** illustration of the role of metal oxides on intrinsic methanol synthesis activity of Cu catalysts [Adapted from Ref. Senanayake et al. (2016)]

particles composed of a CuZn core with a ZnO_x shell (CuZn@ZnO_x) showed low activity with 100% methanol selectivity. In contrast, the Cu@ZnO_x core–shell particles exhibited similar selectivity but an eightfold increase in activity compared to that of CuZn@ZnO_x. They concluded that the ZnO_x overlayer was directly involved in the active site for methanol production. Moreover, in situ neutron diffraction characterization of an industrial Cu/Zn/Al methanol synthesis catalyst operated at industrially relevant conditions indicated that the CuZn alloy is not present during syngas conversion to methanol (Kandemir et al. 2013). From the discussion so far, there are conflicting reports on whether Zn^0 or ZnO is the component responsible for promoting the reaction. Furthermore, the promotion mechanism of Zn is also debated. It has been suggested to directly participate in the reaction through the Cu/ZnO_x interface or CuZn alloy, enhance the rate through electronic promotion, and increase the exposure of certain geometrical or structural active sites in Cu.

It has been demonstrated that the interaction between Cu and Zn can be tuned through the composition of the catalysts, preparation method, and addition of promoters. A higher Zn/(Cu + Zn) surface ratio can be obtained at higher Zn content, which can benefit the methanol selectivity (Martin et al. 2015). Brown et al. (2015) reported a one-pot synthesis approach, where colloidal particles consisting of zinc oxide and Cu(0) were produced from diethyl zinc and bis(carboxylato/phosphinato)copper(II) precursors. The optimum system comprised a 55:45 loading of ZnO/Cu and showed equivalent activity to a commercial Cu/ZnO/Al_2O_3/MgO catalyst. There have also been reports of more effective catalysts with higher Cu dispersion and Cu–ZnO interaction for catalysts derived from Cu/Zn/Al georgeite precursors (Kondrat et al. 2016; Smith et al. 2017), as well as higher intrinsic activity of Cu/Zn/Al produced from hydrotalcite (Kühl et al. 2014). Gao et al. (2015) explored the effect of *Y* loading (*Y* = 0, 1.5, 3.0, 5.8, and 14.5 mol%) of Cu/ZnO/Al_2O_3/Y_2O_3 derived from hydrotalcite precursors. A volcano-shaped trend was observed for the methanol selectivity with a maximum at 3 mol% *Y*. This was attributed to improved Cu dispersion at moderate *Y* loading, resulting in enhanced Cu–ZnO interaction. Li et al. (2016) investigated the effect of Ga loading in Ga modified Cu/ZnO catalysts. Apart from the structural promotion provided by Ga, their results indicated that it also facilitated the deep reduction of ZnO to Zn^0, which formed CuZn alloy after reduction. The improvement in catalytic activity and methanol selectivity could be correlated with the increased Zn^0 concentration. Gao et al. (2013) investigated the influence of different modifiers (Mn, La, Ce, Zr, and Y) on Cu/Zn/Al catalyst obtained via a hydrotalcite-like precursor. They found that the methanol selectivity increased in the series Cu/Zn/Al < Cu/Zn/Al/Mn < Cu/Zn/Al/La < Cu/Zn/Al/Ce < Cu/Zn/Al/Y < Cu/Zn/Al/Zr. This trend was related to the fraction of strong basic sites of the catalysts that facilitated the activation and hydrogenation of CO_2, indicating that the basic sites of the metal oxides influenced the selectivity.

Recent investigations of the deactivation mechanisms of Cu/ZnO/Al_2O_3 catalysts during CO_2 hydrogenation further illustrate the importance of metal–support interaction. Liang et al. (2019) studied a Cu/ZnO/Al_2O_3 catalyst and found that the main causes of deactivation were aggregation of ZnO and partial oxidation of the Cu phase. Prasnikar et al. (2019) found that separate Cu regions formed during CO_2 hydrogenation and that the segregation of Cu/ZnO was promoted when water was added to the feed. Interestingly, Cu/ZnO segregation was not observed when the catalyst was applied for syngas conversion to methanol. Instead, migration of ZnO and partial coverage of Cu were evident during syngas experiments. Thus, the behavior of the catalyst is significantly affected by the gaseous environment, and different strategies might be needed to enhance Cu/ZnO-based catalysts for CO_2 hydrogenation compared to syngas conversion.

There are works that indicate that the reaction pathway on non-promoted and promoted Cu surfaces is different (Studt et al. 2015). In complex real catalyst systems, there

is a combination of different active sites, such as the coexistence of fully covered Cu nanoparticles with partially covered and practically uncovered ones in typical Cu/ZnO/Al_2O_3 catalysts. Consequently, methanol is likely produced from a combination of different reaction pathways (Martinez-Suarez et al. 2015). Therefore, understanding and tuning the interaction between Cu and the promoter(s) is a crucial component of optimizing the activity of Cu-based catalysts. A second observation is that enhancing the stability of the "optimum" catalytic structure(s) is another key challenge in Cu-based catalyst design.

2.1.2 *Effect of other metal oxide components on Cu-based catalysts*

The interaction of Cu with other metal oxides has also been reported, which indicate that the nonstructural promoting role of the metal oxide significantly affects the catalytic behavior. Studt et al. (2015) observed that high methanol formation rates could be obtained over Cu/MgO in CO hydrogenation, whereas the catalyst was significantly less active when CO_2-rich syngas or H_2/CO_2 feedstock was used. This was attributed to poisoning of the Cu surface by CO_2 through the generation of spectator formate species. Chen et al. (2019) found that the addition of La to Cu/SBA-15 increased the methanol selectivity from 26 to 81%. The increase in methanol selectivity was attributed to Cu-LaO_x interface that enhanced the adsorption capacity of CO_2 and facilitated the conversion of CO_2 to methanol. Furthermore, the TOF for methanol synthesis over Cu-LaO_x/SiO_2 was 19×10^{-3} s^{-1} while only 1.3×10^{-3} s^{-1} over Cu/SiO_2.

Graciani et al. (2014) investigated CO_2 hydrogenation to methanol over a model CeO_x/Cu(111) surface. The activation energy of methanol synthesis over the CeO_x/Cu(111) surface was 50 kJ/mol, which is much lower than that obtained over a Cu/ZnO($000\bar{1}$) surface (67 kJ/mol). The reaction mechanism was investigated by in situ infrared reflection adsorption spectroscopy and DFT calculations. The results indicated that methanol and CO were produced through the carboxyl intermediate (HOCO), whereas hydrogenation of formate (HCOO) was inhibited by high barriers. Li et al. (2019) prepared Cu supported on mesostructured Al_2O_3 and AlCeO with different Ce content. They found that Ce enhanced the surface basicity of the catalyst, which could be correlated with the increase in methanol selectivity. Cu/AlCeO showed higher methanol yields than a Cu/ZnO/Al_2O_3 catalyst prepared by co-precipitation despite having a significantly lower Cu surface area.

Zr is by far the most investigated promoter for Cu-based catalysts besides Zn, and it is often combined with Zn in tricomponent catalysts. Rungtaweevoranit et al. (2016) studied Cu confined in Zr-based metal–organic framework (MOF). The XPS analysis indicated a strong interaction between Cu and ZrO_2. They proposed that the presence of multiple Cu oxidation states and the high interfacial contact area between Cu and ZrO_x lead to superior performance relative to a Cu/ZnO/Al_2O_3 catalyst. An et al. (2017) anchored ultra-small Cu/ZnO_x NPs to a pre-assembled 2,2′-bipyridine-5,5′-dicarboxylate and $Zr_6(\mu_3\text{-O})4(\mu_3\text{-OH})_4$ sites in a UiO-bpy MOF. The MOF-cavity-confinement prevented the agglomeration of Cu NPs and phase separation between Cu and ZnO_x, resulting in a highly stable catalyst for 100 h. The catalyst showed a high space-time yield of methanol and a methanol selectivity of 100%, which was attributed to SMSI due to the presence of both Zn and Zr in close proximity to Cu. Ro et al. (2016) prepared Cu/ZrO_2 via controlled surface reactions and atomic layer deposition (ALD) to study the Cu/Zr interface. The oxidation state of Cu and Zr species was primarily Cu^0 and Zr^{4+}. However, Cu^+ and $Zr^{\delta+}$ ($\delta < 4$) were present at the interfacial sites, suggesting partial Cu diffusion into the ZrO_2 lattice to form Cu-ZrO_x. It was found that the formation of Cu–ZrO_2 interfacial sites increased the intrinsic activity of Cu by an order of magnitude. The exact nature of the active site was not addressed, meaning that either the interfacial sites or the pure metal surface modified by the adjacent oxides could be responsible for methanol production.

Samson et al. (2014) showed that Cu supported on *t*-ZrO_2 crystallite phase had a higher activity than Cu supported on *m*-ZrO_2. The presence of oxygen vacancies stabilized both the thermodynamically unstable *t*-ZrO_2 phase and Cu^+ cations, which were present in the vicinity of oxygen vacancies. The catalytic activity toward methanol increased with increasing *t*-ZrO_2 content. Hence, the complexes built from Cu cations and oxygen vacancies preferentially on *t*-ZrO_2 were proposed as the active site for the methanol synthesis reaction. Tada et al. (2019) demonstrated the importance of the interfacial area and surface basicity on the catalytic activity for Cu/ZrO_2 catalysts. Utilizing a Cu nitrate precursor resulted in residual nitrogen that bound to basic sites of the ZrO_2 support, which reduced the activity of the catalysts. In addition, high calcination temperature transformed the amorphous ZrO_2 phase to *t*-ZrO_2, thereby significantly reducing the number of basic sites and, consequently, the activity of the catalyst. Interestingly, an inverse relationship between the Cu surface area determined by N_2O chemisorption and the activity was observed. Calcination at 500 °C resulted in a tenfold increase in Cu surface area compared to the catalyst calcined at 350 °C, but the catalytic activity and the methanol selectivity were significantly lower.

Both direct and indirect promotion of Cu by ZrO_2 has been suggested based on theoretical and experimental investigations. Polierer et al. (2019) studied the Cu/ZrO_2 interface by density functional theory (DFT) calculations. Their results indicate that the intermediates bind too strongly on the ZrO_2 surface as well as on the Cu/ZrO_2 interface for further hydrogenation to methanol. However, electronic promotion of Cu atoms in the vicinity of the Cu/ZrO_2 interface was identified. This increased the binding energy of the key intermediates on the Cu surface and promoted the formation of methanol.

A duel-site reaction path has also been proposed in which Cu activates hydrogen, whereas CO_2 is adsorbed and hydrogenated at the metal/metal oxide interface or neighboring defective sites in the metal oxide. Arena et al. (2008) observed that the specific activity relative to the number of interfacial sites remained constant for Cu–ZnO–ZrO_2 catalysts with different Cu dispersion. The number of interfacial sites was quantified by two independent methods, namely CO and N_2O chemisorption, as well as the oxide-to-metal surface area ratio. Furthermore, they found that the activation energy was lower for Cu/ZrO_2 (57 kJ/mol) compared to Cu–ZnO–ZrO_2 catalysts (69 kJ/mol). This was attributed to a higher reactivity of CO_2 adsorbed on the zirconia surface, where the formate intermediate was further hydrogenated to methanol. Wang et al. (2019) examined the interaction between Cu, ZnO, and ZrO_2 by dispersing ZnO and ZrO_2 on a Cu framework. The Cu–ZnO–ZrO_2 ternary system was more efficient for CO_2 adsorption and subsequent hydrogenation than Cu–ZnO and Cu–ZrO_2. The Cu–ZnO–ZrO_2 catalyst showed excellent activity of 18% conversion and 80% methanol selectivity at relatively mild conditions (220 °C, 30 bar). Based on in situ FTIR combined with DFT calculations, the ZnO–ZrO_2 interface was proposed as the active site for CO_2 adsorption and conversion, while metallic Cu was necessary for generating hydrogen.

The ability of ZnO–ZrO_2 to produce methanol from CO_2 has also been confirmed experimentally. Wang et al. (2017) prepared a ZnO–ZrO_2 solid solution catalyst, which showed methanol selectivity of 86–91% at CO_2 conversion of more than 10% (reaction conditions: 50 bar, 24,000 $mL g_{cat}^{-1} h^{-1}$, H_2/CO_2 = 3:1 to 4:1, 320 to 315 °C, respectively). Based on the observed surface species and DFT calculations, the high methanol selectivity was attributed to a synergetic effect in H_2 activation between the Zn and Zr sites.

2.1.3 Effect of metal alloying on Cu-based catalysts

There are also studies that investigate the effect of metal-doped Cu and Cu alloys. Martin et al. (2015) showed that the addition of small amounts of Au to Cu/ZnO/Al_2O_3 significantly enhanced the methanol formation rate. This was attributed to an increase in Cu^0 surface species, and it was suggested that Au had a stabilizing effect on Cu^0. Choi et al. (2017) found that suitable amounts of Pd added to Cu/CeO_2 generated more reduced Cu sites and also created oxygen vacancies in CeO_2, which enhanced the activity of the catalyst. Jiang et al. (2015) linked the production of methanol to PdCu alloy particles for PdCu supported on different SiO_2 supports. Interestingly, the best performance was obtained with well-mixed PdCu and $PdCu_3$ alloy phases, but further in-depth study is needed to elucidate the synergy between these phases. Whereas a higher amount of Cu^0 enhanced the performance of the catalyst when ZnO or CeO_2 was present, the formation of separate Cu^0 particles lowered the methanol selectivity for Pd–Cu/SiO_2.

Yang et al. (2011) calculated that the methanol yield followed the order of Au/Cu(111) < Cu(111) < Pd/Cu(111) < Rh/Cu(111) < Pt/Cu(111) < Ni/Cu(111) based on DFT computations and kinetic Monte Carlo (kMC) simulations. Zhao et al. (2017) demonstrated that Ni–Cu/Al_2O_3 prepared by ALD was significantly more active and selective in CO_2 hydrogenation to methanol than the catalyst prepared by impregnation. This was attributed to improved dispersion and stronger interaction between Ni and Cu. Tan et al. (2018) found that both the CuNi alloy and CeO_2 support enhanced the conversion to methanol. The role of oxygen vacancies in CeO_2 was to enhance the adsorption of CO_2, while Ni promoted the adsorption and hydrogenation of CO to methanol.

2.2 Pd-based catalysts

Pd-based catalysts have also been extensively studied for CO_2 hydrogenation to methanol, and the performance of different catalysts is summarized in Table 2. They typically exhibit comparable activity and methanol selectivity to Cu-based catalysts during methanol synthesis from CO_2.

The interaction between Pd and the promoter is also crucial for Pd-based catalysts to obtain high methanol selectivity. Bahruji et al. (2016) investigated the structure–activity relationship over Pd/ZnO catalysts prepared by different methods. They found that the preparation method considerably affected the selectivity of the catalyst. Pd/ZnO prepared by impregnation produced almost exclusively CO, whereas the catalyst prepared by sol immobilization had an initial methanol selectivity of 70%. This was attributed to the presence of a mixture of metallic Pd and PdZn alloy clusters, where the former was the active site for CO formation and the latter produced methanol. The methanol selectivity was found to decrease with increasing PdZn alloy particle size. In a later work, Bahruji et al. (2017) found that PdZn supported on TiO_2 was much more active than PdZn supported on Al_2O_3, which was

Table 2 Summary of the reported studies of Pd-based catalysts for CO_2 hydrogenation to methanol

Catalyst	P, T, H_2/CO_2 (bar, °C)	X_{CO2} (%)	SMeOH (%)	GHSV (mL g_{cat}^{-1} h^{-1})	STYMeOH (mg g_{cat}^{-1} h^{-1})	TOFMeOH ($s^{-1} \times 10^{-2}$)	References
Pd/ZnO	20, 250, 3	11	60	3600	78	–	Bahruji et al. (2016)
PdZn/TiO_2	20, 250, 3	10	40	3600	59	–	Bahruji et al. (2017)
Pd/ZnO-CdSe	20, 250, 3	–	70	18,000	–	19	Liao et al. (2017)
Pd/ZnO/Al_2O_3	30, 220, 3	8	50	3600	43	1.37	Xu et al. (2016)
Ca-PdZn/CeO_2	30, 250, 3	11	92	2400	80	–	Malik et al. (2018)
$GaPd_2/SiO_2$	1, 210, 3	–	39	88	–	0.37[b]	Fiordaliso et al. (2015)
Pd_2Ga (CSTR)[a]	50, 210, 3	–	46	67,000	276	0.06[b]	García-Trenco et al. (2017)
Pd/Ga_2O_3	50, 210, 3	17	52	6000	69	–	Qu et al. (2014)

[a]Continuous stirred tank reactor (CSTR)

[b]TOF given in mmol m^{-2} s^{-1}

attributed to higher PdZn dispersion on the TiO_2 support. A Pd/Zn ratio of 1:5 yielded the highest methanol formation rate, while a ratio of 1:10 maximized the methanol selectivity. Liao et al. (2017) prepared PdZn core–shell catalysts with varying degree of Zn decoration of Pd. It was found that the methanol selectivity increased with an increase in neighboring Zn around Pd atoms. Furthermore, the activation energy for the RWGS reaction was increased to 98 kJ/mol. Compared to a conventional Pd/ZnO (71 kJ/mol) and a commercial Cu catalyst (69 kJ/mol), the heavy decoration of Pd with Zn strongly inhibited the RWGS reaction. Xu et al. (2016) also observed that increasing the PdZn alloy content was beneficial to the methanol selectivity. However, Pd species modified by ZnO_x islands were also detected over Pd/ZnO/Al_2O_3 catalysts at low Pd loadings. The methanol selectivity of high alloy content PdZn and ZnO_x containing samples was similar under comparable CO_2 conversion. Therefore, it was proposed that ZnO_x islands could also play a role in methanol synthesis from CO_2. Malik et al. (2018) investigated the effect of Ca-doping on PdZn/CeO_2 catalysts. It was found that the methanol synthesis activity was increased by Ca-doping, which was attributed to an increase in basicity that enhanced CO_2 activation.

Fiordaliso et al. (2015) reported that the $GaPd_2/SiO_2$ catalyst exhibited higher intrinsic activity than that of the conventional Cu/ZnO/Al_2O_3 at atmospheric pressure. The high intrinsic activity was attributed to the $GaPd_2$ intermetallic phase generated during activation. Furthermore, the $GaPd_2$ phase remained stable during CO_2 hydrogenation. García-Trenco et al. (2017) utilized a pyrolysis–reduction method to prepare colloidal Pd/Ga catalysts, which led to the formation of $GaPd_2$ alloy NPs with an average size of 5–6 nm. The colloidal catalyst was tested in liquid-phase methanol synthesis and showed a fourfold increase in activity compared to Cu/ZnO/Al_2O_3 and Pd/ZnO, comparable methanol selectivity, and high stability at 210 °C and 50 bar. Qu et al. (2014) prepared Pd supported on plate and rod Ga_2O_3 nanocrystals. It was observed that Pd supported on plate nanocrystals resulted in higher Pd dispersion and stronger metal–support interaction compared to that of rod nanocrystals supported Pd. This was attributed to the highly unstable surface of the low indexed (002) polar Ga_2O_3 surface present on plate nanocrystals. It contained more oxygen defects and mobile electrons in the conduction band, which was favorable for the formation of Pd/Ga_x active sites for methanol production.

2.3 Indium-based catalysts

Over the last decade, indium-based catalysts have gained significant interest for CO_2 hydrogenation to methanol. The indium-based catalysts typically show low activity for the reverse water–gas shift reaction, which results in high methanol selectivity over a wide temperature range (Table 3). Ye et al. (2013) predicted that methanol formation is favorable on the defective In_2O_3(110) surface containing oxygen vacancies by DFT calculations. Martin et al. (2016) found that In_2O_3 prepared by precipitation had 100% selectivity toward methanol up to 300 °C (50 bar, H_2/CO_2 = 4:1). They also examined In_2O_3 impregnated on various supports and found that ZrO_2 supported In_2O_3 was significantly more active than the others. This was ascribed to the formation of inactive metallic In in samples with

Table 3 Summary of the reported studies of In-based catalysts for CO_2 hydrogenation to methanol

Catalyst	P, T, H_2/CO_2 (bar, °C)	X_{CO2} (%)	SMeOH (%)	GHSV (mL g_{cat}^{-1} h^{-1})	STYMeOH (mg g_{cat}^{-1} h^{-1})	Ea, MeOH (kJ/mol)	References
In_2O_3	50, 300, 4	–	100	16,000[b]	190	–	Martin et al. (2016)
In_2O_3/ZrO_2	50, 300, 4	–	100	16,000[b]	320	–	Martin et al. (2016)
In_2O_3/ZrO_2	40, 300, 4	11	53	52,000	465	66	Chou et al. (2019)
YIn_2O_3/ZrO_2	40, 300, 4	8	69	52,000	420	92	Chou et al. (2019)
Pd/In_2O_3	50, 300, 4	21	72	21,000	885	–	Rui et al. (2017)
PdIn (CSTR)[a]	50, 270, 3	–	61	–	–	35	García-Trenco et al. (2018)
Pd-In/SiO_2	40, 300, 4	–	61	7500	104	–	Snider et al. (2019)
Pd-In_2O_3	50, 280, 4	9	78	48,000	960	84	Frei et al. (2019)
In_2O_3	50, 280, 4	3	89	24,000	180	103	Frei et al. (2019)

[a]Continuous stirred tank reactor (CSTR)

[b]GHSV given in the unit h^{-1}

other carriers than ZrO_2. Only a moderate decrease in the reaction rate was observed over the In_2O_3/ZrO_2 catalyst with H_2O co-feeding ($H_2O/CO_2/H_2$ = 0.3:1:4) at 300 °C. Furthermore, it remained stable over 1000 h on stream, which makes it a very promising catalyst for CO_2 hydrogenation to methanol. Zhang et al. (2018) studied ZrO_2-doped In_2O_3 surfaces through DFT calculations. They found that ZrO_2 can prohibit the excessive formation of oxygen vacancies on the In_2O_3 surface by enhancing the In–O bond near Zr atoms, which is consistent with the effect of different supports on In_2O_3 reported by Martin et al. (2016). In addition, the ZrO_2 species was able to stabilize and activate the intermediates involved in methanol synthesis. Chou and Lobo (2019) found that Y and La promotion of In_2O_3/ZrO_2 can further improve the methanol selectivity by increasing the amount of oxygen defects and CO_2 adsorption sites.

Noble metals have been studied to improve the activity of indium-based catalysts. DFT and microkinetic studies have found that the pathway for methanol formation on Pd–In intermetallic surfaces is comparable to that over Cu surfaces (Wu and Yang 2019). Furthermore, it has been shown that methanol is a more favorable product than CO. Rui et al. (2017) prepared a Pd/In_2O_3 catalyst by mixing In_2O_3 powder with a Pd/peptide composite. The catalyst showed a CO_2 conversion above 20% and methanol selectivity higher than 70% at 300 °C and 50 bar. Both interfacial sites and oxygen vacancies played important roles, while Pd–In bimetallic species was found to reduce the methanol yield. This is consistent with the observation that Pd–In bimetallic NPs supported on SiO_2 are efficient RWGS catalysts at atmospheric pressure (Ye et al. 2015). On the other hand, García-Trenco et al. (2018) found that Pd-In intermetallic compound was highly active and selective for liquid-phase methanol synthesis from CO_2. They observed that the surface was enriched in indium with a significant fraction present as In_2O_3. It was concluded that a synergistic effect between the alloy and In_2O_3 might play an important role in the methanol synthesis reaction pathway over Pd–In catalysts.

Both experimental and theoretical work by Snider et al. (2019) indicated a synergy between PdIn alloy and In_2O_3 for Pd–In/SiO_2 catalysts. The highest methanol selectivity (61%) was obtained at an In/Pd ratio of 2:1, whereas In_2O_3/SiO_2 only had a methanol selectivity of 24%. Frei et al. (2019) showed that the size and location of Pd species influence the performance of Pd-promoted In_2O_3, and their findings are illustrated in Fig. 2. Pd-promoted In_2O_3 prepared by dry impregnation leads to agglomeration of Pd atoms, which lowered the activation energy of the RWGS reaction. On the other hand, a higher methanol selectivity was observed when the catalyst was prepared by co-precipitation, where the Pd species were more strongly embedded into the indium oxide phase. This configuration resulted in a lower activation energy for methanol synthesis (84 kJ/mol), while the activation energy for the RWGS reaction remained unchanged. The lack of agglomeration of Pd species resulted in excellent stability over 500 h time on stream with a CO_2 conversion of 9% and methanol selectivity of 78%. This illustrates the delicate interaction

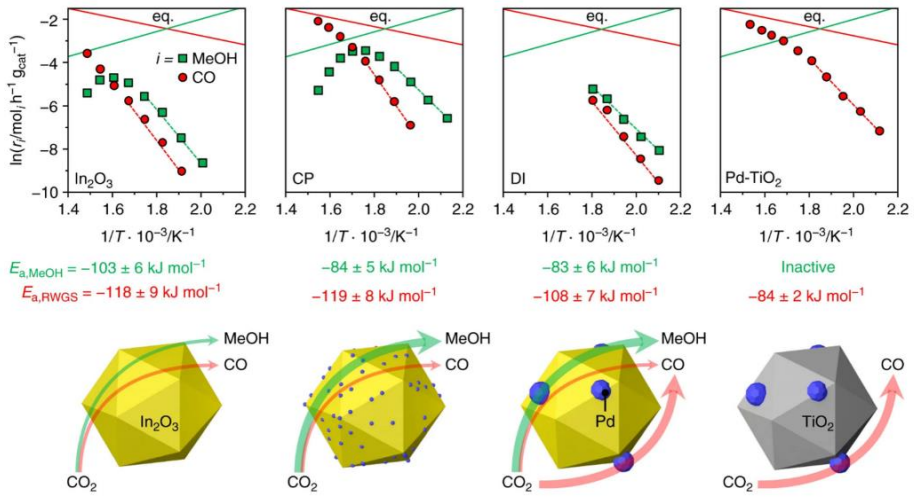

Fig. 2 Activation energies for the main reactions during CO_2 hydrogenation and schematic illustration of the role of Pd in Pd-promoted In_2O_3 and Pd supported on TiO_2. Reproduced from Ref. (Frei et al. 2019) with permission from Springer Nature, copyright 2019

Table 4 Summary of the reported studies of transition metal-based catalysts for CO_2 hydrogenation to methanol

Catalyst	P, T, H_2/CO_2 (bar, °C)	X_{CO2} (%)	SMeOH (%)	GHSV (mL g_{cat}^{-1} h^{-1})	STYMeOH (mg g_{cat}^{-1} h^{-1})	Ea, MeOH (kJ/mol)	References
Au/ZrO_2 (BR)[a]	45, 180, 3	–	73	–	–	51	Wu et al. (2017)
Au/CeO_2	1, 225, 3	–	–	–	1	–	Vourros et al. (2017)
Ni_5Ga_3	1, 200, 3	–	–	–	80	–	Studt et al. (2014)
$Ni\text{-}In\text{-}Al/SiO_2$	1, 260, 3	4	2	4000[b]	18	–	Richard et al. (2017)
$NiSn/InZrO_2$	25, 250, 3	–	99	30,000[b]	120	–	Hengne et al (2018)
MnO_x/Co_3O_4	4, 250, 3	50–60	45	150,000[b]	–	–	Li et al. (2015)
$Mn_xCo_yO_4$	10, 250, 3	45	22	88,800[b]	3106	–	Stangeland et al. (2019)
$CeO_2\text{-}MoP/K\text{-}SiO_2$	31, 230, 3	< 2	76	10.8[b]	–	–	Duyar et al. (2018)

[a]Batch reactor (BR)

[b]GHSV given in the unit h^{-1}

that is required between the catalyst components to selectively enhance the methanol synthesis rate. Other transition metals have also been found to increase the methanol synthesis activity of In_2O_3, such as Ni (Snider et al. 2019) and Rh (Tsang et al. 2018).

2.4 Other transition metal-based catalysts

CO_2 hydrogenation to methanol over various transition metals has also been explored (Table 4). Wu et al. (2017) investigated the effect of Au particle size on various supports (CeO_2, TiO_2, ZnO, and ZrO_2). They demonstrated

that the activity and selectivity of Au particles with an average size smaller than 2 nm were much higher than the catalysts containing particles with an average size larger than 2 nm. In addition, the support significantly influenced the product selectivity as well as the activity. The methanol selectivity followed the order of $Au/ZrO_2 > Au/ZnO > Au/TiO_2 > Au/CeO_2$, and the Au/ZrO_2 catalyst achieved a substantially higher intrinsic activity than the others. There have been different reports regarding the effect of different supports on the activity and selectivity of Au-based catalysts. Hartadi et al. (2015) found that only Au/ZnO was selective toward methanol in CO_2 hydrogenation, while Au/TiO_2 and Au/ZrO_2 mainly produced CO. Vourros et al. (2017) found that Au/TiO_2 and Au/Fe_2O_3 exhibited high CO_2 conversion with low methanol selectivity, whereas Au NPs supported on ZnO and CeO_2 were highly selective toward methanol, but without adequate CO_2 conversion. The discrepancies reported by these groups could be ascribed to the preparation method, the Au particle size of the supported catalysts, and the reaction conditions.

Studt et al. (2014) discovered a Ni-Ga catalyst presenting superior performance than $Cu/ZnO/Al_2O_3$ for CO_2 hydrogenation to methanol at ambient pressure. They prepared different Ni-Ga intermetallic compounds (Ni_3Ga, Ni_5Ga_3, and NiGa). The Ni_5Ga_3 phase displayed the highest methanol selectivity as it was able to inhibit methane generation and suppress the RWGS reaction. Sharafutdinov et al. (2014) reported a detailed study of the relationship between active components and product distribution in intermetallic NiGa catalysts. Methane production was attributed to Ni-rich Ni_3Ga phase, which is present on adjacent Ni–Ni sites on the surface of Ni_5Ga_3. Richard and Fan (2017) synthesized $Ni–In–Al/SiO_2$ catalysts via phyllosilicate precursor and observed that methanol was hardly produced at atmospheric pressure when Ni or In was absent. However, the selectivity toward methanol was below 4% for $Ni–In–Al/SiO_2$. Hengne et al. (2018) discovered that NiSn alloy was selective toward methanol. It was observed that Sn introduction to Ni/ZrO_2 increased the methanol selectivity to 54%. The selectivity was further increased for NiSn supported on In-modified ZrO_2, which showed 99% methanol selectivity and a significant increase in intrinsic activity for CO_2 hydrogenation. This was attributed to improved reducibility of Ni species and enhanced basic strength of the catalyst.

Although Co typically acts as a methanation catalyst during CO_2 hydrogenation, the selectivity can partially be tuned toward methanol by utilizing promoters. Li et al. (2015) investigated MnO_x NPs supported on mesoporous Co_3O_4 and found that MnO_x significantly increased the methanol selectivity of Co_3O_4. The active phase of the catalyst after reduction was proposed to be MnO NPs dispersed over grains of Co comprised of a CoO surface with metallic Co cores. The MnO/CoO interface facilitated an activity enhancement toward methanol synthesis compared with the separate Co/Mn NPs and supports. A methanol selectivity of 45% was achieved at relatively mild conditions (4 bar and 250 °C), but the hydrocarbon selectivity was approximately 50%. Mn-doped mesoporous Co_3O_4 spinel has also been shown to be selective toward methanol and significantly increase the methanol formation rate compared to Co_3O_4 (Stangeland et al. 2019). Khan et al. (2016) prepared Pt_3Co and Pt nanocrystals. The Pt_3Co octapods showed the best catalytic activity, which was attributed to both the presence of multiple sharp tips and charge transfer between Pt and Co. This charge transfer enabled the accumulation of negative charges on the Pt atoms in the vertices of the Pt_3Co octapods, which promoted the activation of CO_2.

Duyar et al. (2018) reported a highly active molybdenum phosphide (MoP) catalysts for methanol synthesis. Interestingly, the catalysts showed a stable performance irrespective of the composition of CO and CO_2 in the feed. The most promising catalyst was comprised of CeO_2 promoted MoP supported on K promoted SiO_2 ($K\text{-}SiO_2$). The addition of CeO_2 to the $MoP/K\text{-}SiO_2$ catalyst enhanced the methanol selectivity, while both methane and CO production was inhibited. The effect of the CeO_2 promoter was to block Mo-rich sites that were responsible for the methanation activity.

3 Conclusions and perspectives

CO_2 hydrogenation to methanol is a promising environment-friendly route to produce fuels and chemicals. One of the main obstacles for industrial implementation is developing effective catalysts. Multi-component catalyst systems are required for this process. The interaction between components is essential for high activity and selectivity of CO_2-to-methanol catalysts. This has been demonstrated by numerous catalyst systems comprised of various metals (i.e., Cu, Pd, Ni) and metal oxides (i.e., ZnO, ZrO_2, In_2O_3). These complex systems can contain a mixture of metallic, alloy, and metal oxide phases, which presents challenges in identifying the structure–activity relationship. Therefore, understanding and tailoring the interaction between the different phases is key to develop more active and stable catalysts. The most promising catalyst systems for large-scale industrial processes are currently Cu-based and In-based catalysts due to their superior catalytic performance.

The synergy between Cu and various metal oxides has been well documented, but different and conflicting mechanistic models have been proposed to explain this effect. These include direct effects such as participating in

the reaction through the Cu-metal oxide interface or partial formation of Cu alloy sites. In addition, electronic promotion or increasing the exposure of certain geometrical or structural active Cu sites has been suggested as indirect promotional mechanisms. Identifying effective active site configurations as well as stabilizing the structure is key to enhance the performance of Cu-based catalysts.

For In-based catalysts, the activity can be increased by promotion with suitable metals and metal oxides. Both noble metals and transition metals have been shown to increase the activity of In-based catalysts. It is important to avoid the formation of metal promoter clusters (i.e., Pd), which leads to higher rates of undesired side reactions. Metal oxides can enhance the activity by providing additional sites for CO_2 activation. Further exploration of In-based catalysts could lead to the development of promising industrial CO_2-to-methanol catalysts.

Acknowledgements Open Access funding provided by University Of Stavanger. The authors would like to thank the financial support from the Norwegian Ministry of Education and Research and the Department of Energy and Petroleum Engineering, University of Stavanger, for this project.

References

Álvarez A et al (2017) Challenges in the greener production of formates/formic acid, methanol, and DME by heterogeneously catalyzed CO_2 hydrogenation processes. Chem Rev 117:9804–9838

An B, Zhang J, Cheng K, Ji P, Wang C, Lin W (2017) Confinement of ultrasmall Cu/ZnO_x nanoparticles in metal-organic frameworks for selective methanol synthesis from catalytic hydrogenation of CO_2. J Am Chem Soc 139:3834–3840

Arena F, Italiano G, Barbera K, Bordiga S, Bonura G, Spadaro L, Frusteri F (2008) Solid-state interactions, adsorption sites and functionality of Cu–ZnO/ZrO_2 catalysts in the CO_2 hydrogenation to CH_3OH. Appl Catal A Gen 350:16–23

Bahruji H et al (2016) Pd/ZnO catalysts for direct CO_2 hydrogenation to methanol. J Catal 343:133–146

Bahruji H, Bowker M, Jones W, Hayward J, Esquius JR, Morgan DJ, Hutchings GJ (2017) PdZn catalysts for CO_2 hydrogenation to methanol using chemical vapour impregnation (CVI). Faraday Discuss 197:309–324

Behrens M et al (2012) The active site of methanol synthesis over Cu/ZnO/Al_2O_3 industrial catalysts. Science 336:893–897

Brown NJ et al (2015) From organometallic zinc and copper complexes to highly active colloidal catalysts for the conversion of CO_2 to methanol. ACS Catal 5:2895–2902

Chatterjee R et al (2019) Mapping support interactions in copper catalysts. Top Catal 62:649–659

Chen K et al (2019) CO_2 hydrogenation to methanol over Cu catalysts supported on La-modified SBA-15: the crucial role of Cu–LaO_x interfaces. Appl Catal B Environ 251:119–129

Choi EJ, Lee YH, Lee D-W, Moon D-J, Lee K-Y (2017) Hydrogenation of CO_2 to methanol over Pd–Cu/CeO_2 catalysts. Mol Catal 434:146–153

Chou C-Y, Lobo RF (2019) Direct conversion of CO_2 into methanol over promoted indium oxide-based catalysts. Appl Catal A Gen 583:117144

Didziulis SV, Butcher KD, Cohen SL, Solomon EI (1989) Chemistry of copper overlayers on zinc oxide single-crystal surfaces: model active sites for copper/zinc oxide methanol synthesis catalysts. J Am Chem Soc 111:7110–7123

Duyar MS et al (2018) A highly active molybdenum phosphide catalyst for methanol synthesis from CO and CO_2. Angew Chem Int Ed 57:15045–15050

Fichtl MB et al (2014) Counting of oxygen defects versus metal surface sites in methanol synthesis catalysts by different probe molecules. Angew Chem Int Ed 53:7043–7047

Fiordaliso EM et al (2015) Intermetallic $GaPd_2$ nanoparticles on SiO_2 for low-pressure CO_2 hydrogenation to methanol: catalytic performance and in situ characterization. ACS Catal 5:5827–5836

Frei MS et al (2019) Atomic-scale engineering of indium oxide promotion by palladium for methanol production via CO_2 hydrogenation. Nat Commun 10:1–11

Gao P, Li F, Zhao N, Xiao F, Wei W, Zhong L, Sun Y (2013) Influence of modifier (Mn, La, Ce, Zr and Y) on the performance of Cu/Zn/Al catalysts via hydrotalcite-like precursors for CO_2 hydrogenation to methanol. Appl Catal A Gen 468:442–452

Gao P, Zhong L, Zhang L, Wang H, Zhao N, Wei W, Sun Y (2015) Yttrium oxide modified Cu/ZnO/Al_2O_3 catalysts via hydrotalcite-like precursors for CO_2 hydrogenation to methanol. Catal Sci Technol 5:4365–4377

García-Trenco A, White ER, Regoutz A, Payne DJ, Shaffer MS, Williams CK (2017) Pd_2Ga-based colloids as highly active catalysts for the hydrogenation of CO_2 to methanol. ACS Catal. 7:1186–1196

García-Trenco A, Regoutz A, White ER, Payne DJ, Shaffer MS, Williams CK (2018) PdIn intermetallic nanoparticles for the hydrogenation of CO_2 to methanol. Appl Catal B Environ 220:9–18

Graciani J et al (2014) Highly active copper-ceria and copper-ceria-titania catalysts for methanol synthesis from CO_2. Science 345:546–550

Hartadi Y, Widmann D, Behm RJ (2015) CO_2 hydrogenation to methanol on supported Au catalysts under moderate reaction conditions: support and particle size effects. Chemsuschem 8:456–465

Hengne AM et al (2018) Ni–Sn-supported ZrO_2 catalysts modified by indium for selective CO_2 hydrogenation to methanol. ACS Omega 3:3688–3701

Jiang X, Koizumi N, Guo X, Song C (2015) Bimetallic Pd–Cu catalysts for selective CO_2 hydrogenation to methanol. Appl Catal B Environ 170:173–185

Kandemir T et al (2013) In situ study of catalytic processes: neutron diffraction of a methanol synthesis catalyst at industrially relevant pressure. Angew Chem Int Ed 52:5166–5170

Kasatkin I, Kurr P, Kniep B, Trunschke A, Schlögl R (2007) Role of lattice strain and defects in copper particles on the activity of Cu/

ZnO/Al_2O_3 catalysts for methanol synthesis. Angew Chem Int Ed 46:7324–7327
Kattel S, Ramírez PJ, Chen JG, Rodriguez JA, Liu P (2017) Active sites for CO_2 hydrogenation to methanol on Cu/ZnO catalysts. Science 355:1296–1299
Khan MU et al (2016) Pt_3Co octapods as superior catalysts of CO_2 hydrogenation. Angew Chem Int Ed 55:9548–9552
Kiss AA, Pragt J, Vos H, Bargeman G, De Groot M (2016) Novel efficient process for methanol synthesis by CO_2 hydrogenation. Chem Eng J 284:260–269
Kondrat SA et al (2016) Stable amorphous georgeite as a precursor to a high-activity catalyst. Nature 531:83
Kopač D, Likozar B, Huš M (2019) Catalysis of material surface defects: Multiscale modeling of methanol synthesis by CO_2 reduction on copper. Appl Surf Sci 497:143783
Kühl S, Tarasov A, Zander S, Kasatkin I, Behrens M (2014) Cu-based catalyst resulting from a Cu, Zn, Al hydrotalcite-like compound: a microstructural, thermoanalytical, and in situ XAS study chemistry. Eur J 20:3782–3792
Kuld S, Conradsen C, Moses PG, Chorkendorff I, Sehested J (2014) Quantification of zinc atoms in a surface alloy on copper in an industrial-type methanol synthesis catalyst. Angew Chem Int Ed 53:5941–5945
Kuld S, Thorhauge M, Falsig H, Elkjær CF, Helveg S, Chorkendorff I, Sehested J (2016) Quantifying the promotion of Cu catalysts by ZnO for methanol synthesis. Science 352:969–974
Le Valant A, Comminges C, Tisseraud C, Canaff C, Pinard L, Pouilloux Y (2015) The Cu–ZnO synergy in methanol synthesis from CO_2, Part 1: origin of active site explained by experimental studies and a sphere contact quantification model on Cu+ZnO mechanical mixtures. J Catal 324:41–49
Li C-S et al (2015) High-performance hybrid oxide catalyst of manganese and cobalt for low-pressure methanol synthesis. Nat Commun 6:6538
Li MM-J, Zeng Z, Liao F, Hong X, Tsang SCE (2016) Enhanced CO_2 hydrogenation to methanol over CuZn nanoalloy in Ga modified Cu/ZnO catalysts. J Catal 343:157–167
Li S, Wang Y, Yang B, Guo LJ (2019) A highly active and selective mesostructured Cu/AlCeO catalyst for CO_2 hydrogenation to methanol. Appl Catal A Gen 571:51–60
Liang B et al (2019) Investigation on deactivation of $Cu/ZnO/Al_2O_3$ catalyst for CO_2 hydrogenation to methanol. Ind Eng Chem Res 58(21):9030–9037
Liao F et al (2011) Morphology-dependent interactions of ZnO with Cu nanoparticles at the materials' interface in selective hydrogenation of CO_2 to CH_3OH. Angew Chem Int Ed 50:2162–2165
Liao F et al (2017) A promising low pressure methanol synthesis route from CO_2 hydrogenation over Pd@Zn core–shell catalysts. Green Chem 19:270–280
Ludviksson A, Ernst K, Zhang R, Campbell CJ (1993) The chemisorption of CO on Cu films on ZnO (0001)-O. J Catal 141:380–388
Lunkenbein T, Schumann J, Behrens M, Schlögl R, Willinger MG (2015) Formation of a ZnO overlayer in industrial $Cu/ZnO/Al_2O_3$ catalysts induced by strong metal–support interactions. Angew Chem Int Ed 54:4544–4548
Malik AS, Zaman SF, Al-Zahrani AA, Daous MA, Driss H, Petrov LA (2018) Development of highly selective $PdZn/CeO_2$ and Ca-doped $PdZn/CeO_2$ catalysts for methanol synthesis from CO_2 hydrogenation. Appl Catal A Gen 560:42–53
Martin O, Mondelli C, Curulla-Ferré D, Drouilly C, Hauert R, Pérez-Ramírez J (2015) Zinc-rich copper catalysts promoted by gold for methanol synthesis. ACS Catal 5:5607–5616
Martin O et al (2016) Indium oxide as a superior catalyst for methanol synthesis by CO_2 hydrogenation. Angew Chem Int Ed 55:6261–6265
Martinez-Suarez L, Siemer N, Frenzel J, Marx D (2015) Reaction network of methanol synthesis over Cu/ZnO nanocatalysts. ACS Catal 5:4201–4218
Nakamura J, Nakamura I, Uchijima T, Kanai Y, Watanabe T, Saito M, Fujitani T (1996) A surface science investigation of methanol synthesis over a Zn-deposited polycrystalline Cu surface. J Catal 160:65–75
Natesakhawat S, Lekse JW, Baltrus JP, Ohodnicki PR Jr, Howard BH, Deng X, Matranga C (2012) Active sites and structure–activity relationships of copper-based catalysts for carbon dioxide hydrogenation to methanol. ACS Catal 2:1667–1676
Ojelade OA, Zaman SF (2019) A review on Pd based catalysts for CO_2 hydrogenation to methanol: in-depth activity and DRIFTS mechanistic study. Catal Surv Asia 4:11–37
Polierer S, Jelic J, Pitter S, Studt F (2019) On the reactivity of the Cu/ZrO_2 system for the hydrogenation of CO_2 to methanol: a density functional theory study. J Phys Chem C 123:26904–26911
Prašnikar A, Pavlišič A, Ruiz-Zepeda F, Kovač J, Likozar B (2019) Mechanisms of copper-based catalyst deactivation during CO_2 reduction to methanol. Ind Eng Chem Res 58:13021–13029
Qu J, Zhou X, Xu F, Gong X-Q, Tsang SCE (2014) Shape effect of Pd-promoted Ga_2O_3 nanocatalysts for methanol synthesis by CO_2 hydrogenation. J Phys Chem C 118:24452–24466
Rasmussen P, Holmblad P, Askgaard T, Ovesen C, Stoltze P, Nørskov J, Chorkendorff I (1994a) Methanol synthesis on Cu(100) from a binary gas mixture of CO_2 and H_2. Catal Lett 26:373–381
Rasmussen P, Kazuta M, Chorkendorff I (1994b) Synthesis of methanol from a mixture of H_2 and CO_2 on Cu(100). Surf Sci 318:267–280
Richard AR, Fan M (2017) Low-pressure hydrogenation of CO_2 to CH_3OH using Ni–In–Al/SiO_2 catalyst synthesized via a phyllosilicate precursor. ACS Catal 7:5679–5692
Ro I et al (2016) Role of the $Cu\text{-}ZrO_2$ interfacial sites for conversion of ethanol to ethyl acetate and synthesis of methanol from CO_2 and H_2. ACS Catal 6:7040–7050
Rui N, Wang Z, Sun K, Ye J, Ge Q, Liu C-j (2017) CO_2 hydrogenation to methanol over Pd/In_2O_3: effects of Pd and oxygen vacancy. Appl Catal B Environ 218:488–497
Rungtaweevoranit B, Baek J, Araujo JR, Archanjo BS, Choi KM, Yaghi OM, Somorjai GA (2016) Copper nanocrystals encapsulated in Zr-based metal–organic frameworks for highly selective CO_2 hydrogenation to methanol. Nano Lett 16:7645–7649
Samson K et al (2014) Influence of ZrO_2 structure and copper electronic state on activity of Cu/ZrO_2 catalysts in methanol synthesis from CO_2. ACS Catal 4:3730–3741
Senanayake SD et al (2016) Hydrogenation of CO_2 to methanol on CeO_x/Cu(111) and ZnO/Cu(111) catalysts: role of the metal-oxide interface and importance of Ce^{3+} sites. J Phys Chem C 120:1778–1784
Sharafutdinov I et al (2014) Intermetallic compounds of Ni and Ga as catalysts for the synthesis of methanol. J Catal 320:77–88
Smith PJ et al (2017) A new class of Cu/ZnO catalysts derived from zincian georgeite precursors prepared by co-precipitation. Chem Sci 8:2436–2447
Snider JL et al (2019) Revealing the synergy between oxide and alloy phases on the performance of bimetallic In–Pd catalysts for CO_2 hydrogenation to methanol. ACS Catal 9:3399–3412
Stangeland K, Li H, Yu Z (2018) Thermodynamic analysis of chemical and phase equilibria in CO_2 hydrogenation to methanol, dimethyl ether, and higher alcohols. Ind Eng Chem Res 57:4081–4094
Stangeland K, Kalai DY, Ding Y, Yu Z (2019) Mesoporous manganese-cobalt oxide spinel catalysts for CO_2 hydrogenation to methanol. J CO2 Util 32:146–154
Studt F et al (2014) Discovery of a Ni–Ga catalyst for carbon dioxide reduction to methanol. Nat Chem 6:320

Studt F et al (2015) The mechanism of CO and CO_2 hydrogenation to methanol over Cu-based catalysts. ChemCatChem 7:1105–1111

Tada S, Oshima K, Noda Y, Kikuchi R, Sohmiya M, Honma T, Satokawa S (2019) Effects of Cu precursor types on the catalytic activity of Cu/ZrO_2 toward methanol synthesis via CO_2 hydrogenation. Ind Eng Chem Res 58:19434–19445

Tan Q, Shi Z, Wu D (2018) CO_2 hydrogenation to methanol over a highly active Cu–Ni/CeO_2–nanotube catalyst. Ind Eng Chem Res 57:10148–10158

Triton Market Research (2019) Global methanol market 2019–2027. https://www.tritonmarketresearch.com/reports/methanol-market

Tsang SCE, Meng-Jung Li M, Zou H (2018) Catalyst composition comprising rhodium and indium, preparation methods and use in methanol synthesis and steam reforming. Patent number WO2019/053452A1

Verhelst S, Turner JW, Sileghem L, Vancoillie J (2019) Methanol as a fuel for internal combustion engines. Prog Energy Combust Sci 70:43–88

Vourros A, Garagounis I, Kyriakou V, Carabineiro S, Maldonado-Hódar F, Marnellos G, Konsolakis M (2017) Carbon dioxide hydrogenation over supported Au nanoparticles: effect of the support. J CO2 Util 19:247–256

Wang J et al (2017) A highly selective and stable ZnO–ZrO_2 solid solution catalyst for CO_2 hydrogenation to methanol. Sci Adv 3:e1701290

Wang Y, Kattel S, Gao W, Li K, Liu P, Chen JG, Wang H (2019) Exploring the ternary interactions in Cu–ZnO–ZrO_2 catalysts for efficient CO_2 hydrogenation to methanol. Nat Commun 10:1166

Wu P, Yang B (2017) Significance of surface formate coverage on the reaction kinetics of methanol synthesis from CO_2 hydrogenation over Cu. ACS Catal 7:7187–7195

Wu P, Yang B (2019) Intermetallic PdIn catalyst for CO_2 hydrogenation to methanol: mechanistic studies with a combined DFT and microkinetic modeling method. Catal Sci Technol 9:6102–6113

Wu C, Zhang P, Zhang Z, Zhang L, Yang G, Han B (2017) Efficient hydrogenation of CO_2 to methanol over supported subnanometer gold catalysts at low temperature. ChemCatChem 9:3691–3696

Xu J et al (2016) Methanol synthesis from CO_2 and H_2 over Pd/ZnO/Al_2O_3: catalyst structure dependence of methanol selectivity. Appl Catal A Gen 514:51–59

Yang Y, Evans J, Rodriguez JA, White MG, Liu PJPCCP (2010) Fundamental studies of methanol synthesis from CO_2 hydrogenation on Cu(111), Cu clusters, and Cu/ZnO(000$\bar{1}$). Phys Chem Chem Phys 12:9909–9917

Yang Y, White MG, Liu P (2011) Theoretical study of methanol synthesis from CO_2 hydrogenation on metal-doped Cu(111) surfaces. J Phys Chem C 116:248–256

Ye J, Liu C, Mei D, Ge Q (2013) Active oxygen vacancy site for methanol synthesis from CO_2 hydrogenation on In_2O_3(110): a DFT study. ACS Catal 3:1296–1306

Ye J, Ge Q, Liu C-j (2015) Effect of PdIn bimetallic particle formation on CO_2 reduction over the Pd–In/SiO_2 catalyst. Chem Eng Sci 135:193–201

Yoshihara J, Campbell CT (1996) Methanol synthesis and reverse water–gas shift kinetics over Cu(110) model catalysts: structural sensitivity. J Catal 161:776–782

Zhang M, Dou M, Yu Y (2018) Theoretical study of the promotional effect of ZrO_2 on In_2O_3 catalyzed methanol synthesis from CO_2 hydrogenation. Appl Surf Sci 433:780–789

Zhao F, Gong M, Cao K, Zhang Y, Li J, Chen R (2017) Atomic layer deposition of Ni on Cu nanoparticles for methanol synthesis from CO_2 hydrogenation. ChemCatChem 9:3772–3778

Appendix B Paper II and Supporting Information

Paper II

Thermodynamic Analysis of Chemical and Phase Equilibria in CO_2 Hydrogenation to Methanol, Dimethyl Ether, and Higher Alcohols

Kristian Stangeland, Hailong Li, and Zhixin Yu

Ind. Eng. Chem. Res., 2018, 57, 4081-4094.

DOI: 10.1021/acs.iecr.7b04866

This paper is not in Brage due to the copyright.

Appendix C Paper III and Supporting Information

Paper III

Mesoporous manganese-cobalt oxide spinel catalysts for CO_2 hydrogenation to methanol

Kristian Stangeland, Dori Yosef Kalai, Yi Ding, and Zhixin Yu

Journal of CO_2 Utilization, 2019, 32, 146-154.

Journal of CO_2 Utilization 32 (2019) 146–154

Contents lists available at ScienceDirect

Journal of CO_2 Utilization

journal homepage: www.elsevier.com/locate/jcou

Mesoporous manganese-cobalt oxide spinel catalysts for CO_2 hydrogenation to methanol

Kristian Stangeland[a], Dori Yosef Kalai[a], Yi Ding[b], Zhixin Yu[a,*]

[a] Department of Energy and Petroleum Engineering, University of Stavanger, 4036 Stavanger, Norway
[b] Institute for New Energy Materials & Low-Carbon Technologies, School of Materials Science and Engineering, Tianjin University of Technology, Tianjin 300384, China

ARTICLE INFO

Keywords:
CO_2 hydrogenation
Methanol
Manganese
Cobalt
Spinel

ABSTRACT

The conversion of CO_2 to methanol is seen as a potential environmental benign alternative source of fuel and chemicals. Manganese-cobalt catalyst shows promise for CO_2 hydrogenation to methanol, but its selectivity towards hydrocarbons and other oxygenates needs to be suppressed. In this work, we report the activity of mesoporous manganese-cobalt spinel oxides with different Co/Mn ratios for CO_2 hydrogenation to methanol. The catalysts were thoroughly characterized by N_2 adsorption-desorption, XRD, XPS, TEM, ICP-OES, H_2-TPR, and CO_2-TPD. A significant improvement in methanol selectivity was observed over the manganese doped catalysts compared to the monometallic catalysts. The highest methanol selectivity of 29.8% (reaction conditions: 250 °C, 10 bar, 44, 400 h^{-1}) was obtained with 20 wt.% manganese with a CO2 conversion of 49.1%, resulting in a methanol formation rate of 2280 mg/(g_{cat} h). The enhanced methanol selectivity was attributed to a synergistic effect between cobalt and manganese as well as an increase in surface basicity.

1. Introduction

The conversion of CO_2 into valuable fuels and chemicals has received great attention in recent years to counteract rising atmospheric CO_2 levels and meet the increasing demand for sustainable energy [1–4]. Methanol synthesis from CO_2 is attractive as it has a wide range of applications in the chemical industry (e.g., methanol-to-olefins process) as well as great potential as fuel within the transportation sector [5]. The research on CO_2 hydrogenation to methanol has focused mostly on the classical Cu-based catalysts by using various supports and promoters [6–13]. However, limiting the activity of the reverse water-gas shift reaction and improving the stability of these Cu-based catalysts remain a challenge.

Recently, scientists have discovered several novel catalytic systems that show promise for CO_2 hydrogenation to methanol. A high methanol selectivity was reported for In_2O_3, and the methanol yield further increased for ZrO_2 supported In_2O_3 [14]. The methanol selectivity of these catalysts was maintained even at temperatures up to 300 °C. Similarly, a binary metal oxide ZnO-ZrO_2 catalyst showed a high methanol selectivity at temperatures of 200–320 °C [15]. However, the high methanol selectivity of these bimetallic metal oxide catalysts was compromised by low CO_2 conversions (< 10%). Encouraging results have also been reported for nickel-based catalysts for CO_2 hydrogenation to methanol [16–19]. Superior performance at atmospheric pressure has been reported for Ni_5Ga_3 [16,17] and Ni-In-Al/SiO_2 [18] catalysts compared to a benchmark Cu/ZnO/Al_2O_3 catalyst. Hengne et al. [19] found that Ni-Sn alloy significantly improved the methanol formation rate of $InZrO_2$ with a methanol selectivity of 99%. Enhanced production of methanol from CO_2 hydrogenation has also been achieved with cobalt-based catalysts. Khan et al. [20] found that bimetallic Pt_3Co octapods substantially improved the methanol production compared to monometallic Pt nanocubes and octapods. Li et al. [21] showed that MnO_x supported on mesoporous spinel cobalt oxide were efficient for methanol production at mild pressure, but a range of byproducts were also produced.

One of the interesting aspects of cobalt-based catalysts is its ability to catalyze various CO_2 hydrogenation reactions, including CO_2 methanation [22–26], higher alcohol synthesis [27,28] and methanol synthesis [20,21]. These studies indicate that the selectivity of Co-based catalysts can be strongly influenced by utilizing suitable promoters or supports. Furthermore, the selectivity of the catalyst was also linked to the oxidation state of the surface cobalt species [21,26,28]. The CH_4 selectivity was found to be higher for the reduced Co/SiO_2 catalyst compared to the oxidized catalyst, while the opposite behavior was observed for Co/TiO_2 [26]. Wang et al. [28] found that the alcohol selectivity of a Co-Al hydrotalcite derived catalyst was sensitive to the reduction temperature. This behavior was attributed to changes in surface species, which played a key role in promoting the production of

* Corresponding author.
E-mail address: Zhixin.yu@uis.no (Z. Yu).

https://doi.org/10.1016/j.jcou.2019.04.018
Received 30 January 2019; Received in revised form 17 April 2019; Accepted 22 April 2019
Available online 01 May 2019
2212-9820/

intermediates in the ethanol reaction pathway. Similarly, Li et al. [21] observed that the turn over frequency (TOF) of MnO_x particles dispersed on mesoporous spinel cobalt oxide reduced as the reduction temperature was increased from 250 to 450 °C. The drop in TOF was ascribed to an increase in metallic cobalt at the surface, which is in agreement with that of Pt/Co_3O_4 [27]. Furthermore, close to a 10-fold increase in methanol yield was achieved over MnO_x/Co_3O_4 compared to a Cu/ZnO-based catalysts at similar reaction conditions [21]. Therefore, identifying active structures and tuning the selectivity of Co-based catalysts for CO_2 hydrogenation to methanol is an interesting field of study.

Functionalization of spinel metal oxide nanomaterials has gained increasing interest in multidisciplinary areas including catalysis, photocatalysis, magneto-optical, bio-medical application, and energy storage [29–34]. The properties of spinel metal oxide nanomaterials depend on the cations and their distribution over tetrahedral and octahedral lattice sites. Furthermore, the catalytic properties are also influenced by other factors such as crystallite size, structure, defects, and synthesis method. The structural stability and tunable properties of functionalized spinel metal oxides provides an ideal candidate for investigating cobalt catalysts for the conversion of CO_2 to methanol.

Herein, we report the activity of mesoporous manganese-cobalt oxide spinel catalysts in CO_2 hydrogenation. A series of mesoporous Co_3O_4, MnO_x, and $x MnO_x$-Co_3O_4 (Mn loading x = 10, 20, and 50%) catalysts were prepared by a modified sol-gel inverse micelle method. The Co_3O_4 and MnO_x catalysts produced primarily CH_4 and CO, respectively. The combination of manganese and cobalt significantly increased the methanol selectivity. XRD and XPS indicated that manganese was incorporated into the lattice of Co_3O_4 spinel. The highest methanol selectivity (29.8%) was obtained over the $20MnO_x$-Co_3O_4 catalyst at 250 °C and 20 bar. The superior performance of the $20MnO_x$-Co_3O_4 catalysts was further demonstrated at different reaction conditions.

2. Experimental

2.1. Materials

The chemicals used for catalyst preparation were cobalt(II) nitrate hexahydrate ($Co(NO_3)_2{\cdot}6H_2O$), > 99%, Sigma-Aldrich), manganese(II) nitrate hydrate ($Mn(NO_3)_2{\cdot}H_2O$, > 99.8%, Sigma-Aldrich), 1-butanol (anhydrous, 99.8%, Sigma-Aldrich), HNO_3 (66%, Sigma-Aldrich), ethanol (CH_3CH_2OH, 99%, Sigma-Aldrich), and Poly (ethylene glycol)-block-Poly(propylene glycol)-block-Poly(ethylene glycol) PEO20–PPO70–PEO20 (Pluronic P123).

2.2. Catalyst preparation

The mesoporous catalysts consisting of different manganese/cobalt loadings were prepared by a modified sol-gel inverse micelle method [35]. Briefly, cobalt(II) nitrate hexahydrate and manganese(II) nitrate hydrate were dissolved in a solution containing 1-butanol, HNO_3, and P123 in a 200 ml beaker at room temperature (RT) under magnetic stirring. The obtained clear gel was placed in an oven at 100 °C for 6 h. The resulting powder was crushed, washed several times with ethanol and centrifuged. Finally, the powder was dried in an oven at 100 °C overnight. The dried powders were calcined under flowing synthetic air at 150 °C for 12 h, 250 °C for 4 h, and 350 °C for 2 h with a heating rate of 2 °C/min to the designated temperature. Supplementary Table S1 shows the detailed amount of chemicals used for the synthesis of each catalyst.

2.3. Catalyst characterization

Crystallographic information of the catalysts was obtained by X-ray diffraction (XRD). XRD patterns were recorded on a Bruker-AXS Microdiffractometer (D8 ADVANCE) using a Cu Kα radiation source (λ = 1.5406 Å, 40 kV, and 40 mA). The XRD patterns were obtained at 2θ of 10-90° with a step interval of 2°/min. The peaks were indexed according to the Joint Committee on Powder Diffraction Standards (JCPDS) database.

Nitrogen adsorption-desorption measurements were conducted at 77 K on a Micromeritics TriStar II surface area and porosity analyzer, after degassing under vacuum at 120 °C for 8 h using a sample degas system (Micromeritics VacPrep 061). Specific surface area and pore size distribution were calculated by Brunauer-Emmett-Teller (BET) and Barrett-Joyner-Halenda (BJH) methods, respectively.

The microstructures and morphology of the catalysts were characterized by transmission electron microscopy (TEM) with a JEOL JEM-2100 F instrument operating at 200 kV.

The elemental composition of the samples was measured by inductively coupled plasma optical emission spectrometry (ICP-OES, PerkinElmer OPTIMA 4300 DV). For ICP analysis, approximately 50 mg of the sample was dissolved in aqua regia. Then 10 mL of the diluted solution was mixed with 240 mL of de-ionized water and analyzed.

X-ray photoelectron spectroscopy (XPS) analysis was performed on the ESCALAB 250 Xi (Thermo Scientific) XPS system utilizing a monochromatic Al Kα source (1486.6 eV). High-resolution spectra were obtained at a pass energy of 30.0 eV, step size of 0.1 eV, and dwell time of 500 ms per step. All spectra were referenced to the C 1 s peak (284.8 eV).

Temperature programmed reduction (H_2-TPR) study of the calcined catalysts was performed on a Micromeritics Autochem II ASAP 2920. The sample was first pretreated at 200 °C in He flow for 30 min A 7% H_2/Ar mixture at 50 mL/min was used while the temperature was ramped from ambient to 700 °C at 10 °C/min. The same instrument was used to perform temperature programmed desorption of CO_2 (CO_2-TPD). First, the sample was heated to 200 °C in He flow for 30 min, reduced at 250 °C for 30 min, and purged with He as the temperature was reduced to 80 °C. Thereafter, a 6% CO_2/He mixture passed over the catalyst for 15 min, and followed by purging in He for 30 min. Finally, CO_2-TPD was performed from 50 to 700 °C at a ramp rate of 10 °C/min.

2.4. Catalytic activity study

CO_2 hydrogenation to methanol was carried out in a custom built fixed-bed continuous-flow reactor. The catalyst powder (50 mg) mixed with alpha alumina (500 mg) was placed in a stainless tube reactor with an internal diameter of 0.5 cm and a length of 50 cm. Prior to testing, the catalysts were reduced in-situ in a flow of 10% H_2/N_2 at 100 ml/min with a heating rate of 2 °C/min. The system was then pressurized to the desired operating pressure with the reactant gas ($CO_2/H_2/N_2$ = 1/3/1). All post-reactor lines and valves were heated to 140 °C to avoid product condensation. Products were analyzed via on-line gas chromatography using an Agilent 7890 B system fitted with two TCD detectors. Nitrogen was used as an internal standard for calculating the CO_2 conversion and product selectivity.

3. Results

3.1. Catalyst characterization

3.1.1. XRD study

Fig. 1 shows the XRD patterns of the catalysts after calcination. The pure manganese oxide showed a complex diffraction pattern, where the most intense peaks correspond to crystalline Mn_3O_4 (JCPDS 80-0382). The additional peaks indicate that other phases such as MnO_2 and Mn_2O_3 were present. For the pure cobalt oxide sample, only diffraction peaks attributed to cubic Co_3O_4 phase (JCPDS 74-1657) could be identified. No obvious change in diffraction pattern was detected for $10MnO_x$-Co_3O_4 and $20MnO_x$-Co_3O_4 compared to Co_3O_4. However, there was a small shift in the peak positions, indicating manganese

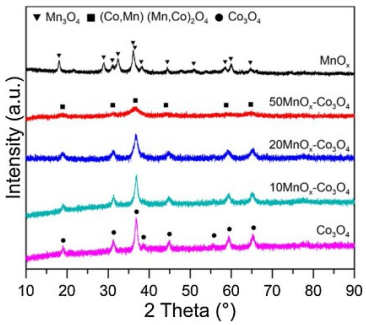

Fig. 1. XRD patterns of Co_3O_4, MnO_x, and MnO_x-Co_3O_4 catalysts after calcination.

incorporation into the face-centered cubic structure of spinel type. The peaks of the $50MnO_x$-Co_3O_4 catalyst were broadened and their intensity significantly decreased compared to the other catalysts. Additionally, a notable shift can be seen in peak positions towards lower diffraction angles. The signal can be ascribed to structured (Co, Mn)(Mn, Co)$_2O_4$ spinel (JCPDS 018-0410), which has been reported to exhibit a broad diffraction peak around 36.5° [36,37]. No additional diffraction peaks were detected for the bimetallic catalysts, indicating high phase purity. Spinel (Co, Mn)(Mn, Co)$_2O_4$ is a mixed valence ternary oxide, where the cobalt and manganese ions in its crystal structure are dispersed over tetrahedral and octahedral stacking interstices as demonstrated in Figure S1.

The crystallite size of the catalysts was calculated according to the Scherrer equation, and the results are summarized in Table 1. It can be seen that the crystallite size decreased with an increase in manganese loading. The crystallite sizes of $50MnO_x$-Co_3O_4 and $20MnO_x$-Co_3O_4 were 8 and 10 nm, respectively, while the other catalysts exhibited comparable crystallite sizes in the range of 13–14 nm.

3.1.2. N_2 adsorption-desorption study

The porous structure of the catalysts was examined by N_2 adsorption-desorption experiments. The N_2 adsorption-desorption isotherms and the pore size distribution of the calcined catalysts are shown in Figure S2 (a) and (b). The resulting data are summarized in Table 1. The isotherm of all catalysts were of type IV, indicating mesoporous structure. The surface area of the catalysts was found to correlate with the crystallite size, where a smaller crystallite size resulted in a higher surface area. The Co_3O_4, $10MnO_x$-Co_3O_4 and MnO_x samples exhibited comparable surface area in the range of 54-60 m^2/g. The surface area increased to 106 m^2/g and 197 m^2/g for the $20MnO_x$-Co_3O_4 and $50MnO_x$-Co_3O_4 catalysts, respectively. A similar trend was also observed for the average pore size, which reduced with a decrease in crystallite size. The catalysts also possessed a high pore volume in the range of 0.20-0.31 cm^3/g.

Table 1
Crystallite size from XRD and N_2 adsorption-desorption results of the catalysts.

Catalyst	d_{XRD} (nm)	BET surface area (m^2/g)	Pore size (nm)	Pore volume (cm^3/g)
Co_3O_4	14	56	13.7	0.27
$10MnO_x$-Co_3O_4	13	54	9.5	0.21
$20MnO_x$-Co_3O_4	10	106	7.9	0.31
$50MnO_x$-Co_3O_4	8	197	4.4	0.24
MnO_x	14	60	10.3	0.20

3.1.3. TEM characterization

The morphology of the catalysts was characterized by TEM. The TEM images are presented in Fig. 2 (a)-(e) and all images are recorded at the same magnification. As can be seen, the catalysts consisted of nanoparticle aggregates with a narrow particle size distribution. The average particle sizes calculated statistically from the TEM images were found to be close to the crystallite sizes obtained from XRD.

3.1.4. ICP-OES and XPS studies

The ICP-OES analysis was conducted to analyze the elemental composition of the bimetallic oxide catalysts. The nominal composition of bimetallic oxides and the measured compositions are summarized in Table S2. It can be seen that the measured values are close to the nominal values.

XPS was employed to analyze the surface composition of the bimetallic catalysts. The Co 2p and Mn 2p regions are presented in Fig. 3 (a) and (b), respectively. For the Co 2p spectra (Fig. 3a), two spin-orbit doublets, corresponding to Co $2p_{1/2}$ and Co $2p_{3/2}$, and two shakeup satellite peaks were obtained. The Co $2p_{3/2}$ and Co $2p_{1/2}$ main peaks were consistently fitted with three peaks, according to Biesinger et al. [38]. These three fitted peaks do not correspond to different valence states of Co. The shape and position of the satellite peaks however, particularly the Co $2p_{3/2}$ satellite peak, are widely used to identify the valence state of Co [39–42]. The Co $2p_{3/2}$ satellite peaks consists of Co^{2+} and Co^{3+}, located at binding energies of ~786 eV and ~789 eV, respectively. To qualitatively assess the Co^{2+}/Co^{3+} fraction of the catalysts, the ratio of Co^{2+} $2p_{3/2}$ satellite peak area to the area of the Co^{3+} $2p_{3/2}$ satellite peak was calculated. This is denoted as $(Co^{2+}/Co^{3+})_{ss}$ and summarized in Table 2. It should be noted that there is no evidence for a linear correlation between the satellite peak areas of Co^{2+}/Co^{3+} and the absolute Co^{2+}/Co^{3+} ratio. However, it has been shown that a higher intensity of the Co^{2+} satellite arises from a higher Co^{2+} content, and similarly for the Co^{3+} satellite [42]. It was found that the $(Co^{2+}/Co^{3+})_{ss}$ ratio of $10MnO_x$-Co_3O_4 and $20MnO_x$-Co_3O_4 were relatively close to the reference ratio of Co_3O_4 at 1.16 and 0.93, respectively [38]. The calculated $(Co^{2+}/Co^{3+})_{ss}$ value for $50MnO_x$-Co_3O_4 was 2.25, indicating that a larger fraction of Co^{2+} was present.

The Mn 2p spectrum was resolved into two spin-orbit doublets, i.e., Mn $2p_{1/2}$ and Mn $2p_{3/2}$, with binding energies centered at 641.7 eV and 653.4 eV (Fig. 3b). Determining the contribution of different Mn species is difficult due to multiplet splitting of the Mn^{2+}, Mn^{3+} and Mn^{4+} valance states [38,43]. Therefore, no attempt at fitting the Mn 2p spectra was performed. The position and shape of Mn $2p_{1/2}$ and Mn $2p_{3/2}$ are close to those of $MnCo_2O_4$ [37,44] and $CoMn_2O_4$ [45] reported in literature. It can also be seen from Table 2 that the Co $2p_{1/2}$ and Co $2p_{3/2}$ peaks shifted towards slightly higher binding energy with increased manganese loading, which is consistent with the reported data for mixed Co-Mn oxide spinel [37,44,45].

The O1 s region of the bimetallic catalysts is shown in Figure S3. The spectra were deconvoluted into three peaks corresponding to O^{2-} (529.9–530 eV), OH^- (531.0–531.6), and H_2O (532.6–533.6) [38, HYPERLINK \l "Ref43" \o " [43] M. Oku, J. of Solid State Chem. 23 (1978) 177-185. https://doi.org/10.1016/0022-4596(78)90063-4" \h 38/43]. The full width at half maximum (FWHM) of the fitted O^{2-} peaks are slightly higher than that reported for monometallic cobalt and manganese oxides. This is probably because both Co-O and Mn-O species are present and these species have slightly different binding energies. Nevertheless, the position of the fitted peaks are within the range of the reported values of cobalt and manganese oxides. The high-energy tail may originate from different configurations of H_2O, such as physisorbed, chemisorbed and structural H_2O [43].

Cations in spinel are located in two different sites: tetrahedral sites [A] sites and octahedral [B] sites (Figure S1). In the normal distribution of spinel, divalent ions are located on the tetrahedral sites, while trivalent ones on the octahedral sites. The situation is the opposite in the inverse distribution, and most spinels have partially inversed structures.

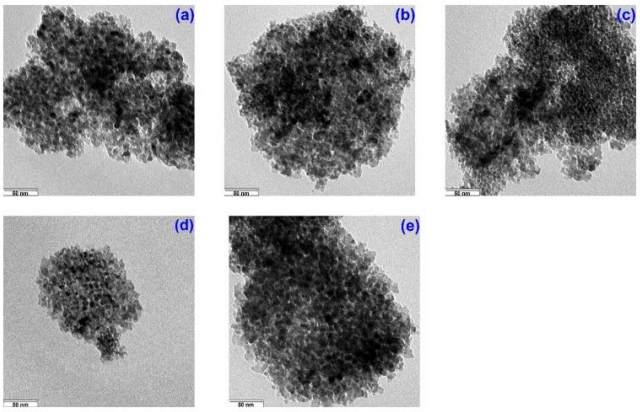

Fig. 2. TEM images for mesoporous (a) Co_3O_4, (b) $10MnO_x$-Co_3O_4, (c) $20MnO_x$-Co_3O_4, (d) $50MnO_x$-Co_3O_4, and (e) MnO_x after calcination.

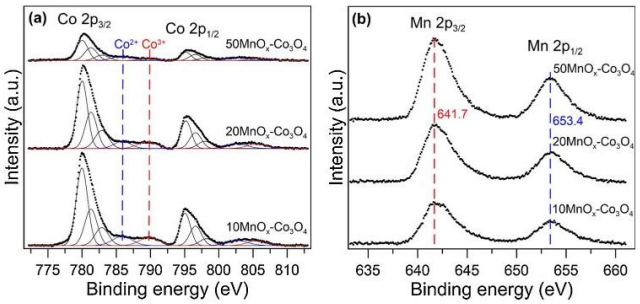

Fig. 3. High-resolution XPS spectra of the (a) Co 2p and (b) Mn 2p regions for the bimetallic catalysts.

The distribution of cations between the sites is influenced by their structural and redox properties, but can also be affected by the preparation conditions [44,46]. XPS is not suitable to identify the fraction of manganese and cobalt positioned in the octahedral and tetrahedral sites. However, we propose from the XPS analyses that the Co and Mn are incorporated into a mixed oxide spinel phase. This is based on the following observations: (1) the significant change in $(Co^{2+}/Co^{3+})_{ss}$ for 50MnOx-Co_3O_4 without notable change in the fitting parameters of the main Co 2p peaks; (2) the slight shift of the Co 2p peak positions to higher binding energy with increasing Mn loading; (3) the shape and peak positions of the Mn 2p peaks comparable to that reported for $MnCo_2O_4$ and $CoMn_2O_4$; and (4) consistency with the crystalline phase detected by XRD.

3.1.5. H_2-TPR study

The H_2-TPR study was carried out to investigate the effect of manganese on the reducibility of the catalysts. The H_2-TPR profiles of the catalysts are shown in Fig. 4. For Co_3O_4, the reduction proceeded via two steps. The first step at 264 °C is the reduction of Co_3O_4 to CoO, followed by the second step at 347 °C where CoO is reduced to metallic cobalt. The intensity of the first peak was lower than the second peak, which is in accordance with the stepwise reduction behavior of fine Co_3O_4 particles [34]. The TPR profile of MnO_x displayed two main peaks located at 279 °C and 426 °C. The low-temperature peak can be attributed to the reduction of Mn^{3+} ion located in tetrahedral sites, and the wide signal at high temperature corresponds to the reduction of Mn_3O_4 to MnO [47]. The bimetallic MnO_x-Co_3O_4 catalysts showed

Table 2
Surface atomic composition, binding energies, and area raio of Co^{2+}/Co^{3+} O_I/O_{II} for the MnO_x-Co_3O_4 catalysts.

Catalyst	Surface atomic composition (%)		Binding energy (eV)				$(Co^{2+}/Co^{3+})_{ss}$
	Co	Mn	Co $2p_{3/2}$	Co $2p_{1/2}$	Mn $2p_{3/2}$	Mn $2p_{1/2}$	
$10MnO_x$-Co_3O_4	84.7	15.3	780.0	795.1	641.6	653.3	1.16
$20MnO_x$-Co_3O_4	78.2	21.8	780.1	795.3	641.7	653.5	0.93
$50MnO_x$-Co_3O_4	44.5	55.5	780.3	795.6	641.7	653.4	2.25

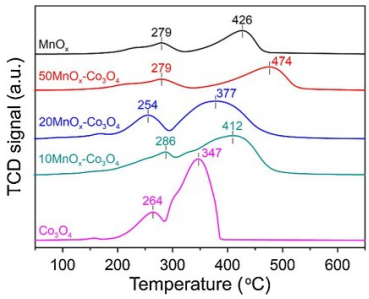

Fig. 4. H_2-TPR profiles of the mesoporous Co_3O_4, MnO_x, and MnO_x-Co_3O_4 catalysts.

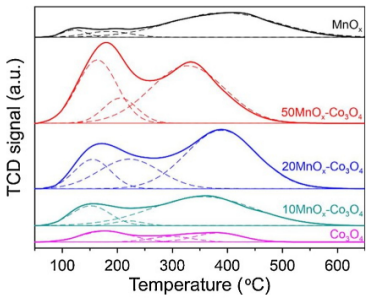

Fig. 5. CO_2-TPD profiles of the mesoporous Co_3o_4, MnO_x, and MnO_x-Co_3O_4 catalysts.

similar reduction patterns as the monometallic oxides. For the $10MnO_x$-Co_3O_4 sample, both main reduction peaks shifted towards higher temperatures compared to Co_3O_4 (286 °C and 412 °C). The reducibility of $20MnO_x$-Co_3O_4 was better than $10MnO_x$-Co_3O_4 with reduction peaks at 254 °C and 377 °C. The profile of $50MnO_x$-Co_3O_4 was similar to the pattern of MnO_x, displaying a low-temperature band at 279 °C and a broad peak at 474 °C. The high temperature of the second reduction band suggests higher stability of the metal oxide species.

To further assess the reducibility of the catalysts, the total H_2-consumption of the catalysts during TPR study was calculated and the values are summarized in Table 3. As can be seen, the Co_3O_4 sample had the highest H_2 consumption during TPR measurements. Increasing the manganese loading resulted in a decrease in overall reducibility. The MnO_x sample contained the least amount of reducible species. Recent reports on Mn-Co catalysts differ in their findings regarding the synergistic effect between manganese and cobalt on the reducibility. Tang et al. [36] found that manganese promoted the reduction of cobalt for porous Mn-Co mixed oxide nanorods (Mn:Co = 1:1). On the other hand, Liu et al. [34] found no correlation between manganese loading and Co_3O_4 reducibility for mesoporous manganese doped Co_3O_4. In this work, the introduction of manganese into the spinel structure of Co_3O_4 resulted in a decrease in reducibility and a higher reduction temperature was required to fully reduce the cobalt species.

3.1.6. Temperature programed CO_2 desorption analysis

Fig. 5 shows the CO_2 desorption profiles of the catalysts. The profiles were deconvoluted into three Gaussian peaks (dotted curves), corresponding to weak- (denoted as α), medium- (denoted as β) and strong basic sites (denoted as γ). The Co_3O_4 sample consisted of a combination of α-, β- and γ-basic sites, while the MnO_x sample mainly exhibited γ-basic sites. The incorporation of manganese into the spinel structure of Co_3O_4 significantly enhanced the surface basicity of the catalyst. Furthermore, an increase in total basicity can be inferred with increasing manganese loading. This can be partially attributed to the manganese concentration at the surface, but also to the increase in surface area. It can be observed that the deconvoluted peaks are located at different temperatures, which indicates that the catalysts possess different basic site strength.

The basicity of the catalysts was also evaluated by calculating the integral of each deconvoluted peak. The total basicity and the contribution of different basic sites and their peak temperatures are summarized in Table 3. It can be seen that the total basicity was relatively low for the monometallic catalysts, but strongly increased with the addition of 10% manganese. Increasing the manganese loading from 10% to 20% also resulted in a substantial increase in basicity, while only a mild increase occurred upon further addition of manganese to 50%.

3.2. Catalytic activity

3.2.1. The effect of manganese loading

The catalytic activity of the catalysts was compared at 250 °C, 10 bar, CO_2/H_2 = 3/1, and gas hourly space velocity (GHSV) of 88 800 h^{-1}. The CO_2 conversion and product selectivity are summarized in Table 4. Figure S4 shows the CO_2 conversion and product selectivity over 24 h time on stream (TOS). As the catalysts remained relatively stable, the average values were used for comparison. The highest CO_2 conversion of 56.5% was obtained over the Co_3O_4 sample, whereas the MnO_x catalyst had a CO_2 conversion of 2.9%. The CO_2 conversion was lower over the bimetallic catalysts compared to Co_3O_4 and followed the order $20MnO_x$-Co_3O_4 (45.1%) > $10MnO_x$-Co_3O_4 (36.9%) > $50MnO_x$-Co_3O_4 (19.8%). The catalytic activity of spinel depends mainly on the cations occupying the octahedral sites as these are exposed at the surface [44]. As the MnO_x showed very low CO_2 conversion, the decrease in CO_2 conversion for manganese containing catalysts is likely due to substitution of octahedrally coordinated cobalt by manganese. The difference in CO_2 conversion between the $20MnO_x$-Co_3O_4 and $10MnO_x$-Co_3O_4 can be explained by the significant difference in surface area.

Table 3
The H_2-consumption during H_2-TPR study, and the distribution of basic sites determined from CO_2-TPD over Co_3O_4, MnO_x, and MnOx-Co_3O_4 catalysts.

Catalyst	H_2-consumption (mmol/g_{cat})	Total number of basic sites (μmol/g_{cat})	Number of basic sites (μmol /g) and their peak desorption temperature (°C)		
			Site α	Site β	Site γ
Co_3O_4	182	1.2	0.5 (179)	0.2 (297)	0.4 (383)
$10MnO_x$-Co_3O_4	168	3.8	0.8 (152)	0.1 (219)	2.9 (354)
$20MnO_x$-Co_3O_4	159	7.0	1.1 (154)	1.8 (223)	4.1 (386)
$50MnO_x$-Co_3O_4	104	7.5	2.5 (163)	0.8 (206)	4.2 (327)
MnO_x	56	2.9	0.2 (122)	0.2 (184)	2.5 (389)

Table 4
CO_2 conversion and product selectivity over different catalysts after reduction at 250 °C (reaction conditions: T = 250 °C, P = 10 bar, gas flow ($CO_2/N_2/H_2$) = 20/20/60 mL/min, GHSV = 88 800 h^{-1}).

Catalyst	X(CO_2) (%)	S(CH_4) (%)	S(CH_3OH) (%)	S(CO) (%)	S(C_2H_4) (%)	S(C_{3+} HC) and S(C_{2+} oxygenates)
Co_3O_4	56.5	94.8	2.3	1.0	1.8	Traces
10MnO_x-Co_3O_4	36.9	81.1	12.0	3.4	3.5	Traces
20MnO_x-Co_3O_4	45.1	71.1	22.1	3.2	3.6	Traces
50MnO_x-Co_3O_4	19.8	76.7	12.7	9.1	1.5	0
MnO_x	2.9	27.2	2.4	70.2	0.2	0

The main products detected during catalytic testing were CH_4, CH_3OH, CO, and C_2H_4, while only traces of C_{3+} hydrocarbons and C_{2+} oxygenates were observed. The monometallic catalysts showed very low methanol selectivity. The Co_3O_4 produced almost exclusively CH_4 (94.9%) and minor amounts of CH_3OH, CO, and C_2H_4. The CO and CH_4 selectivity over the MnO_x catalyst was 70.4% and 27.2%, respectively. A significant enhancement in methanol selectivity was observed for the bimetallic catalysts. This suggests that a synergistic effect between cobalt and manganese is responsible for the methanol production. The increase in methanol selectivity could also be related to the improvement in surface basicity for the bimetallic catalysts, as shown in the CO_2-TPD study. An improvement in methanol selectivity with increasing basicity has also been demonstrated for Cu based catalysts [1,3]. The 20MnO_x-Co_3O_4 catalyst showed the highest selectivity to methanol at 22.1%, while the methanol selectivity over 10MnO_x-Co_3O_4 and 50MnO_x-Co_3O_4 was 12.0% and 12.7%, respectively. An increase in CO selectivity was also observed for the bimetallic catalysts, and the 50MnO_x-Co_3O_4 exhibited the highest CO selectivity (9.1%). The C_2H_4 selectivity was slightly higher for 10MnO_x-Co_3O_4 and 20MnO_x-Co_3O_4 compared to that obtained over the Co_3O_4 and 50MnO_x-Co_3O_4 catalysts.

The turnover frequency (TOF) was calculated to compare the activity of the catalysts. The TOF was calculated from BET surface areas and known surface packing densities of cubic (space group Fm-3 m) CoO [21]. The presence of manganese at the surface was neglected as the MnO_x showed very low CO_2 conversion. Fig. 6 (a) shows the TOF for CO_2 conversion as a function of manganese surface content. The maximum TOF was obtained for the Co_3O_4 catalyst. A linear decline in TOF can be observed with increasing manganese surface concentration. Correlation of the TOF with the particle size estimated from XRD is depicted in Fig. 6 (b). It can be seen that the TOF increased with particle sizes. This is consistent with the particle size effect reported for supported cobalt catalyst for CO_2 hydrogenation and Fischer-Tropsch (FT) synthesis [24,48].

The effect of manganese loading (0, 10, 20, 50, and 100%) on the formation rate of methanol is shown in Figure S5. Compared to Co_3O_4 (403 mg/(g_{cat} h)), a significant increase in methanol formation rate to 3106 mg/(g_{cat} h) was obtained over the 20MnO_x-Co_3O_4 catalyst. The 10MnO_x-Co_3O_4 and 50MnO_x-Co_3O_4 catalysts achieved a methanol formation rate of 1374 and 705 mg/(g_{cat} h), respectively.

3.2.2. The effect of reaction temperature

The effect of temperature on CO_2 conversion and product selectivity was investigated over the 10MnO_x-Co_3O_4 and 20MnO_x-Co_3O_4 catalysts, and the results are presented in Fig. 7 (a) and (b). As the catalysts remained relatively stable over 24 h (Figure S4), the temperature was increased stepwise from 200 to 280 °C. The temperature in each step was maintained for 2 h, and the average values were used to calculate the CO_2 conversion and product selectivity. As can be seen, both catalysts exhibit similar trends in CO_2 conversion and product selectivity. A gradual increase in CO_2 conversion was observed as the temperature was elevated. The methanol selectivity showed a volcano-shaped trend, where the maximum was located at about 250 °C. The opposite trend occurred for the CH_4 selectivity, which first declined to the minimum at 250 °C and then gradually increased. In addition, the C_2H_4 and CO selectivity slightly increased with temperature. The change in product selectivity with temperature can be explained by the thermodynamics of the reactions involved and the competing effect. The CO_2 methanation reaction is only mildly affected at these temperatures while the rWGS reaction becomes more favorable as the temperature is increased. On the other hand, methanol synthesis from CO_2 generally suffers at temperatures above 250 °C.

3.2.3. The effect of reaction pressure

The influence of reaction pressure on the CO_2 conversion and the product selectivity was investigated over the 10MnO_x-Co_3O_4 and 20MnO_x-Co_3O_4 catalysts at 10–20 bar, and the results are shown in Fig. 8 (a) and (b), respectively. High reaction pressure is beneficial for the selective hydrogenation of CO_2 to methanol, which is controlled by the kinetics and thermodynamics of CO_2 hydrogenation [3]. The CO_2 conversion and the methanol selectivity increases with pressure over both catalysts. The highest methanol selectivity of 28.2% was achieved over 20MnO_x-Co_3O_4 at 20 bar, while it was 19.1% over the 10MnO_x-Co_3O_4 catalyst. The selectivity for the undesired byproducts, namely CH_4 and CO, was found to decrease with pressure over the catalysts. Therefore, the methanol synthesis reaction is more sensitive to pressure

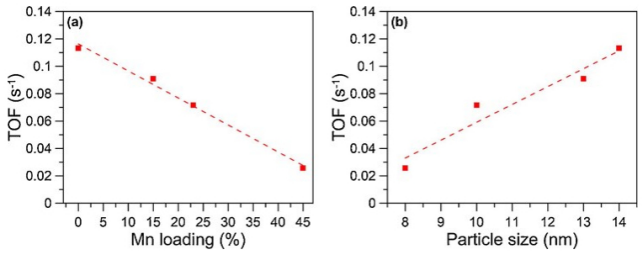

Fig. 6. (a) TOF for CO_2 conversion as a function of manganese surface concentration and (b) spinel oxides particle size.

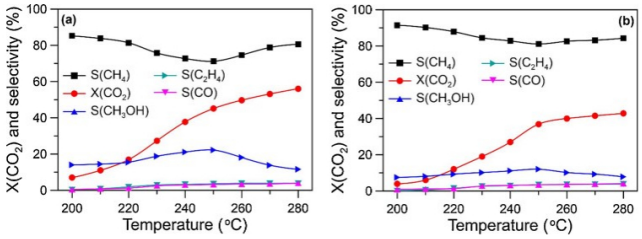

Fig. 7. Effect of temperature over (a) $10MnO_x$-Co_3O_4 and (b) $20MnO_x$-Co_3O_4 (reaction conditions: P = 10 bar, gas flow ($CO_2/N_2/H_2$) = 20/20/60 mL/min, GHSV = 88 800 h^{-1}).

than the CO_2 methanation reaction. A decrease in CO selectivity with pressure is expected as the rWGS reaction is independent of the reaction pressure. The methanol formation rate (Figure S6) increased more strongly with pressure over the $20MnO_x$-Co_3O_4 catalyst, which indicates a larger quantity of methanol synthesis active sites.

3.2.4. The effect of gas hourly space velocity

The effect of GHSV was investigated over the MnO_x-Co_3O_4 catalysts. A fixed amount of catalyst (50 mg) was used while the flow rate was varied to achieve different GHSV in the range of 44 400 to 177 800 h^{-1}. The CO_2 conversion and product selectivity over the $10MnO_x$-Co_3O_4 and $20MnO_x$-Co_3O_4 catalysts are presented in Fig. 9 (a) and (b). The GHSV had a similar effect on CO_2 conversion and product selectivity over both catalysts. The CO_2 conversion decreased approximately linearly with increasing GHSV, as expected. Increasing the GHSV resulted in a higher CO selectivity and lower C_2H_4 selectivity. In addition, the methanol selectivity decreased and a slight increase in CH_4 selectivity occurred when the GHSV was increased. The methanol selectivity was more strongly affected by the GHSV for the $20MnO_x$-Co_3O_4 (Fig. 9 b), and the highest methanol selectivity of 29.8% was achieved at a GHSV of 44 400 h^{-1}. The results obtained over the $50MnO_x$-Co_3O_4 catalyst is shown in Figure S7 and exhibited similar behavior.

3.2.5. The effect of reduction temperature

Previous reports on cobalt-based catalysts for CO_2 hydrogenation have indicated that the activity and selectivity were greatly affected by the oxidation state of the cobalt phases [21,26,28]. The influence of the surface oxidation degree was investigated by pretreating the MnO_x-Co_3O_4 catalysts at different reduction temperatures. Table 5 shows the CO_2 conversion and product selectivity obtained after reduction at temperatures of 200–300 °C. All catalysts exhibited less than 5% CO_2 conversion after reduction at 200 °C, which was attributed to the low reduction degree of the catalysts [49]. The CO selectivity was also significantly higher, particularly for the $50MnO_x$-Co_3O_4. Interestingly, only traces of methanol could be detected over all catalysts. This indicates that the active sites for methanol synthesis are generated during reduction at higher temperatures than 200 °C.

Increasing the reduction temperature enhanced the CO_2 conversion of all catalysts. The reduction conditions had a similar effect on the product selectivity of the catalysts. The CH_4 selectivity increased with an increase in reduction temperature, which is likely due to a higher concentration of metallic cobalt or partially reduced cobalt species [21,27]. The opposite trend was observed for the CO selectivity, which was dramatically reduced after reduction at 250 °C compared to 200 °C. On the other hand, the methanol selectivity first increased and then declined with the increase in reduction temperature, whereas the C_2H_4 selectivity remained approximately constant. These results illustrate that the product selectivity of the MnO_x-Co_3O_4 catalysts is closely related to the oxidation state of the surface species.

4. Discussion

The change in activity and product selectivity for manganese doped Co_3O_4 indicates that the catalytic properties of cobalt have been altered with the introduction of manganese into the spinel structure. This has been shown to influence the oxidation states and textural properties relative to their monometallic spinel counterparts. Furthermore, it can lead to partial disorder of the spinel structure, affecting the catalytic properties [44]. It has also been reported that the lower activity of smaller Co particles is caused by a greater susceptibility to oxidation [24]. This might explain the observed drop in TOF for smaller particles (Fig. 6b). However, the drop in TOF might also be due to increased oxidation degree of cobalt species when manganese is present. An altercation of cobalt oxidation state could also be partially responsible for the differences in product selectivity [21,26,28].

The active phase of mesoporous Co_3O_4 supported MnO_x after

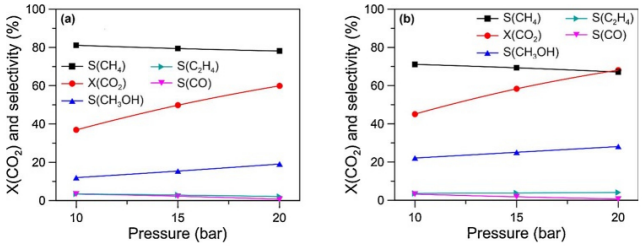

Fig. 8. Effect of pressure over (a) $10MnO_x$-Co_3O_4 and (b) $20MnO_x$-Co_3O_4 (reaction conditions: T = 250 °C, gas flow ($CO_2/N_2/H_2$) = 20/20/60 mL/min, GHSV = 88 800 h^{-1}).

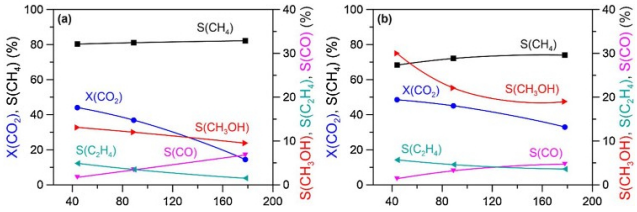

Fig. 9. Effect of GHSV over (a) $10MnO_x$-Co_3O_4 and (b) $20MnO_x$-Co_3O_4 catalysts (reaction conditions: T = 250 °C, P = 10 bar, CO_2/H_2 = 1:3).

Table 5
CO_2 conversion and product selectivity at different reduction temperatures (reaction conditions: T = 250 °C, P = 10 bar, gas flow ($CO_2/N_2/H_2$) = 20/20/60 mL/min, GHSV = 88 800 h^{-1}).

Catalyst	Reduction temperature (°C)	X(CO_2) (%)	S(CH_4) (%)	S(CH_3OH) (%)	S(CO) (%)
$10MnO_x$-Co_3O_4	200	3.9	72.7	Traces	24.9
	250	36.9	81.1	12.0	3.4
	300	40.8	87.1	7.5	2.1
$20MnO_x$-Co_3O_4	200	5.0	72.3	Traces	24.8
	250	45.1	71.1	22.1	3.2
	300	47.4	82.1	14.8	2.3
$50MnO_x$-Co_3O_4	200	3.4	36.7	Traces	63.1
	250	19.8	76.7	12.7	9.1
	300	30.3	87.3	4.7	7.3

reduction was proposed to be MnO nanoparticles (NPs) dispersed over grains of cobalt comprised of a CoO surface with metallic cobalt cores. The MnO/CoO interface facilitated an activity enhancement towards methanol synthesis compared with the separate Co/Mn NPs and supports [21]. Li et al. [21] suggested that the MnO_x NPs helped reduce CO_2 to CO species, which could further react with surface layer CoO to form methanol. We speculate that the reaction mechanism over our catalysts follows a similar pathway. Due to the high CO selectivity of MnO_x, manganese species located at octahedral sites are probably responsible for CO formation. Subsequently, these CO species can be converted to methanol on octahedral cobalt cations or interfacial Co-Mn sites. This would also explain the high CO selectivity of the $50MnO_x$-Co_3O_4 catalyst, which has less cobalt active sites for methanol synthesis due to the high manganese surface content. The increase in CO selectivity at high GHSV further suggests that CO might be an intermediate in the methanol reaction pathway.

Cobalt catalysts are widely used in FT synthesis from syngas but performs as a methanation catalyst upon switching to CO_2/H_2 gas mixtures [26,50]. Therefore, the high methane selectivity of the MnO_x-Co_3O_4 catalysts in this study can be attributed to the Co phase. With regards to other byproducts, the Co_3O_4 had a combined C_{2+} selectivity of less than 2%, which mainly consisted of C_2H_4 (1.8%). A mild increase was observed for manganese doped samples. The combined selectivity towards C_{2+} hydrocarbons and other oxygenates was about 4% for $10MnO_x$-Co_3O_4 and $20MnO_x$-Co_3O_4. The higher C_2H_4 selectivity of manganese doped Co_3O_4 was likely a result of the CO species generated at octahedrally coordinated manganese sites, which to some extent also promote chain growth. Compared to Co_3O_4 supported MnO_x NPs [21], a lower selectivity towards C_{2+} hydrocarbons and other oxygenates was observed for the catalysts investigated in this work. This indicates that the interaction between surface carbon species is more limited for manganese doped Co_3O_4 spinel, which limits the formation of C_{2+} products.

5. Conclusion

Manganese doping of mesoporous Co_3O_4 lowered the activity of Co species and significantly increased the methanol selectivity in CO_2 hydrogenation. XRD and XPS indicated that manganese was incorporated into a mixed spinel structure. The highest methanol selectivity of 29.8% was obtained over the $20MnO_x$-Co_3O_4 catalyst (250 °C, 10 bar, 44 400h^{-1}), whereas the $10MnO_x$-Co_3O_4 and $50MnO_x$-Co_3O_4 were unable to reach a methanol selectivity above 19% regardless of the reaction conditions. The results suggest a synergistic effect between manganese and cobalt surface species that promote methanol production, as monometallic spinel exhibited very low methanol selectivity. The CO_2-TPD study showed that the surface basicity was higher for the bimetallic catalysts compared to the monometallic catalysts, which could be partially responsible for the increased methanol selectivity. Methanol formation rates of 1374 mg/(g_{cat} h) and 3106 mg/(g_{cat} h) was achieved over $10MnO_x$-Co_3O_4 and $20MnO_x$-Co_3O_4, respectively. The superior performance of $20MnO_x$-Co_3O_4 compared to $10MnO_x$-Co_3O_4 was attributed to a higher surface concentration of manganese, increased total basicity, and a higher surface area. However, methane was by far the majority product over the manganese-cobalt spinel catalysts. Therefore, further effort is necessary to minimize the methane production pathway, through either optimizing the surface composition or addition of promoters.

Declaration of interest

The authors of this manuscript certify that they have NO affiliations with or involvement in any organization or entity with any financial interest or non-financial interest in the subject matter or materials discussed in this manuscript.

Acknowledgement

The authors would like to thank the financial support from the Norwegian Ministry of Education and Research and the Department of Energy and Petroleum Engineering, University of Stavanger for this project.

Appendix A. Supplementary data

Supplementary material related to this article can be found, in the online version, at doi:https://doi.org/10.1016/j.jcou.2019.04.018.

References

[1] A.M. Appel, J.E. Bercaw, A.B. Bocarsly, H. Dobbek, D.L. DuBois, M. Dupuis, J.G. Ferry, E. Fujita, R. Hille, P.J. Kenis, Chem. Rev. 113 (2013) 6621–6658, https://doi.org/10.1021/cr300463y.
[2] J. Wei, Q. Ge, R. Yao, Z. Wen, C. Fang, L. Guo, H. Xu, J. Sun, Nat. Commun. 8 (2017) 15174, https://doi.org/10.1038/ncomms15174.
[3] A. Álvarez, A. Bansode, A. Urakawa, A.V. Bavykina, T.A. Wezendonk, M. Makkee, J. Gascon, F. Kapteijn, Chem. Rev. 117 (2017) 9804–9838, https://doi.org/10.

1021/acs.chemrev.6b00816.
[4] C. Zhang, K.-W. Jun, K.-S. Ha, Y.-J. Lee, S.C. Kang, Environ. Sci. Technol. 48 (2014) 8251–8257, https://doi.org/10.1021/es501021u.
[5] G.A. Olah, A. Goeppert, G.S. Prakash, Beyond Oil and Gas: the Methanol Economy, John Wiley & Sons, New Jearsey, 2011.
[6] X. Dong, F. Li, N. Zhao, Y. Tan, J. Wang, F. Xiao, Chin. J. of Catal. 38 (2017) 717–725, https://doi.org/10.1016/S1872-2067(17)62793-1.
[7] G. Wang, L. Chen, Y. Sun, J. Wu, M. Fu, D. Ye, RSC Adv. 5 (2015) 45320–45330, https://doi.org/10.1039/C5RA04774A.
[8] Y. Sun, L. Chen, Y. Bao, G. Wang, Y. Zhang, M. Fu, J. Wu, D. Ye, Catal. Today 307 (2018) 212–223, https://doi.org/10.1016/j.cattod.2017.04.017.
[9] Y.J. Fan, S.F. Wu, J. of CO2 Utilization 16 (2016) 150–156, https://doi.org/10.1016/j.jcou.2016.07.001.
[10] M. Behrens, Angew. Chem. Int. Ed. 55 (2016) 14906–14908, https://doi.org/10.1002/anie.201607600.
[11] S.A. Kondrat, P.J. Smith, P.P. Wells, P.A. Chater, J.H. Carter, D.J. Morgan, E.M. Fiordaliso, J.B. Wagner, T.E. Davies, L. Lu, Nat. 531 (2016) 83, https://doi.org/10.1038/nature16935.
[12] J. Graciani, K. Mudiyanselage, F. Xu, A.E. Baber, J. Evans, S.D. Senanayake, D.J. Stacchiola, P. Liu, J. Hrbek, J.F. Sanz, Sci. 345 (2014) 546–550, https://doi.org/10.1126/science.1253057.
[13] B. Zohour, I. Yilgor, M.A. Gulgun, O. Birer, U. Unal, C. Leidholm, S. Senkan, ChemCatChem 8 (2016) 1464–1469, https://doi.org/10.1002/cctc.201600020.
[14] O. Martin, A.J. Martín, C. Mondelli, S. Mitchell, T.F. Segawa, R. Hauert, C. Drouilly, D. Curulla Ferré, J. Pérez-Ramírez, Angew. Chem. Int. Ed. 55 (2016) 6261–6265, https://doi.org/10.1002/anie.201600943.
[15] J. Wang, G. Li, Z. Li, C. Tang, Z. Feng, H. An, H. Liu, T. Liu, C. Li, Sci. Adv. 3 (10) (2017) e1701290, , https://doi.org/10.1126/sciadv.1701290.
[16] F. Studt, I. Sharafutdinov, F. Abild-Pedersen, C.F. Elkjær, J.S. Hummelshøj, S. Dahl, I. Chorkendorff, J.K. Nørskov, Nat. Chem. 6 (2014) 320, https://doi.org/10.1038/nchem.1873.
[17] I. Sharafutdinov, C.F. Elkjær, H.W.P. de Carvalho, D. Gardini, G.L. Chiarello, C.D. Damsgaard, J.B. Wagner, J.-D. Grunwaldt, S. Dahl, I. Chorkendorff, J. Catal. 320 (2014) 77–88, https://doi.org/10.1016/j.jcat.2014.09.025.
[18] A.R. Richard, M. Fan, ACS Catal. 7 (2017) 5679–5692, https://doi.org/10.1021/acscatal.7b00848.
[19] A.M. Hengne, A.K. Samal, L.R. Enakonda, M. Harb, L.E. Gevers, D.H. Anjum, M.N. Hedhili, Y. Saih, K.W. Huang, J.M. Basset, ACS Omega 3 (2018) 3688–3701, https://doi.org/10.1021/acsomega.8b00211.
[20] M.U. Khan, L. Wang, Z. Liu, Z. Gao, S. Wang, H. Li, W. Zhang, M. Wang, Z. Wang, C. Ma, Angew. Chem. Int. Ed. 55 (2016) 9548–9552, https://doi.org/10.1002/anie.201602512.
[21] C.-S. Li, G. Melaet, W.T. Ralston, K. An, C. Brooks, Y. Ye, Y.-S. Liu, J. Zhu, J. Guo, S. Alayoglu, Nat. Commun. 6 (2015) 6538, https://doi.org/10.1038/ncomms7538.
[22] Y. Zhou, Y. Jiang, Z. Qin, Q. Xie, H. Ji, Chin. J. Chem. Eng. 26 (2018) 768–774, https://doi.org/10.1016/j.cjche.2017.10.014.
[23] O. Tursunov, Z. Tilyabaev, J. of the Energy Inst. 92 (2019) 18–26, https://doi.org/10.1016/j.joei.2017.12.004.
[24] V. Iablokov, S.K. Beaumont, S. Alayoglu, V.V. Pushkarev, C. Specht, J. Gao, A.P. Alivisatos, N. Kruse, G.A. Somorjai, Nano Lett. 12 (2012) 3091–3096, https://doi.org/10.1021/nl300973b.
[25] E. Suslova, S. Chernyak, A. Egorov, S. Savilov, V. Lunin, React. Kinet. Catal. Lett. 56 (2015) 646–654, https://doi.org/10.1134/S0023158415050183.
[26] G. Melaet, W.T. Ralston, C.-S. Li, S. Alayoglu, K. An, N. Musselwhite, B. Kalkan, G.A. Somorjai, J. Am. Chem. Soc. 136 (2014) 2260–2263 https://10.1021/ja412447q.
[27] B. Ouyang, S. Xiong, Y. Zhang, B. Liu, J. Li, Appl. Catal. A Gen. 543 (2017) 189–195, https://doi.org/10.1016/j.apcata.2017.06.031.
[28] L. Wang, L. Wang, L. Zhang, X. Liu, H. Wang, W. Zhang, Q. Yang, J. Ma, X. Dong, S.J. Yoo, Angew. Chem. 57 (2018) 6104–6108, https://doi.org/10.1002/anie.201800729.
[29] Y. Slimani, H. Güngüneş, M. Nawaz, A. Manikandan, H. El Sayed, M. Almessiere, H. Sözeri, S. Shirsath, I. Ercan, A. Baykal, Ceram. Int. 44 (2018) 14242–14250, https://doi.org/10.1016/j.ceramint.2018.05.028.
[30] S. Asiri, M. Sertkol, S. Guner, H. Gungunes, K. Batoo, T. Saleh, H. Sozeri, M. Almessiere, A. Manikandan, A. Baykal, Ceram. Int. 44 (2018) 5751–5759, https://doi.org/10.1016/j.ceramint.2017.12.233.
[31] A. Ravichandran, J. Srinivas, R. Karthick, A. Manikandan, A. Baykal, Ceram. Int. 44 (2018) 13247–13252, https://doi.org/10.1016/j.ceramint.2018.04.153.
[32] I.J.C. Lynda, M. Durka, A. Dinesh, A. Manikandan, S. Jaganathan, A. Baykal, S.A. Antony, J. Supercond. Nov. Magn. 31 (2018) 3637–3647, https://doi.org/10.1007/s10948-018-4623-x.
[33] D. Maruthamani, S. Vadivel, M. Kumaravel, B. Saravanakumar, B. Paul, S.S. Dhar, A. Habibi-Yangjeh, A. Manikandan, G. Ramadoss, J. Colloid Interface Sci. 48 (2017) 449–459, https://doi.org/10.1016/j.jcis.2017.03.086.
[34] C. Liu, L. Gong, R. Dai, M. Lu, T. Sun, Q. Liu, X. Huang, Z. Huang, Solid State Sci. 71 (2017) 69–74, https://doi.org/10.1016/j.solidstatesciences.2017.07.006.
[35] A.S. Poyraz, C.-H. Kuo, S. Biswas, C.K. King'ondu, S.L. Suib, Nat. Commun. 4 (2013) 2952, https://doi.org/10.1038/ncomms3952.
[36] W. Tang, X. Wu, S. Li, W. Li, Y. Chen, Catal. Commun. 56 (2014) 134–138, https://doi.org/10.1016/j.catcom.2014.07.023.
[37] S. Wang, Y. Hou, X. Wang, ACS Appl. Mater. Interfaces 7 (2015) 4327–4335, https://doi.org/10.1021/am508766s.
[38] M.C. Biesinger, B.P. Payne, A.P. Grosvenor, L.W. Lau, A.R. Gerson, R.S.C. Smart, Appl. Surf. Sci. 257 (2011) 2717–2730, https://doi.org/10.1016/j.apsusc.2010.10.051.
[39] M. Oku, J. Solid State Chem. 23 (1978) 177–185, https://doi.org/10.1016/0022-4596(78)90063-4.
[40] A.W. Moses, H.G.G. Flores, J.-G. Kim, M.A. Langell, Appl. Surf. Sci. 253 (2007) 4782–4791, https://doi.org/10.1016/j.apsusc.2006.10.044.
[41] A. Galenda, M.M. Natile, V. Krishnan, H. Bertagnolli, A. Glisenti, Chem. Mater. 19 (2007) 2796–2808, https://doi.org/10.1021/cm062742i.
[42] Y. Chen, D.D. Fong, F.W. Herbert, J. Rault, J.-P. Rueff, N. Tsvetkov, B. Yildiz, Chem. Mater. 30 (2018) 3359–3371, https://doi.org/10.1021/acs.chemmater.8b00808.
[43] H. Nesbitt, D. Banerjee, Am. Mineral. 83 (1998) 305–315, https://doi.org/10.2138/am-1998-3-414.
[44] J. Li, X. Liang, S. Xu, J. Hao, Appl. Catal. B: Environ. 90 (2009) 307–312, https://doi.org/10.1016/j.apcatb.2009.03.027.
[45] M. Oku, K. Hirokawa, J. Electron Spectros. Relat. Phenomena 8 (1976) 475–481, https://doi.org/10.1016/0368-2048(76)80034-5.
[46] C. Wei, Z. Feng, G.G. Scherer, J. Barber, Y. Shao-Horn, Z.J. Xu, Adv. Mater 29 (2017) 1606800, , https://doi.org/10.1002/adma.201606800.
[47] M. Piumetti, D. Fino, N. Russo, Appl. Catal. B: Environ. 163 (2015) 277–287, https://doi.org/10.1016/j.apcatb.2014.08.012.
[48] Z.-J. Wang, S. Skiles, F. Yang, Z. Yan, D.W. Goodman, Catal. Today 181 (2012) 75–81, https://doi.org/10.1016/j.cattod.2011.06.021.
[49] C.H. Bartholomew, Catal. Lett. 7 (1990) 27–51, https://doi.org/10.1007/BF00764490.
[50] W. Li, H. Wang, X. Jiang, J. Zhu, Z. Liu, X. Guo, C. Song, RSC Adv. 8 (2018) 7651–7669, https://doi.org/10.1039/C7RA13546G.

Supporting Information

Mesoporous manganese-cobalt oxide spinel catalyst for CO_2 hydrogenation to methanol

Kristian Stangeland[1], Dori Yosef Kalai[1], Yi Ding[2], and Zhixin Yu[1]*

[1] *Department of Energy and Petroleum Engineering, University of Stavanger, 4036 Stavanger, Norway*

[2] *Institute for New Energy Materials & Low-Carbon Technologies, School of Materials Science and Engineering, Tianjin University of Technology, Tianjin 300384, China*

*Corresponding author:

Zhixin Yu

Tel.: +47 51 83 22 38;

Fax: +47 51 83 20 50;

E-mail: zhixin.yu@uis.no

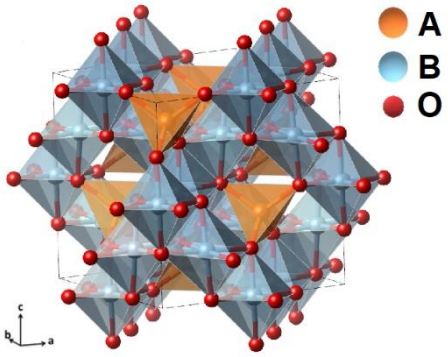

Figure S1. Illustration of the spinel-type crystal structure of AB_2O_4 (A, B = Co and Mn). Metal A cations occupy tetrahedral sites and metal B cations occupy octahedral sites.

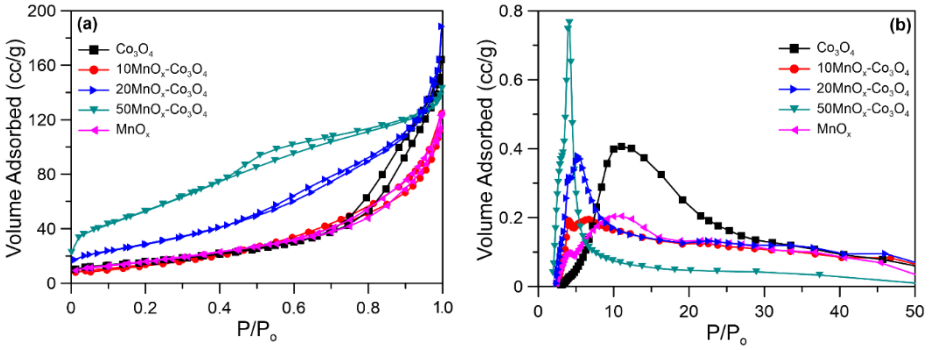

Figure S2. (a) N_2 adsorption-desorption isotherms and (b) pore size distribution of mesoporous Co_3O_4, $10MnO_x$-Co_3O_4, $20MnO_x$-Co_3O_4, $50MnO_x$-Co_3O_4, and MnO_x.

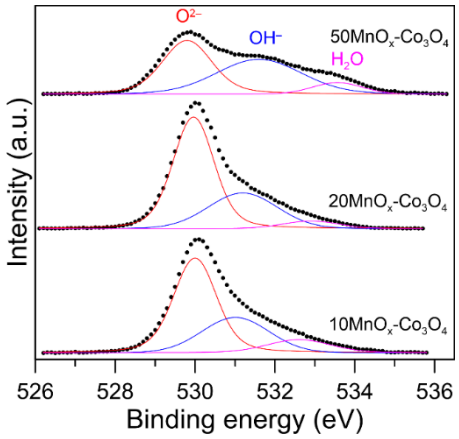

Figure S3. High-resolution XPS spectra of the O1s regions for $10MnO_x$-Co_3O_4, $20MnO_x$-Co_3O_4, and $50MnO_x$-Co_3O_4 catalysts.

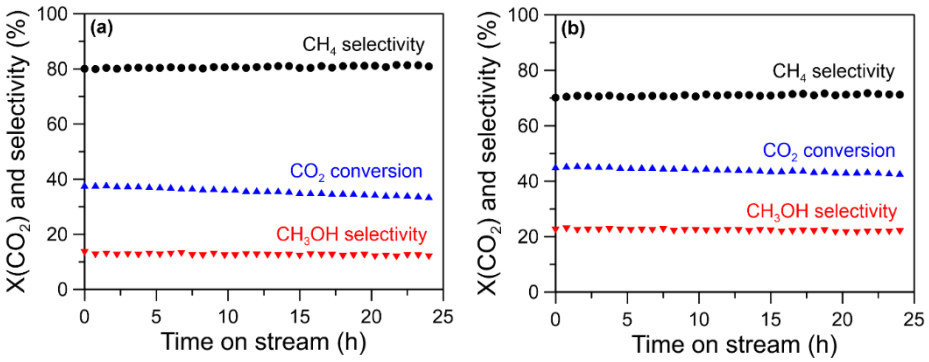

Figure S4. CO_2 conversion and product selectivity over 24 h time on stream for (a) $10MnO_x$-Co_3O_4 and (b) $20MnO_x$-Co_3O_4 (reaction conditions: T = 250 °C, P = 10 bar, gas flow (CO_2/N_2/H_2) = 20/20/60 mL/min, GHSV = 88 800 h^{-1}).

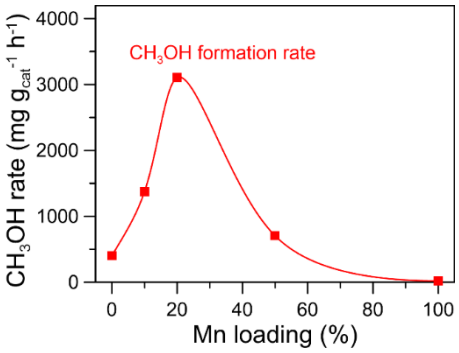

Figure S5. Effect of Mn loading on the formation rate of methanol (reaction conditions: T = 250 °C, P = 10 bar, gas flow ($CO_2/N_2/H_2$) = 20/20/60 mL/min, GHSV = 88 800 h^{-1}).

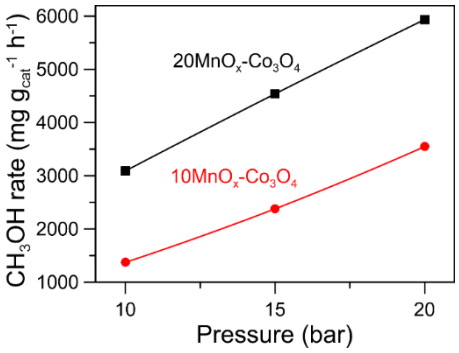

Figure S6. Effect of reaction pressure on the methanol formation rate over $10MnO_x$-Co_3O_4 and $20MnO_x$-Co_3O_4 (reaction conditions: T = 250 °C, gas flow (CO_2/N_2/H_2) = 20/20/60 mL/min, GHSV = 88 800 h^{-1}).

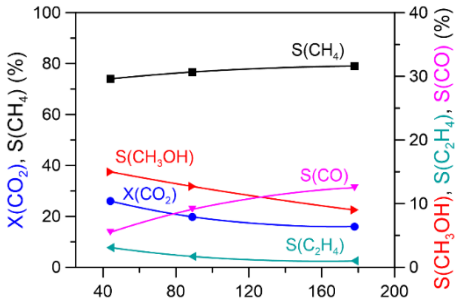

Figure S7. Effect of GHSV over $50MnO_x$-Co_3O_4 (reaction conditions: T = 250 °C, P = 10 bar, CO_2/H_2 = 1:3).

Table S1. Detailed amounts of metal precursors and chemicals used for the synthesis of the catalysts.

Catalyst	Cobalt(II) nitrate hexahydrate (mol)	Manganese(II) nitrate hydrate (mol)	1-butanol (mol)	HNO_3 (mol)	P123 (mol)
Co_3O_4	0.0200	–	0.230	0.038	$4.08*10^{-4}$
$10MnO_x$-Co_3O_4	0.0200	0.0024	0.253	0.042	$4.49*10^{-4}$
$20MnO_x$-Co_3O_4	0.0200	0.0054	0.281	0.047	$4.99*10^{-4}$
$50MnO_x$-Co_3O_4	0.0100	0.0110	0.218	0.037	$3.91*10^{-4}$
MnO_x	–	0.0200	0.188	0.032	$3.40*10^{-4}$

Table S2. Nominal metal content and measured metal content by ICP-OES.

Catlayst	Nominal values (mol %)		Measured values from ICP-OES (mol %)	
	Mn	Co	Mn	Co
Co_3O_4	0	100	–	–
$10MnO_x$-Co_3O_4	11	89	13.6	86.4
$20MnO_x$-Co_3O_4	21	79	21.0	79.0
$50MnO_x$-Co_3O_4	52	48	55.4	44.6
MnO_x	100	0	–	–

Appendix D Paper IV and Supporting Information

Paper IV

CO_2 hydrogenation to methanol over partially embedded Cu within Zn-Al oxide and the effect of indium promotion

Kristian Stangeland, Fawzi Chamssine, Wenzhao Fu, Zikun Huang, Xuezhi Duan, and Zhixin Yu

Submitted.

CO_2 hydrogenation to methanol over partially embedded Cu within Zn-Al oxide and the effect of indium promotion

Kristian Stangeland[a], Fawzi Chamssine[a], Wenzhao Fu[b], Zikun Huang[b], Xuezhi Duan[b,*], Zhixin Yu[a,*]

[a] Department of Energy and Petroleum Engineering, University of Stavanger, 4036 Stavanger, Norway

[b] State Key Laboratory of Chemical Engineering, East China University of Science and Technology, 200237 Shanghai, China

Keywords: CO_2 hydrogenation; Methanol; Copper; Indium; Hydrotalcite

*Corresponding authors. Email address: xzduan@ecust.edu.cn

Zhixin.yu@uis.no

Abstract:

Developing effective catalysts for CO_2 hydrogenation to methanol is key to improve the efficiency of a promising process for the green synthesis of fuels and chemicals. A crucial aspect of developing enhanced CO_2-to-methanol catalysts is optimizing the Cu-ZnO interaction. Herein, a series of hydrotalcite-derived $Cu/ZnO/Al_2O_3$ catalysts were prepared, which consists of partially embedded Cu particles within a Zn-Al oxide matrix. This microstructure exhibits higher intrinsic activity and methanol selectivity. However, sintering of the Cu particles and the Zn-Al oxide phase results in catalyst deactivation. The addition of In can stabilize the Cu-metal oxide interface and improve the methanol selectivity, but significantly decreases the activity. The lower activity of the In-containing catalysts is linked to the inhibition of Cu active sites by Cu_xIn_y species. Thus, stabilizing the In species within the oxide phase is key to avoid the negative influence of In on the activity.

1. Introduction

The increasing atmospheric CO_2 concentration has led to extensive efforts to develop environmental-friendly solutions for high-emission sectors. CO_2 hydrogenation to methanol is one of the most promising methods for producing fuels and chemicals from renewable sources [1]. This is because methanol synthesis from syngas (CO, CO_2, H_2) is already a well-established process. Furthermore, methanol is an important feedstock for several processes in the chemical industry, such as chloromethane, acetic acid, methyl tert-butyl ether (MTBE), alkyl halides, and formaldehyde [2-4]. As such, the infrastructure is already in place to handle methanol or methanol-derived fuels as primary energy carriers. One of the main issues is the current high price of hydrogen produced from renewable sources [5]. However, the price of renewable hydrogen is expected to decrease in the future, which can improve the economic viability of the CO_2-to-methanol process.

Methanol synthesis from CO_2 (Eq. 1) is exothermic and a volume-reducing reaction. The main side reaction is the reverse water-gas shift (RWGS) reaction (Eq. 2), which converts CO_2 into CO and becomes more favorable at higher temperatures. Hence, low temperature (200–300 °C) and moderate pressure (50–100 bar) are typically employed in CO_2 hydrogenation to methanol [6, 7].

$$CO_2 + 3H_2 \rightleftarrows CH_3OH + H_2O \qquad \Delta H = -49.5 \text{ kJ/mol} \qquad \text{(Eq. 1)}$$

$$CO_2 + H_2 \rightleftarrows CO + H_2O \qquad \Delta H = 41.2 \text{ kJ/mol} \qquad \text{(Eq. 2)}$$

The $Cu/ZnO/Al_2O_3$ system has been studied for decades. The industrial $Cu/ZnO/Al_2O_3$ catalyst consists of an intimate mixture of Cu and metal oxide nanoparticles, typically obtained from co-precipitation of metal nitrates and forming a Cu, Zn carbonate precursor [8]. This synthesis route usually results in a high Cu surface area and highly active catalysts. Besides the Cu dispersion, the activity of Cu/ZnO-based catalysts has also been linked to synergetic effects between Cu and ZnO, which is often referred to as the strong metal-support interaction (SMSI). Several models of the Cu-ZnO synergy in Cu-based catalysts have been proposed. Experimental and computational studies have identified Cu lattice strain or defects as indicative of high performance, which might also be influenced by the properties of the metal oxide phase [4, 9, 10]. There is also compelling evidence that the SMSI between Cu and ZnO is crucially involved in the active sites of methanol synthesis [4, 11-14]. Studt et al. [12] showed that a relatively inactive Cu/MgO catalyst can be converted into an efficient CO_2-to-methanol catalyst by impregnating ZnO onto Cu/MgO. The SMSI has been ascribed to the formation of CuZn [4, 15] or $CuZnO_x$ [16] surface alloy species. This is supported by a correlation between the Zn coverage of Cu and the methanol synthesis activity, which has been demonstrated for conventional catalysts [17] and model structures [15, 18]. Furthermore, oxygen vacancies in the ZnO at the Cu-ZnO interface might assist in CO_2 activation and conversion to methanol [19]. The optimization of Cu dispersion can be regarded as highly advanced for this system. However, higher intrinsic activity, i.e., normalized to the Cu surface area, has been reported for partially

embedded Cu nanoparticles into a mixed Zn-Al oxide matrix [20, 21]. Therefore, tuning the microstructural properties and the Cu-metal oxide interface are key areas for enhancing the activity of Cu/ZnO-based catalysts.

Recently, In_2O_3-based catalysts, typically promoted by metal oxides (e.g., Zr [22], Y [23], La [23]) or Pd [24-26] have received significant interest due to their high methanol selectivity and stability over a wide range of reaction temperatures (200–320 °C). Only a limited number of studies have investigated In incorporation into Cu-based catalysts [27-34]. Matsumura et al. [27] found that the addition of In_2O_3 reduces the activity but enhances the stability and suppresses the formation of CO in high-temperature methanol steam reforming over Cu/ZnO-based catalysts. Similar effects of In_2O_3 have also been reported in CO_2 hydrogenation to methanol [30, 34]. On the other hand, Shi et al. [32] obtained active and selective Cu-In_2O_3 catalysts prepared by co-precipitation for CO_2 hydrogenation to methanol. The most active catalyst consisted of Cu_9In_{11} alloy in intimate contact with an In_2O_3 phase. They proposed that a synergistic effect is present for $Cu_{11}In_9$-In_2O_3 catalyst in which H_2 is dissociatively adsorbed on the $Cu_{11}In_9$ surface and CO_2 is activated at In_2O_3 oxygen vacancies. These species subsequently migrate to the interfacial sites where CO_2 is hydrogenated to methanol. Gao et al. [31] found that the activity and selectivity of Cu-In_2O_3-ZrO_2 catalyst containing Cu_2In alloy are higher than In_2O_3 and In_2O_3-ZrO_2 catalysts. These contradictory findings highlight that different Cu-In speciation and their effects on CO_2 hydrogenation to

methanol are not fully understood. Furthermore, the cause of the highly inhibiting effect of small amounts of In_2O_3 on the activity of Cu/ZnO catalysts has not been identified.

Herein, we report a facile strategy for the synthesis of active Cu/ZnO-based catalysts for CO_2 hydrogenation to methanol. Partially embedding Cu within a Zn-Al oxide matrix is obtained via a hydrotalcite-like precursor and compared to a coprecipitated Cu/ZnO catalyst. We show that enhancing the Cu-metal oxide interfacial contact can be utilized to develop more active Cu/ZnO-based catalysts. Furthermore, the influence of In on Cu/ZnO-based catalysts is also elucidated, where the incorporation of In can stabilize the Cu-metal oxide interface but reduces the catalyst activity. Anchoring In within the Zn-Al oxide phase seems to be the key to avoid the negative effects of In on the activity. The present findings provide a promising approach for optimizing the Cu-metal oxide interaction, which can further enhance the catalytic performance of Cu-based catalysts for CO_2 hydrogenation to methanol.

2. Experimental

2.1. Catalyst preparation

The HT-like catalyst precursors containing Cu, Zn, Al, and In were prepared by co-precipitation at room temperature. For a typical synthesis, an aqueous solution of metal salts ($Cu(NO_3)_2{\cdot}3H_2O$, $Zn(NO_3)_2{\cdot}6H_2O$, $Al(NO_3)_3{\cdot}9H_2O$, and $In(NO_3)_3{\cdot}H_2O$) was added

dropwise into a mixed solution of NaOH and Na_2CO_3 precipitant under vigorous stirring. The pH of the precipitate solution after mixing was adjusted to 9.0 ± 0.2 if needed. The precursor solution was aged at 60 °C for 15 h before the precipitate was filtered and washed with deionized water. Finally, the product was dried overnight at 80 °C and then calcined in flowing synthetic air at 500 °C for 4 h. The HT-derived catalysts with a Cu:Zn ratio of 2 are denoted as 2CZA-In*Y*, where *Y* refers to the mol% of In (*Y* = 0–7 mol%). Table 1 lists the nominal and the actual metal content determined from ICP-AES of the 2CZA-In*Y* catalysts.

Table 1. Nominal and actual catalyst compositions determined from ICP-AES of the 2CZA-In*Y* catalysts.

Catalysts	Nominal metal content (mol%)				Metal content determined by ICP-AES (mol%)			
	Cu	Zn	Al	In	Cu	Zn	Al	In
2CZA-In0	50	25	25	0	51.3	24.3	24.4	–
2CZA-In2	50	25	23	2	50.9	24.1	22.9	2.1
2CZA-In3	50	25	22	3	51.5	24.6	20.8	3.1
2CZA-In5	50	25	20	5	51.7	23.9	19.3	5.1
Cu-ZnO	83	17	–	–	83.2	16.8	–	–
In/Cu-ZnO	82	17	–	1	82.2	16.5	–	1.3

We also prepared a binary Cu-ZnO by co-precipitation following a procedure described by Behrens and Shlögle [8]. In brief, aqueous nitrate solutions with appropriate amounts of the metal precursors were co-precipitated at a constant pH of 6.5 using sodium carbonate as precipitating agent. The co-precipitate was aged in the mother liquor at 60 °C for 15 h. The precipitate was washed several times with deionized water, dried, and then the precursors were calcined in flowing air at 350 °C for 4 h. The ternary In/Cu-ZnO catalyst was obtained by impregnating

Cu/ZnO with In nitrate. The impregnated catalyst was calcined again at 350 °C for 4 h. The composition of the Cu-ZnO and In/Cu-ZnO catalysts is given in Table 1.

2.2 Catalyst characterization

The specific surface area and pore size distribution of the catalysts were determined from N_2 adsorption-desorption at 77 K by the Brunauer-Emmet-Teller (BET) and Barret-Joyner-Halenda (BJH) methods, respectively. The measurements were conducted using a Micromeritics TriStar II instrument. Degassing of the samples prior to analysis was done at 120 °C for 14 h with a Micromeritics VacPrep 061 degas system.

Elemental analysis of the catalysts was performed by ICP-AES on an Agilent 725-ES apparatus. Typically, 200 mg of sample was dissolved in a HNO_3:HCl mixture with a ratio of 1:3 at elevated temperature until complete dissolution of the catalyst. The sample was further diluted and filtered prior to elemental analysis.

The high-angle annular dark-field scanning transmission microscopy (HAADF-STEM) images were collected on a Tecnai G2F20 S-Twin instrument operated at 200 kV. The reduced and passivated catalysts were dispersed in ethanol by ultrasonication, then one drop of the solution was deposited on a holey carbon-coated support grid.

X-ray diffraction (XRD) patterns were recorded on either a Rigaku D/Max 2550 VB/PC or Bruker-AXS Microdiffractometer (D8 ADVANCE) instrument using a Cu Kα radiation source (λ = 1.5406, 40 kV, and 40 mA). The patterns were typically obtained at 2θ between 10–90° with a step interval of 2 °/min. The peaks were indexed according to the Joint Committee on Powder Diffraction Standards (JCPDS) database.

X-ray photoelectron spectroscopy (XPS) and Auger (XAES) spectra were recorded on a ThermoFisher ESCALAB250Xi equipped with a monochromatic Al K_α source (1486.6 eV) operated at 15 kV. High-resolution spectra were obtained at a pass energy of 30.0 eV, step size of 0.05 eV, and dwell time of 500 ms per step. All spectra were referenced to the C 1s peak (284.8 eV).

Temperature programmed reduction (H_2-TPR) profiles were recorded using a Micromeritics Autochem II ASAP 2920 instrument. Prior to the measurements, the samples were pretreated at 200 °C in He flow for 30 min. The profiles were recorded by passing a 7% H_2/Ar mixture at 50 mL/min over the sample while the temperature was ramped from ambient to 500 °C at 10 °C/min.

The Cu surface area (SA_{Cu}) was determined by dissociative N_2O adsorption [35] using a Micromeritics Autochem 2920 instrument. The sample was first pretreated in He at 120 °C for 1 h followed by reduction in 7% H_2/Ar mixture (50 mL/min) for 2 h at 350 °C. Then, the catalyst bed was purged with He until the temperature reached 50 °C. The oxidation of surface Cu atoms to Cu_2O by N_2O adsorptive decomposition

was carried out in a flow of 1% N_2O/He at 50 °C for 1 h. After that, the sample tube was purged with He for 1 h to remove the unreacted N_2O. Finally, the H_2 consumption of surface Cu_2O was measured by a second TPR experiment from 50 to 400 °C at a rate of 10 °C/min in a 7% H_2/Ar mixture.

2.3 Catalytic activity tests

The catalysts were tested for CO_2 hydrogenation to methanol in a custom-built fixed-bed continuous-flow reactor. Typically, 0.2 g of catalyst was mixed with SiC (2 g) and placed in a stainless tube reactor with an internal diameter of 0.5 cm and a length of 50 cm. The catalysts were reduced at 350 °C with a heating rate of 2 °C/min by 10% H_2/N_2 (50 ml/min). Finally, the reactor was cooled to ambient temperature, pressurized with the reactant gases ($H_2/CO_2/N_2$ = 3/1/1), and then heated to the desired reaction temperature. The post-reactor lines and valves were heated to 140 °C to avoid product condensation. An Agilent 7890 B gas chromatogram (GC) system fitted with two TCD detectors was used for on-line analysis of the products. The CO_2 conversion, methanol selectivity, and space-time yield (STY) of methanol were calculated by utilizing N_2 as internal standard. The TOF was calculated as the number of methanol molecules produced per surface Cu atom of the reduced catalyst per second. A CO_2 conversion of approximately 5% CO_2 was used for the TOF measurements to exclude the effect of water inhibition.

3. Results and discussion

3.1 Catalyst characterization

3.1.1 Textural and structural properties of the XCZA-InY catalysts

The N_2 adsorption-desorption isotherms of the calcined catalysts are shown in Figure S1. The BET surface area (SA_{BET}), pore volume, and average pore diameter of the calcined catalysts are summarized in Table 2. It can be seen that the incorporation of In slightly increases the BET surface area of the 2CZA-In*Y* catalysts, which is in the range of 36–41 m^2/g. Furthermore, the pore volume is also higher for the In-containing catalysts (0.08–0.09 cm^3/g) compared to the 2CZA-In0 catalyst (0.06 cm^3/g).

Table 2. Summary of N_2-physisorption, crystallite size, and average particle size of the 2CZA-In*Y* catalysts.

Catalyst	SA_{BET} (m^2/g)	Pore volume (cm^3/g)	Average pore diameter (nm)	d_{Cu} (nm)[a]	d_{Cu} (nm)[b]
2CZA-In0	36	0.06	6.2	13.1	9.5
2CZA-In2	39	0.09	6.7	11.8	9.4
2CZA-In3	41	0.09	6.7	12.1	9.4
2CZA-In5	37	0.08	6.6	12.3	8.7
Cu-ZnO	72	0.17	7.7	23.7	–
In/Cu-ZnO	46	0.11	7.6	20.1	–

[a] Calculated from the (111) peak by the Scherrer equation
[b] Determined by counting particles in HAADF-STEM images

The XRD patterns of the HT precursors are shown in Figure 1a. The patterns are typical for HT-like structures such as $Cu_2Zn_4Al_2(OH)_{16}CO_3{\cdot}H_2O$ (PDF 38-0484) [21]. The peaks at 2θ of 35.5°

and 38.7° are attributed to CuO (PDF #48-1548). Crystalline CuO can be formed by the oxolation reaction, which transforms $Cu(OH)_2$ into CuO. The oxolation reaction can occur at relatively low temperatures for $Cu(OH)_2$ at high pH and can also take place during the drying process [36]. At high In content, additional reflections corresponding to $In(OH)_3$ (PDF #76-1463) are present at ~22.3° and ~31.7° for the 2CZA-In5 catalyst. The full width at half maximum (FWHM) of the 003 reflection at 2θ of ~11.8° is related to lattice strain or crystal domain size in the stacking direction. As shown in Figure 1b, a volcano-type trend with respect to In content can be observed. The volcano-trend in the FWHM of the 003 reflection indicates that a small fraction of In is incorporated into the HT-like structure [37-39]. The XRD pattern of the Cu-ZnO precursor is shown in the Supporting Information (Figure S2a) and is typical of Cu, Zn malachite [40].

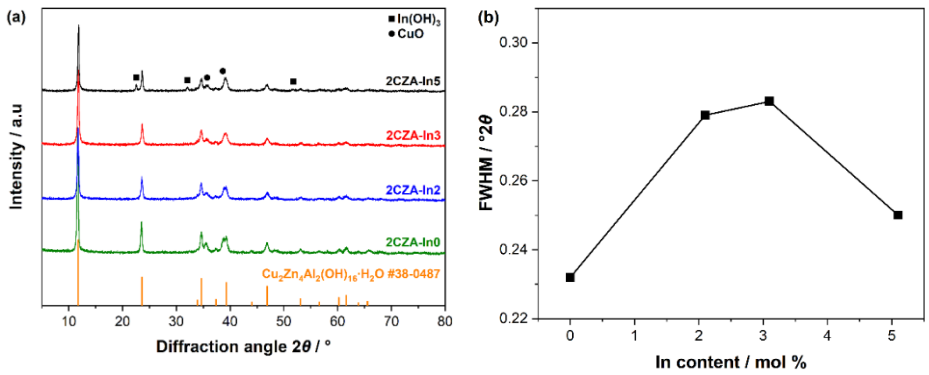

Figure 1. (a) XRD patterns of the 2CZA-In*Y* precursors and (b) FWHM of the 003 peak as a function of In content.

The calcined 2CZA-In*Y* samples show weak reflections corresponding to CuO, whereas Zn or Al species cannot be identified (Figure S3). The

XRD patterns of the reduced-passivated 2CZA-In*Y* catalysts are shown in Figure 2a. The reflections at 2θ of 43.3°, 50.4, and 74.1° correspond to metallic Cu (PDF #04-0836). The crystallite size of Cu was estimated from the Cu(111) peak, and the crystallite size is relatively similar for the 2CZA-In*Y* catalysts between 11.8–13.1 nm (Table 2). The weak reflection at 2θ of 36.3° is attributed to ZnO (PDF #36-1415) and indicates that the Zn-Al species are highly dispersed, which is typical for HT-derived CZA catalysts [21, 41]. The regions of the Cu peaks are magnified in Figure 2b. A shift in the Cu peaks towards lower diffraction angles is observed with increasing In content. Furthermore, weak reflections are present between 42–43° for the 2CZA-In5 catalyst. This is attributed to the formation of Cu_xIn_y alloy because the most intense peaks of different Cu_xIn_y alloys are located in this region. Moreover, it has been demonstrated that Cu_xIn_y alloys can form at the reduction conditions used in this work [32, 42, 43]. Crystalline Cu and ZnO phases can be identified for the Cu-ZnO and In/Cu-ZnO catalysts (Figure S2b). The crystallite size of Cu-ZnO (23.7 nm) is slightly larger than that of the In/Cu-ZnO catalyst (Table 2).

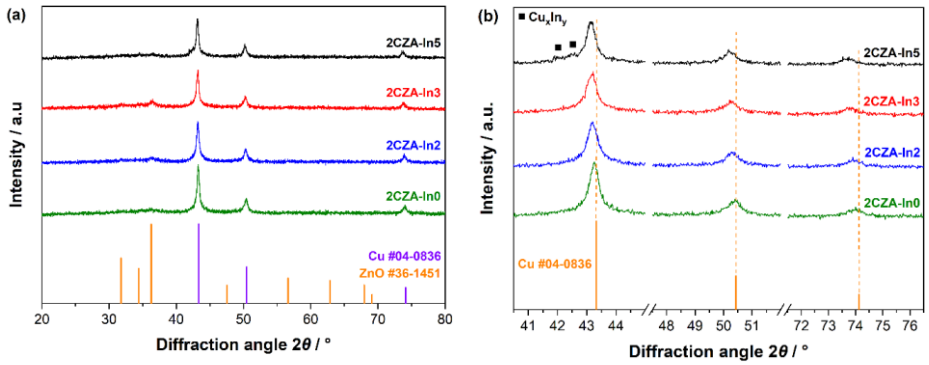

Figure 2. (a) XRD patterns of the reduced 2CZA-In*Y* catalysts and (b) the region containing the Cu diffraction peaks.

HAADF-STEM was used to investigate the microstructure of the 2CZA-In*Y* catalysts. The calcined catalysts consist of a largely amorphous mixed oxide phase, as depicted in Figure 3a for the 2CZA-In0 catalyst. This is typical for HT precursors, which is composed of a homogeneous mixture of the metal oxides after calcination [44]. As illustrated in Figure 3b, larger Cu particles are formed for the 2CZA-In*Y* catalyst after reduction, which are embedded within a metal oxide matrix. In literature, the metal oxide matrix is reported to contain a spinel-like $ZnAl_2O_4$ structure [21, 36]. The structure of the other reduced In-containing 2CZA-In*Y* catalysts is similar (Figure S4a–c). The structure of the 2CZA-In*Y* catalysts is obviously different from the conventionally prepared Cu/ZnO catalysts, which is characterized by crystalline CuO particles dispersed by discrete ZnO particles (Figure 3c). The continuous embedding metal oxide matrix for the 2CZA-In*Y* catalysts probably leads to a larger Cu-metal oxide interface compared to the Cu/ZnO catalyst. The average Cu particle size of the 2CZA-In*Y* catalysts was

determined by measuring at least 400 particles and are summarized in Table 2. The particle size distribution is shown in Figure S5a–d. The average Cu particle size is comparable for the 2CZA-In*Y* catalysts (8.7–9.5 nm), which is smaller than the crystallite size estimated by XRD. This is probably because XRD is a volume-averaged technique and is more sensitive to larger than smaller crystallites [14].

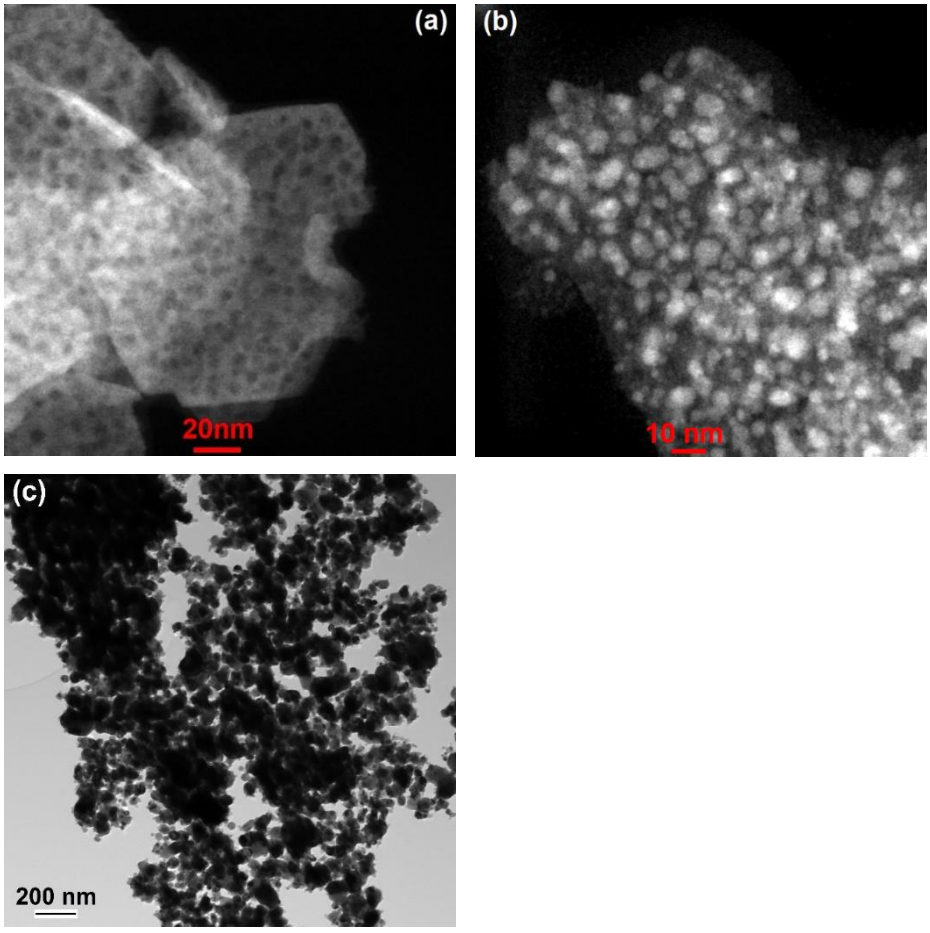

Figure 3. HAADF-STEM images of the (a) calcined and (b) reduced 2CZA-In0 catalyst; (c) TEM image of the reduced Cu-ZnO catalyst.

3.1.4 XPS study of the 2CZA-InY catalysts

The surface composition of the 2CZA-In*Y* catalysts before and after reduction is summarized in Table 3. It can be seen that the surface composition of the 2CZA-In*Y* catalysts deviates from the nominal composition. The Cu:Zn ratio on the surface is close to 1.2 for the calcined samples, whereas the Cu:Zn ratio determined from ICP-AES is around 2. This is probably because the CuO species are embedded in the mixed metal oxide matrix after calcination, leading to a higher surface concentration of Zn and Al. In agreement with previous studies [4, 30, 45], the Cu/Zn surface ratio further decreases to ~0.9–0.6 after reduction, where the surface Zn concentration increases with increasing In content.

Table 3. Surface composition of calcined and reduced 2CZA-In*Y* catalysts determined by XPS.

Catalyst	Surface composition after calcination (atom%)				Surface composition after reduction (atom%)				$Cu^0 / (Cu^+ + Cu^0)$
	Cu	Zn	Al	In	Cu	Zn	Al	In	
2CZA-In0	37	31	32	0	33	36	30	0	0.15
2CZA-In2	38	31	28	3	32	37	28	3	0.17
2CZA-In3	38	32	25	5	30	40	25	5	0.22
2CZA-In5	39	33	22	6	27	42	24	7	0.21

Figure 4a shows the Cu $2p_{3/2}$ spectra of the calcined and reduced 2CZA-In*Y* catalysts. The calcined samples exhibit a principal peak at ~934 eV and a characteristic satellite feature around 940–944 eV [46]. The satellite feature disappears after reduction, indicating that CuO species are not present after reduction. Furthermore, the main peak shifts towards

lower binding energy, which is in the region of Cu^0 (932.6 eV) and Cu_2O (932.4 eV). The Cu L_3VV Auger line was investigated to obtain further information about the chemical state of Cu in the catalysts after reduction. For the calcined samples, a peak at 917.7 eV is detected (Figure S6), which is close to the expected peak position of CuO [47]. The CuL_3VV Auger spectra of the reduced and passivated catalysts are shown in Figure 4b. Since CuO species are not present after reduction in the Cu2p spectra, the profiles are deconvoluted into Cu^0 (~918.5 eV) eV) and Cu^+ (~916.4 eV). This estimation is widely used to determine the relative amount of Cu^0 and Cu^+ species in the sample [48-52]. It is clear that the majority of the Cu species exist as Cu^+ for all the catalysts, indicating high interaction between Cu and the metal oxide phase [48, 49]. The Cu^0 fraction of the 2CZA-In*Y* catalysts increases with increasing In content (Table 3).

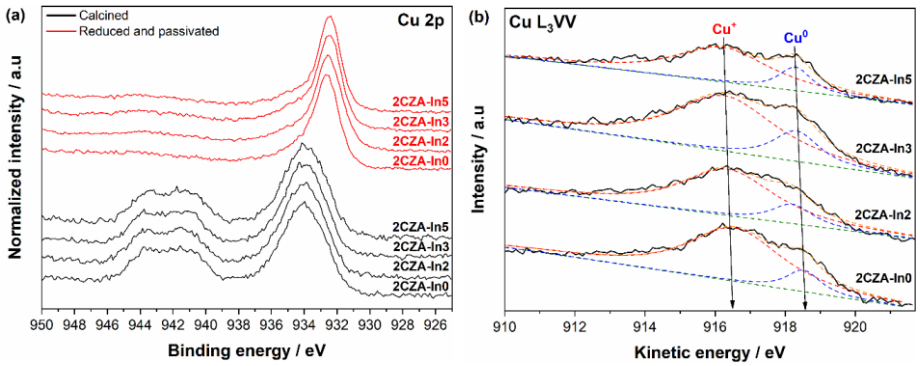

Figure 4. (a) Cu $2p_{3/2}$ XPS spectra of the calcined and reduced 2CZA-In*Y* catalysts. (b) Cu L_3VV Auger spectra of the reduced 2CZA-In*Y* catalysts.

To address the chemical state of Zn, the Zn $L_3M_{4,5}M_{4,5}$ Auger line was recorded. The Zn $L_3M_{4,5}M_{4,5}$ spectra of calcined and reduced 2CZA-In*Y* are shown in Figure 5a. It can be seen that the spectra of the calcined and reduced sample overlap, indicating that the chemical state of ZnO is largely unchanged after reduction. The chemical state of In was also examined, and the In 3d spectra contain two peaks at 444.8 eV and 452.3 eV corresponding to the In $3d_{5/2}$ and In $3d_{3/2}$ spin-orbit doublets (Figure 5b) [53]. The peaks shift slightly towards lower binding energy after reduction. It is likely that the shift in the In3d spectra is related to the formation of Cu_xIn_y alloys, in agreement with the XRD observations. The slight shift in the In 3d spectra indicate that a mix of In_2O_3 and Cu_xIn_y species are present after reduction [32, 43, 54].

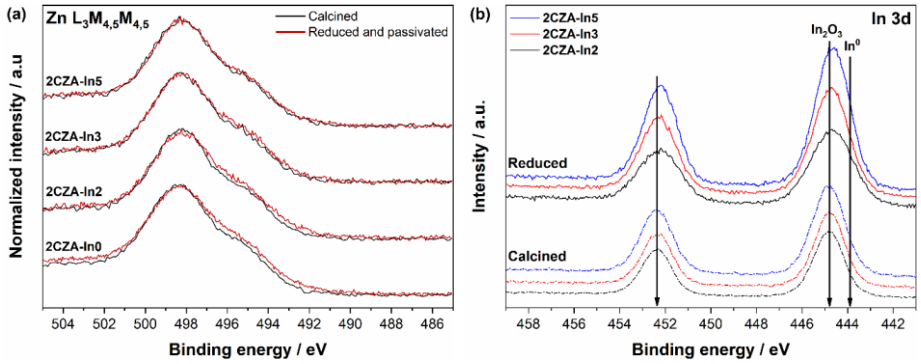

Figure 5. (a) Zn L3M4,5M4,5 Auger spectra of calcined and reduced 2CZA-In*Y* catalysts. (b) In 3d XPS spectra of calcined and reduced 2CZA-In*Y* catalyst.

3.1.3 Reducibility of the catalysts

H_2-TPR was carried out to investigate the reducibility of the catalysts. The TPR profiles of the 2CZAIn-*Y* catalysts are shown in Figure 6a. The reduction of the 2CZA-In*Y* catalysts occurs over a wide temperature range, and the profiles are deconvoluted into four peaks, namely α, β, γ_1, and γ_2. The low-temperature peaks are assigned to CuO particles dispersed on the catalyst's surface (α) and CuO particles in the bulk of the Zn-Al oxide (β) [48, 55]. Additional high-temperature peaks are only observed for the HT-derived catalysts. The γ_1 and γ_2 peaks located between 250–300°C are attributed to the reduction of Cu^{2+} species highly dispersed within the metal oxide matrix [21]. These Cu^{2+} species are strongly bound to the Zn-Al oxides, which results in a stabilization of the Cu_2O intermediate and a step-wise reduction of CuO (CuO → Cu_2O and Cu_2O → Cu) [9, 56-58]. At moderate In content, the α and β peaks shift towards higher reduction temperature for 2CZA-In*Y*. On the other hand, the γ peaks shift towards lower temperature with increasing In content. These observations indicate that moderate amounts of In enhance the interaction of CuO with the metal-oxide phase, whereas the Cu^{2+} species present in the metal oxide matrix are more easily reduced when the In content increases. In contrast, the complete reduction of the CuO particles of the Cu/ZnO and In/Cu-ZnO catalysts occurs at lower temperatures due to the weaker interaction with the metal oxide phase (Figure 6b).

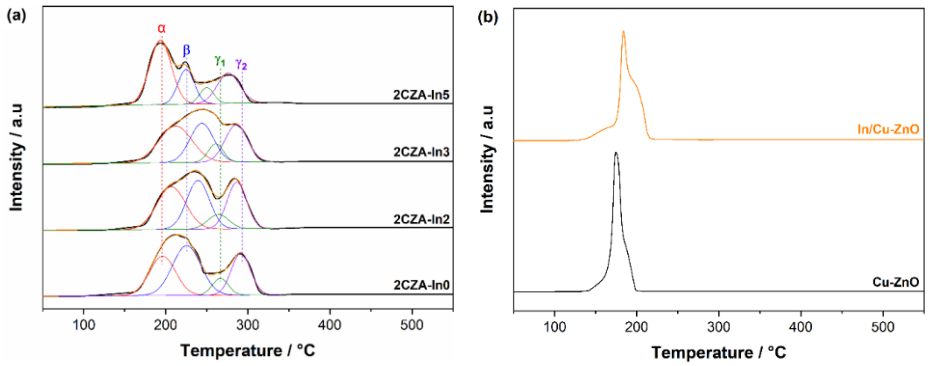

Figure 6. (a) Deconvoluted H_2-TPR profiles of the 2CZA-In*Y* catalysts and (b) H_2-TPR profiles of the Cu-ZnO and In/Cu-ZnO catalysts.

The H_2/CuO ratio was calculated to assess the H_2 consumption relative to the Cu content (Table 4). The H_2/CuO ratio is close to 100% for all the catalysts, indicating the complete reduction of CuO. A slight increase in the H_2/CuO ratio is observed with increasing In content for the 2CZA-In*Y* catalysts, which is ascribed to the formation of Cu_xIn_y alloys. Similarly, the H_2/CuO ratio is higher when In is impregnated onto the Cu-ZnO catalyst.

Table 4. Summary of the H_2-TPR data and the Cu surface area of the 2CZA-In*Y* catalysts.

Catalyst	H_2/CuO (%)	TPR peak contribution (%)				SA_{Cu} (m^2/g_{cat})
		α	β	γ_1	γ_2	
2CZA-In0	99	29	40	8	23	13
2CZA-In2	101	34	32	8	26	16
2CZA-In3	101	36	29	8	27	15
2CZA-In5	103	48	20	9	23	11
Cu-ZnO	98	–	–	–	–	18
In/Cu-ZnO	101	–	–	–	–	14

3.1.4 N_2O titration measurements

The Cu surface area was estimated by N_2O dissociative adsorption. The Cu surface area of 2CZA-In*Y* first increases from 13 to 16 m^2/g with the addition of 2 mol% In and then decreases with increasing In content (Table 4). The Cu surface concentration obtained by XPS indicates that the number of Cu atoms on the surface decreases with increasing In content, which can explain the lower Cu surface area of the 2CZA-In3 and 2CZA-In5 catalysts. In addition, the formation of Cu-In surface alloys might also influence the Cu surface area. The Cu surface area also drops from 18 m^2/g to 14 m^2/g when In is impregnated onto the Cu-ZnO catalyst.

3.2 Catalytic activity tests

3.2.1 Influence of Cu-metal oxide interface and In on activity

To assess the influence of the Cu surface area on the catalytic activity of HT-derived catalysts, we also prepared 1CZA-In*Y* and 4CZA-In*Y* catalysts with an In content of 0–7 mol%, where 1 and 4 refer to the Cu/Zn ratio. Table S1 summarizes the characterization results of the 1CZA-In*Y* and 4CZA-In*Y* catalysts. Figure 7 shows the steady-state STY of methanol after 12 h testing plotted against the Cu surface area. It is evident that the methanol synthesis activity of the HT-derived catalysts is strongly correlated to the Cu surface area. This is often the case for Cu-based catalysts with a similar preparation history [59]. The highest STY of methanol (12.4 mmol g_{cat}^{-1} h^{-1}) is obtained over the 4CZA-In0 catalyst, which also has the highest Cu surface area (14 m^2/g) of the HT-

derived catalysts. The activity of the 4CZA-In0 catalyst is higher than that of Cu/ZnO (11.9 mmol g_{cat}^{-1} h^{-1}), even though the 4CZA-In0 catalyst has a lower Cu surface area. This is attributed to the larger number of interfacial sites due to the partial embedment of Cu in the Zn-Al matrix. The higher intrinsic activity of the HT-derived catalysts indicates that a compromise between high Cu surface area and Cu-metal oxide interfacial area is needed to maximize the activity of Cu/ZnO-based catalysts. The Zn-Al matrix obtained from HT-like precursor is a promising candidate for obtaining large Cu-metal oxide contact.

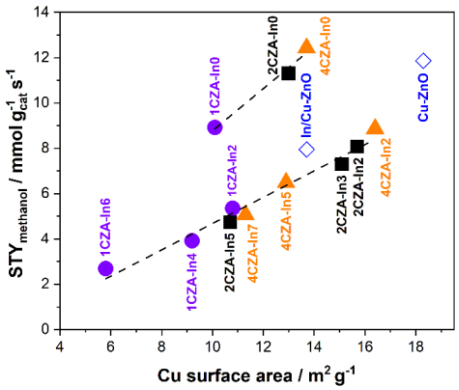

Figure 7. (a) STY of methanol as a function of Cu surface area of the CZA-In*Y* catalysts. Reaction conditions: 250 °C, 30 bar, $H_2/CO_2/N_2$ = 3/1/1, WHSV = 30 000 cm^3 g_{cat}^{-1} h^{-1}.

The activity of the In-containing HT-derived catalysts is also correlated to the Cu surface area, but is significantly lower compared to the In-free catalysts. Although the addition of less than 3 mol% In to HT-derived CZA catalysts increases the Cu surface area, the STY of methanol is significantly reduced. The STY of methanol also decreases substantially

when In is impregnated onto the Cu-ZnO catalyst. This suggests that In species covers or inhibits the active sites on the Cu surface. The lower activity of the In-doped catalysts is consistent with earlier studies [27, 30, 34].

To further assess the influence of the catalyst's composition, the turnover frequency (TOF) for methanol formation of the CZA-In*Y*, Cu-ZnO, and In/Cu-ZnO catalysts is compared in Figure 8. The TOF of the CZA-In0 catalysts is comparable at approximately 0.018 s^{-1}, which is higher than that obtained over the Cu/ZnO catalysts (0.014 s^{-1}). These TOFs are in the medium to high range compared with reported values in literature [21, 59]. The vigorous debate regarding the Cu-ZnO synergy highlights the difficulty in identifying the dominant promotional mechanism in Cu/ZnO-based systems. Thus, the enhanced Cu-metal oxide interaction of the HT-derived catalysts might promote methanol synthesis by modifying the active Cu surface (e.g., inducing defects or promoting surface CuZn/$CuZnO_x$ formation [4, 9, 10]), providing a higher number of Cu-metal oxide interfacial sites [19], or a combination of these phenomena. It is interesting that the intrinsic activity of the CZA-In0 catalysts is similar despite the differences in Cu particle size and composition. This further indicates that the enhanced Cu-metal oxide interaction is the main reason for the higher intrinsic activity of the HT-derived catalysts. When In is incorporated into the catalyst, the TOF decreases significantly. Furthermore, the TOF decreases with increasing In content for the HT-derived catalysts. Thus, In seems to have a dramatic effect on the ability of Cu to produce methanol. This is probably

due to the presence of In species on the Cu surface or the formation of Cu_xIn_y alloy species, which seems to inhibit the activity of the Cu surface sites.

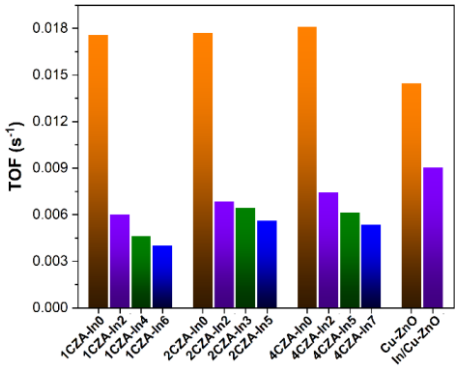

Figure 8. TOF of methanol formation of the CZA-In*Y*, Cu-ZnO, and In/Cu-ZnO catalysts. Reaction conditions: 250 °C, 30 bar, $H_2/CO_2/N_2$ = 3/1/1, CO_2 conversion ≈ 5%.

3.2.1 Influence of Cu-metal oxide interface and In on methanol selectivity

The methanol selectivity as a function of CO_2 conversion for the 2CZA-In*Y*, Cu-ZnO, and In/Cu-ZnO catalysts is plotted in Figure 9. The 2CZA-In*Y* catalysts exhibit higher methanol selectivity compared to the conventional Cu/ZnO catalyst. The methanol selectivity is also higher for the In-containing catalysts compared to the In-free catalysts. The maximum methanol selectivity is obtained at 3 mol% In. The higher selectivity of the In-containing 2CZA-In*Y* catalysts is ascribed to the inhibition of CO formation. This is in agreement with Matsumura et al. [27], who observed that CO formation was suppressed by the presence

of In on the Cu surface during methanol steam reforming over a Cu/ZnO-based catalyst.

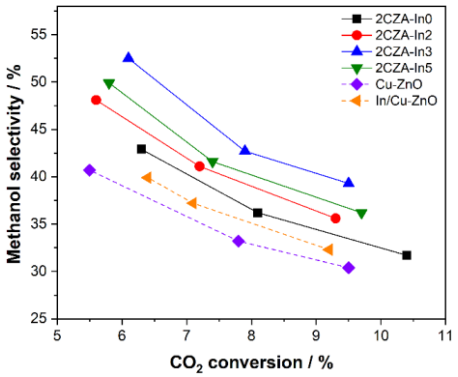

Figure 9. Methanol selectivity at different CO_2 conversions for 2CZA-In*Y*, Cu-ZnO and In/Cu-ZnO. The CO_2 conversion was varied by changing the contact time between 10 000 to 100 000 $cm^3/(g_{cat}$ h). Reaction conditions: 250 °C, 30 bar, $H_2/CO_2 = 3$.

3.2.3 Stability of HT-derived catalysts

The stability of the 2CZA-In0 and 2CZA-In3 catalysts was investigated over 72 h time on stream (TOS), and the CO_2 conversion and methanol selectivity are shown in Figure 10. The CO_2 conversion and methanol selectivity remains relatively stable for the 2CZA-In3 catalyst. A slight increase in CO_2 conversion is observed for the 2CZA-In0 catalyst, whereas the methanol selectivity decreases from 35 to 28%. Consequently, the STY of methanol is reduced by 8% for the 2CZA-In0 catalyst. Therefore, In could help to limit the deactivation of Cu-based catalysts during CO_2 hydrogenation to methanol if In can be stabilized in the Zn-Al oxide phase.

.

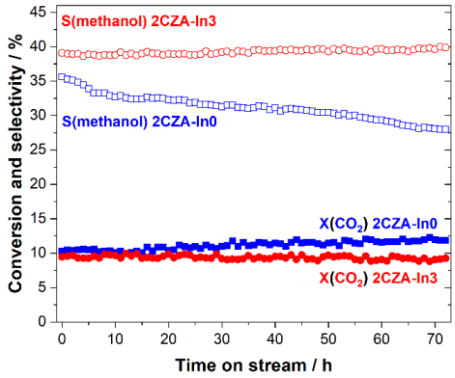

Figure 10. CO_2 conversion and methanol selectivity over the 2CZA-In0 and 2CZA-In3 catalysts over 72 h TOS. Reaction conditions: 250 °C, 30 bar, H_2/CO_2 = 3.

To gain further insight into the deactivation mechanism of the HT-derived catalysts, the spent catalysts were analyzed by N_2-physisorption, XRD, and N_2O chemisorption. Interestingly, the Cu surface area increases from 13 to 21 m^2/g for the 2CZA-In0 catalyst after 72 h, whereas the Cu surface area is relatively unchanged for 2CZA-In3 (Table 6). According to these results, the intrinsic activity of 2CZA-In3 decreases by 8%, whereas the intrinsic activity is substantially reduced for the 2CZA-In0 catalyst by 43%. The XRD patterns of the spent catalysts indicate that the increase in Cu surface area for 2CZA-In0 is related to sintering of the Cu particles and Zn-Al oxide matrix (Figure 11). The Zn-Al matrix appears to be more stable for the In-containing catalyst as crystalline $ZnAl_2O_4$ is only observed for the spent 2CZA-In0 catalyst. This further demonstrates the importance of the Cu-metal oxide

interface on the methanol synthesis activity of the HT-derived catalysts. The structural changes of the 2CZA-In0 catalyst are probably also responsible for the increase in the BET surface area. Thus, it seems that In prevents deactivation of the 2CZA-In3 catalyst by stabilizing the Cu particles and the Zn-Al mixed oxide phase.

Table 6. Physicochemical properties of the spent 2CZA-In0 and 2CZA-In3 catalyst.

Catalyst	d_{Cu} (nm)[a]	SA_{BET} (m^2/g)	SA_{Cu} (m^2/g)
2CZA-In0	20.3	74 (56)[b]	21
2CZA-In3	14.5	58 (54)[b]	16

[a] Determined by XRD of the Cu(111) peak

[b] BET surface area of the reduced catalysts

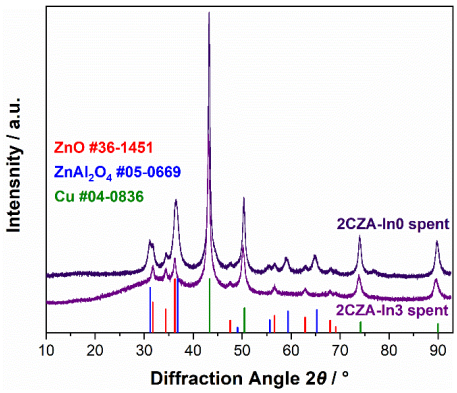

Figure 11. XRD patterns of the spent 2CZA-In0 and 2CZA-In3 catalysts.

5. Conclusion

In summary, partially embedded Cu particles into a Zn-Al oxide matrix were prepared via HT-like precursors. It was demonstrated that the intrinsic activity of the HT-derived catalysts is significantly higher than

a Cu/ZnO catalyst. Thus, a higher space-time yield is achieved for the HT-derived catalyst despite having a smaller Cu surface area. Furthermore, the methanol selectivity is also higher for the HT-derived catalysts. The superior performance is attributed to the enhanced interaction between Cu and the Zn-Al oxide phase. The influence of In on the catalytic performance was also studied. Although the methanol selectivity is higher for the In-containing catalysts, the addition of In to Cu/ZnO-based catalysts significantly reduces the activity. The lower activity of the In-containing catalysts is attributed to the inhibition of active sites on the Cu surface.

The importance of the Cu-metal oxide interaction is supported by the long-term stability tests. The intrinsic activity decreases substantially for the In-free catalyst. This is attributed to the reduced Cu-metal oxide interaction due to the sintering of the Cu particles and Zn-Al oxide matrix. On the other hand, the incorporation of In stabilizes the Cu particles and Zn-Al mixed oxide phase, which significantly limit the deactivation of the catalyst. The present study demonstrates the importance of the microstructure and Cu-metal oxide interface for CO_2 hydrogenation to methanol.

Acknowledgements

The authors would like to thank the financial support from the Norwegian Ministry of Education and Research and the Department of Energy and Petroleum Engineering, University of Stavanger for this project.

References

[1] M. Aresta, A. Dibenedetto, E. Quaranta, State of the art and perspectives in catalytic processes for CO_2 conversion into chemicals and fuels: The distinctive contribution of chemical catalysis and biotechnology, Journal of Catalysis, 343 (2016) 2-45.
[2] X.-M. Liu, G. Lu, Z.-F. Yan, J. Beltramini, Recent advances in catalysts for methanol synthesis via hydrogenation of CO and CO_2, Industrial Engineering Chemistry Research, 42 (2003) 6518-6530.
[3] G.A. Olah, Towards oil independence through renewable methanol chemistry, Angewandte Chemie International Edition, 52 (2013) 104-107.
[4] M. Behrens, F. Studt, I. Kasatkin, S. Kühl, M. Hävecker, F. Abild-Pedersen, S. Zander, F. Girgsdies, P. Kurr, B.-L. Kniep, The active site of methanol synthesis over $Cu/ZnO/Al_2O_3$ industrial catalysts, Science, 336 (2012) 893-897.
[5] Y. He, L. Zhu, J. Fan, L. Li, Comparative exergy and exergoeconomic analysis between liquid fuels production through chemical looping hydrogen generation and methane reforming with CO_2, Energy Conversion Management, 222 (2020) 113239.
[6] A. Álvarez, A. Bansode, A. Urakawa, A.V. Bavykina, T.A. Wezendonk, M. Makkee, J. Gascon, F. Kapteijn, Challenges in the greener production of formates/formic acid, methanol, and DME by heterogeneously catalyzed CO_2 hydrogenation processes, Chemical reviews, 117 (2017) 9804-9838.
[7] K. Stangeland, H. Li, Z. Yu, Thermodynamic analysis of chemical and phase equilibria in CO_2 hydrogenation to methanol, dimethyl ether, and higher alcohols, Industrial & Engineering Chemistry Research, 57 (2018) 4081-4094.
[8] M. Behrens, R. Schlögl, How to prepare a good Cu/ZnO catalyst or the role of solid state chemistry for the synthesis of nanostructured catalysts, Zeitschrift für anorganische und allgemeine Chemie, 639 (2013) 2683-2695.
[9] M.M. Günter, T. Ressler, B. Bems, C. Büscher, T. Genger, O. Hinrichsen, M. Muhler, R. Schlögl, Implication of the microstructure of

binary Cu/ZnO catalysts for their catalytic activity in methanol synthesis, Catalysis letters, 71 (2001) 37-44.
[10] I. Kasatkin, P. Kurr, B. Kniep, A. Trunschke, R. Schlögl, Role of lattice strain and defects in copper particles on the activity of $Cu/ZnO/Al_2O_3$ catalysts for methanol synthesis, Angewandte Chemie International Edition, 46 (2007) 7324-7327.
[11] K. Stangeland, H. Li, Z. Yu, CO_2 hydrogenation to methanol: the structure–activity relationships of different catalyst systems, Energy, Ecology Environment, (2020) 1-14.
[12] F. Studt, M. Behrens, E.L. Kunkes, N. Thomas, S. Zander, A. Tarasov, J. Schumann, E. Frei, J.B. Varley, F. Abild‐Pedersen, The mechanism of CO and CO_2 hydrogenation to methanol over Cu‐based catalysts, ChemCatChem, 7 (2015) 1105-1111.
[13] S. Tada, S. Kayamori, T. Honma, H. Kamei, A. Nariyuki, K. Kon, T. Toyao, K.-i. Shimizu, S. Satokawa, Design of interfacial sites between Cu and amorphous ZrO_2 dedicated to CO_2-to-methanol hydrogenation, ACS Catalysis, 8 (2018) 7809-7819.
[14] R. Van Den Berg, G. Prieto, G. Korpershoek, L.I. Van Der Wal, A.J. Van Bunningen, S. Lægsgaard-Jørgensen, P.E. De Jongh, K.P. De Jong, Structure sensitivity of Cu and CuZn catalysts relevant to industrial methanol synthesis, Nature communications, 7 (2016) 1-7.
[15] J. Nakamura, I. Nakamura, T. Uchijima, Y. Kanai, T. Watanabe, M. Saito, T. Fujitani, A surface science investigation of methanol synthesis over a Zn-deposited polycrystalline Cu surface, Journal of Catalysis, 160 (1996) 65-75.
[16] S. Kattel, P.J. Ramírez, J.G. Chen, J.A. Rodriguez, P. Liu, Active sites for CO_2 hydrogenation to methanol on Cu/ZnO catalysts, Science, 355 (2017) 1296-1299.
[17] S. Kuld, M. Thorhauge, H. Falsig, C.F. Elkjær, S. Helveg, I. Chorkendorff, J. Sehested, Quantifying the promotion of Cu catalysts by ZnO for methanol synthesis, Science, 352 (2016) 969-974.
[18] S.D. Senanayake, P.J. Ramírez, I. Waluyo, S. Kundu, K. Mudiyanselage, Z. Liu, Z. Liu, S. Axnanda, D.J. Stacchiola, J. Evans, Hydrogenation of CO_2 to Methanol on CeO_x/Cu (111) and ZnO/Cu (111) Catalysts: Role of the Metal–Oxide Interface and Importance of Ce^{3+} Sites, The Journal of Physical Chemistry C, 120 (2016) 1778-1784.
[19] F. Liao, Y. Huang, J. Ge, W. Zheng, K. Tedsree, P. Collier, X. Hong, S.C. Tsang, Morphology-Dependent Interactions of ZnO with Cu

Nanoparticles at the Materials' Interface in Selective Hydrogenation of CO_2 to CH_3OH, Angewandte Chemie, 123 (2011) 2210-2213.
[20] M. Behrens, A. Furche, I. Kasatkin, A. Trunschke, W. Busser, M. Muhler, B. Kniep, R. Fischer, R. Schlögl, The potential of microstructural optimization in metal/oxide catalysts: higher intrinsic activity of copper by partial embedding of copper nanoparticles, ChemCatChem, 2 (2010) 816-818.
[21] S. Kühl, A. Tarasov, S. Zander, I. Kasatkin, M. Behrens, Cu-Based Catalyst Resulting from a Cu, Zn, Al Hydrotalcite-Like Compound: A Microstructural, Thermoanalytical, and In Situ XAS Study, Chemistry–A European Journal, 20 (2014) 3782-3792.
[22] O. Martin, A.J. Martín, C. Mondelli, S. Mitchell, T.F. Segawa, R. Hauert, C. Drouilly, D. Curulla-Ferré, J. Pérez-Ramírez, Indium oxide as a superior catalyst for methanol synthesis by CO_2 hydrogenation, Angewandte Chemie International Edition, 55 (2016) 6261-6265.
[23] C.-Y. Chou, R.F. Lobo, Direct conversion of CO_2 into methanol over promoted indium oxide-based catalysts, Applied Catalysis A: General, 583 (2019) 117144.
[24] N. Rui, Z. Wang, K. Sun, J. Ye, Q. Ge, C.-j. Liu, CO_2 hydrogenation to methanol over Pd/In_2O_3: effects of Pd and oxygen vacancy, Applied Catalysis B: Environmental, 218 (2017) 488-497.
[25] J.L. Snider, V. Streibel, M.A. Hubert, T.S. Choksi, E. Valle, D.C. Upham, J. Schumann, M.S. Duyar, A. Gallo, F. Abild-Pedersen, Revealing the synergy between oxide and alloy phases on the performance of bimetallic In–Pd catalysts for CO_2 hydrogenation to methanol, ACS Catalysis, 9 (2019) 3399-3412.
[26] M.S. Frei, C. Mondelli, R. García-Muelas, K.S. Kley, B. Puértolas, N. López, O.V. Safonova, J.A. Stewart, D.C. Ferré, J. Pérez-Ramírez, Atomic-scale engineering of indium oxide promotion by palladium for methanol production via CO 2 hydrogenation, Nature Communications, 10 (2019) 1-11.
[27] Y. Matsumura, H. Ishibe, Durable copper–zinc catalysts modified with indium oxide in high temperature steam reforming of methanol for hydrogen production, Journal of Power Sources, 209 (2012) 72-80.
[28] Y. Matsumura, Development of durable copper catalyst for hydrogen production by high temperature methanol steam reforming, International Journal of Hydrogen Energy, 38 (2013) 13950-13960.

[29] Y. Matsumura, Durable Cu composite catalyst for hydrogen production by high temperature methanol steam reforming, Journal of Power Sources, 272 (2014) 961-969.
[30] J. Słoczyński, R. Grabowski, P. Olszewski, A. Kozłowska, J. Stoch, M. Lachowska, J. Skrzypek, Effect of metal oxide additives on the activity and stability of Cu/ZnO/ZrO2 catalysts in the synthesis of methanol from CO_2 and H_2, Applied Catalysis A: General, 310 (2006) 127-137.
[31] J. Gao, F. Song, Y. Li, W. Cheng, H. Yuan, Q. Xu, Cu_2In nanoalloy enhanced performance of Cu/ZrO_2 catalysts for the CO2 hydrogenation to methanol, Industrial Engineering Chemistry Research, (2020).
[32] Z. Shi, Q. Tan, C. Tian, Y. Pan, X. Sun, J. Zhang, D. Wu, CO_2 hydrogenation to methanol over Cu-In intermetallic catalysts: Effect of reduction temperature, Journal of Catalysis, 379 (2019) 78-89.
[33] L. Yao, X. Shen, Y. Pan, Z. Peng, Synergy between active sites of Cu-In-Zr-O catalyst in CO_2 hydrogenation to methanol, Journal of Catalysis, 372 (2019) 74-85.
[34] M. Sadeghinia, M. Rezaei, A.N. Kharat, M.N. Jorabchi, B. Nematollahi, F. Zareiekordshouli, Effect of In_2O_3 on the structural properties and catalytic performance of the $CuO/ZnO/Al_2O_3$ catalyst in CO_2 and CO hydrogenation to methanol, Molecular Catalysis, 484 (2020) 110776.
[35] B. Liang, J. Ma, X. Su, C. Yang, H. Duan, H. Zhou, S. Deng, L. Li, Y. Huang, Investigation on deactivation of $Cu/ZnO/Al_2O_3$ catalyst for CO_2 hydrogenation to methanol, Industrial Engineering Chemistry Research, 58 (2019) 9030-9037.
[36] M. Behrens, I. Kasatkin, S. Kühl, G. Weinberg, Phase-pure Cu, Zn, Al hydrotalcite-like materials as precursors for copper rich $Cu/ZnO/Al_2O_3$ catalysts, Chemistry of Materials, 22 (2010) 386-397.
[37] R. Wang, Z. Yang, Synthesis and high cycle performance of Zn–Al–In-hydrotalcite as anode materials for Ni–Zn secondary batteries, Rsc Advances, 3 (2013) 19924-19928.
[38] O. Krasnobaeva, I. Belomestnykh, V. Kogan, T. Nosova, V. Skorikov, T. Elizarova, V. Danilov, Indium-containing catalysts for oxidative dehydrogenation of organic compounds, Russian Journal of Inorganic Chemistry, 59 (2014) 693-698.
[39] R. Wang, Z. Yang, B. Yang, T. Wang, Z. Chu, Superior cycle stability and high rate capability of Zn–Al–In-hydrotalcite as negative

electrode materials for Ni–Zn secondary batteries, Journal of Power Sources, 251 (2014) 344-350.
[40] M. Behrens, F. Girgsdies, A. Trunschke, R. Schlögl, Minerals as model compounds for Cu/ZnO catalyst precursors: structural and thermal properties and IR spectra of mineral and synthetic (zincian) malachite, rosasite and aurichalcite and a catalyst precursor mixture, European Journal of Inorganic Chemistry, 2009 (2009) 1347-1357.
[41] P. Kowalik, M. Konkol, M. Kondracka, W. Próchniak, R. Bicki, P. Wiercioch, Memory effect of the CuZnAl-LDH derived catalyst precursor—In situ XRD studies, Applied Catalysis A: General, 464 (2013) 339-347.
[42] K. Ploner, L. Schlicker, A. Gili, A. Gurlo, A. Doran, L. Zhang, M. Armbrüster, D. Obendorf, J. Bernardi, B. Klötzer, Reactive metal-support interaction in the Cu-In_2O_3 system: intermetallic compound formation and its consequences for CO_2-selective methanol steam reforming, Science Technology of Advanced Materials 20 (2019) 356-366.
[43] A. Jedidi, S. Rasul, D. Masih, L. Cavallo, K. Takanabe, Generation of Cu–In alloy surfaces from $CuInO_2$ as selective catalytic sites for CO_2 electroreduction, Journal of Materials Chemistry A, 3 (2015) 19085-19092.
[44] S. Kuld, C. Conradsen, P.G. Moses, I. Chorkendorff, J. Sehested, Quantification of zinc atoms in a surface alloy on copper in an industrial-type methanol synthesis catalyst, Angewandte Chemie, 126 (2014) 6051-6055.
[45] W. Jansen, J. Beckers, J. vd Heuvel, A.D. vd Gon, A. Bliek, H. Brongersma, Dynamic behavior of the surface structure of Cu/ZnO/SiO_2 catalysts, Journal of Catalysis, 210 (2002) 229-236.
[46] M.C. Biesinger, L.W. Lau, A.R. Gerson, R.S.C. Smart, Resolving surface chemical states in XPS analysis of first row transition metals, oxides and hydroxides: Sc, Ti, V, Cu and Zn, Applied Surface Science, 257 (2010) 887-898.
[47] M.C. Biesinger, Advanced analysis of copper X-ray photoelectron spectra, Surface Interface Analysis, 49 (2017) 1325-1334.
[48] P. Gao, F. Li, F. Xiao, N. Zhao, N. Sun, W. Wei, L. Zhong, Y. Sun, Preparation and activity of Cu/Zn/Al/Zr catalysts via hydrotalcite-containing precursors for methanol synthesis from CO_2 hydrogenation, Catalysis Science Technology, 2 (2012) 1447-1454.

[49] F. Li, H. Zhan, N. Zhao, F. Xiao, Copper-based Perovskite Design and Its Performance in CO_2 Hydrogenation to Methanol, Perovskite Materials-Synthesis, Characterisation, Properties, and Applications, IntechOpen2016.
[50] A. Yin, X. Guo, W.-L. Dai, K. Fan, The nature of active copper species in Cu-HMS catalyst for hydrogenation of dimethyl oxalate to ethylene glycol: New insights on the synergetic effect between Cu^0 and Cu^+, The Journal of Physical Chemistry C, 113 (2009) 11003-11013.
[51] J. Wu, S. Yang, Q. Liu, P. He, H. Tian, J. Ren, Z. Guan, T. Hu, B. Ni, C. Zhang, Cu Nanoparticles inlaid mesoporous carbon aerogels as a high performance desulfurizer, Environmental Science Technology, 50 (2016) 5370-5378.
[52] X. Zheng, H. Lin, J. Zheng, X. Duan, Y. Yuan, Lanthanum oxide-modified Cu/SiO_2 as a high-performance catalyst for chemoselective hydrogenation of dimethyl oxalate to ethylene glycol, ACS Catalysis, 3 (2013) 2738-2749.
[53] S. Roso, C. Bittencourt, P. Umek, O. González, F. Güell, A. Urakawa, E. Llobet, Synthesis of single crystalline In_2O_3 octahedra for the selective detection of NO_2 and H_2 at trace levels, Journal of Materials Chemistry C, 4 (2016) 9418-9427.
[54] B. Pujilaksono, U. Klement, L. Nyborg, U. Jelvestam, S. Hill, D. Burgard, X-ray photoelectron spectroscopy studies of indium tin oxide nanocrystalline powder, Materials Characterization, 54 (2005) 1-7.
[55] P. Gao, F. Li, N. Zhao, F. Xiao, W. Wei, L. Zhong, Y. Sun, Influence of modifier (Mn, La, Ce, Zr and Y) on the performance of Cu/Zn/Al catalysts via hydrotalcite-like precursors for CO_2 hydrogenation to methanol, Applied Catalysis A: General, 468 (2013) 442-452.
[56] C. Li, X. Yuan, K. Fujimoto, Development of highly stable catalyst for methanol synthesis from carbon dioxide, Applied Catalysis A: General, 469 (2014) 306-311.
[57] S. Kühl, J. Schumann, I. Kasatkin, M. Hävecker, R. Schlögl, M. Behrens, Ternary and quaternary Cr or Ga-containing ex-LDH catalysts—Influence of the additional oxides onto the microstructure and activity of $Cu/ZnAl_2O_4$ catalysts, Catalysis Today, 246 (2015) 92-100.
[58] S. Xiao, Y. Zhang, P. Gao, L. Zhong, X. Li, Z. Zhang, H. Wang, W. Wei, Y.J.C.T. Sun, Highly efficient Cu-based catalysts via hydrotalcite-like precursors for CO_2 hydrogenation to methanol, Catalysis Today, 281 (2017) 327-336.

[59] S. Natesakhawat, J.W. Lekse, J.P. Baltrus, P.R. Ohodnicki Jr, B.H. Howard, X. Deng, C. Matranga, Active sites and structure–activity relationships of copper-based catalysts for carbon dioxide hydrogenation to methanol, ACS Catalysis, 2 (2012) 1667-1676.

Supporting Information

CO_2 hydrogenation to methanol over partially embedded Cu within Zn-Al oxide the effect of indium promotion

Kristian Stangeland[a], Fawzi Chamssine[a], Wenzhao Fu[b], Zikun Huang[b], Xuezhi Duan[b,*], Zhixin Yu[a,*]

[a] *Department of Energy and Petroleum Engineering, University of Stavanger, 4036 Stavanger, Norway*

[b] *State Key Laboratory of Chemical Engineering, East China University of Science and Technology, 200237 Shanghai, China*

*Corresponding authors:

Zhixin Yu

E-mail: zhixin.yu@uis.no

Xuezhi Duan

E-mail: xzduan@ecust.edu.cn

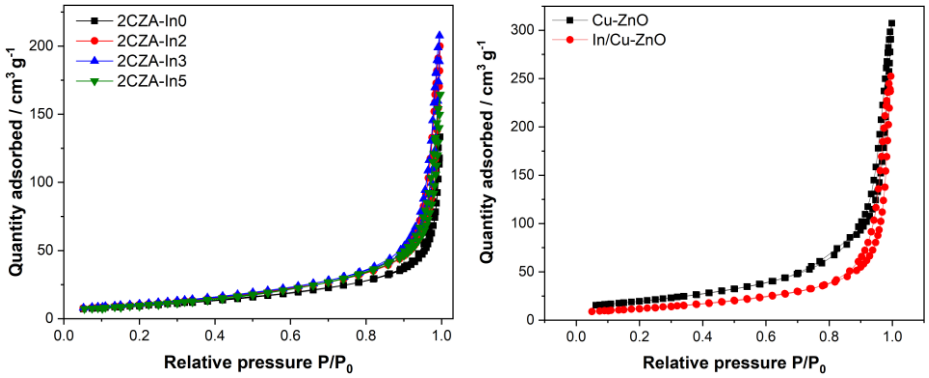

Figure S1. N_2 adsorption-desorption isotherms of the calcined (a) 2CZA-In*Y* and (b) Cu-ZnO and In/Cu-ZnO catalysts.

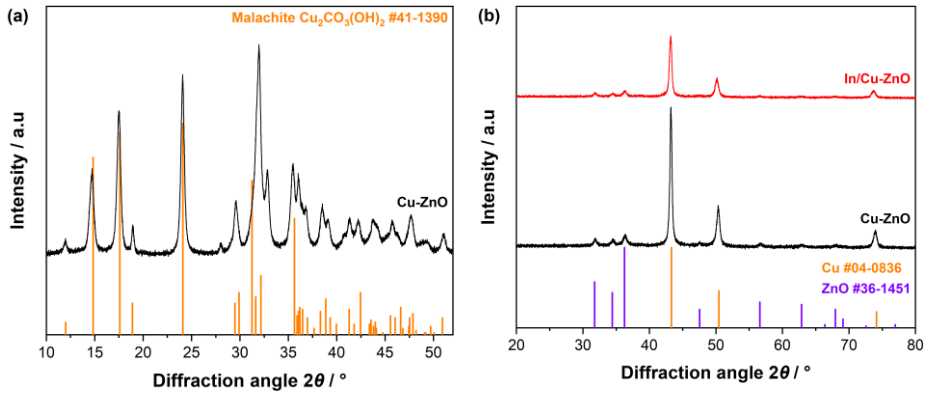

Figure S2. XRD patterns of the (a) Cu-ZnO precursor and (b) reduced-passivated Cu-ZnO and In/Cu-ZnO catalysts.

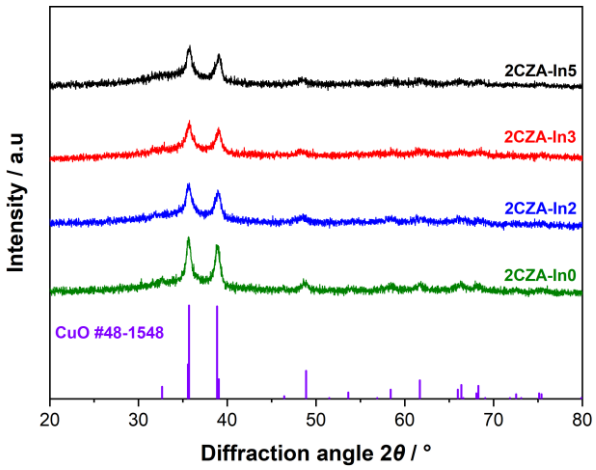

Figure S3. XRD of the calcined 2CZA-In*Y* catalysts.

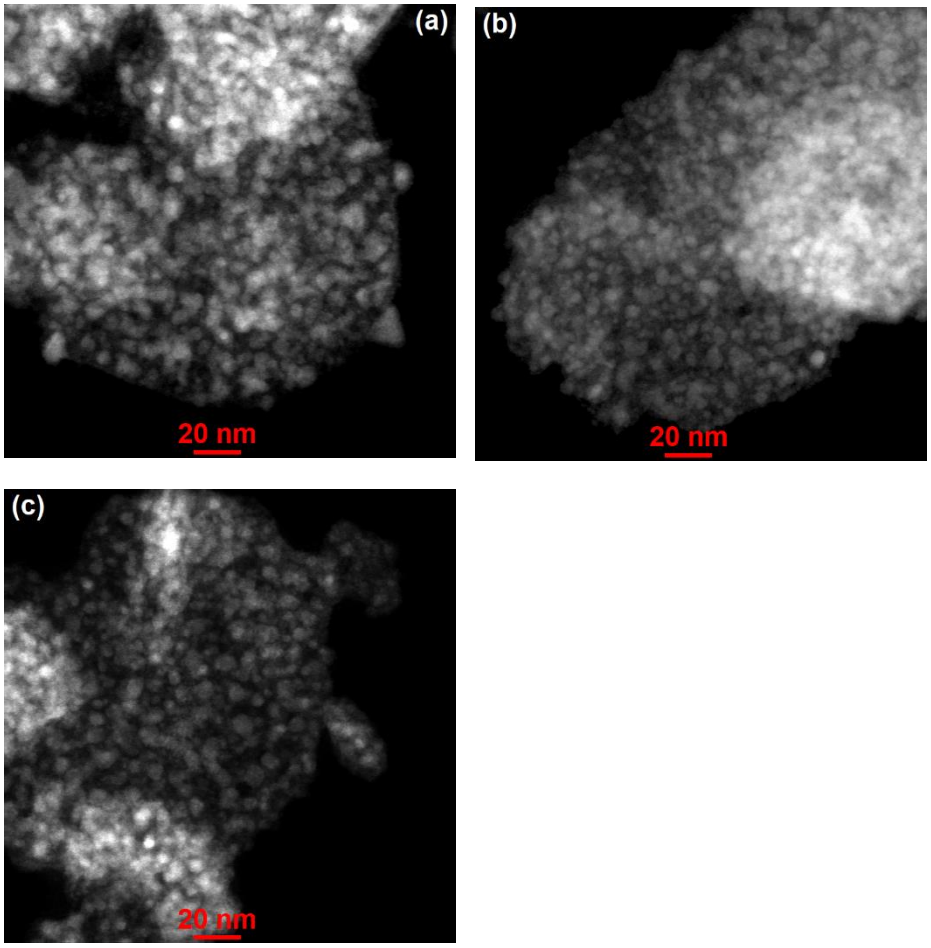

Figure S4. HAADF-STEM images of the reduced (a) 2CZA-In2, (b) 2CZA-In3, and (c) 2CZA-In5 catalysts.

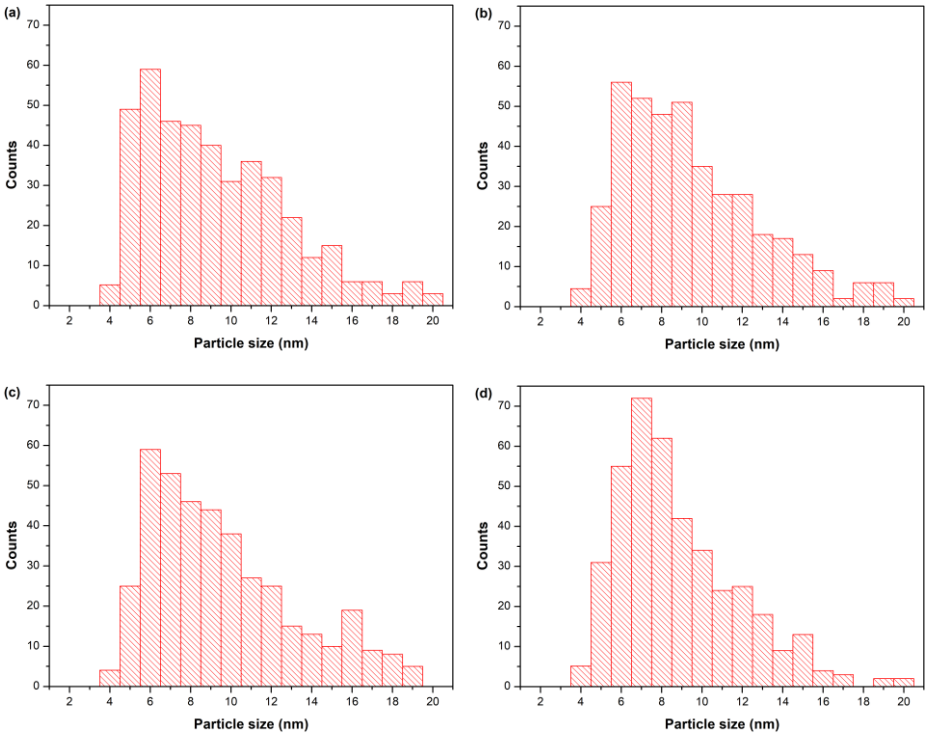

Figure S5. Cu particle size distribution of the (a) 2CZA-In0, (b) 2CZA-In2, (c) 2CZA-In3, and (d) 2CZA-In5 with particle sizes ranging from 4-20 nm.

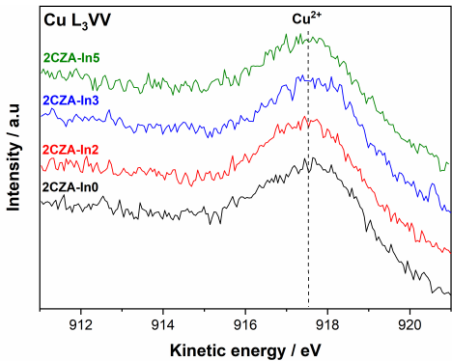

Figure S6. Cu L_3VV Auger spectra of the calcined 2CZA-In*Y* catalysts.

Table S1. BET surface area, Cu crystallite size, and Cu surface area of the 4CZA-In*Y* and 1CZA-In*Y* catalysts.

Catalyst	SA_{BET} (m^2/g)	d_{Cu} (nm)[a]	Cu surface area (m^2/g)[b]
1CZA-In0	38	10.4	10
1CZA-In2	112	11.0	11
1CZA-In4	116	11.4	9
1CZA-In6	96	10.4	6
4CZA-In0	29	18.1	14
4CZA-In2	52	15.3	17
4CZA-In5	51	16.0	13
4CZA-In7	43	17.4	11

[a] Calculated from the (111) peak by the Scherrer equation;

[b] Cu SA determined by N_2O adsorption of reduced catalysts at 350 °C in 7% H_2 for 2 h.

Appendix E Paper V and Supporting Information

Paper V

Tuning the interfacial sites between copper and metal oxides (Zn, Zr, In) for CO2 hydrogenation to methanol.

Kristian Stangeland, Hans H. Nevarro, Huong L. Huynh, Wakshum M. Tucho, and Zhixin Yu

Submitted.

Tuning the interfacial sites between copper and metal oxides (Zn, Zr, In) for CO_2 hydrogenation to methanol

Kristian Stangeland[a], Hans Herrera Nevarro[a], Huong Lan Hoynh[a], Wakshum Mekonnen Tucho[b], Zhixin Yu[a]*

[a] Department of Energy and Petroleum Engineering, University of Stavanger, 4036 Stavanger, Norway

[b] Department of Mechanical and Structural Engineering and Materials Science, University of Stavanger, 4036 Stavanger, Norway

Keywords: CO_2 hydrogenation; methanol; Copper; Indium oxide; Zinc oxide; Zirconium oxide

*Corresponding author. Tel.: +47-5183-2238; fax: +47-5183-2050; Email address: Zhixin.yu@uis.no

Abstract:

The influence of different metal oxides (ZnO, ZrO_2, In_2O_3) in CO_2 hydrogenation to methanol over Cu-based catalysts was studied. The catalysts were characterized using XRD, TGA, TEM, BET, N_2O chemisorption, H_2-TPR, and CO_2-TPD. It was found that impregnation of ZrO_2 onto Cu/ZnO enhanced the activity of the catalyst, whereas the activity was decreased when ZnO was impregnated onto Cu/ZrO_2. The methanol synthesis activity was strongly linked to the basicity of the catalysts. The results also indicate that In-doping of Cu/ZnO and Cu/ZrO_2 results in the formation of Cu_xIn_y alloys, which reduces the activity at high In content. However, the Cu_xIn_y alloys limit the CO production rate to a larger extent than methanol synthesis. It is also demonstrated that new active sites for methanol synthesis are generated for In-doped Cu/ZrO_2 but not for Cu/ZnO. This is attributed to the formation of In-Zr mixed oxide species that enhance the methanol formation rate.

1. Introduction

Recently, the need to combat the effects of greenhouse gas emissions has generated significant interest in developing various technologies for capturing and transforming CO_2 into useful products. CO_2 hydrogenation to methanol is among the most promising approaches for sustainable production of fuels and chemicals from renewable sources (Aresta et al., 2016). Methanol is currently widely employed within the petrochemical industry to produce various compounds, such as olefins, aromatics, and gasoline. Furthermore, methanol is also increasingly used in fuel blends or as an alternative fuel in the transportation sector. Methanol synthesis from synthesis gas (CO, CO_2, H_2) is already a well-established industry, which could assist in the development and large-scale implementation of the CO_2-to-methanol process. Provided a sustainable source of hydrogen becomes available at reasonable costs, recycling CO_2 could become economically viable with sufficient political incentives.

The $Cu/ZnO/Al_2O_3$-based catalysts have been utilized for decades in the industrial methanol synthesis process from syngas (CO, CO_2, H_2), which is operated at 200–300 °C and 50–100 bar. The different behavior of metal oxide-promoted Cu-based catalysts, in terms of activity and stability under different feeds, highlights that optimizing the surface-interface structures is a viable strategy for obtaining efficient CO_2-to-methanol catalysts. (Denise and Sneeden, 1986; Jansen et al., 2002; Studt et al., 2015; Topsøe et al., 1997; Topsøe and Topsøe, 1999). There is compelling evidence that the strong metal-support interaction (SMSI) due to the partial reducibility of metal oxides plays a key role in the CO_2 hydrogenation to methanol over Cu-based catalysts. For Cu/ZnO-based systems, the SMSI is typically attributed to the presence of Zn or ZnO_x species on the Cu surface (Behrens et al., 2012; Fujitani et al., 1997a; Fujitani et al., 1997b; Kattel et al., 2017; Martinez-Suarez et al., 2015; Nakamura et al., 1996a), which stabilizes the oxygen-bound intermediates and enhances the methanol synthesis activity. Furthermore, computational modeling using density functional theory (DFT) and kinetic simulations also indicate that these Zn species play an essential role by activating the formate intermediate and reducing the barrier of the rate-determining step

(Behrens et al., 2012; Kattel et al., 2017; Reichenbach et al., 2018; Zheng et al., 2020). The Cu-ZrO_2 interfacial sites are widely reported to enhance the activation and transformation of CO_2 into methanol over Cu/ZrO_2-based catalysts (Arena et al., 2008; Fujiwara et al., 2019; Gao et al., 2012; Larmier et al., 2017; Tada et al., 2018a; Tada et al., 2018b; Wang et al., 2019b). Cu/ZrO_2 catalysts containing different polymeric phases of ZrO_2 have been reported for methanol synthesis, such as monoclinic (*m*-), tetragonal (*t*-), and amorphous (*a*-) ZrO_2. Jung and Bell (Jung and Bell, 2002) and Rhodes and Bell (Rhodes and Bell, 2005) reported that the activity of Cu/*m*-ZrO_2 is superior compared to Cu/*t*-ZrO_2. In contrast, the results of Baiker et al. (Baiker et al., 1993), Koppel et al. (Köppel et al., 1998), Ma et al. (Ma et al., 2005), and Samson et al. (Samson et al., 2014) suggest that *t*-ZrO_2 is more suitable to promote methanol synthesis over Cu/ZrO_2 catalysts. Highly active and selective catalysts have also been reported over Cu/a-ZrO_2 (Tada et al., 2018a; Witoon et al., 2016). The evidence for SMSI being crucially involved in CO_2 hydrogenation to methanol over Cu-based catalysts also extends to other partially reducible metal oxides, such as CeO_x deposited on Cu (Graciani et al., 2014; Senanayake et al., 2016) and Cu/La_2O_3 (Chen et al., 2019).

Although highly active In_2O_3-based catalysts have been demonstrated (Chou and Lobo, 2019; Frei et al., 2019), the reported activity of In-doped Cu-based catalysts are ambiguous. Słoczyński et al. (Słoczyński et al., 2006) and Sadeghinia et al. (Sadeghinia et al., 2020) found that incorporating a small amount of In into Cu/ZnO-based catalysts significantly reduced the catalytic activity. On the other hand, Shi et al. (Shi et al., 2019) reported synergistic effects between Cu_xIn_y and In_2O_3, resulting in highly selective methanol synthesis catalysts. Gao et al. (Gao et al., 2020) proposed that hydrogen is activated on Cu_xIn_y sites, while the In_2O_3-ZrO_2 phase facilitates CO_2 adsorption and conversion to methanol. Recently, Zhang et al. (Zhang et al., 2020) observed that low amounts of In enhanced the methanol formation rate and selectivity of Cu/ZrO_2. The greater reducibility of In_2O_3 compared to ZnO, ZrO_2, and CeO_2 means that In_2O_3 species migrate readily during reduction and that the formation of surface and bulk Cu_xIn_y alloys is facile. However, these studies indicate that ZrO_2 might have a stabilizing effect on In_2O_3 and generate additional In-Zr mixed oxide sites for methanol synthesis.

Elucidating the relationship between the catalytic structure and interfacial sites of Cu-based catalysts can offer valuable insight for developing high-performance CO_2-to-methanol catalysts. Herein, we provide insight into the highly structure-sensitive nature of Cu-based catalysts and the interplay between different metal oxide promoters. It is demonstrated that impregnating Cu/ZnO with ZrO_2 enhances the methanol synthesis activity, which is attributed to the formation of Cu-ZrO_2 interfacial sites for CO_2 activation and conversion to methanol. In contrast, ZnO-doping of Cu/ZrO_2 reduces the number of active interfacial sites and thereby the methanol formation rate. It is also shown that In-doping of Cu/ZrO_2 can enhance the catalyst's performance, whereas the activity is significantly reduced when In is impregnated onto Cu/ZnO. This is linked to a stabilizing effect of ZrO_2 on In_2O_3, resulting in In-Zr mixed oxide sites for CO_2 conversion to methanol. On the other hand, the In_2O_3 species on Cu/ZnO are easily reduced, leading to In migration to the Cu surface and blockage of active sites. It is also demonstrated that the methanol formation rate is correlated to the surface basicity rather than the Cu surface area of these catalysts.

2. Materials and methods

2.1. Catalyst preparation

The co-precipitated catalysts were prepared following a procedure explained in detail elsewhere (Behrens and Schlögl, 2013). Briefly, an aqueous nitrate solution containing an appropriate ratio of metal nitrates was co-precipitated at a constant pH of 6.5 using sodium carbonate as precipitating agent. The precipitate was aged in the mother liquor for 14 h under vigorous stirring at 65 °C in a sealed cell under a constant flow of N_2. The precipitate was filtered and washed several times with deionized water. The precursors were dried overnight at 90 °C prior to

calcination at 350 or 500 °C for 3 h. The co-precipitated catalysts are denoted as Cu*M*-*X*, where *M* is ZnO, ZrO_2, or In_2O_3 and *X* refers to the calcination temperature. The calcined CuZn-350 was impregnated with an In nitrate or Zr nitrate solution to yield a metal content of 1 mol%. Similarly, the calcined CuZr-350 catalyst was impregnated with In nitrate or Zn nitrate. The impregnated samples were dried and calcined again at 350 °C for 3 h. The impregnated samples are denoted as *M*/CuZn-350 or *M*/CuZr-350, where *M* is ZnO, ZrO_2, or In_2O_3. The nominal and real metal content determined from ICP-AES of the prepared catalysts are summarized in Table 1.

Table 1. Nominal and actual metal content of the Cu-based catalysts determined by ICP-AES.

Catalyst	Nominal metal content (mol%)				Metal content determined by ICP-AES (mol%)			
	Cu	Zn	Zr	In	Cu	Zn	Zr	In
CuZn-350	83.3	16.7	–	–	83.2	16.8	–	–
In/CuZn-350	82.5	16.5	–	1.0	82.2	16.5	–	1.3
Zr/CuZn-350	82.5	16.5	1.0	–	82.2	16.7	1.1	–
CuZr-350	83.3	–	16.7	–	89.1	–	10.9	–
CuZrIn-350	82.9	–	16.6	0.5	88.7	–	11.0	0.3
In/CuZr-350	82.5	–	16.5	1.0	88.0	–	10.9	1.1
Zn/CuZr-350	82.5	1.0	16.5	–	87.8	1.0	11.2	–
CuIn-350	83.3	–	–	16.7	84.1	–	–	15.9

2.2 Characterization of catalysts

N_2 adsorption-desorption measurements were obtained at 77 K using a Micromeritics TriStar II instrument. The samples were degassed prior to

analysis at 120 °C for 14 h with a Micromeritics VacPrep 061 degas system. The specific surface areas and pore size distribution were determined by the Brunauer-Emmet-Teller (BET) and Barret-Joyner-Halenda (BJH) methods, respectively.

The elemental composition of the catalysts was analyzed by ICP-AES on an Agilent 725-ES apparatus. Typically, 200 mg of sample was dissolved in a boiling HNO_3:HCl mixture with a ratio of 1:3 until complete dissolution of the catalyst. The sample was further diluted and filtered prior to elemental analysis.

The X-ray diffraction (XRD) patterns were recorded on a Bruker-AXS Microdiffractometer (D8 ADVANCE) instrument using a Cu Kα radiation source (λ = 1.5406, 40 kV, and 40 mA). The reduced samples were passivated in 1% O_2/N_2 before being transferred to the sample holder. The patterns were collected at 2θ of 10–90° with a step interval of 2 °/min. The peaks were identified using the Joint Committee on Powder Diffraction Standards (JCPDS) database.

The simultaneous thermal gravimetric (TG) and differential scanning calorimetry (DSC) curves were recorded on Netzsch STA449 Jupiter F3 instrument. In a typical experiment, a small amount of sample (10 mg) was heated from room temperature to 700 ^oC at a heating rate of 10 °C/min in synthetic air at a flow rate of 20 mL/min.

The morphology of the reduced catalysts was investigated by transmission electron microscopy (TEM) with a JEOL JEM-2100F instrument operated at 200 kV. The reduced-passivated powders were

dispersed in ethanol by ultrasonication and deposited on a holey carbon-coated copper grid.

Temperature programmed reduction (H_2-TPR) measurements were conducted using a Micromeritics Autochem II ASAP 2920 instrument. First, the sample was heated to 200 °C in He flow for 30 min. Then, the profiles were recorded by passing a 7% H_2/Ar mixture at 50 mL/min over the sample while the temperature was ramped from ambient to 550 °C at 10 °C/min.

Temperature programmed desorption (CO_2-TPD) was carried out using the same instrument as for H_2-TPR. About 100 mg of sample was pretreated at 200 °C for 30 min under He, reduced at 350 °C for 2 h, and then purged with He for 1 h. CO_2 adsorption was performed with a 6 vol% CO_2/Ar mixture at 50 °C for 1 h. Physically adsorbed CO_2 was removed by purging the sample in He flow for 1 h. CO_2-TPD was carried out under constant He flow (40 mL/min) from ambient to 800 °C at a heating rate of 10 °C/min.

The exposed Cu surface area (SA_{Cu}) was determined by a dissociative N_2O adsorption method using a Micromeritics Autochem 2920 instrument. Before N_2O adsorption, the sample was heated to 200 °C in He flow for 30 min and reduced at 350 °C in 7% H_2/Ar mixture (50 mL/min) for 2 h. Then, He was passed over the sample until the temperature reached 50 °C. The N_2O adsorptive decomposition was carried out in a 1% N_2O/He mixture at 50 °C for 1 h following a procedure described by Van Der Grift et al (Gervasini and Bennici, 2005;

Liang et al., 2019; Van Der Grift et al., 1991). After that, the sample tube was purged with He for 1 h to remove the unreacted N_2O. Finally, the H_2 consumption was determined by a second H_2-TPR experiment from 50 to 400 °C at a rate of 10 °C/min in a 7% H_2/Ar mixture. The Cu surface area (SA_{Cu}) was calculated using Eq. 1.

$$SA_{Cu}\ (m^2 \cdot g_{cat}^{-1}) = \frac{Y \times SF \times N_A}{C_M \times W_{cat}} \qquad \text{(Eq. 1)}$$

Where Y is the moles of H_2 consumed in the TPR following N_2O chemisorption, SF is the stoichiometric factor (2), N_A is Avogadro's number (6.022×10^{23} mol^{-1}), C_M is the number of surface Cu atoms per unit surface area (1.47×10^{19} atoms·m^{-2}), and W_{cat} is the amount of catalyst (g).

2.3 Catalytic activity tests

The CO_2 hydrogenation experiments were carried out in a custom-built fixed-bed continuous-flow reactor. Typically, 0.1 g of the sieved catalyst was mixed with SiC (1 g) and placed in a stainless tube reactor with an internal diameter of 0.5 cm and a length of 50 cm. The catalysts were reduced for 2 h at 350 °C with a heating rate of 2 °C/min by 10% H_2/N_2 (50 ml/min). The reactor was cooled to ambient temperature, pressurized with the reactant gases ($H_2/CO_2/N_2$ = 3/1/1), and then heated to the desired reaction temperature before the activity tests. Product condensation was avoided by heating the post-reactor lines and valves to 140 °C. On-line analysis of the exit stream was performed with an

Agilent 7890 B system fitted with two TCD detectors. The CO_2 conversion was calculated utilizing N_2 as internal standard based on Eq. 2. The methanol selectivity ($S_{methanol}$) and space-time yield of methanol ($STY_{methanol}$) were calculated using Eq. 3 and Eq. 4, respectively.

$$X_{CO_2}(\%) = \left[1 - \frac{\text{moles } CO_{2,out}}{\text{moles } CO_{2,in}} \times \frac{\text{moles } N_{2,in}}{\text{moles } N_{2,out}}\right] \times 100 \qquad \text{(Eq. 2)}$$

$$S_{methanol}(\%) = \frac{\text{moles methanol}_{out}}{\text{moles methanol}_{out} + \text{moles } CO_{out}} \times 100 \qquad \text{(Eq. 3)}$$

$$STY_{methanol}\ (mmol_{methanol} \cdot g_{cat}^{-1} \cdot h^{-1}) = \frac{F_{CO_2,in} \times X_{CO_2}/100 \times S_{methanol}/100}{W_{cat}} \qquad \text{(Eq. 4)}$$

Where $F_{CO2,in}$ (mmol/h) is the molar flow rate of CO_2 at the inlet of the reactor and Wcat (g) is the amount of catalyst.

3. Results and discussion

3.1 Catalyst characterization

3.1.1 N_2 physisorption

The N_2 physisorption results of the CuZn and CuZr catalysts are summarized in Table 2. The BET surface area of the CuZn-350, CuZr-350, and CuZrIn-350 catalysts prepared by co-precipitation are similar in the range of 72–77 m^2/g. Furthermore, the pore volume is also comparable for these catalysts (0.17-0.19 cm^3/g). The impregnated catalysts exhibit lower BET surface area and pore volume, which is

expected due to the second heat treatment of these samples. The decrease in BET surface area is more significant for In/CuZn-350 (46 m^2/g) and Zr/CuZn-350 (48 m^2/g) compared to In/CuZr-350 (63 m^2/g) and Zn/CuZr-350 (61 m^2/g).

Table 2. Structural properties of the CuZn and CuZr catalysts.

Catalyst	SA_{BET} (m^2/g)	Pore volume (cm^3/g)	Pore diameter (nm)	$d_{CuO(111)}$ (nm)	$d_{Cu(111)}$ (nm)	$d_{ZnO(101)}$ (nm)
CuZn-350	72	0.17	7.7	5.9	23.7	10.4
In/CuZn-350	46	0.11	7.6	7.8	20.1	9.1
Zr/CuZn-350	48	0.11	7.4	8.1	21.8	9.8
CuZr-350	73	0.18	7.9	7.8	21.3	–
CuInZr-350	77	0.18	8.8	8.2	21.7	–
In/CuZr-350	63	0.15	9.2	8.8	22.2	–
Zn/CuZr-350	61	0.15	7.8	8.7	21.9	–

3.1.2 XRD

Figure 1 shows the XRD patterns of the CuZn, CuZr, and CuZrIn catalyst precursors. It can be seen that the diffraction patterns are in excellent agreement with the reference pattern of crystalline malachite (PDF #41-1390). For the CuZn sample, the shift of the $20\bar{1}$ (~31.5°2θ) and the $21\bar{1}$ (~32.5°2θ) peaks towards higher angels is due to Zn^{2+} incorporation into the malachite structure (Behrens et al., 2009). No shift in the position of the peaks is observed for the other precipitated samples. The presence of In (~0.3 mol%) in the CuZrIn sample results in less intense and broader

reflections compared to CuZr. This suggests that In is highly dispersed and prevents the crystallite growth of malachite.

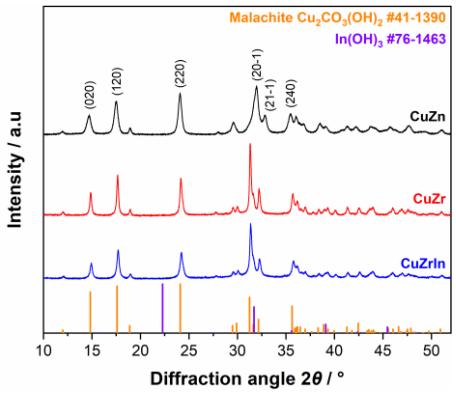

Figure 1. XRD patterns of the CuZn, CuZr, and CuZrIn precursors prepared by co-precipitation.

The XRD patterns of the calcined CuZn-350, In/CuZn-350, and Zr/CuZn-350 catalysts are shown in Figure 2a, while Figure 2b shows the patterns of the CuZr-350, CuZrIn-350, In/CuZr-350, and Zn/CuZr-350 catalysts. It can be seen that all of the calcined samples contain well-crystalline CuO (PDF #48-1548) with reflections at 2θ of 32.5°, 35.5°, 38.7°, and 48.7°. The CuO crystallite sizes estimated by the Scherrer equation are summarized in Table 2. The CuO crystallite size increased from 5.9 nm (CuZn-350) to 7.8 and 8.1 nm for the In/CuZn-350 and Zr/CuZr-350 catalysts, respectively. Furthermore, peaks corresponding to ZnO are present for the In/CuZn-350 and Zr/CuZn-350 samples with reflections at 31.8° and 56.6° (#36-1451). A slight increase in crystallite size from 7.8 to 8.8 nm is also observed for the impregnated CuZr-350 catalysts. The crystallite size of the CuZrIn-350 catalyst (8.2 nm) is

similar to that of CuZr-350, indicating that In did not improve the dispersion of CuO after calcination. No reflections corresponding to In_2O_3 or ZrO_2 are present in the XRD patterns, indicating that these species are amorphous or highly dispersed.

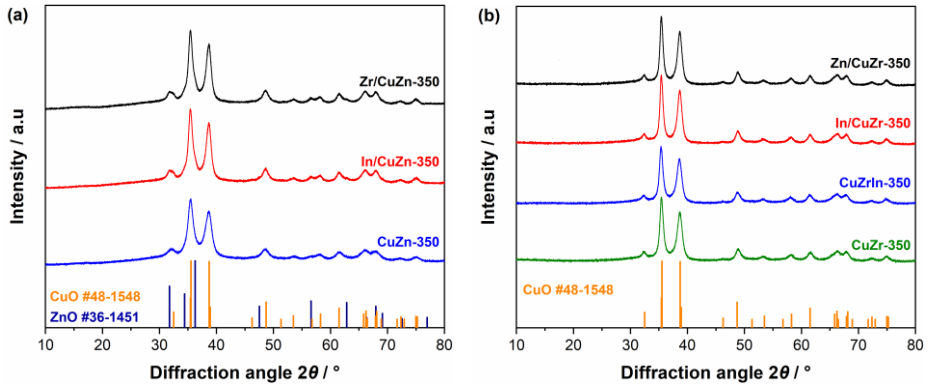

Figure 2. XRD patterns of calcined (a) CuZn-350, In/CuZn-350, and Zr/CuZn-350; and (b) CuZr-350, CuZrIn-350, In/CuZr-350, and Zn/CuZr-350.

Figure 3a shows the XRD pattern of the CuZn-350, In/CuZn-350, and Zr/CuZn-350 catalysts after reduction at 350 °C. The diffractograms of the reduced CuZr-350, CuZrIn-350, In/CuZr-350, and Zn/CuZr-350 catalysts are shown in Figure 3b. The patterns of all the reduced catalysts show reflections at 43.3°, 50.4°, 74.1°, and 89.9°, which correspond to metallic Cu (PDF #04-0836). The crystallite size of Cu is relatively similar for the CuZn and CuZr catalysts between 20.1 to 23.7 nm (Table 2). For the CuZn catalysts, the peaks corresponding to ZnO can be observed at 31.8°, 34.4°, and 36.3° (PDF #36-1451). On the other hand, amorphous ZrO_2 (*a*-ZrO_2) is present for the CuZr samples, in agreement

with literature (Tada et al., 2018b). The XRD pattern of the reduced CuIn-350 sample is shown in Figure S1c. It was found that the peaks of Cu are shifted towards lower diffraction angles for the CuIn-350 sample, indicating the incorporation of In into the bulk of the Cu crystallites. Furthermore, peaks matching fairly well with that of Cu_7In_3 (PDF #65-2249) was observed, whereas crystalline In_2O_3 was not detected. To assess the migration of In into the bulk of Cu for the In-containing CuZn and CuZr catalysts, the *d*-spacing was calculated from the Cu(311) peak (Figure 3c). The *d*-spacing increases when In is impregnated onto the CuZn-350 catalyst. Interestingly, In does not appear to migrate into the bulk of Cu crystallites when In is impregnated onto the CuZr-350 catalyst, but the *d*-spacing increases for CuZrIn-350 prepared by co-precipitation. The *d*-spacing is slightly higher for CuZn and Zr/CuZn compared to the CuZr-350 and CuZrIn-350 catalysts, which might be related to distortion of the Cu lattice by Zn (Günter et al., 2001).

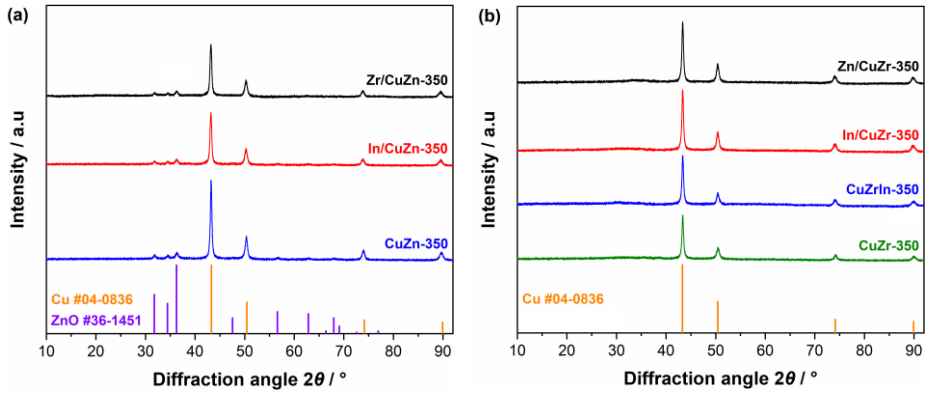

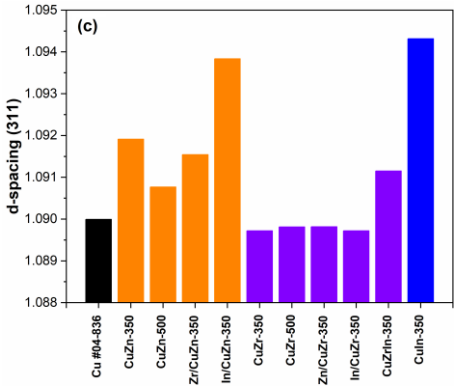

Figure 3. XRD patterns of reduced-passivated (a) CuZn-350, In/CuZn-350, and Zr/CuZn-350; and (b) CuZr-350, CuZrIn-350, In/CuZr-350, and Zn/CuZr-350; The *d*-spacing of the Cu(311) peak of the reduced CuZn and CuZr catalysts (c).

3.1.3 TGA

The TGA coupled with DSC study results of the CuZn, CuZr, and CuZrIn precursors are shown in Figure 4a–c. The first segment below ca. 110 °C and the mass loss between ca. 200–280 °C on the TG curves correspond to the desorption of adsorbed water on the surface and loss of lattice hydroxyl groups, respectively. The significant mass loss between ca. 300–350 °C is attributed to the decomposition of the malachite phase. An additional mass loss step centered at ca. 420 °C can be observed for the CuZn precursor, which is reported to be due to carbonate decomposition and is often referred to as “high-temperature carbonate” (Kondrat et al., 2018; Kondrat et al., 2016; Tarasov et al., 2014). The higher decomposition temperature of this carbonate species

for the CuZn sample is due to the incorporation of Zn into the malachite phase, as indicated by XRD. For the Zr-containing precursors, an exothermic peak can be observed at 627 °C, which is ascribed to the transformation of *t*-ZrO_2 to *m*-ZrO_2 (Tada et al., 2018b). The TGA and DSC curves of the CuIn precursor is shown in Figure S2 and are similar to that of the CuZn, CuZr, and CuZrIn samples.

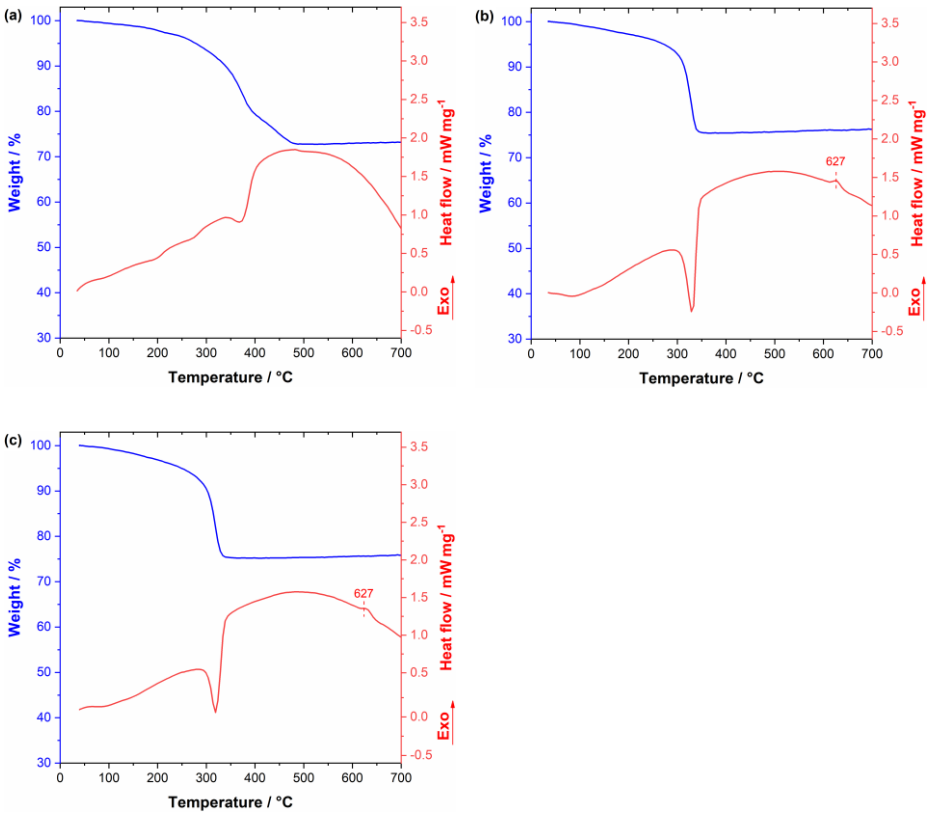

Figure 4. TG and DSC curves for the (a) CuZn, (b) CuZr, and (c) CuZrIn precursors. Blue and red lines are the TG and DSC curves, respectively. Heating rate: 10 °C/min.

3.1.3 TEM

Figure 5 shows representative TEM images of the reduced (a) CuZn-350 and (b) In/CuZn.350 catalysts. It can be seen that the morphology of CuZn-350 and In/CuZn-350 is similar. This is consistent with the comparable Cu and ZnO crystallite size of these catalysts, as indicated by XRD. A range of different particle sizes can be observed for all the samples. Several large particles and agglomerates are present, and these particles are primarily composed of Cu. The smaller particles are probably ZnO, which is supported by the smaller crystallite size of ZnO compared to Cu (Table 2). This is also consistent with literature (Van Den Berg et al., 2016), and one of the roles of ZnO is to act as a spacer to help disperse the Cu phase. No new features can be detected in the TEM images due to the presence of In for the In/CuZn-350 catalyst.

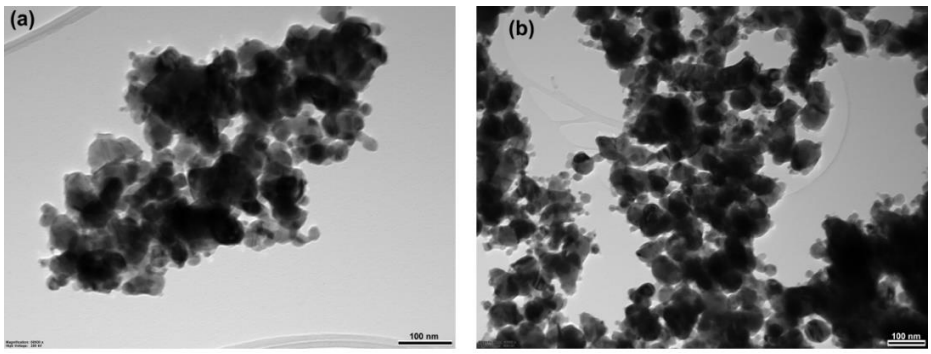

Figure 5. TEM images of the reduced-passivated (a) CuZn-350 and (b) In/CuZn-350 catalysts.

Figure 6 shows the TEM images of the reduced (a) CuZr-350, (b) CuZrIn-350, and (c) In/CuZr-350 catalysts. It can be seen that dense and

less dense areas are present in all of the samples. This demonstrates that ZnO is a more suitable structural promoter compared to ZrO_2. Additional TEM images comparing the morphology of CuZn-350 and CuZr-350 is shown in Figure S3a and Figure S3b, respectively. The denser regions are probably arise because of the significantly smaller size of ZrO_2 compared to ZnO. This results in the Cu particles being in closer proximity to each other and can agglomerate more easily. The ZrO_2 species in the CuZr catalysts are composed of particles around 5 nm (Figure 6d), and their size is not affected by the preparation history of the catalysts. For all the CuZr catalysts, ZrO_2-rich and ZrO_2-deficient areas can be identified. Thus, the ZrO_2 coverage of Cu ranges from fully covered Cu species to practically uncovered ones. No information about the In species can be deduced from the TEM images of the In/CuZr-350 and CuZrIn-350 catalysts.

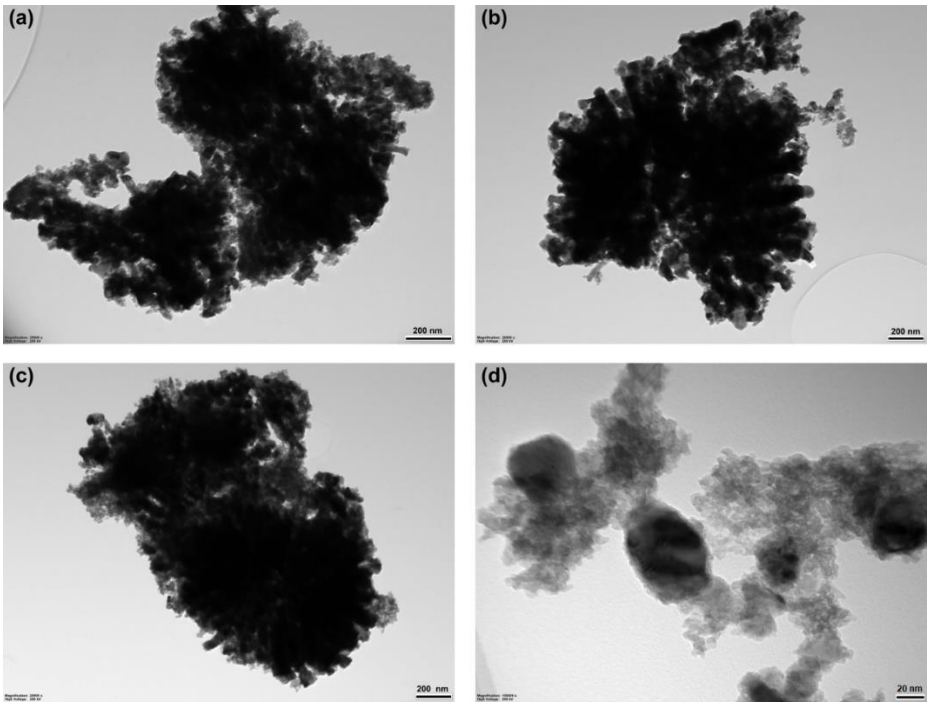

Figure 6. TEM images of the reduced-passivated (a) CuZr-350, (b) CuZrIn-350, (c) In/CuZr-350, and (d) CuZr-350 (higher magnification) catalysts.

3.1.3 Reducibility of the catalysts

The deconvoluted TPR patters of CuZn-350, In/CuZn-350, and Zr/CuZn-350 catalysts are shown in Figure 7. Three deconvoluted peaks are identified, namely α, β, and γ, related to different CuO species. For the CuZn-350 catalysts, the reduction peaks corresponding to β- and γ-species can be observed. The β-peak is due to the reduction of surface CuO species, while the γ-peak is ascribed to the reduction of bulk CuO

(Gao et al., 2012; Gao et al., 2013). The impregnation of In_2O_3 or ZrO_2 onto the CuZn-350 catalyst results in the formation of an α-peak located at a lower temperature. *In situ* X-ray adsorption near edge structure (XANES) has identified that the reduction of CuO proceeds through two steps ($CuO \rightarrow Cu_2O \rightarrow Cu$) when CuO is in intimate contact with ZnO (Kühl et al., 2014), $ZnAl_2O_4$ (Kühl et al., 2014), and ZrO_2 (Ro et al., 2016). In contrast to ZnO, the $ZnAl_2O_4$ and ZrO_2 can stabilize the Cu_2O intermediate, which results in a pronounced shoulder in the TPR pattern. The α-peak can also be observed in the TPR profile of the CuIn-350 catalyst (Figure S4). Therefore, the α-species are related to stabilized Cu_2O species formed at lower reduction temperature due to the enhanced reducibility of CuO in contact with In_2O_3 and ZrO_2. The H_2/CuO ratios were estimated from the TPR peak areas and are summarized in Table 3. The H_2/Cu ratio is close to 1 for CuZn catalysts, indicating complete reduction of CuO. For the CuIn-350 catalysts, the H_2/Cu ratio is 1.12 below 240 °C, indicating that highly dispersed In_2O_3 species also are reduced at relatively low temperature.

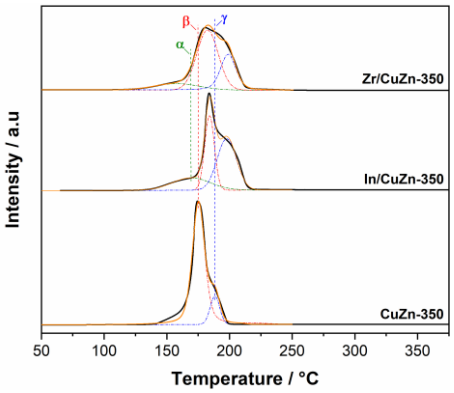

Figure 7. Deconvoluted H_2-TPR patterns of the CuZn-350, In/CuZn-350, and Zr/CuZn-350 catalysts.

Table 3. Summary of H_2-TPR results, Cu surface areas, and relative number of MB sites of the CuZn and CuZr catalysts.

Catalyst	H_2/CuO ratio	α (%)[a]	β (%)[a]	γ (%)[a]	SA_{Cu} (m^2/g)[b]	Relative number of MB sites	$A_{HT\text{-}MB}/A_{MB}$
CuZn-350	0.98[a]	0	85.5	15.5	18	0.22[c]	0
In/CuZn-350	1.01[a]	13.3	59.1	27.6	14	0.18[c]	0
Zr/CuZn-350	1.00[a]	32.9	45.8	21.3	17	0.35[c]	0
CuZr-350	0.92[a]	38.1	48.9	13.0	34	1.00[c]	0.24[d]
CuZrIn-350	0.99[a]	37.7	37.0	25.3	36	0.86[c]	0.42[d]
In/CuZr-350	0.93[a]	26.1	40.2	33.7	26	0.55[c]	0.35[d]
Zn/CuZr-350	0.98[a]	29.1	49.5	21.4	32	0.88[c]	0.26[d]

[a] Determined from H_2-TPR; [b] Estimated from N_2O chemisorption; [c] Obtained from CO_2-TPD; [d] Ratio of high-temperature MB sites to total number of MB sites.

The deconvoluted TPR patterns of the CuZr-350, CuZrIn-350, In/CuZr-350, and Zn/CuZr-350 catalysts are shown in Figure 8. It can be seen that

the α-peak areas are higher for the CuZr catalysts compared to the Zr/CuZn-350 and In/CuZn-350 samples because of the higher ZrO_2 content. The incorporation of In by co-precipitation shift the reduction profile towards lower temperature, which might be due to the presence of In in the bulk of CuO. Interestingly, In/CuZr-350 contains the lowest number of α-species of the CuZr catalysts, whereas the formation α-species occurs when In is impregnated onto CuZn-350 (Table 3). The number of α-species is also reduced when Zn is impregnated onto the CuZr-350 catalysts. The lower amount of α-species suggests that In and Zn adsorption is more favorable on the ZrO_2 phase during impregnation, which reduces the interaction between Cu and ZrO_2. The H_2/Cu ratio is 0.92 and 0.93 for the CuZr-350 and In/CuZr-350, respectively, which could be due to the formation of stable Cu^+ species. On the other hand, the H_2/Cu ratio is close to 1 for the CuZrIn-350 and Zn/CuZr-350 catalysts.

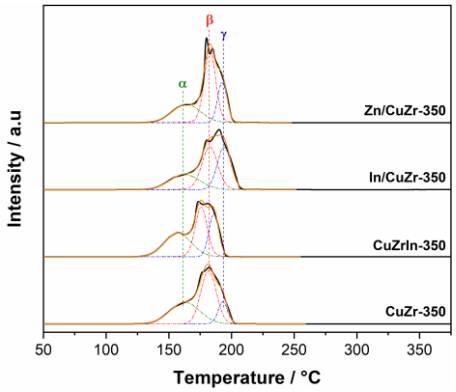

Figure 8. Deconvoluted H_2-TPR patterns of the CuZr-350, CuZrIn-350, In/CuZr-350, and Zn/CuZr-350 catalysts.

3.1.4 N_2O adsorption measurements

The Cu surface areas were estimated by N_2O adsorption and are summarized in Table 3. The Cu surface area of the CuZn-350 is 18 m^2/g, which decreases to 14 m^2/g when In is impregnated onto the CuZn-350 catalyst. On the other hand, the Cu surface area of the Zr/CuZn-350 catalyst (17 m^2/g) is comparable to that of CuZn-350. The smaller number of Cu atoms on the surface of In/CuZn-350 is attributed to In-migration onto the Cu surface during reduction. This is supported by the significant drop in Cu surface area when the reduction temperature is increased for the CuIn-350 catalyst (Figure S5). The CuZr-350, CuZrIn-350, and Zn/CuZr-350 catalysts exhibit similar Cu surface areas in the range of 31–36 m^2/g. It can be seen that the Cu surface area is also significantly reduced when In is impregnated onto the CuZr-350 catalyst (26 m^2/g). It has been reported that the oxygen vacancies of metal oxides can contribute to the N_2O consumption (Chatterjee et al., 2019; Fichtl et al., 2014; Kuld et al., 2014). Nevertheless, the decrease in Cu surface area is relatively high when In is impregnated onto CuZn-350 and CuZr-350, which suggests that the Cu surface is partially covered by In after reduction for both catalysts.

3.1.5 CO_2-TPD

The surface basicity of the catalysts was studied by CO_2-TPD. Figure 9a shows the CO_2-TPD profiles of CuZn-350, In/CuZn-350, and Zr/CuZn-350, while the profiles of CuZr-350, CuZrIn-350, In/CuZr-350, and Zn/CuZr-350 are shown in Figure 9b. The profiles were deconvoluted into three regions: weak basic (WB) sites related to the Cu surface (Bönicke et al., 1994) or OH^- groups (50–200 °C), medium-strength basic (MB) sites associated with metal-oxygen pairs (e.g., Zr–O, In–O) (200–480 °C), and strong basic sites due to low-coordination O^{2-} species (480-800 °C) (Zhang et al., 2020). The MB sites of the CuZn catalyst might be due to oxygen defects in ZnO or ZnO_x species present on the Cu surface after reduction (Zhao et al., 2018). It can be seen the number of moderate basic sites increases when ZrO_2 is impregnated onto the CuZn-350 catalyst. Furthermore, the Zr/CuZn-350 catalyst also contains a significant amount of strong basic sites. On the other hand, the addition of In reduces the surface basicity of the CuZn-350 catalyst. Different types of MB and SB sites are also present in the CO_2 TPD profiles of the CuZr catalysts. The CuZr-350 has the highest quantity of MB sites (Table 3). Incorporation of In by co-precipitation results in a higher fraction of high-temperature MB sites for the CuZrIn-350 catalyst. When Zn or In is impregnated onto the CuZr-350 catalyst, the amount of MB sites decreases accompanied by a significant increase in SB sites. Since the amount of SB sites is also very high for the Zr/CuZn-350 sample, the increase in SB sites for the impregnated catalysts is probably related to the interaction between ZnO or In_2O_3 species with ZrO_2. The CO_2-TPD profiles of CuIn-350, CuZn-500, and CuZr-500 are shown in Figure S6.

Notably, the surface basicity of the CuIn-350 catalyst is much lower than that of the other samples.

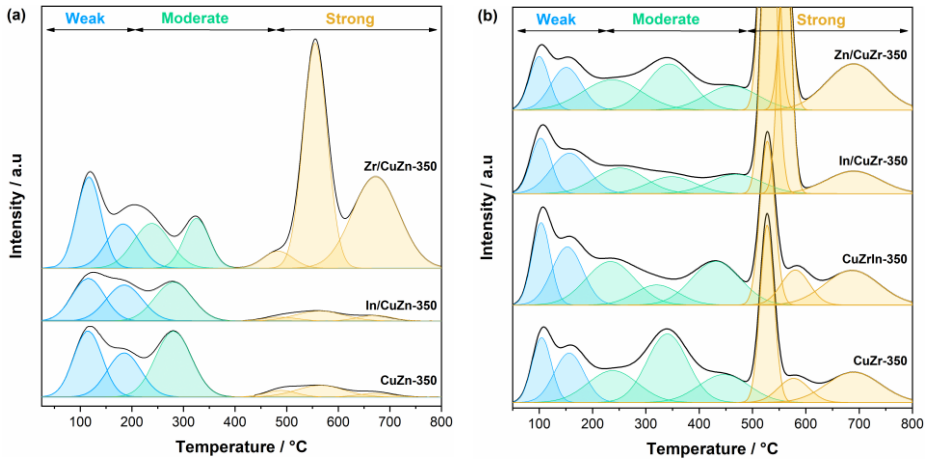

Figure 9. CO_2-TPD profiles of the (a) CuZn-350, In/CuZn-350, and Zr/CuZn-350 catalysts; and the (b) CuZr-350, CuZrIn-350, In/CuZr-350, and Zn/CuZr-350 catalysts.

3.2 Catalytic activity tests

3.2.1 Comparison of the CuZr and CuZn catalysts

Figure 10 shows the steady-state production rates of methanol and CO for the CuZn and CuZr catalysts. A summary of the characterization results of the CuZn-500 and CuZr-500 catalysts can be found in the Table S1. A methanol formation rate of 14.7 $mmol \cdot g_{cat}^{-1} \cdot h^{-}1$ is obtained over the CuZn-350 catalyst. Although the CuZn-500 catalyst shows similar overall activity, a decrease in the methanol formation rate accompanied by an increase in the CO production rate can be observed. There is strong

evidence that the metal-support interaction is an important factor for the methanol synthesis activity of Cu/ZnO-based catalysts. Therefore, the lower methanol production rate (12.4 mmol·g_{cat}^{-1}·h^{-1}) of the CuZn-500 catalyst is attributed to the decrease in metal-support interaction, as indicated by XRD and CO_2-TPD. The highest methanol formation rate is obtained over the Zr/CuZn-350 catalyst (15.6 mmol·g_{cat}^{-1}·h^{-1}), which is ascribed to the formation of Cu-ZrO_2 interfacial sites. It can also be seen the CO production rate is significantly lower at these reaction conditions for the Zr/CuZn-350 catalyst compared to CuZn-350 and CuZn-500.

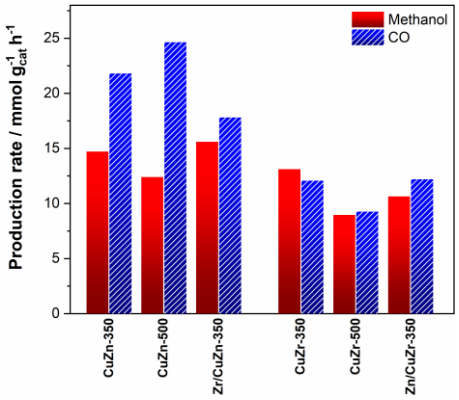

Figure 10. Methanol and CO production rates for the CuZn and CuZr catalysts. Reaction conditions: 230 °C, 30 bar, 38 000 $cm^3/(g_{cat}$ h), H_2/CO_2 = 3.

The methanol formation rate of the CuZr-350 catalyst (13.1 mmol·g_{cat}^{-1}·h^{-1}) is lower than that of CuZn-350 despite the higher N_2O consumption. We expect that the main reason for this is that the number of Cu-Zr interfacial sites is not reflected by the Cu surface area obtained

from N_2O chemisorption for our CuZr catalysts. The activity of Cu/ZrO_2-based catalysts is critically linked to the interfacial sites, which facilitate CO_2 activation and hydrogenation to methanol (Ro et al., 2016; Rungtaweevoranit et al., 2016; Samson et al., 2014; Tada et al., 2018b; Wang et al., 2019b). Zr-rich and Zr-deficient regions are present in the TEM images of the CuZr catalysts, indicating that the preparation method used in this work is not optimal for obtaining well-mixed Cu/ZrO_2 catalysts. Thus, the lower Cu surface-normalized activity of the CuZr catalysts is probably due to a limited number of interfacial sites. Furthermore, oxidation of unpromoted Cu sites might also contribute to the lower activity per Cu surface area of the CuZr catalysts (Liang et al., 2019). The drop in activity of the CuZr-500 catalysts is attributed to the decrease in basicity after calcination at 500 °C, as evidenced by CO_2-TPD. It can be seen that the addition of ZnO to Cu/ZrO_2 has the opposite effect of impregnating ZrO_2 onto Cu/ZnO. This is attributed to the decrease in MB basic sites of Zn/CuZr-350 catalyst compared to CuZr-350. Furthermore, the lower activity of Zn/CuZr-350 also indicates that the SB sites formed when ZnO is located at the surface of ZrO_2 do not contribute to methanol synthesis.

To compare the methanol selectivity of the CuZn and CuZr catalysts, the effect of contact time was investigated by varying the GHSV between 20 000 and 100 000 $cm^3 \cdot g_{cat}^{-1} \cdot h^{-1}$. The methanol selectivity is plotted against the CO_2 conversion after reaching stable production rates for the CuZn and CuZr catalyst in Figure 11a and b, respectively. As expected, the methanol selectivity increases with decreasing CO_2 conversion, i.e.,

increasing GHSV, for all the catalysts (Tada et al., 2018b). Extrapolation of the methanol selectivity to zero conversion (zero contact time) of the CuZn and CuZr catalysts yields a positive initial formation rate for both methanol and CO. This indicates that methanol and CO are primary products over the CuZn and CuZr catalysts (Larmier et al., 2017). The shape and location of the trend lines are related to the active sites present on the catalysts' surface. The active sites of CuZn-350 and CuZn-500 can generally be divided into (i) surface metallic Cu and (ii) Cu-ZnO interfacial sites. The methanol selectivity of CuZn-350 and CuZn-500 indicates that CO formation primarily occurs on the Cu surface and a higher quantity of Cu-ZnO interfacial sites is favorable for methanol synthesis. This is supported by the comparable Cu surface area of these catalysts, whereas XRD and CO_2-TPD indicate superior Cu-ZnO interaction for CuZn-350. The increase in methanol selectivity and activity when Zr is impregnated onto CuZn-350 indicate that a third kind of active site is present for the Zr/CuZr-350 catalyst, namely (iii) Cu-ZrO_2 interfacial sites. Interestingly, the initial methanol selectivity of the Zr/CuZn-350 catalyst is above 60 % at ~12% conversion. However, the methanol selectivity and CO_2 conversion rapidly decrease and stabilize at 46.4% and 9.5%, respectively (Figure S7). In contrast, the activity of the CuZn-350 catalyst is relatively stable (Figure S7). Nevertheless, the incorporation of ZrO_2 increases the number of active sites for methanol synthesis at steady-state, resulting in a higher methanol selectivity compared to CuZn-350.

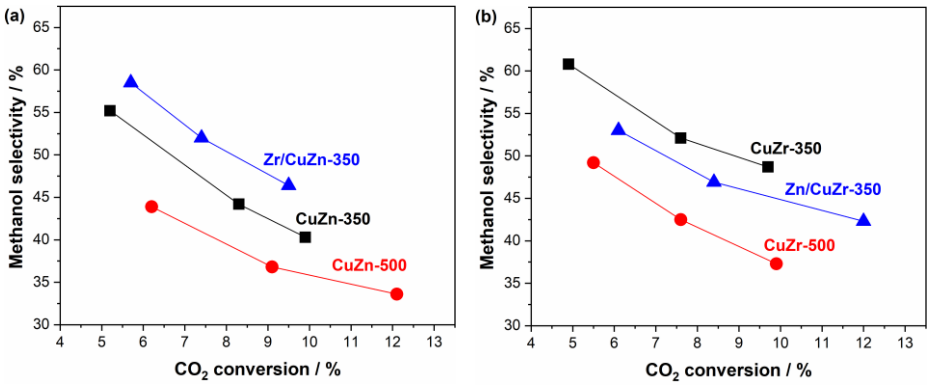

Figure 11. Methanol selectivity as a function of CO_2 conversion for (a) CuZn-350, CuZn-500, and Zr/CuZn-350; and (b) CuZr-350, CuZr-500, and Zr/CuZn-350 catalysts. Reaction conditions: 230 °C, 30 bar, H_2/CO_2 = 3.

It can be seen in Figure 11b that the methanol selectivity is significantly higher for the CuZr-350 catalysts compared to CuZr-500. Generally, three types of active sites are probably present for these catalysts, namely (i) surface metallic Cu, (ii) Cu/*a*-ZrO_2, and (iii) Cu/*t*-ZrO_2. It has been reported that the methanol synthesis activity of Cu supported on *a*-ZrO_2 is higher than that of *t*-ZrO_2 (Tada et al., 2018b). Therefore, the lower methanol selectivity of CuZr-500 is attributed to the transformation of *a*-ZrO_2 into *t*-ZrO_2, as indicated by XRD (Figure S1d). Based on the CO_2-TPD results, one of the reasons for the higher activity of Cu/*a*-ZrO_2 is probably due to the presence of a significantly higher fraction of moderate basic sites. The methanol selectivity decreases when Zn is impregnated onto the CuZr-350 catalyst. A drop in moderate basic sites is also evident for Zn/CuZr-350, indicating a smaller number of interfacial Cu/*a*-ZrO_2 sites for CO_2 activation and conversion to

methanol. We calcined the CuZr-350 catalyst again at 350 °C for 3 h (CuZr-350*) to investigate the effect of the additional heat treatment on the impregnated catalysts. The methanol selectivity of CuZr-350* is slightly higher than that of Zn/CuZr-350, indicating that the addition of Zn decreases the number of active interfacial sites and thereby the methanol selectivity of the catalyst.

3.2.2 Influence of In on CuZn and CuZr catalysts

The steady-state methanol formation rates of the CuZn-350*, In/CuZn-350, CuZr-350, CuZr-350*, CuZrIn-350, and In/CuZr-350 catalysts at 230 °C and 270 °C are shown in Figure 12. A significant decrease in the methanol formation rate is observed when In is impregnated onto the CuZn-350 and CuZr-350 catalysts. This can be explained by the lower Cu surface area and a decrease in the number of MB sites. Interestingly, the methanol formation rate of the CuZrIn-350 catalyst is clearly higher than that of CuZr-350 at 270 °C. The activity of the In/CuZr-350 catalyst also increases more strongly than CuZr-350 when the temperature is increased. The ratio of high-temperature MB sites to the total amount of MB sites ($A_{HT\text{-}MB}/A_{MB}$, Table 3) is higher for CuZrIn-350 and In/CuZr-350 compared to the CuZr-350, Zn/CuZr-350, and CuZr-500 (Table S1) catalysts. This shift in the basic site composition might be related to the presence of In-Zr mixed oxide sites. Typically, In_2O_3 and ZrO_2-promoted In_2O_3 catalysts are reported to require higher temperatures than Cu/ZnO and Cu/ZrO_2 to achieve significant methanol synthesis activity (Chou

and Lobo, 2019; Dang et al., 2020; Frei et al., 2019; Martin et al., 2016). Therefore, the superior activity of CuZrIn-350 at 270 °C might be related to the contribution of In-Zr mixed oxide sites that are not particularly active at 230 °C.

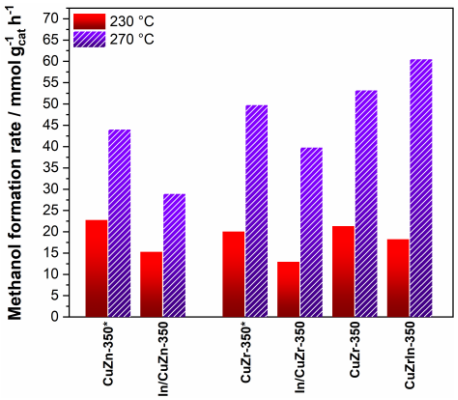

Figure 12. Methanol formation rates for the CuZn-350*, In/CuZn-350, CuZr-350, CuZr-350*, CuZrIn-350, and In/CuZr-350 catalysts. Reaction conditions: 30 bar, 80 000 $cm^3/(g_{cat}\,h)$, $H_2/CO_2 = 3$.

The methanol selectivity as a function of CO_2 conversion is plotted for the CuZn-350*, In/CuZn-350, CuZr-350*, CuZrIn-350, and In/CuZr-350 catalysts at 230 °C and 270 °C in Figure 13a and b, respectively. It can be seen that the trend curves appear at higher methanol selectivity when In is impregnated onto the CuZn-350 and CuZr-350 catalysts at both temperatures. For the CuZrIn-350 catalyst, the methanol selectivity is higher than the CuZr-350* catalyst only at 270 °C. Furthermore, the methanol selectivity is more significantly improved for In/CuZr-350 and CuZrIn-350 compared to In/CuZn-350 when the reaction temperature is increased. The activity of the CuIn-350 catalyst was negligible at 270 °C

(see Table S1 for summary of characterization results of CuIn-350). Therefore, In addition to the catalysts might improve the methanol selectivity in two different ways: (i) by decreasing the number of metallic Cu sites for the RWGS reaction by forming Cu_xIn_y surface species; and (ii) generating In-Zr mixed oxide sites for methanol synthesis. For the In/CuZn-350 catalyst, the methanol selectivity is probably improved due to a decrease in metallic Cu sites, whereas a combination of (i) and (ii) explains the performance of the In/CuZr-350 catalyst. On the other hand, the results of the CuZrIn-350 catalyst indicate that Cu_xIn_y surface species are not present for this catalyst. This is probably due to the lower In content and a consequence of the preparation method, which leads to In being mostly incorporated into the bulk of Cu and the ZrO_2 phase. It is also likely that this helps stabilize the interfacial sites, which limits the deactivation of CuZrIn-350 compared to CuZr-350 at 270 °C (Figure S8).

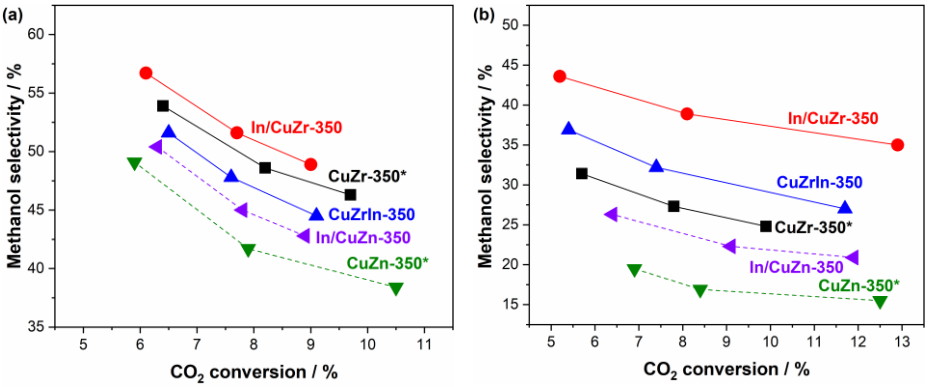

Figure 13. Methanol selectivity as a function of CO_2 conversion for the CuZn-350*, In/CuZn-350, CuZr-350*, CuZrIn-350, and In/CuZr-350

catalysts at (a) 230 °C and (b) 270 °C. Reaction conditions: 30 bar, $H_2/CO_2 = 3$.

3.2.3 Influence of surface properties on catalytic performance

Figure 14 shows the STY of methanol as a function of the Cu surface area. It can be seen that a higher Cu surface area generally enhances the methanol formation rate. However, the Cu surface area of the CuZn-500 catalyst is comparable to that of CuZn-350 and Zr/CuZn-350, but the STY of methanol is significantly lower. Microstrain in Cu crystallites has been suggested to influence the activity of Cu-based catalysts for methanol synthesis, steam reforming of methanol, and low-temperature water-gas shift reaction (Behrens et al., 2012; Chen et al., 1999; Choi et al., 2001; Fujitani and Nakamura, 1998, 2000; Kurtz et al., 2004; Nakamura et al., 1996b). This phenomenon has been proposed to arise due to the presence of (i) Zn in the bulk, (ii) incomplete reduction of CuO, and (iii) epitaxial bonding of the ZnO lattice to Cu (Günter et al., 2001). The higher calcination temperature might have reduced the number of defects in the Cu particles and thereby contributed to the lower methanol formation rate of the CuZn-500 catalyst. It can also be observed that the CuZrIn-350 catalyst is less active at 230 °C than CuZr-350 despite having a higher Cu surface area. Thus, the results indicate that the Cu surface area is not the only factor that influences the activity of the catalysts.

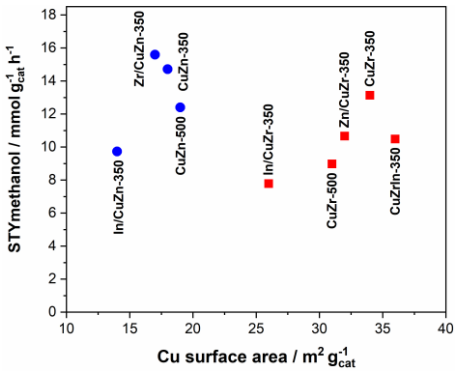

Figure 14. STY of methanol at 230 °C as a function of Cu surface area for the CuZn and CuZr catalysts.

The STY of methanol as a function of the relative number of MB sites is shown in Figure 15. A correlation between the methanol formation rate and the number of MB sites can be observed with the exception of the In/CuZn-350 catalyst. There is strong evidence that the methanol synthesis activity of Cu-based catalysts is critically linked to the interfacial sites for various Cu-metal oxide systems, such as ZnO (Behrens et al., 2012; Fujitani et al., 1997a; Fujitani et al., 1997b; Kattel et al., 2017; Martinez-Suarez et al., 2015; Nakamura et al., 1996a; Reichenbach et al., 2018; Zheng et al., 2020), ZrO_2 (Arena et al., 2008; Fujiwara et al., 2019; Gao et al., 2012; Larmier et al., 2017; Samson et al., 2014; Tada et al., 2018a; Tada et al., 2018b; Wang et al., 2019b; Witoon et al., 2016), CeO_2 (Graciani et al., 2014; Senanayake et al., 2016), and LaO_2 (Chen et al., 2019). A correlation between the methanol synthesis activity and the basicity of Cu-based catalysts has been reported in literature (Gao et al., 2013; Gao et al., 2016; Guo et al., 2011; Wang et al., 2019a). Thus, the results indicate that the number of

interfacial sites is reflected by the MB sites and is an important descriptor of the methanol synthesis activity over these catalysts.

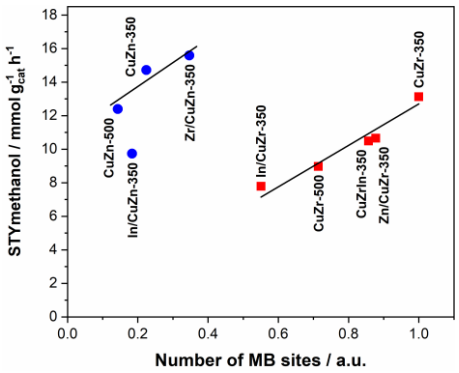

Figure 15. STY of methanol at 230 °C as a function of the relative number of MB sites for the CuZn and CuZr catalysts.

5. Conclusion

The model catalysts investigated in this work provides insights into the generation and inhibition of active sites of Cu-based catalysts for CO_2 hydrogenation. The impregnation of a small amount of ZrO_2 onto Cu/ZnO significantly improves the methanol selectivity of the catalyst. Furthermore, the initial methanol formation rate is approximately two times higher for the ZrO_2-containing Cu/ZnO catalyst. The introduction of ZrO_2 generates medium-strength basic sites for CO_2 activation and conversion to methanol. However, the catalyst deactivates rapidly, but the steady-state methanol selectivity and methanol formation rate (15.6 mmol/gcat) are still higher than the unpromoted Cu/ZnO catalyst (14.7 mmol/gcat). In contrast, when ZnO is impregnated onto Cu/ZrO_2, both

the methanol selectivity and methanol formation rate are reduced. This is attributed to a decrease in surface basicity, resulting in a lower amount of Cu-ZrO_2 interfacial sites that can facilitate CO_2 conversion into methanol.

We also demonstrate that In can inhibit the RWGS reaction on the Cu/ZnO and Cu/ZrO_2 catalysts. The results suggest that inactive Cu_xIn_y surface species are formed that block CO production on the Cu surface. Furthermore, the methanol formation rate increases from 52.7 to 60.5 mmol/g_{cat} at 270 °C when 0.3 mol% In is incorporated into the Cu/ZrO_2 catalyst by co-precipitation. The higher activity of In-doped Cu/ZrO_2 is attributed to In-Zr mixed oxide sites that are more active for methanol synthesis at higher temperatures. It is also demonstrated that In improves the stability of the catalyst, which is attributed to the presence of In in the bulk of Cu and in the ZrO_2 phase that stabilizes the interfacial sites. The present findings provide insight into tuning the active sites and enhancing the stability of Cu-based catalyst promoted by metal oxides for CO_2 hydrogenation to methanol.

Acknowledgements

The authors would like to thank the financial support from the Norwegian Ministry of Education and Research and the Department of Energy and Petroleum Engineering, University of Stavanger for this project.

References

Arena, F., Italiano, G., Barbera, K., Bordiga, S., Bonura, G., Spadaro, L., Frusteri, F., 2008. Solid-state interactions, adsorption sites and functionality of Cu-ZnO/ZrO_2 catalysts in the CO_2 hydrogenation to CH_3OH. Applied Catalysis A: General 350, 16-23. https://doi.org/10.1016/j.apcata.2008.07.028

Aresta, M., Dibenedetto, A., Quaranta, E., 2016. State of the art and perspectives in catalytic processes for CO_2 conversion into chemicals and fuels: The distinctive contribution of chemical catalysis and biotechnology. Journal of catalysis 343, 2-45. https://doi.org/10.1016/j.jcat.2016.04.003

Baiker, A., Kilo, M., Maciejewski, M., Menzi, S., Wokaun, A., 1993. Hydrogenation of CO_2 over copper, silver and gold/zirconia catalysts: Comparative study of catalyst properties and reaction pathways, Studies in Surface Science and Catalysis. Elsevier, pp. 1257-1272. https://doi.org/10.1016/S0167-2991(08)64449-3

Behrens, M., Girgsdies, F., Trunschke, A., Schlögl, R., 2009. Minerals as model compounds for Cu/ZnO catalyst precursors: structural and thermal properties and IR spectra of mineral and synthetic (zincian) malachite, rosasite and aurichalcite and a catalyst precursor mixture. European Journal of Inorganic Chemistry 2009, 1347-1357. https://doi.org/10.1002/ejic.200801216

Behrens, M., Schlögl, R., 2013. How to prepare a good Cu/ZnO catalyst or the role of solid state chemistry for the synthesis of nanostructured catalysts. Zeitschrift für anorganische und allgemeine Chemie 639, 2683-2695. https://doi.org/10.1002/zaac.201300356

Behrens, M., Studt, F., Kasatkin, I., Kühl, S., Hävecker, M., Abild-Pedersen, F., Zander, S., Girgsdies, F., Kurr, P., Kniep, B.-L., 2012. The active site of methanol synthesis over Cu/ZnO/Al_2O_3 industrial catalysts. Science 336, 893-897. https://doi.org/10.1126/science.1219831

Bönicke, I.A., Kirstein, W., Thieme, F., 1994. A study on CO_2 dissociation on a stepped (332) copper surface. Surface science 307, 177-181. https://doi.org/10.1016/0039-6028(94)90390-5

Chatterjee, R., Kuld, S., van den Berg, R., Chen, A., Shen, W., Christensen, J.M., Jensen, A.D., Sehested, J., 2019. Mapping support interactions in copper catalysts. Topics in catalysis 62, 649-659. https://doi.org/10.1007/s11244-019-01150-9

Chen, H., Lau, S., Chen, L., Lin, J., Huan, C.H., Tan, K., Pan, J., 1999. Synergism between Cu and Zn sites in Cu/Zn catalysts for methanol synthesis. Applied Surface Science 152, 193-199. https://doi.org/10.1016/S0169-4332(99)00317-7

Chen, K., Fang, H., Wu, S., Liu, X., Zheng, J., Zhou, S., Duan, X., Zhuang, Y., Tsang, S.C.E., Yuan, Y., 2019. CO_2 hydrogenation to methanol over Cu catalysts supported on La-modified SBA-15: The crucial role of Cu–LaO_x interfaces. Applied Catalysis B: Environmental 251, 119-129. https://doi.org/10.1016/j.apcatb.2019.03.059

Choi, Y., Futagami, K., Fujitani, T., Nakamura, J., 2001. The role of ZnO in Cu/ZnO methanol synthesis catalysts—morphology effect or active site model? Applied Catalysis A: General 208, 163-167. https://doi.org/10.1016/S0926-860X(00)00712-2

Chou, C.-Y., Lobo, R.F., 2019. Direct conversion of CO_2 into methanol over promoted indium oxide-based catalysts. Applied Catalysis A: General 583, 117144. https://doi.org/10.1016/j.apcata.2019.117144

Dang, S., Qin, B., Yang, Y., Wang, H., Cai, J., Han, Y., Li, S., Gao, P., Sun, Y., 2020. Rationally designed indium oxide catalysts for CO_2 hydrogenation to methanol with high activity and selectivity. Science Advances 6, eaaz2060. https://doi.org/10.1126/sciadv.aaz2060

Denise, B., Sneeden, R., 1986. Oxide-supported copper catalysts prepared from copper formate: Differences in behavior in methanol synthesis from CO/H_2 and CO_2/H_2 mixtures. Applied Catalysis 28, 235-239. https://doi.org/10.1016/S0166-9834(00)82507-5

Fichtl, M.B., Schumann, J., Kasatkin, I., Jacobsen, N., Behrens, M., Schlögl, R., Muhler, M., Hinrichsen, O., 2014. Counting of oxygen defects versus metal surface sites in methanol synthesis catalysts by different probe molecules. Angewandte Chemie International Edition 53, 7043-7047. https://doi.org/10.1002/anie.201400575

Frei, M.S., Mondelli, C., García-Muelas, R., Kley, K.S., Puértolas, B., López, N., Safonova, O.V., Stewart, J.A., Ferré, D.C., Pérez-Ramírez, J., 2019. Atomic-scale engineering of indium oxide promotion by palladium for methanol production via CO_2 hydrogenation. Nature communications 10, 1-11. https://doi.org/10.19061/iochem-bd-1-106

Fujitani, T., Nakamura, I., Uchijima, T., Nakamura, J., 1997a. The kinetics and mechanism of methanol synthesis by hydrogenation of CO_2 over a Zn-deposited Cu(111) surface. Surface science 383, 285-298. https://doi.org/10.1016/S0039-6028(97)00192-1

Fujitani, T., Nakamura, I., Ueno, S., Uchijima, T., Nakamura, J., 1997b. Methanol synthesis by hydrogenation of CO_2 over a Zn-deposited Cu(111): formate intermediate. Applied Surface Science 121, 583-586. https://doi.org/10.1016/S0169-4332(97)00372-3

Fujitani, T., Nakamura, J., 1998. The effect of ZnO in methanol synthesis catalysts on Cu dispersion and the specific activity. Catalysis Letters 56, 119-124. https://doi.org/10.1023/A:1019000927366

Fujitani, T., Nakamura, J., 2000. The chemical modification seen in the Cu/ZnO methanol synthesis catalysts. Applied Catalysis A: General 191, 111-129. https://doi.org/10.1016/S0926-860X(99)00313-0

Fujiwara, K., Tada, S., Honma, T., Sasaki, H., Nishijima, M., Kikuchi, R., 2019. Influences of particle size and crystallinity of highly loaded CuO/ZrO_2 on CO_2 hydrogenation to methanol. AIChE Journal 65, e16717. https://doi.org/10.1002/aic.16717

Gao, J., Song, F., Li, Y., Cheng, W., Yuan, H., Xu, Q., 2020. Cu2In nanoalloy enhanced performance of Cu/ZrO_2 catalysts for the CO_2 hydrogenation to methanol. Industrial Engineering Chemistry Research. https://doi.org/10.1021/acs.iecr.9b06956

Gao, P., Li, F., Xiao, F., Zhao, N., Sun, N., Wei, W., Zhong, L., Sun, Y., 2012. Preparation and activity of Cu/Zn/Al/Zr catalysts via hydrotalcite-containing precursors for methanol synthesis from CO_2 hydrogenation. Catalysis Science Technology 2, 1447-1454. https:/doi.org/10.1039/C2CY00481J

Gao, P., Li, F., Zhao, N., Xiao, F., Wei, W., Zhong, L., Sun, Y., 2013. Influence of modifier (Mn, La, Ce, Zr and Y) on the performance of Cu/Zn/Al catalysts

via hydrotalcite-like precursors for CO_2 hydrogenation to methanol. Applied Catalysis A: General 468, 442-452. https://doi.org/10.1016/j.apcata.2013.09.026

Gao, P., Yang, H., Zhang, L., Zhang, C., Zhong, L., Wang, H., Wei, W., Sun, Y., 2016. Fluorinated Cu/Zn/Al/Zr hydrotalcites derived nanocatalysts for CO_2 hydrogenation to methanol. Journal of CO_2 Utilization 16, 32-41. https://doi.org/10.1016/j.jcou.2016.06.001

Gervasini, A., Bennici, S., 2005. Dispersion and surface states of copper catalysts by temperature-programmed-reduction of oxidized surfaces (s-TPR). Applied Catalysis A: General 281, 199-205. https://doi.org/10.1016/j.apcata.2004.11.030

Graciani, J., Mudiyanselage, K., Xu, F., Baber, A.E., Evans, J., Senanayake, S.D., Stacchiola, D.J., Liu, P., Hrbek, J., Sanz, J.F., 2014. Highly active copper-ceria and copper-ceria-titania catalysts for methanol synthesis from CO_2. Science 345, 546-550. https://doi.org/10.1126/science.1253057

Günter, M.M., Ressler, T., Bems, B., Büscher, C., Genger, T., Hinrichsen, O., Muhler, M., Schlögl, R., 2001. Implication of the microstructure of binary Cu/ZnO catalysts for their catalytic activity in methanol synthesis. Catalysis Letters 71, 37-44. https://doi.org/10.1023/A:1016696022840

Guo, X., Mao, D., Lu, G., Wang, S., Wu, G., 2011. The influence of La doping on the catalytic behavior of Cu/ZrO_2 for methanol synthesis from CO_2 hydrogenation. Journal of Molecular Catalysis A: Chemical 345, 60-68. https://doi.org/10.1016/j.molcata.2011.05.019

Jansen, W., Beckers, J., vd Heuvel, J., vd Gon, A.D., Bliek, A., Brongersma, H., 2002. Dynamic behavior of the surface structure of $Cu/ZnO/SiO_2$ catalysts. Journal of catalysis 210, 229-236. https://doi.org/10.1006/jcat.2002.3679

Jung, K.T., Bell, A.T., 2002. Effects of zirconia phase on the synthesis of methanol over zirconia-supported copper. Catalysis Letters 80, 63-68. https://doi.org/10.1023/A:1015326726898

Kattel, S., Ramírez, P.J., Chen, J.G., Rodriguez, J.A., Liu, P., 2017. Active sites for CO_2 hydrogenation to methanol on Cu/ZnO catalysts. Science 355, 1296-1299. https://doi.org/10.1126/science.aal3573

Kondrat, S.A., Smith, P.J., Lu, L., Bartley, J.K., Taylor, S.H., Spencer, M.S., Kelly, G.J., Park, C.W., Kiely, C.J., Hutchings, G.J., 2018. Preparation of a highly active ternary Cu-Zn-Al oxide methanol synthesis catalyst by supercritical CO_2 anti-solvent precipitation. Catalysis Today 317, 12-20. https://doi.org/10.1016/j.cattod.2018.03.046

Kondrat, S.A., Smith, P.J., Wells, P.P., Chater, P.A., Carter, J.H., Morgan, D.J., Fiordaliso, E.M., Wagner, J.B., Davies, T.E., Lu, L., 2016. Stable amorphous georgeite as a precursor to a high-activity catalyst. Nature 531, 83-87. http://dx.doi.org/10.17035/d.2015.0008102108

Köppel, R.A., Stöcker, C., Baiker, A., 1998. Copper-and silver–zirconia aerogels: preparation, structural properties and catalytic behavior in methanol synthesis from carbon dioxide. Journal of catalysis 179, 515-527. https://doi.org/10.1006/jcat.1998.2252

Kühl, S., Tarasov, A., Zander, S., Kasatkin, I., Behrens, M., 2014. Cu-Based Catalyst Resulting from a Cu, Zn, Al Hydrotalcite-Like Compound: A Microstructural, Thermoanalytical, and In Situ XAS Study. Chemistry–A European Journal 20, 3782-3792. https://doi.org/10.1002/chem.201302599

Kuld, S., Conradsen, C., Moses, P.G., Chorkendorff, I., Sehested, J., 2014. Quantification of zinc atoms in a surface alloy on copper in an industrial-type methanol synthesis catalyst. Angewandte Chemie 126, 6051-6055. https://doi.org/10.1002/ange.201311073

Kurtz, M., Bauer, N., Büscher, C., Wilmer, H., Hinrichsen, O., Becker, R., Rabe, S., Merz, K., Driess, M., Fischer, R.A., 2004. New synthetic routes to more active Cu/ZnO catalysts used for methanol synthesis. Catalysis Letters 92, 49-52. https://doi.org/10.1023/B:CATL.0000011085.88267.a6

Larmier, K., Liao, W.C., Tada, S., Lam, E., Verel, R., Bansode, A., Urakawa, A., Comas-Vives, A., Copéret, C., 2017. CO_2-to-methanol hydrogenation on zirconia-supported copper nanoparticles: reaction intermediates and the role of the metal–support interface. Angewandte Chemie International Edition 56, 2318-2323. https://doi.org/10.1002/anie.201610166

Liang, B., Ma, J., Su, X., Yang, C., Duan, H., Zhou, H., Deng, S., Li, L., Huang, Y., 2019. Investigation on deactivation of $Cu/ZnO/Al_2O_3$ catalyst for CO_2 hydrogenation to methanol. Industrial Engineering Chemistry Research 58, 9030-9037. https://doi.org/10.1021/acs.iecr.9b01546

Ma, Z.-Y., Yang, C., Wei, W., Li, W.-H., Sun, Y.-H., 2005. Catalytic performance of copper supported on zirconia polymorphs for CO hydrogenation. Journal of Molecular Catalysis A: Chemical 231, 75-81. https://doi.org/10.1016/j.molcata.2004.12.026

Martin, O., Martín, A.J., Mondelli, C., Mitchell, S., Segawa, T.F., Hauert, R., Drouilly, C., Curulla-Ferré, D., Pérez-Ramírez, J., 2016. Indium oxide as a superior catalyst for methanol synthesis by CO_2 hydrogenation. Angewandte Chemie International Edition 55, 6261-6265. https://doi.org/10.1002/anie.201600943

Martinez-Suarez, L., Siemer, N., Frenzel, J., Marx, D., 2015. Reaction network of methanol synthesis over Cu/ZnO nanocatalysts. Acs Catalysis 5, 4201-4218. https://doi.org/10.1021/acscatal.5b00442

Nakamura, I., Fujitani, T., Uchijima, T., Nakamura, J., 1996a. A model catalyst for methanol synthesis: Zn-deposited and Zn-free Cu surfaces. Journal of Vacuum Science & Technology A: Vacuum, Surfaces, and Films 14, 1464-1468. https://doi.org/10.1116/1.579970

Nakamura, J., Uchijima, T., Kanai, Y., Fujitani, T., 1996b. The role of ZnO in Cu/ZnO methanol synthesis catalysts. Catalysis Today 28, 223-230. https://doi.org/10.1016/0920-5861(95)00240-5

Reichenbach, T., Mondal, K., Jäger, M., Vent-Schmidt, T., Himmel, D., Dybbert, V., Bruix, A., Krossing, I., Walter, M., Moseler, M., 2018. Ab initio study of CO_2 hydrogenation mechanisms on inverse ZnO/Cu catalysts. Journal of catalysis 360, 168-174. https://doi.org/10.1016/j.jcat.2018.01.035

Rhodes, M.D., Bell, A.T., 2005. The effects of zirconia morphology on methanol synthesis from CO and H2 over Cu/ZrO_2 catalysts: Part I. Steady-state studies. Journal of catalysis 233, 198-209. https://doi.org/10.1016/j.jcat.2005.04.026

Ro, I., Liu, Y., Ball, M.R., Jackson, D.H., Chada, J.P., Sener, C., Kuech, T.F., Madon, R.J., Huber, G.W., Dumesic, J.A., 2016. Role of the $Cu\text{-}ZrO_2$ interfacial sites for conversion of ethanol to ethyl acetate and synthesis of

methanol from CO_2 and H_2. Acs Catalysis 6, 7040-7050. https://doi.org/10.1021/acscatal.6b01805

Rungtaweevoranit, B., Baek, J., Araujo, J.R., Archanjo, B.S., Choi, K.M., Yaghi, O.M., Somorjai, G.A., 2016. Copper nanocrystals encapsulated in Zr-based metal–organic frameworks for highly selective CO_2 hydrogenation to methanol. Nano letters 16, 7645-7649. https://doi.org/10.1021/acs.nanolett.6b03637

Sadeghinia, M., Rezaei, M., Kharat, A.N., Jorabchi, M.N., Nematollahi, B., Zareiekordshouli, F., 2020. Effect of In_2O_3 on the structural properties and catalytic performance of the $CuO/ZnO/Al_2O_3$ catalyst in CO_2 and CO hydrogenation to methanol. Molecular Catalysis 484, 110776. https://doi.org/10.1016/j.mcat.2020.110776

Samson, K., Sliwa, M., Socha, R.P., Góra-Marek, K., Mucha, D., Rutkowska-Zbik, D., Paul, J., Ruggiero-Mikołajczyk, M., Grabowski, R., Słoczynski, J., 2014. Influence of ZrO_2 structure and copper electronic state on activity of Cu/ZrO_2 catalysts in methanol synthesis from CO_2. Acs Catalysis 4, 3730-3741. https://doi.org/10.1021/cs500979c

Senanayake, S.D., Ramírez, P.J., Waluyo, I., Kundu, S., Mudiyanselage, K., Liu, Z., Liu, Z., Axnanda, S., Stacchiola, D.J., Evans, J., 2016. Hydrogenation of CO_2 to Methanol on $CeO_x/Cu(111)$ and ZnO/Cu(111) Catalysts: Role of the Metal–Oxide Interface and Importance of Ce^{3+} Sites. The Journal of Physical Chemistry C 120, 1778-1784. https://doi.org/10.1021/acs.jpcc.5b12012

Shi, Z., Tan, Q., Tian, C., Pan, Y., Sun, X., Zhang, J., Wu, D., 2019. CO_2 hydrogenation to methanol over Cu-In intermetallic catalysts: Effect of reduction temperature. Journal of catalysis 379, 78-89. https://doi.org/10.1016/j.jcat.2019.09.024

Słoczyński, J., Grabowski, R., Olszewski, P., Kozłowska, A., Stoch, J., Lachowska, M., Skrzypek, J., 2006. Effect of metal oxide additives on the activity and stability of $Cu/ZnO/ZrO_2$ catalysts in the synthesis of methanol from CO_2 and H_2. Applied Catalysis A: General 310, 127-137. https://doi.org/10.1016/j.apcata.2006.05.035

Studt, F., Behrens, M., Kunkes, E.L., Thomas, N., Zander, S., Tarasov, A., Schumann, J., Frei, E., Varley, J.B., Abild-Pedersen, F., 2015. The mechanism of CO and CO_2 hydrogenation to methanol over Cu-based catalysts. ChemCatChem 7, 1105-1111. https://doi.org/10.1002/cctc.201500123

Tada, S., Katagiri, A., Kiyota, K., Honma, T., Kamei, H., Nariyuki, A., Uchida, S., Satokawa, S., 2018a. Cu species incorporated into amorphous ZrO_2 with high activity and selectivity in CO_2-to-methanol hydrogenation. The Journal of Physical Chemistry C 122, 5430-5442. https://doi.org/10.1021/acs.jpcc.7b11284

Tada, S., Kayamori, S., Honma, T., Kamei, H., Nariyuki, A., Kon, K., Toyao, T., Shimizu, K.-i., Satokawa, S., 2018b. Design of interfacial sites between Cu and amorphous ZrO_2 dedicated to CO_2-to-methanol hydrogenation. Acs Catalysis 8, 7809-7819. https://doi.org/10.1021/acscatal.8b01396

Tarasov, A., Schumann, J., Girgsdies, F., Thomas, N., Behrens, M., 2014. Thermokinetic investigation of binary Cu/Zn hydroxycarbonates as precursors for Cu/ZnO catalysts. Thermochimica Acta 591, 1-9. https://doi.org/10.1016/j.tca.2014.04.025

Topsøe, H., Ovesen, C., Clausen, B., Topsøe, N.-Y., Nielsen, P.H., Törnqvist, E., Nørskov, J., 1997. Importance of dynamics in real catalyst systems, Studies in Surface Science and Catalysis. Elsevier, pp. 121-139. https://doi.org/10.1016/S0167-2991(97)80402-8

Topsøe, N.-Y., Topsøe, H., 1999. FTIR studies of dynamic surface structural changes in Cu-based methanol synthesis catalysts. Journal of Molecular Catalysis A: Chemical 141, 95-105. https://doi.org/10.1016/S1381-1169(98)00253-2

Van Den Berg, R., Prieto, G., Korpershoek, G., Van Der Wal, L.I., Van Bunningen, A.J., Lægsgaard-Jørgensen, S., De Jongh, P.E., De Jong, K.P., 2016. Structure sensitivity of Cu and CuZn catalysts relevant to industrial methanol synthesis. Nature communications 7, 1-7. https://doi.org/10.1038/ncomms13057

Van Der Grift, C., Wielers, A., Jogh, B., Van Beunum, J., De Boer, M., Versluijs-Helder, M., Geus, J., 1991. Effect of the reduction treatment on the structure and reactivity of silica-supported copper particles. Journal of catalysis 131, 178-189. https://doi.org/10.1016/0021-9517(91)90334-Z

Wang, G., Mao, D., Guo, X., Yu, J., 2019a. Methanol synthesis from CO_2 hydrogenation over CuO-ZnO-ZrO_2-M_xO_y catalysts (M= Cr, Mo and W). International Journal of Hydrogen Energy 44, 4197-4207. https://doi.org/10.1016/j.ijhydene.2018.12.131

Wang, Y., Kattel, S., Gao, W., Li, K., Liu, P., Chen, J.G., Wang, H., 2019b. Exploring the ternary interactions in Cu–ZnO–ZrO_2 catalysts for efficient CO_2 hydrogenation to methanol. Nature communications 10, 1-10. https://doi.org/10.1038/s41467-019-09072-6

Witoon, T., Chalorngtham, J., Dumrongbunditkul, P., Chareonpanich, M., Limtrakul, J., 2016. CO_2 hydrogenation to methanol over Cu/ZrO_2 catalysts: Effects of zirconia phases. Chemical Engineering Journal 293, 327-336. https://doi.org/10.1016/j.cej.2016.02.069

Zhang, G., Fan, G., Yang, L., Li, F., 2020. Tuning surface-interface structures of ZrO_2 supported copper catalysts by in situ introduction of indium to promote CO_2 hydrogenation to methanol. Applied Catalysis A: General, 117805. https://doi.org/10.1016/j.apcata.2020.117805

Zhao, Y., Shan, B., Wang, Y., Zhou, J., Wang, S., Ma, X., 2018. An effective CuZn–SiO_2 bimetallic catalyst prepared by hydrolysis precipitation method for the hydrogenation of methyl acetate to ethanol. Industrial Engineering Chemistry Research 57, 4526-4534. https://doi.org/10.1021/acs.iecr.7b05391

Zheng, H., Narkhede, N., Han, L., Zhang, H., Li, Z., 2020. Methanol synthesis from CO_2: a DFT investigation on Zn-promoted Cu catalyst. Research on Chemical Intermediates 46, 1749-1769. https://doi.org/10.1007/s11164-019-04061-2

Supporting Information

Tuning the interfacial sites between copper and metal oxides (Zn, Zr, In) for CO_2 hydrogenation to methanol

Kristian Stangeland[1], Hans Herrera Nevarro[1], Huong Lan Hoynh[1], Wakshum Mekonnen Tucho[2], Zhixin Yu[1,*]

[1] *Department of Energy and Petroleum Engineering, University of Stavanger, 4036 Stavanger, Norway*

[2] *Department of Mechanical and Structural Engineering and Materials Science, University of Stavanger, 4036 Stavanger, Norway*

*Corresponding author:

Zhixin Yu

Tel.: +47 51 83 22 38;

Fax: +47 51 83 20 50;

E-mail: zhixin.yu@uis.no

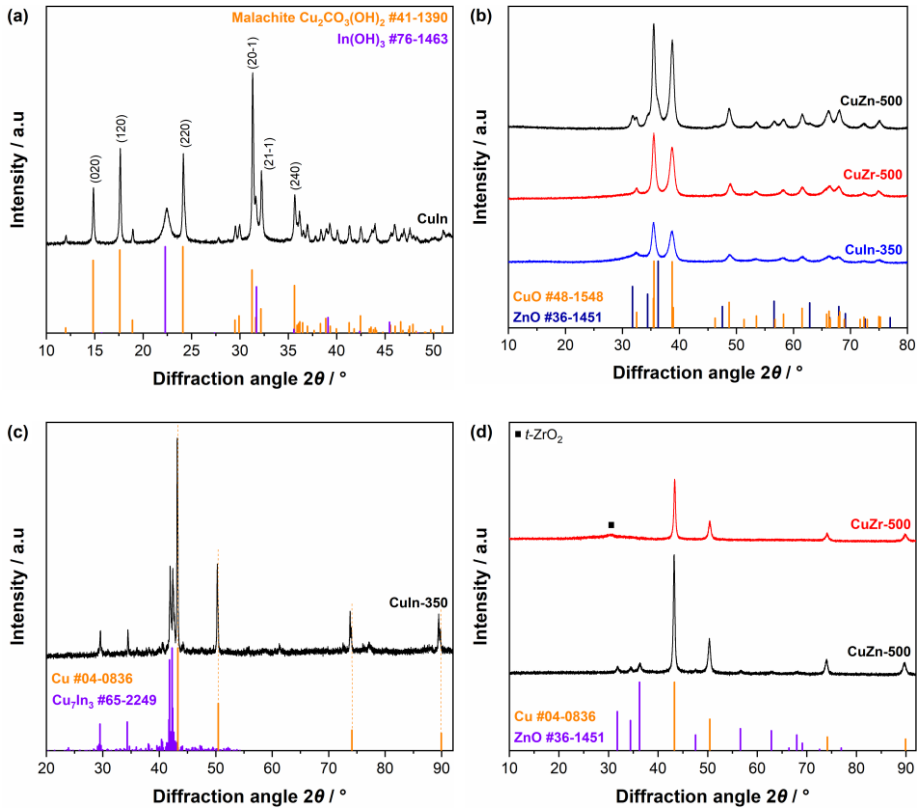

Figure S1. XRD patterns of (a) CuIn precursor; (b) calcined CuIn-350, CuZr-500, and CuZn-500; (c) reduced-passivated CuIn-350; and (d) reduced-passivated CuZn-500 and CuZr-500. It is observed that In does not appear to affect the crystallization process of malachite for the CuIn sample (Figure S1a), as was observed for the CuZrIn precursor. Instead, a second phase is detected for the CuIn precursor with a prominent reflection at 2θ of ~22.3°, corresponding to $In(OH)_3$ (PDF #76-1463). It can be seen in Figure S1c that the peaks of Cu are shifted towards lower diffraction angles after reduction of CuIn-350. This indicates that In is incorporated into the bulk of Cu crystallites. Furthermore, peaks corresponding to Cu_xIn_y alloys are present, which matches fairly well

with that of Cu_7In_3 (PDF #65-2249). Crystalline In_2O_3 species are not detected after reduction. A weak reflection can be observed at ~31° for the CuZr-500 sample (Figure 1d). This is attributed to tetragonal ZrO_2 (*t*-ZrO_2) since its most intense reflection is located in this region. It has also been reported that crystalline *t*-ZrO_2 can form during calcination at 500 °C (1).

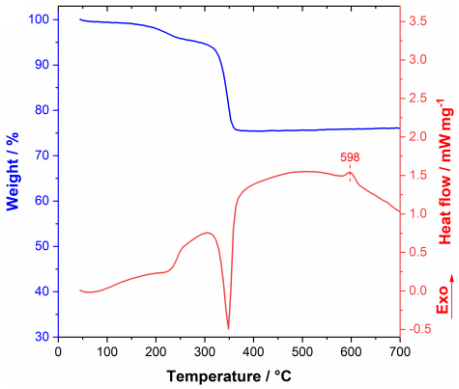

Figure S2. TGA and DSC curves of the CuIn precursor. The additional mass loss and endothermic peak at ca. 240 °C is attributed to the decomposition of $In(OH)_3$ (2). The exothermic peak at 598 °C might be related to structural changes in In_2O_3 or the formation of $Cu_xIn_{(1-x)}O_y$ species.

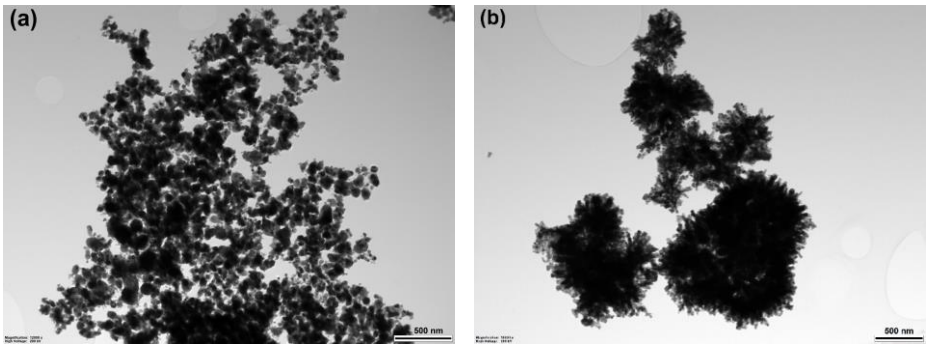

Figure S3. TEM images of the reduced-passivated (a) CuZn-350 and (b) CuZr-350 catalyst.

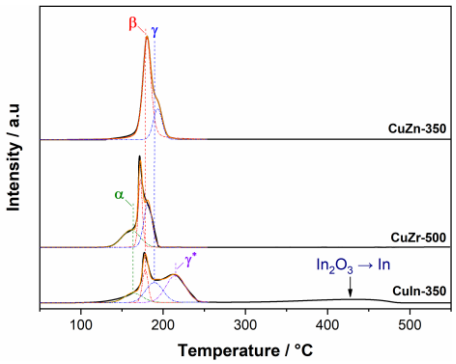

Figure S4. TPR patterns of CuIn-350, CuZr-500, and CuZn-500. The γ^{*}-peak present for CuIn-350 might be related to bulk CuO species strongly bound to In_2O_3. The wide peak at 350-480 °C is ascribed to the reduction of the In_2O_3 phase.

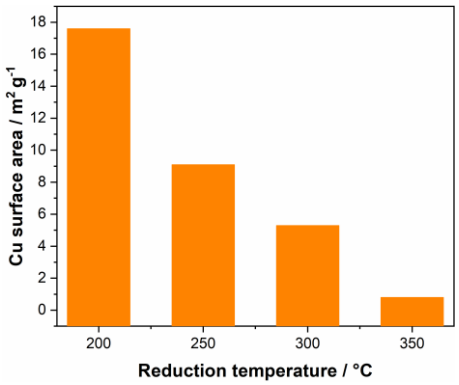

Figure S5. Cu surface area of the CuIn-350 catalyst after reduction at different temperatures.

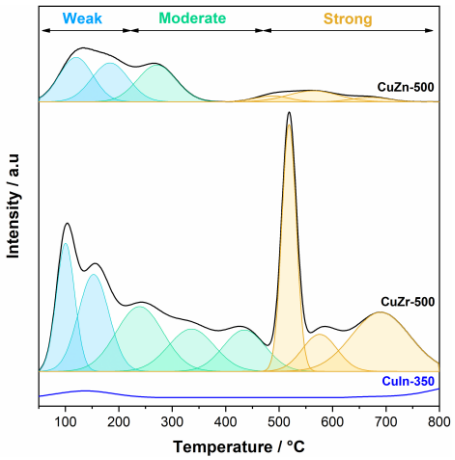

Figure S6. CO_2-TPD of the CuIn-350, CuZr-500, and CuZn-500 catalysts. The number of MB sites is reduced when the CuZn precursor is calcined at 500 °C compared to 350 °C (Table S2). The smaller number of MB sites of CuZr-500 compared to CuZr-350 might be due to the crystallization of *a*-ZrO_2 into *t*-ZrO_2, as indicated by XRD (Figure S1d).

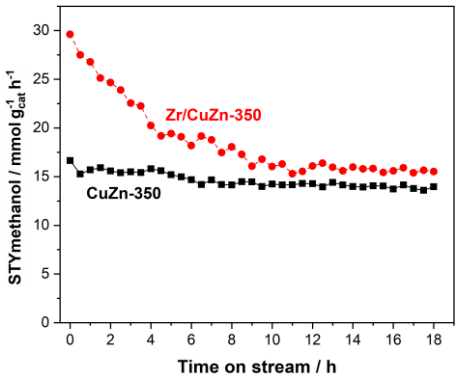

Figure S7. STY of methanol over 18 h TOS at 230 °C for the CuZn-350 and Zr/CuZn-350 catalysts.

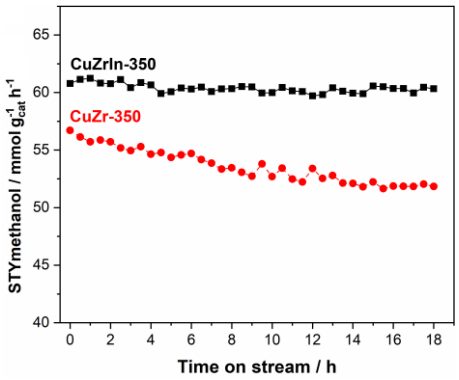

Figure S8. STY of methanol over 18 h TOS at 270 °C for the CuZrIn-350 and CuZr-350 catalysts.

Table S1. Properties of the CuZn-500, CuZr-500, and CuIn-350 catalysts.

	CuZn-500	CuZr-500	CuIn-350
Specific SA[a] / $m^2\ g_{cat}^{-1}$	42	55	74
Pore volume[a] / cm^3/g	0.10	0.14	0.19
Cu SA[b] / $m^2\ g_{cat}^{-1}$	19	31	<1
CuO crystallite size[c] / nm	11.9	9.1	7.9
Cu crystallite size[c] / nm	26.4 (12.8)	23.1	32.6
Metal oxide crystallite size[d] / nm	12.8	n.d.	n.d.
H_2/CuO ratio[d]	0.99	0.97	1.39
Relative number of moderate basic sites[e]	0.14	0.71	–
$A_{HT\text{-}MB}/A_{MB}$	0[f]	0.25[f]	0[f]

[a] BET surface area of the reduced catalysts;

[b] Cu SA determined by N_2O adsorption of reduced catalysts at 350 °C in 7% H_2 for 2 h;

[c] Estimated from XRD by the Scherrer equation;

[d] Calculated from the H_2-TPR peak area;

[e] Relative number of moderate basic sites compared to CuZr-350 estimated by CO_2-TPD;

[f] Ratio of high-temperature MB sites to total number of MB sites.

References

1. Tada S, Kayamori S, Honma T, Kamei H, Nariyuki A, Kon K, et al. Design of interfacial sites between Cu and amorphous ZrO_2 dedicated to CO_2-to-methanol hydrogenation. *ACS Catalysis* 2018;8(9):7809-19.
2. Kim S-H, Choi H-S, Jung K-DJCG, Design. Synthesis of cubic In_2O_3 by a liquid plasma method without chemical additives. *Crystal Growth & Design* 2016;16(3):1387-94.